CUSTOM FIT COMPRESSION TEXTILES WITH ERGONOMIC WEARING COMFORT

SHI YU

PhD

The Hong Kong Polytechnic University

2025

The Hong Kong Polytechnic University

School of Fashion and Textiles

Custom Fit Compression Textiles with Ergonomic Wearing Comfort

Shi Yu

A thesis submitted in partial fulfillment of the requirements for the degree
of Doctor of Philosophy

August 2024

CERTIFICATE OF ORIGINALITY

I hereby declare that this thesis is my own work and that, to the best of my knowledge and belief, it reproduces no material previously published or written, nor material that has been accepted for the award of any other degree or diploma, except where due acknowledgement has been made in the text.

(Signed):

(Name of student): Shi Yu

ABSTRACT

Compression textiles (CTs), as the traditional adjuvant physical interventions, are extensively applied based on the acceptable beneficial effects for the daily healthcare prophylaxis and clinical treatment of chronic venous disorders. However, conventional ready-made CTs with improper morphologies and ill-fitting pressure exertions frequently limit clinical efficacy and user compliance. The exact physical-mechanical working mechanisms of CTs remain controversial, and the wearing comfort also needs to be improved in practical applications. Thus, an efficient and operable design-development-evaluation system to achieve custom fit CTs with ergonomic wearing comfort (EWC) needs to be proposed to promote precision medicine and user adherence. This thesis consists of six parts. In the first part, the influencing mechanisms of the yarn-machinery knitting settings on fabric physical-mechanical properties and pressure behaviors were explored. The obtained findings primarily achieved the fabric morphological and pressure control based on the leg mannequin measurements with ideal circular sectional profiles and rigid material properties. In the second part, the effects of leg morphological variations on compression generations of CTs were investigated. Through the novel body classification and pressure prediction systems, the pressure gap ranges between the irregular bio-bodies and circular leg models were obtained as the recommended pressure redistribution strategies for the bio-design of CTs. In the third part, the biomechanical influences of leg soft tissue stiffness on pressure performances of CTs were explored by the three-dimensional (3D) finite element (FE) modelling, theoretical analysis, and experimental validation studies. In

the fourth part, the FE laid-in loop mesoscale models were constructed to simulate the stress mappings of yarn components to facilitate the selection of yarn material combinations. In the fifth part, the design variables were optimized for the determination of user-oriented production parameters. In the sixth part, through the body characterization, determination of knitting settings, construction of biomechanical systems, and subjective assessments, the biodigital design, development, and biomechanical visualization systems were proposed for the custom fit of CTs with EWC. Therefore, based on the above research objectives and major results, the custom fit CTs were developed with individual functional requirements. This study led the operable guidance for the knitting setting determination, 3D seamless fabrication, pressure performance visualization, and subjective evaluation of user oriented CTs. This study provides fundamental and valuable ideas for the working mechanisms and engineering design principles of CTs in further studies. The results not only contribute to improving the clinical effectiveness and practical user compliance of compression therapeutic textile products but also promote the quality and healthy life for human beings.

PUBLICATIONS ARISING FROM THE THESIS

Journal papers:

- Shi, Y., Ye, C.Y., Liu, R. (2024). Three-dimensional dynamic homogenous modelling: the biomechanical influences of leg Tissue stiffness on pressure performance of compression biomedical therapeutic textiles. *Frontiers in Bioengineering and Biotechnology,* 12, 1418047.
- Shi, Y., Liu, R., Ye, C.Y. (2024). Personalized compression therapeutic textiles: digital design, development, and biomechanical evaluation. *Frontiers in Bioengineering and Biotechnology,* 12, 1405576.
- Shi, Y., Liu, R., Wong, C., Ye, C.Y., Lv, J.Y. (2024). Prediction of tensile behavior of compression therapeutic biomedical materials by mesoscale laid-in loop model. *Polymer,* 127094.
- Shi, Y., Liu, R., Lv, J.Y., Ye, C.Y. (2024). Biomedical therapeutic compression textiles: physical-mechanical property analysis to precise pressure management. *Journal of the Mechanical Behavior of Biomedical Materials,* 151, 106392.
- Shi, Y., Ye, C.Y., Liu, R. (2024). A novel optimization approach for bio-design of therapeutic compression stockings with pressure fit. *Computers in Biology and Medicine,* 168, 107768.
- Shi, Y., Liu, R., Lv, J.Y. (2023). Effects of knitting variables for pressure controlling of tubular compression fabrics. *International Journal of Materials and Textile Engineering,* 17(7), 90-94.

● Ye, C., Liu, R., Ying, M.T., Liang, F.Y., Shi, Y. (2023). Characterizing the biomechanical transmission effects of elastic compression stockings on lower limb tissues by using 3D finite element modelling. *Materials & Design,* 232, 112182.

Conference paper:

● Shi, Y., Liu, R., Lv, J.Y. (2022). Effects of knitting variables for pressure controlling of tubular compression fabrics. *In: Three-dimensional Textiles and Textile Engineering Conference*, *World Academy of Science, Engineering and Technology.* December 2022, Paris.

ACKNOWLEDGEMENTS

I am grateful to my chief supervisor, Dr. Rong Liu, for her kind guidance, professional comments for my PhD studies. I would like to extend my sincere gratitude to my co-supervisor, Prof. Calvin Wong, who provided funding supports and necessary comments in my thesis report.

I would like to thank my family members for their greatest supports in my life and studies. I also would like to thank colleagues, Dr. Xinbo Wu, Dr. Shumi Zhao, Dr. Chongyang Ye, Mr. Zhenxing Ye, Mr. Andy Ho, and Mr. Mohiuddin Choudhry for their useful comments and kind support. I would like to thank all staff and students in the Hong Kong Polytechnic University to give me the support and environment through the studies.

TABLE OF CONTENTS

LIST OF TABLES

LIST OF FIGURES

LIST OF ABBREVIATIONS

CVD ——Chronic venous disorder

CT ——Compression textile

CS ——Compression stocking

3D ——Three-dimensional

3D-BS——Three-dimensional body scanning

SDC ——Standard deviations of curvature

IR ——Irregular

FE ——Finite element

ST ——Soft tissue

SWE ——Shear wave elastography

LRU ——Loop repeat unit

VAS ——Visual analogue scale

EWC ——Ergonomic wearing comfort

MRI ——Magnetic resonance imaging

CT ——Computed tomography scanning

DRO ——Deviation ratio

BMI ——Body mass index

PM ——Prediction model

HzT ——Hertz contact theory

LWC ——Laid-in weft-knitted compression

CDM——Central difference method

ROM——The rule of mixture

FRF ——Fabric reduction ratio

CHAPTER 1 INTRODUCTION

1.1 Research Background

Chronic venous disorder (CVD) is attributable to valvular incompetence in the venous system of the lower extremity, which has been considered as the clinical spectrum ranging from asymptomatic symptoms to deep vein thrombosis, lymphedema, and venous ulceration [1]. The frequent incidences of CVD and venous reflux in the United States were presented in 69.1% and 82.1%, respectively [2]. In Spain, the prevalence of deep vein thrombosis was 53%, with 56.2% having a mild character, 20.6% moderate, and 23.2% severe [3]. In the Qassim region, 69% of females and 45% of males were diagnosed as having vein disorders [4]. The incidence rate of CVD in China was increased to 20.3% based on the epidemiological study [5]. Relative reports also indicated that the high risks of varicose veins in relevant occupations were estimated to be 16.2% to 62.9% [6]. Venous ulcers, swelling, limb pain, stasis changes, or frank ulceration not only can lead to leg discomfort but also may persist for a long period. In the condition of advanced stages even accompanied by ulcerations and thrombotic complications, especially superficial and deep venous thrombosis [7], they eventually have a negative influence on the quality of daily life. Consequently, there is an urgent matter for researchers and producers to prevent venous leg ulcers of lower limbs and contribute to a healthy life for human beings.

Commonly, compression therapy as an established medical treatment method for CVD, is utilized to enhance the venous return and reduce the leg edema to promote wound healing. In particular, traditional physical-based functional compression textiles (CTs) 2can substantially provide the required pressure magnitudes on the surface of the targeted body area for stabilizing, compressing, and supporting underlying tissues [8]. Current conservative modalities of CTs encompass compression bandage and compression hosiery with varying material stiffness for different pressure generations [9]. Additionally, the irreplaceable advantages of consistent pressure performances, optional compression levels, easy daily cleaning, low cost, and soft hand feelings have crucial impacts on the frequency of user application. Moreover, considerable studies [10-12] have demonstrated the effectiveness of CTs for venous and lymphatic disorders, especially for patient groups with poor health conditions, less tolerance for clinic surgery, disease limitation, etc. Therefore, CTs could reduce the heavy burden of varicose veins, and support an available solution for the CVD daily prophylaxis and clinic treatment.

For instance, originated in the 16th century, extensive clinical studies recognized compression stockings (CSs) as the cornerstone of a successful physical intervention for chronic leg ulcers [12, 13]. By providing the standardized pressure gradient along lower limbs, CSs could increase venous flow velocity and reduce venous wall distension, thus ultimately improving venous hemodynamics [14]. Additionally, based on the experimental explorations, CSs could not only improve perceived fatigue, muscle soreness, hemodynamic responses, tissue oxygenation and skin temperature, but also reduce tissue vibrations and muscle activation [15-19]. For example, Guillermo et al. found that CSs attenuated the expression of biomarkers that associated with vascular damage in varicose veins [20]. Through a randomized controlled trial and scientific data analysis, Ozyilmaz et al. stated that the symptoms of pain even edema caused by CVD could be decreased more efficiently with CSs than Kinesio Taping intervention [21]. Moreover, investigators [22-24] also indicated that CSs were cost-effective in preventing venous leg ulcers compared with usual care and other modalities. Therefore, CSs are recommended for the physical prevention of CVD based on their effective therapeutic functions and simultaneous economic merits.

However, although there is adequate evidence for the beneficial effects of CTs, the practical use is relatively infrequent (35.1%) [25, 26]. Detailly, Kankam et al. [27] found that only 31.8% of the patients reported wearing CSs as prescribed, 31.4% reported wearing most days, 28.3% reported wearing compression intermittently, but 8.5% of the patients reported never wearing any therapeutic modalities ever before. Thus, present studies have explored and summarized the common causes of non-compliance of CTs in different cohorts of patients. The major reasons for non-compliance comprise four aspects, including the knowledge gaps of CTs as the treatment or management, few recommendations from medical staff, intrinsic disadvantages of CTs, and other sociopsychological factors [28-30]. Most patients considered that the existing challenges of CTs are the provision of skin problems, unattractive appearances, and lack of comfort perceptions [31]. Furthermore, Liu et al. [32, 33] also concluded that poor compliance may be due to insufficient distribution of interfacial pressure, which causes undesired side effects, including varying degrees of ischemia, necrosis, ulcerations, and even exposing the tibialis anterior tendon. Consequently, user compliance with CTs still needs to be improved in practical applications by the achievements of controllable pressure performances and wearing comfortable perceptions based on systematic improvements and professional promotions through relevant researchers and manufacturers.

1.2 Research Objective and Significance

The research aims of this study were to investigate the physical-mechanical mechanisms of CTs in multiple scales and to achieve the bio-digital design, development, and biomechanical visualization of custom fit CTs with controllable pressure performances and comfortable perceptions for required users. The major research objectives were listed as follows.

(1) To study the effects of multiple knitting settings on fabric physical-mechanical properties and pressure performances of CTs.

(2) To investigate the effects of body morphological variations of lower extremities on compression generations of CTs.

(3) To explore the effects of physiological tissue characteristics of lower extremities on compression generations of CTs.

(4) To construct the mesoscale modeling for loop component simulation and yarn material determination of CTs.

(5) To optimize the design variables through multiscale theoretical analysis and parametric models for user-oriented CTs.

(6) To build a realization system for a design-development-evaluation framework of

functional CTs with custom fit and ergonomic wearing comfort.

Therefore, based on the above investigations, this study provides researchers with more fundamental and valuable ideas for the working mechanisms and engineering design principles of CTs in further studies. And can not only improve the effectiveness and practical user-compliance of CT products but also promote the quality and healthy life for human beings.

1.3 Research Methodology

To achieve the aforementioned objectives, six corresponding research methodologies were applied as follows.

(1) Parameterization of Knitting Settings and Quantification of Material Properties

Various elastic tubular fabric samples with multiple knitting settings (three yarn combinations and two types of machinery parameters) were designed and fabricated based on the laid-in structural characteristics and three-dimensional (3D) seamless knitting technologies. The varied knitting settings were yarn diameters and feeding velocities of inlay yarns, as well as loop size settings. The physical fabric tests included the dimensional characteristics, stitch densities, and fabric thickness. Young's moduli and elastic recovery ratios along both transverse and longitudinal directions were selected to objectively evaluate the mechanical tensile behaviors of knitted samples. The interfacial pressure magnitudes under the same fabric course stretch ratios were estimated along the determined test points of wooden leg mannequins. Through the obtained experimental results, yarn-machinery settings were parameterized to perform the correlation analysis, multiple regression analysis, and sensitivity assessment for determining the qualitative and quantitative relationships among the knitting settings and fabric properties as well as pressure magnitudes. Moreover, through the parameterized knitting settings and quantified fabric morphological and pressure equations, the required fabric dimensions and performances were achieved through the digital design and fabrication processes.

(2) New Body Morphological Classification and Pressure Prediction Systems

Firstly, by applying the 3D body scanning (3D-BS) technology, the original anthropometric data was captured from the recruited 22 subjects with diverse leg morphological characteristics. Then, based on the reverse engineering methodology and reconstructed 3D entity leg model, the biological cross-sectional curves were plotted by the scattered point data for the geometric circumferential and curvature variation measurements. Secondly, the standard deviations of curvature (SDC) of each leg slice were imported into the clustering algorithm and classified as four irregular (IR) levels for morphological classification. Simultaneously, the new pressure prediction model related to the characterized geometric variables was established through the accuracy calculations of leg curvature radius, fabric strain and thickness. Knitted tubes with varying physical and mechanical tensile properties were prepared for the practical wearing validation study. Thirdly, through the proposed prediction model, the pressure gap ranges between the irregular and ideal circular legs were predicted and summarized for the practical CT design and production, to reshape the pressure supply generated at various user’s lower limbs.

(3) Homogenous CT-leg Modelling and Theoretical Contact Analysis

Three subjects were recruited for the lower extremity modelling constructions and experimental investigations. Through the standard of Germany RAL-GZ 387/1 (Medical Compression Hosiery Quality Assurance), different compression knitted fabrics were designed to achieve the standardized pressure magnitudes for the light (Class: I; 18-21 mmHg) and strong (Class: III; 34-46 mmHg) levels of compression generation. For the 3D finite element (FE) homogenous CT-leg system, the entity lower limb models were reconstructed by 3D-BS and reverse engineering technologies. The geometric models of CT samples were constructed by applying ANSYS Workbench Design Modeler software (v19.2, ANSYS, Pennsylvania, Pittsburgh, USA) according to the practical fabric dimensions. The boundary conditions were determined as the longitudinal CT sliding displacements for pressure behavior simulation in ANSYS LS-DYNA explicit dynamic solver. The acceptability of proposed FE models was examined by 3D printing legs with controlled lower limb morphological shapes and identical material characteristics. Then, the pressure performance diversities between legs among varied soft tissue (ST) stiffnesses were qualitatively compared through the FE CT-leg systems by inputting varying biomaterial parameters referred to the literature. Simultaneously, the theoretical contact analysis model was constructed to quantitively explore the impacting mechanisms of tissue stiffness on pressure behaviors of CTs by inputting leg circumferential deformations. Finally, based on the shear wave elastography (SWE) measured data from recruited subjects, experimental validations were adopted to evaluate the applicability of the studied outcomes and major findings.

(4) Establishments of Geometric and FE Mechanical Laid-in Loop Models

Firstly, the 3D geometric loop models were established based on the structural explorations of laid-in characteristics with real knitted loop morphology through ANSYS Workbench Design Modeler v19.2 (ANSYS, Pittsburgh, PA, USA). The 1×1 laid-in loop repeat unit (LRU) comprised two knitted ground loops and two courses of inlay yarns in the technical front and back views based on realistic structures. The main structural parameters of an LRU included the course and wale distances, the diameters of ground and inlay yarns, as well as the defined distances between each loop component. Secondly, the tensile behaviors of linear viscoelastic yarn materials were described using the Maxwell mechanical model, to determine the elastic solid and viscous fluid properties through stress-relaxation tests. Thirdly, through the defined geometric parameters, the FE mechanical models with three yarn combinations in mesoscale were constructed using the explicit dynamic solver in LS-DYNA software. The tensile behaviors of the laid-in loops were simulated under 0%-80% stretching, which fell in the elongation range of Germany RAL-GZ 387/1 quality standard for medical compression hosiery. Thus, the boundary conditions were determined by the loop displacements under course and wale stretches. Additionally, the accuracy of the proposed mechanical laid-in models was validated by comparative studies using an Instron tension tester (Norwood, MA, USA).

(5) Determination of Optimized Variations and Construction of FE Multiscale

Parametric Systems

Firstly, the theoretical analytical models in macro- and meso-scales were utilized to determine the optimized variations for the FE parametric systems. For macro- CT-leg system, the design variables included the fabric mechanical properties and stretch ratios along the course direction. The yarn materials with different physical-mechanical properties and loop structural parameters were the design variables for the mesoscale loop systems. Secondly, based on the lower body circumferential dimensions and compression levels from the Germany RAL-GZ 387/1 standard, fabric stretch ratios and Young's moduli for each leg position were optimized by the FE parametric system. Sequentially, based on the varied loop structural settings, the determined variables of yarn material combinations were optimized for CTs with various tensile behaviors through the established FE laid-in loop mechanical model and parametric system. Thirdly, according to the individual leg circumferential dimensions and pressure requirements, the applied yarn combinations and fabric stretch ratios could be specifically guided for personalized CT development.

(6) Bio-Digital design, development, and Biomechanical Visualization Systems

Various subjects with individual psychological characteristics and pressure requirements were recruited for the development of customized CTs. By using the 3D-BS and reverse engineering techniques, the geometric and morphological properties of the lower extremities were obtained as the design principles for the fabric circumference and pressure redistribution, respectively. Through the SDC values and clustered IR levels of each lower limb position, the reshaped pressure values were obtained to scientifically enhance the delivered dosages of CTs. Then, the applied knitting yarn combinations and machinery parameters were obtained based on the proposed digital fabric morphological and pressure equations for 3D seamless fabrication. Through the reconstructed geometric lower extremity models, the user-specific 3D FE CT-leg models were established for the biomechanical evaluation of pressure performances. Moreover, the subjective visual analogue scale (VAS) assessments were performed for the ergonomic wearing comfort (EWC) estimation of CTs. The VAS assessments were applied to estimate the movement ability and comfortable sensation by wearing trials.

1.4 Thesis Outline

This thesis report included nine chapters.

Chapter 1 introduced the research background and existing research gaps, and then listed the major research objectives, significances, applied methodologies, and workflow chart for this study. This chapter firstly introduced the general background and gaps in relevant research fields. Based on the targeted six research objectives, the corresponding methodologies were proposed. The study framework of this thesis is displayed at the end of this chapter.

Chapter 2 reviewed the related published papers and summarized the research gaps for this study through six research topics. Detailly, the 1st section presented the definitions and evaluation techniques for the custom size and pressure fits of CTs. Then, the subjective EWC was introduced relating to the definitions and assessment methods in the 2nd section. Through the introduction of the materials and fabrication of CTs, the 3rd section presented applied raw materials (i.e. fibers and yarns), knitted structures, knitting methodologies, and relevant material analysis literatures for CTs. The 4th section demonstrated the functional physiological and physical mechanisms of CTs in compression therapy. For the 5th section, the existed FE models in macroscale and mesoscale were introduced including the establishment of geometric and mechanical models. The 6th section summarized the previous optimization methods for the parametric design of knitted compression fabrics. Through the presented literature review, the research gaps were summarized at the end of this chapter.

Based on the six research objectives, the corresponding explorations and major findings were presented from Chapter 3 to Chapter 8.

Chapter 3 included the qualitative and quantitative investigations of the influencing mechanisms of knitting settings on fabric physical-mechanical properties and pressure behaviors of CTs. The primary relationships between the production parameters and fabric morphological dimensions and generated pressure magnitudes were obtained as the mathematical equations for the fabrication process. However, the proposed quantitative relationships were based on the wooden leg mannequin measurements with ideal circular sectional profiles and rigid material properties. The design variables, such as the applied yarn materials and fabric stretch ratios, still need to be optimized in our further studies for the determination of user-specific production prescriptions.

Chapter 4 introduced a novel operable approach for the bio-design of CTs with enhanced compression performances. Through the body anthropometric characterization and clustering algorithm, the morphological curvature variations of lower limb cross sections were classified as four IR levels. And then, a new prediction model was proposed based on the characterized geometric variables. Finally, through the predicted pressure magnitudes, the pressure gap ranges between the irregular bio-bodies and circular leg models were obtained as the recommend pressure redistribution strategies for the design of CTs.

Chapter 5 presented the biomechanical influences of leg ST stiffness on pressure performances of CTs. It included the FE modelling, theoretical analysis, and experimental validation. Through the biomaterial parameters referred from the literature, the exerted compression magnitudes were qualitatively compared through FE homogenous CT-leg systems with various ST stiffness. Then, a contact analysis model was utilized to theoretically and quantitatively explore the influences of ST stiffness on the pressure performances of CTs. Finally, based on the SWE data, the experimental validations were performed by comparing the simulated pressure results with the pressure data obtained from the wearing trials of the recruited subjects.

Chapter 6 established the novel geometric and FE mechanical laid-in loop models for CTs, to simulate the stress mappings of yarn components along stretching states and to optimize the yarn materials for our further study. Through the mesoscale models, the dynamic tensile behaviors of CTs were visualized along various stretching states. The geometric models were established based on the real loop morphology investigations from the laid-in structural characteristics. The viscoelastic properties of yarn materials were analyzed by the Maxwell mechanical model through stress-relaxation testing. The boundary conditions of mechanical FE models were determined by the loop displacements under external stretches. The uniaxial tension tests were used for the estimation of the prediction accuracy. The proposed loop models could be applied to yarn material optimization in the next FE parametric systems.

Chapter 7 optimized the design variables for the determination of user-oriented production parameters. The design variables (i.e. fabric stretch ratios and yarn material properties) were determined through the theoretical analysis models in macro- and meso-scales. Then, based on the FE parametric multiscale systems and the German standard, the yarn combination and the guidance tables on fabric stretch ratios were obtained for the design of CTs with various individual needed fabric circumferential dimensions and pressure requirements.

Chapter 8 introduced the bio-digital design, development, and biomechanical visualization systems for custom fit CTs with EWC. Firstly, the geometric dimensions and morphological characteristics of the subject’s lower limbs were obtained through the 3D-BS and reconstructed entity leg models. Through the individual expected pressure magnitudes and body sectional IR levels, the required pressure values were obtained for the design process. Then, based on the optimized yarn combinations and fabric stretch ratios, the user-oriented yarn-machinery parameters were calculated and determined through the proposed fabric digital morphological and pressure equations in Chapter 3. After 3D seamless fabrication, the pressure mappings and EWC of the prepared personalized CTs were estimated by the constructed FE CT-leg modelling and VAS assessments, respectively.

Chapter 9 summarized and concluded the main findings, research limitations, and future works for this study. In future work, various yarn materials will be utilized for improving moisture management and comfortable perceptions of CTs. Moreover, different loop patterns would be used for the heterogeneous structural combinations to generate more uniform compression distributions along the lower limbs, to achieve precise pressure management, and to improve the clinical treatment efficacy for compression therapy.

The flowchart of this thesis is displayed in Fig. 1.1.

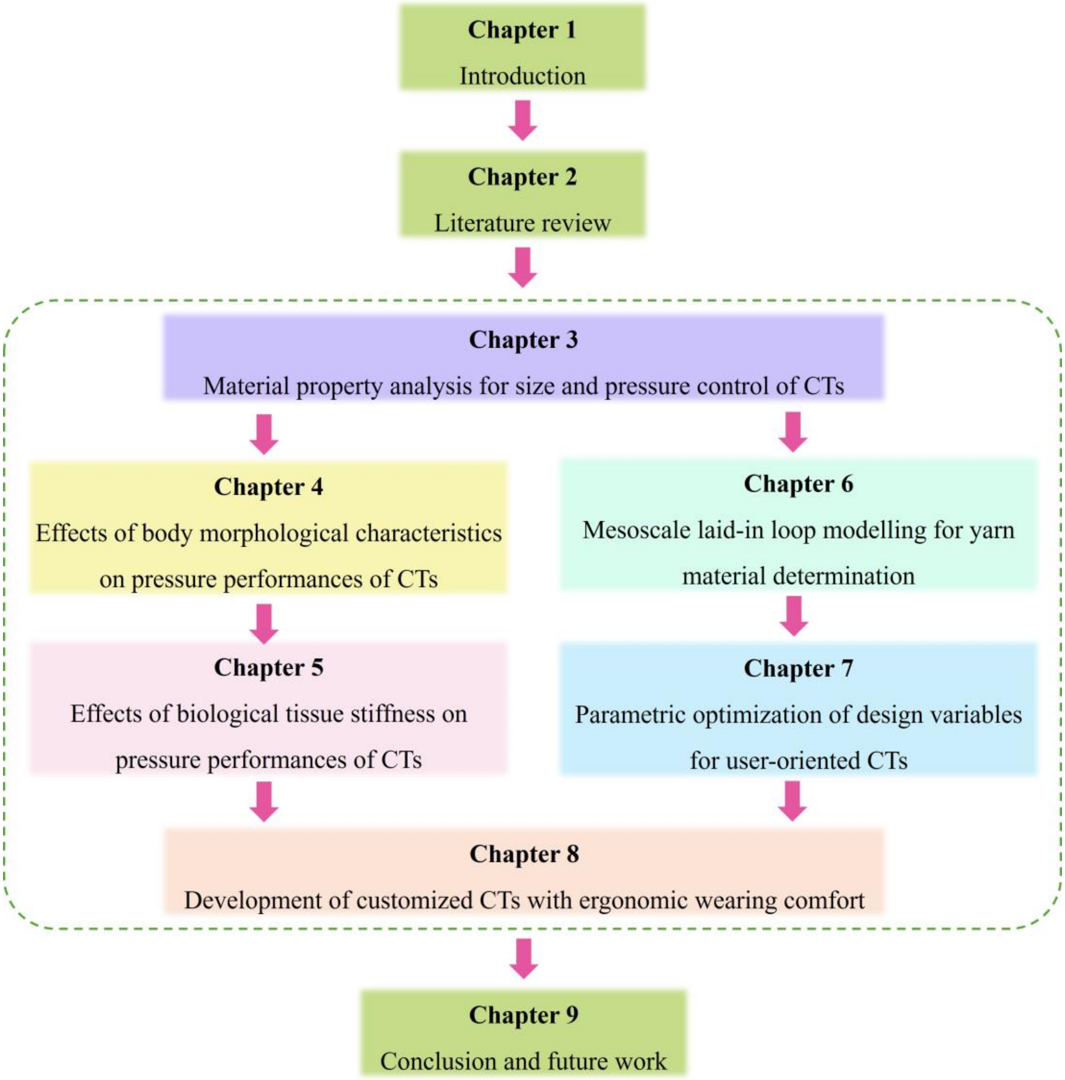

Figure 1.1 Flowchart of this thesis.

CHAPTER 2 LITERATURE REVIEW

2.1 Custom Fit of CTs

2.1.1 Size Fit

Apparel-fit generally is defined as the relationship between the size and contour of clothing with body morphology [34]. For elastic CTs with therapeutic functions of CVD treatment, the fitted fabric dimensions and expected pressure profiles need to be selected appropriately to meet the user's requirements [35].

For the existing ready-made commercial CSs, based on the measuring discipline (Fig. 2.1 (a)), the geographical diversities from different user groups with geometric and morphological characteristics led to various determinations of dimensional tables from their respective producers (Fig. 2.1 (b)), which frequently results in the wrong selection and inappropriate applications. For instance, a comparative study found that 29% of hospitalized postoperative patients commonly adopted incorrect sizes accounting for anthropometric variables through the recommended table from the manufacturer [36]. Especially in Asian Indian [37], the inadequate instructions and measurement discrepancy prescribed by Western companies led to not only the increasing risks of threading difficulties, wrinkle, and slippage [38], but also equal pressure values and incompatible pressure gradient along the ankle and calf points. In addition, some studies also claimed that the internationally agreed tested points were only based on an average of measurements in healthy female and male subjects, and not in practical patients who may already have physiological changes in their lower limb proportion with muscle atrophy due to the venous leg ulcer and venous hypertension [39]. Thus, the proper size fit plays a crucial role in the pressure performance and user compliance of compression therapy, and adequate dimensional selections or the personalized development of CTs are highly needed.

2.1.2 Pressure Fit

There are no international standardized pressure classification systems for compression therapy presently. Therefore, through literature reviews, Fig. 2.1 (c) summarized each compression dosage at B point (ankle region with minimum girth) from various regions or countries. However, due to the defined range differences of relevant production standards, it may lead to some contradictions and misunderstandings for users or consumers.

Moreover, for the correct selection of pressure levels, based on the updated Clinical-Etiology-Anatomy-Pathophysiology (CEAP) internationalized description and standardized classification for CVD [40], the patients with reflux or obstruction have been suggested for their medical endovascular or surgical management [41] (Fig. 2.1 (d)). Moreover, Fig. 2.2 shows the guidelines and recommendations for different medical diagnoses, precautions, contraindications, and underlying oedema etiologies based on resting pressure measurements [42]. Nevertheless, researchers demonstrated that the previously prepared CSs with the ill-fitting of pressure profiles may not only prevent the basic treatment, but also exacerbate the unexpected tourniquet effect such as skin break, ulcers, and blister, as well as limit the compromised movement and mobility during daily life [43-46]. Consequently, numerous studies [32, 47] considered that the effective compression prescription should not only solely depend on the diagnosis alone but also require matching the pressure selection to the patient presentation as well as their individual characteristics.

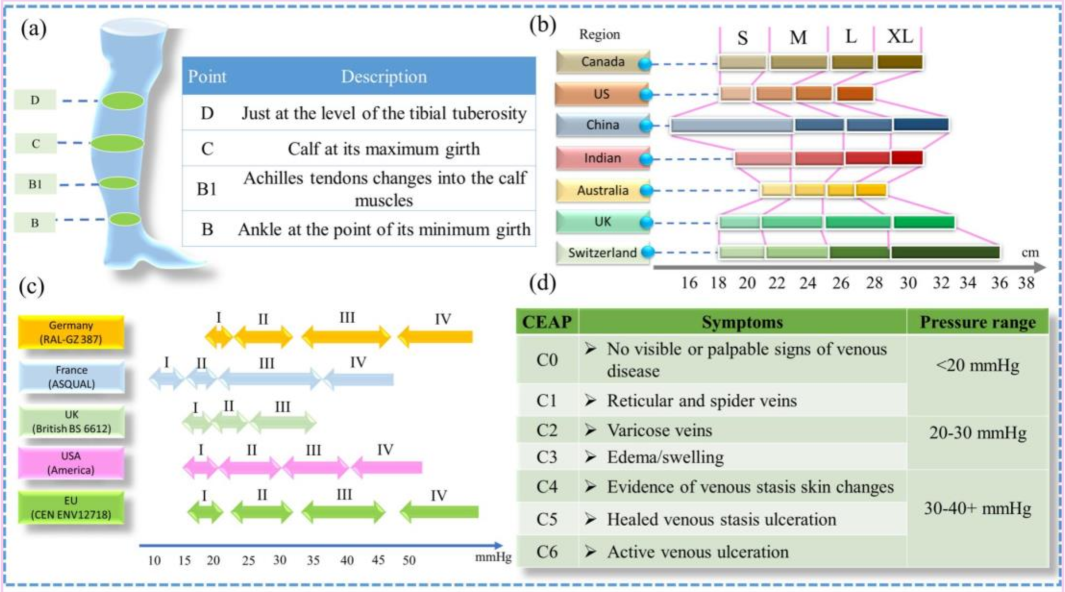

(a)

Point	Description
D	Just at the level of the tibial tuberosity
C	Calf at its maximum girth
B1	Achilles tendons changes into the calf muscles
B	Ankle at the point of its minimum girth

(d)

CEAP	Symptoms	Pressure range
C0	➢ No visible or palpable signs of venous disease	<20 mmHg
C1	➢ Reticular and spider veins	
C2	➢ Varicose veins	20-30 mmHg
C3	➢ Edema/swelling	
C4	➢ Evidence of venous stasis skin changes	30-40+ mmHg
C5	➢ Healed venous stasis ulceration	
C6	➢ Active venous ulceration	

Figure 2.1 (a) Measurement guidance of CTs, (b) examples of size selections (at ankle point) around different regions, (c) pressure level standards through different organizations or associations, and (d) recommendations of pressure requirements from the CEAP indication [48].

Pressure range	Indication
< 20 mmHg	❖ Improvement of venous symptoms in patients with CEAP C0s-C1s and in varicose veins of pregnancy
	❖ Prevention of leg swelling related to prolonged sitting and standing (“occupational leg oedema”)
	❖ Prevention of venous thromboembolism in bed-ridden patients especially after general surgery
20-30 mmHg	❖ Better results and less adverse outcome after sclerotherapy of small telangiectasias (C1)
	❖ Improvement of subjective symptoms in varicose veins of pregnancy
	❖ Less pain and swelling in the acute phase of deep vein thrombosis
30-40 mmHg	❖ Less side-effects after sclerotherapy of large veins (C2) compared to light bandages
	❖ Reduction of lipodermatosclerotic areas on the leg (C4b)
	❖ Improved healing of venous leg ulcers (C6)
	❖ Prevention of ulcer recurrence, higher pressure ranges seem to be superior
	❖ Prevention of PTS after proximal DVT Maintenance therapy in lymphoedema

Figure 2.2 Recommended compression magnitudes for applications of CTs [42].

Through the above reviews, conventional ready-made therapeutic CTs with improper morphologies and ill-fitting of pressure exertions frequently limited user compliance in practical applications. Although there are various selections of CTs products for patient's choices in different regions, user compliance and medical effectiveness still need to be improved by the development of personalized CTs with size and pressure fits for target users. The development of CTs with user-specific suitable morphological circumferential shape and pressure fit could improve the medical therapeutic efficacy and user compliance.

2.2 Ergonomic Wearing Comfort of CTs

2.2.1 Ergonomics and Comfort

Ergonomic comfort of garments is concerned with the multidisciplinary studies of anthropometry, anatomy, psychology, and biomechanics. Commonly, clothing ergonomics focus on the appropriate size, improvements of ventilation and mobility, as well as the reductions of hotness, weight, and obstruction during practical wearing [49]. Especially, relating to the interactions between body and clothing, the relationships among the body shape, pressure perceptions, and moveable compliance are crucial for the EWC of CTs [50, 51].

The material design, structural development, and fabrication technique crucially contribute to the EWC of CTs. The selections of yarn component basically influence the fabric breathability, moisture management and flexibility based on its material characteristics and mechanical properties. Thus, the raw material composition and yarn spinning approach, yarn specification should be determined appropriately to obtain the fundamental comfortable and elastic recovery requirements. Moreover, fabric patterns and production parameters significantly determine the EWC by influencing the fabric thickness, tactile stiffness, tensile property, and compactness of CTs. Especially, the proper size, functional pressure generation and comfortable wearing perception should be achieved scientifically allowing freedom of body movement [52], thus promoting the requirement of EWC.

Furthermore, researchers emphasized that computation-aided technology could facilitate in improving comfort perceptions for CTs. For example, 3D-BS could identify the specific spaces between the body and fabrics to promote the dynamic moveable ability of CTs. Numerical simulation modelling could predict and visualize the mechanical interactions and pressure distributions to further enhance the functional compression comfort. For instance, recently, numerous attempts have been made through digitalized design and advanced technologies to improve the EWC of CTs. Liu et al. [53] obtained the individual anatomic characteristics to design and fabricate the user-oriented CSs, thus enhancing the EWC with size fit and required pressure profile by employing 3D-BS and biomechanical FE visualization. Dan et al. [54] presented a numerical simulation study to optimize compression garment ergonomic design based on the investigations of the relationships between pressure and displacement during the wearing process.

2.2.2 Evaluation Techniques

The clothing EWC primarily focuses on physical and psychological explorations, thus commonly evaluated by subjective and objective assessments. As shown in Fig. 2.3, the range of motion during the dynamic wearing condition is applied to evaluate the objective movable ability by physical measurement devices, such as the Flexometer, Goniometer, and Inclinometer, etc. [55]. For the measurements of interfacial pressure performance, various sensors are selected through device advantages and different experimental requirements in vivo tests (as listed in Table 2.1). Additionally, relevant strain sensors are frequently adopted to appraise compression comfort by determining the practical displacement of the CT system. To comprehensively assess the EWC of CTs, some studies simultaneously used subjective and objective methodologies in their evaluation studies.

For CTs, the evaluation of EWC is commonly performed through the movement ability and comfort sensation by actual wearing trials [56]. Through various designed protocols, the post-experiment comfort survey [57, 58], VAS [59], and wearing sensation questionnaire [60] are performed for the EWC estimations and subjective preferences. For instance, Jung et al. [61] applied the range of motion and pressure sensation as well as other physical index to test the applicability of compression fabrics. Barhoumi et al. [62] used the pressure sensor and subjective questionnaire to test the pressure values, movement ability, and comfort sensation of the novel-designed CSs.

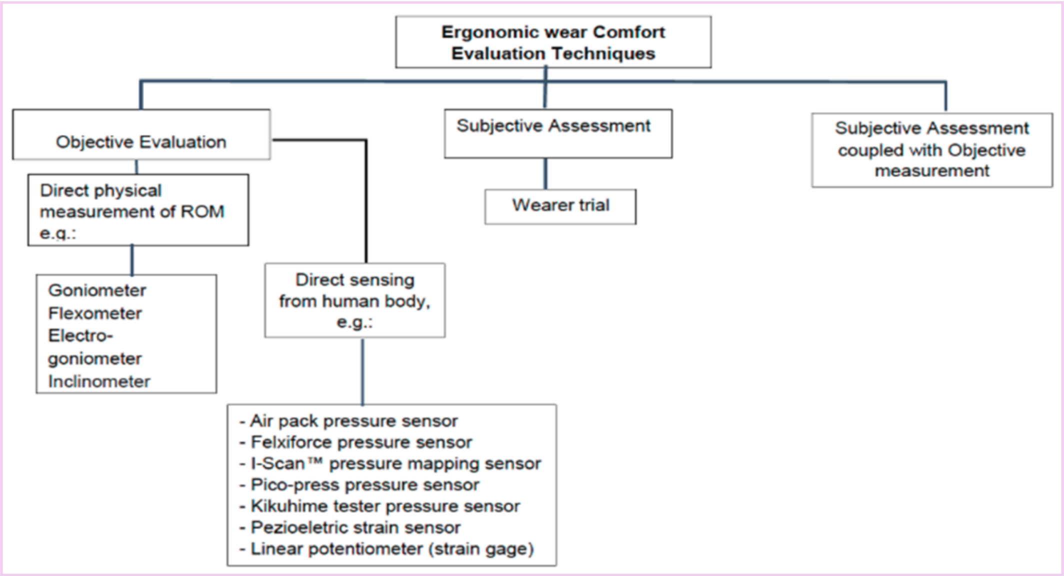

Figure 2.3 Contemporary evaluation framework for the EWC of CTs [55].

Table 2.1 Various pressure sensor types for compression experimental measurements [63]

Sensor type	Advantage	Limitation	Typical device
Pneumatic transducers	Thin and flexible probes, cheap, easy, and handy	Dynamic measurement is only possible with additional special equipment. Sensitive for temperature and hysteresis	Oxford Pressure Monitor (Talley Ltd, Ramsey, Hampshire, UK); Talley Pressure Evaluator (Talley Ltd); MST MKIII Salzmann (Salzmann Medico, St Gallen, Switzerland); Digital Interface Pressure Evaluator (Next Generation Co., Temecula CA, USA); Scimedics Pressure Evaluator Pad (Vista Medical, Winnipeg, MB, Canada); Kikuhime (Meditrade, Soro, Denmark); Juzo Tester (Elcat, Wolfratshausen, Germany); Sigat Tester (Ganzoni-Sigvaris, St. Gallen, Switzerland)
Fluid filled	Flexible, dynamic measurements	Thick when filled, problems during motion	Strathclyde Pressure Monitor, (University of Strathclyde, Scotland); FlexiForce (Tekscan, South Boston, MA, USA); Skip Air pack Analyzer (AMI Co., Japan)
Resistance	Thin sensors, dynamic measurements	Sensitive to curvature, stiff and thick, not useful for long term measurements	FSR, FSA (Vista Medical, Winnipeg, MB, Canada); Fscan, Iscan (Tekscan, South Boston, MA, USA); Rincoe SFS (Rincoe and Associates, Golden, CO, USA); MCDM

	(Mammendorfer Inst. Physik, Munich, Germany); Fontanometer (Gaeltec Ltd, Dunvegan, Isle of Skye, Scotland); Diastron (Diastron Ltd, Andover, Hampshire, UK)

Based on the above literature, the fundamental knowledge and evaluation techniques of the EWC for CTs were systematically reviewed. Compression assessment systems of CTs could not only facilitate the evaluation of evidence-based treatment efficacy but also provide scientific information for material property optimization. To improve the EWC for physical compression therapeutic modalities, the individual subjective comfort of personalized CTs should be estimated through in vivo wearing trials, especially for the evaluations of the moveable abilities and comfortable perceptions.

2.3 Materials and Fabrication of CTs

2.3.1 Yarn Materials and Knitting Techniques of CTs

Commonly, to provide basic wearability, functional performance, and comfortable perception, natural and synthetic fibers can be adopted as textile-based raw materials for CT preparation. The major types of fibrous materials include cotton, polyamide, polyester, lyocell, viscose, polyurethane, and their blends in practical production [64]. To generate adequate interfacial pressure magnitudes along the human body, the elastomers are frequently applied to provide the required elasticity and recovery for further fabric elongations. According to literature [65, 66], the elongation of commercial elastic yarns could range from high elongation (300-800%) to low elongation (20-100%).

Based on the manufacturing technology, elastic yarns can be classified as core-spun yarns, texture yarns, and conventional covered yarns through the techniques of core spinning, air-texturing, and cover spinning, respectively. Especially, covered yarn utilizes spandex as the core sheath and other natural or staple fibers as the covering components (Fig. 2.4), thus it shows not only higher elasticity and extensibility but also enough strength and tenacity, which are the fundamental and important mechanical properties for development and application of CTs [66]. Moreover, for the double-covered elastic yarns, the stretching elongation can reach 200% (Fig. 2.5 (a)), and sometimes approximately 50% of elasticity can be obtained in knitted fabrics (Fig. 2.5 (b)). Consequently, double-covered yarn is more appropriate for the fabrication of CTs due to its considerable mechanical tensile characteristics.

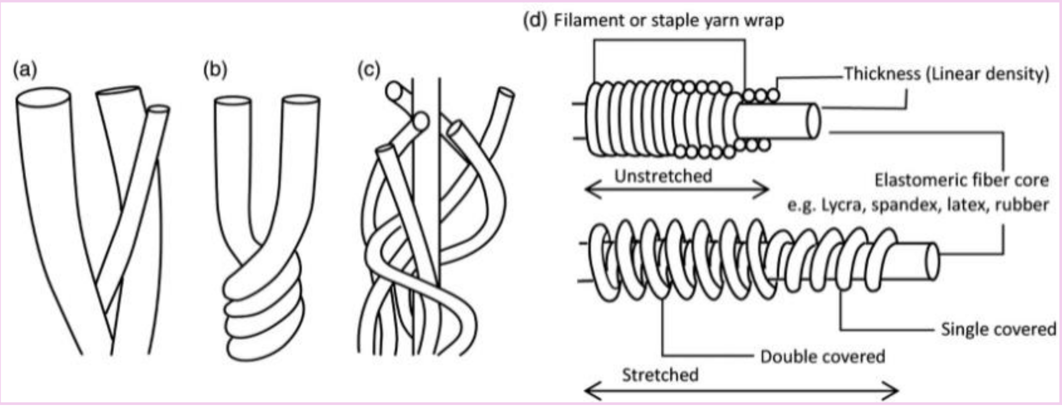

Figure 2.4 Elastic yarn types of (a) core spinning, (b) core twisting, (c) air-covering, (d) single/double covering [67].

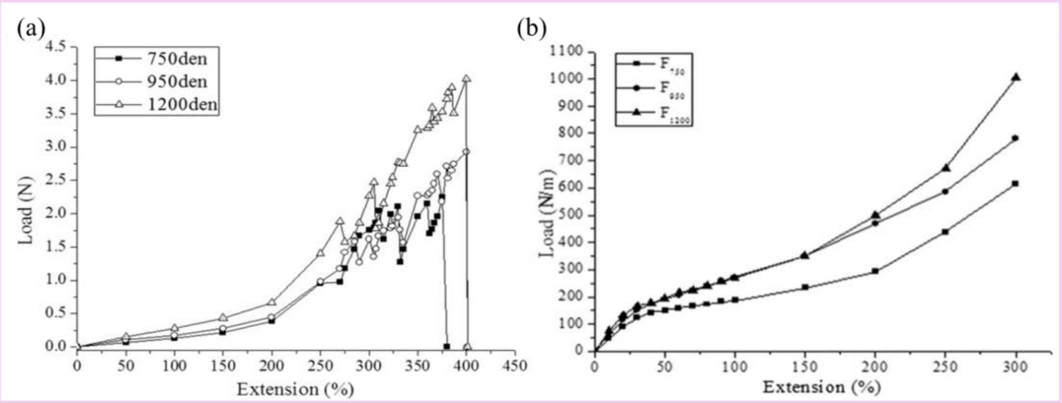

Figure 2.5 Load extension curves of (a) elastic-covered yarns and (b) generated elastic fabrics [68].

CTs can be formed by different types of knitted structures through the designed loop patterns. Table 2.2 summarizes the typical loop structures and corresponding characteristics utilized in the fabrication of elastic CTs. It can be divided into single- and double-sided structures with different handle feelings knitted by various machinery operational components. Thus, through reviews, different knitting forms of laid-in stitches are positively used in compression studies by the following advantages: (a) the physical and mechanical properties are easily controlled by the adjustments of the amounts of miss stitches and laid-in stitches, (b) better wearability and thinner handle feeling by the single-bed knitting techniques, (c) easy to be fabricated without cumbersome accessory knitting devices.

Table 2.2 Typical knitted structures and corresponding characteristics for CT fabrication

Knitted structures	Characteristics		References
	Structural	Physical-mechanical	
Rib stitch	Double-sided structure with the face and reverse knitted loops	Good elasticity and elongation	Wang et al. (2011) [69] Ališauskienė et al. (2013) [70] Gohar et al. (2020) [71]
Mock rib	Elastic yarns as weft are clamed between the face and reverse loops	Mechanical properties depend on the insertion density of elastic yarns	Özbayrak et al. (2009) [72] Xiong et al. (2018) [73]
Plain stitch	Only knitted loops to form the compact structure	Greater transverse extension than that of longitudinal, high stretching strength	Sang et al. (2015) [74] Soltanzadeh et al. (2016) [75] Barhoumi et al. (2018) [76] Yuan et al. (2021) [77]

Laid-in stitches	Inlay yarns are formed into tuck stitches or miss stitches in the basic plain structure	Good dimensional stability, enough elastic stretch and recovery to achieve available pressure generation	Gaied et al. (2006) [78] Bruniaux et al. (2012) [79] Chattopadhyay et al. (2012) [80] Liu et al. (2013) [81] Laplanche et al. (2014) [82] Ke et al. (2015) [83] Sarı et al. (2018) [84] Narayana et al. (2018) [85] Zhang et al. (2019) [86] Kırcı et al. (2021) [87]
Plating stitches	Except for basic ground yarns, floating lines also exist at the fabric technical back	Smaller extensibility, it's easy to be scratched and snagged	Xiong et al. (2018) [73]
Knit-miss stitches	Long transverse floating lines between two adjacent loops	Smaller transverse elongation	Liu et al. (2013) [33] Soltanzadeh et al. (2016) [75]

On the other hand, by applying corresponding technical knitting machines, CTs can be formed into different manufactured knits, such as flat knits and circular knits (also known as round or seamless knit) (as shown in Fig. 2.6). Flat knits allow more flexible fabric shape and size by the arrangement of a varying number of stitches. Circular knits could minimize the manpower operation during the fabrication process without the cutting and sewing requirements, sequentially providing softer and lighter feelings without the bulky and rigid seamlines [88]. Therefore, circular knitted CTs dominate the market with good user adherence due to easy handling and lower costs [89].

Figure 2.6 Different types of knits for fabrication of compression intervention materials [90].

2.3.2 Material Property Studies of CTs

To explore the physical-mechanical mechanisms of CTs for achievement of controllable performances, researchers have investigated the influences of various knitting settings (including the knitting materials, loop patterns, and machinery parameters) on fabric properties and pressure behaviors of CTs. Firstly, for the yarn properties and machinery settings, Özbayrak et al. [72] confirmed the correlations between the linear density and feeding pre-tension of inlay yarn materials with the extensibility and bursting strength of CTs. Ališauskienė et al. [91, 92] found the properties of covering materials of inlay yarns had slight influence on pressure behaviors especially under the low fabric extension (stretch ratio of 10%). Then, Bera et al. [68] emphasized that the basic characteristics of elastic core components in inlay yarns showed significant effects on the tensile properties of CTs. Secondly, researchers [74, 81, 86] explored the impacts of knitted structures on not only the fabric physical and stretch properties but also the clothing pressure. For instance, Mikučionienė [93] and Narayana et al. [85] applied the laid-in structural characteristics to the pressure performances of tubular fabrics generated by various designed loop patterns.

Further, existing studies have obtained the qualitative impacts of knitting settings on pressure behaviors of CTs but lack of exact available numerical relationships for practical design. For instance, Chattopadhyay et al. [80] demonstrated that the pressure exerted on rigid cylindrical tubes increased with fabric tensile strain and the curvature of the cylinder. Lozo et al. [94] designed CSs with gradient pressure generations by varying fabric tensile properties. Therefore, to facilitate the user fit of compression materials quantitively, relevant statistical methodology, especially for the multiple regression analysis, was applied to establish the fitting equations for achievements of required fabric dimensions and pressure values [95, 96]. For example, Bruniaux et al. [79] proposed the yarn-scale mechanic model to predict pressure behaviors by characterizing the elastic properties of inlay yarn. Similarly, Unal [97], CĂRPUS [98] and Sarı [84] et al. described the mathematical relationships between fabric's basic physical properties and pressure values. However, the generation of predicted pressure can only be achieved after the fabric extensive tests with multiple knitting attempts through different machine parameters or yarn combinations.

Therefore, the double-covered yarn materials and laid-in knitted structures are appropriately applied for the development of functional CTs by providing good elasticity and sustainable elongation. The correlation and sensitivity of each knitting parameter on fabric properties need to be explored numerically to select the key settings, and then to achieve controllable performances without considering a great number of parameters in the identification procedure. Thus, to provide a fundamental reference for the design and development of CT materials with proper dimension and controllable pressure behavior for CVD treatment, Chapter 3 investigated the scientific influencing mechanisms of CTs systematically through the qualitative and quantitative relationships among knitting settings, fabric properties, and pressure performances.

2.4 Functional Mechanisms of CTs

2.4.1 Physiological Mechanisms

The venous system of biological lower limbs, hierarchically includes three major components (i.e. superficial and deep, and perforating veins) defined by their relationships with the muscle fascia. As illustrated by Fig. 2.7, the superficial venous system includes the great saphenous vein, small saphenous vein, and superficial or epifascial tributaries [99], it could drain the blood flow from the skin and subcutaneous tissues. For the deep venous system, it supports the muscle and fascia and provides approximately 90% venous return to the heart. Additionally, perforating veins are commonly arranged and connected by numerous variables and vascular size, they perforate the deep fascia and equilibrate blood flow during calf muscle contraction to prevent reflux from the deep venous system to the superficial venous system [100].

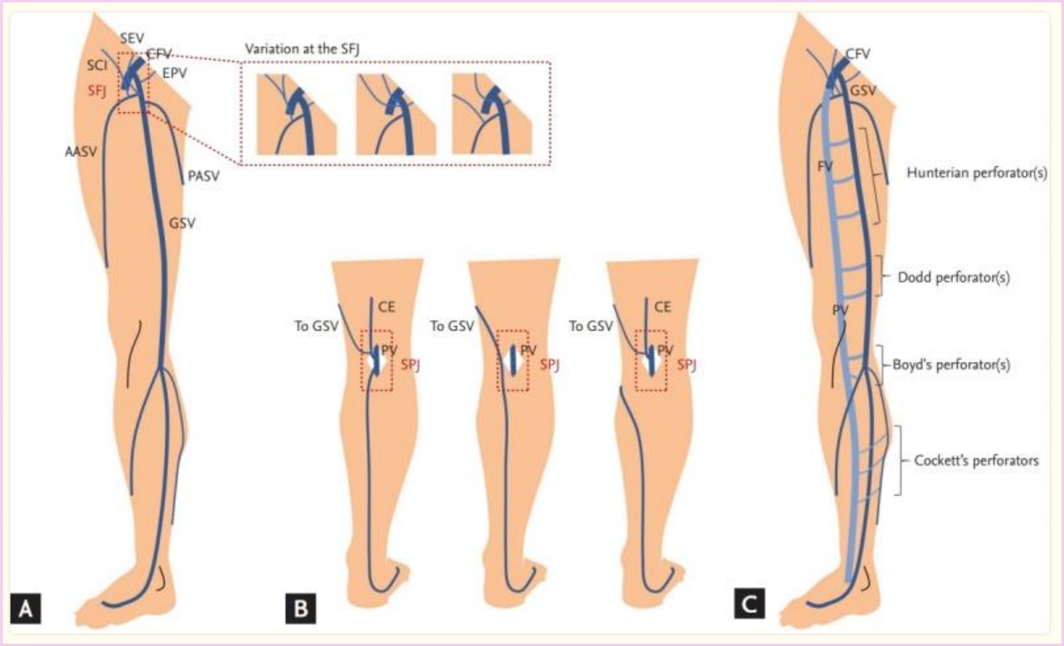

Figure 2.7 Venous system of lower extremity [101] (A, B, and C are the great saphenous vein, small saphenous vein, and perforating veins, respectively.)

Furthermore, Fig. 2.8 displays the physiological mechanism and treatment effect of CTs. Compared with the non-compression modality, the greatest amounts of pressure at the ankle are generated to ensure the blood flow with a long distance from the leg to the heart. Based on clinical investigations [102, 103], external compression increases the volume and velocity of blood flow by reducing the veins' diameter, thus promoting vein flow in the ambulant individual with venous insufficiency. For instance, Espeit et al. [14] demonstrated an increase of 64.1±58.0% (*p* (*Sig.*) <0.001) in popliteal venous blood velocity after compression therapy by CSs and local vibration application than non-compression therapy condition. Zhuang et al. [104] presented that the CT application significantly reduced the peak flow velocity of the femoral vein during ankle plantar flexion (from 61.85cm/s to 38.01cm/s) and dorsiflexion (from 80.65cm/s to 51.15cm/s) exercises, respectively. Therefore, textile-based compression interventions could effectively provide medical benefits in chronic venous insufficiency treatment.

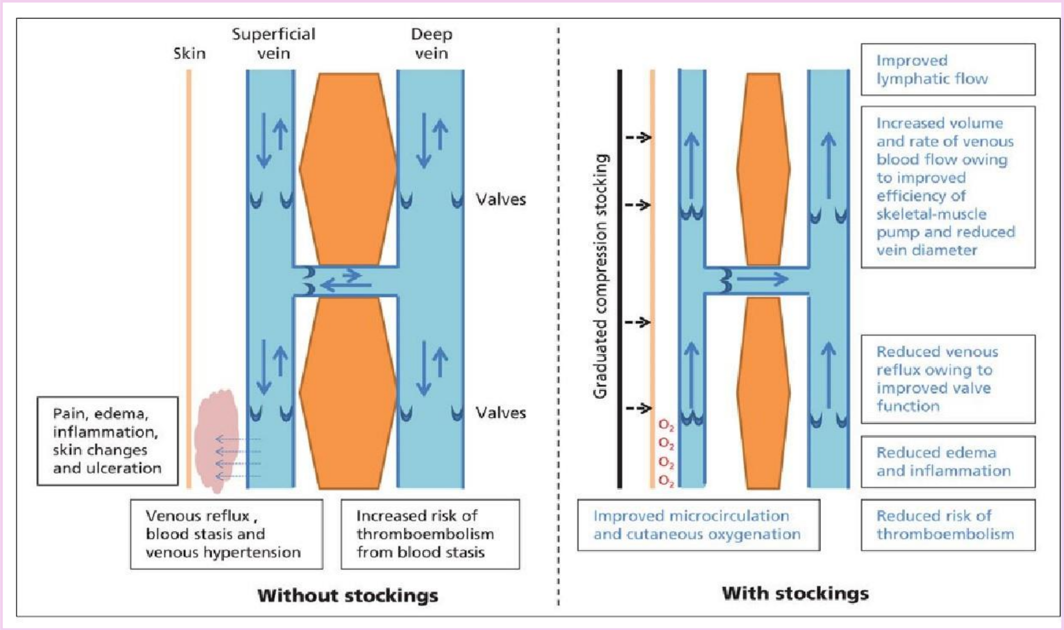

Figure 2.8 Action and physiological mechanism of CTs [105].

2.4.2 Physical Mechanisms

CTs commonly known as the elastic functional fabrics, can provide graduated and substantial coaxial pressure on the body surface to promote venous hemodynamics and vascular construction. As the traditional adjuvant physical interventions, CTs contain elastomeric fibers and yarns to provide the benefits of calibrated compression and controllable stretches. Through Partsch [106], CTs mechanistically apply the higher external pressure exertion than intravenous pressure to narrow the superficial and deep veins. The physical principles of CTs are based on Pascal’s Law and Laplace’s Law models in dynamic and static conditions, respectively. The external pressure exerted on the confined fluid is distributed evenly based on Pascal’s Law [107]. It states that the interfacial pressure could equally exert and transmit along the human body underlying the biological body assumed as an incompressible fluid.

Meanwhile, through the Laplace's Law model (as shown in Fig. 2.9) and Eq. 2.1, interfacial pressure (*P*) between the body and compression fabrics is directly proportional to the fabric tension (*T*) and inversely proportional to the radius (*r*) of curvature of the applied body surfaces [108].

$$P = \frac{T}{r} \tag{2.1}$$

where *P* is the interfacial pressure, *T* denotes the fabric tension, and *r* is the applied body radius.

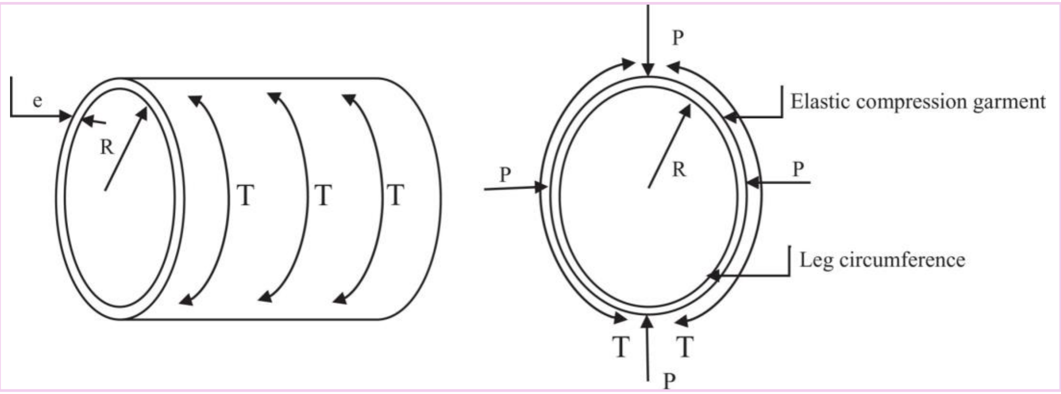

Figure 2.9 Interfacial pressure generated by CSs based on the Laplace's Law [108].

Researchers have modified the Laplace's Law through the theoretical and experimental analysis, to determine the pressure magnitudes and distributions of elastic compression fabrics accurately and flexibly for applying various available inputting parameters. For instance, Hui et al. [109] developed a theoretical model for predicting the interfacial pressure exerted by multilayer tubular fabrics with varying tensile properties. Macintyre et al. [34] established the cylinder pressure garment construction model with leg circumference and fabric stretch ratio. On the other hand, Leung [110], Siddique [111], and Barhoumi et al. [108] facilitated the pressure prediction model by using fabric elastic modulus obtained from the mathematically fitted force-elongation curves, instead of using discrete experimental tension data. Moreover, Teyeme et al. [112] simplified the calculation pressure model by employing fabric circumferences measured during initial and final stretching states. However, existing studies have established the introduced pressure models applied on regular cylinders with an ideal circular shape, constant fabric stretch strain, and rigid material properties. The external compression distributions generated by elastic fabrics were only exhibited as consistent calculated average pressure magnitudes, which led to the incorrect interfacial pressure prediction for the human body with varying curved surfaces and tissue stiffnesses.

In the majority of practical production, the pressure profiles and distributions of fabricated commercial CTs are measured necessarily through the quality controlling evaluations by standard-sized wooden leg models before being applied by users (Fig. 2.10). However, relevant researchers indicated that the interfacial pressure values of CTs tested in vivo measurement by human lower limbs were far lower than that of wooden legs caused by the material characteristics and anatomic structural diversities [113, 114]. Therefore, insufficient compression deliveries are frequently generated, caused by the cross-sectional shape profile and material property discrepancies between the applied leg models and biological bodies. Due to individual physiological diversities and anatomic structural differences, including morphological irregularities and heterogeneous tissue characteristics [32, 115], the medical efficiency and user adherence of readymade CTs have been limited by inappropriate pressure generation in practical bio-applications.

Figure 2.10 Pressure evaluation by leg model and practical use by bio-leg.

Thus, insufficient pressure performances of CTs need to be improved and reshaped through pressure optimization design according to the applied leg shape and tissue diversities between productive and bio-wearing scenario states. The relationships of individual curvature characteristics and irregularity of soft lower limb with practical pressure generation need to be explored quantitatively, to provide an effective design principle for CTs. For anatomic morphological characteristics, Chapter 4 created the novel classification and quantitative prediction systems, through the quantified and classified curvature characteristics of cross sections and proposed prediction model, the recommended pressure gaps between the industrial cylinder legs and user limbs were obtained to promote the accuracy performance prediction for development of CTs. For tissue diversities, Chapter 5 explored the biomechanical interactions between CTs and lower extremities with various biomaterial characteristics, to facilitate the scientific development of pressure dosages for CTs and promote model material selection for pressure evaluations.

2.5 Numerical Modelling of CTs

2.5.1 Macroscale Modelling

Computational FE modelling, as the advanced technology for prediction and assessment of mechanical behavior and pressure performance of CTs, can reveal the anatomic details of targeted body parts and biomechanical mechanisms of compression therapy based on the minimum total potential energy principle [116, 117]. In compression FE CT-leg systems, the subject lower limbs were reconstructed through reverse engineering technologies by employing magnetic resonance imaging (MRI) or computed tomography scanning (CT) [118-120]. The distributions of stress and strain, interfacial pressure mapping, and hemodynamic response, could be visually simulated through the FE biomechanical approaches [53, 121, 122].

For instance, Lu et al. [118] investigated the influences of external compression on the biomechanical effects of medical CSs by using highly anatomical fidelity FE models, then simulated the hemodynamic response in the deep venous flow along the biological leg. Zhang et al. [123] applied FE macroscale modelling to appraise pressure comfort by establishing the quadratic functional equation between the angle and pressure-displacement ratio of stockings. In addition, researchers [124, 125] assessed pressure distribution by the FE stocking system to provide scientific information for optimizing the material mechanical properties in the development process for economic production.

Furthermore, relevant studies also demonstrated the good agreements between experimental and FE simulated results [126, 127]. For example, Ye et al. [128]

improved the analysis efficiency by reducing the error ratio to approximately 10.3% through the proposed approach based on the investigation of 3D elastic material properties. Therefore, compared with the instrumental pressure sensors, FE modelling could visually and accurately provide the biomechanical distributions and profiles along lower limbs for material performance evaluation and property optimization.

In relevant existing FE CT-leg systems, the lower limbs were reconstrued through the massive medical captured images from MRI or CT techniques, and each leg slice needed to be processed individually for composition segmentation and tissue characterization. The mechanical properties of each part of the slices were determined exactly through regional biomaterial measurement. Based on the nonlinear mechanical behaviors, the applied strain energy functions of biological STs can be commonly defined by Neo-Hookean, Mooney-Rivlin, First-order Ogden, or Fung orthotropic material models, etc. [129, 130]. For the biomaterial property investigations, ST constitutive parameters were measured by direct identification experiments through the ultrasound SWE [131-133]. Thus, the FE models could effectively be established for user-specific mechanical analysis with individual body tissue characteristics. Nevertheless, limited studies have utilized FE CT-leg systems to investigate the pressure performance diversities caused by lower limb stiffness variations through parametric comparisons.

2.5.2 Mesoscale Modelling

Recently, researchers [134, 135] suggested combining mesoscopic structural characteristics with FE technology to explore the mechanical behavior of elastic knitted fabrics. The modelled mesoscopic loops not only promote the basic understanding of the mechanical contribution of different loop components in knitted fabrics, but also facilitate the effective prediction of pressure performance, and optimization of production parameters for cost-effective consumption.

For the construction of the geometric knitted loop model, the majority of studies applied the Pierce model with several semicircles (e.g., Leaf-Glaskin model, Munden model, B-spline curve or ellipse), and the flexible and authentic models based on the Piecewise function (e.g., Kurbak and Vassiliadis models) as well as the Spline curves (e.g., Bezier cubic curve, Non-uniform Rational B-spline (as shown in Fig. 2.11) [136]. Li et al. [137] proposed the 3D surface model by using the second-order continuous curves to enhance the visual simulation effect of weft-knitted fabric. Wadekar et al. [138] defined the centerline of the yarn as a Catmull-Rom spline, thus optimizing the yarn-level models based on physical parameter variations.

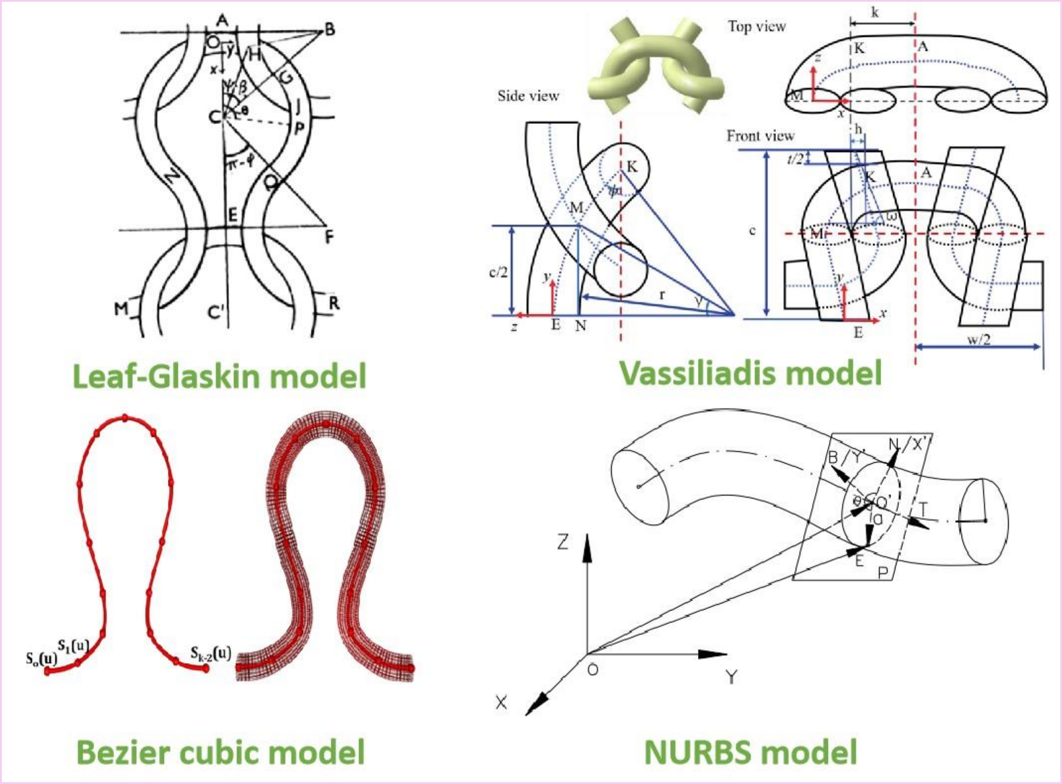

Figure 2.11 Established geometric loop models for knitted fabric simulation through previous studies [137, 139-141].

For compression knitted textiles, even though Fong et al. [79] presented a new scenario-based geometric model for a 1×1 laid-in loop pattern as displayed in Fig. 2.12, the loop morphology and its stress were still idealized without considering the actual yarn deformation and loop geometric morphology after knitted especially under the external tensile forces.

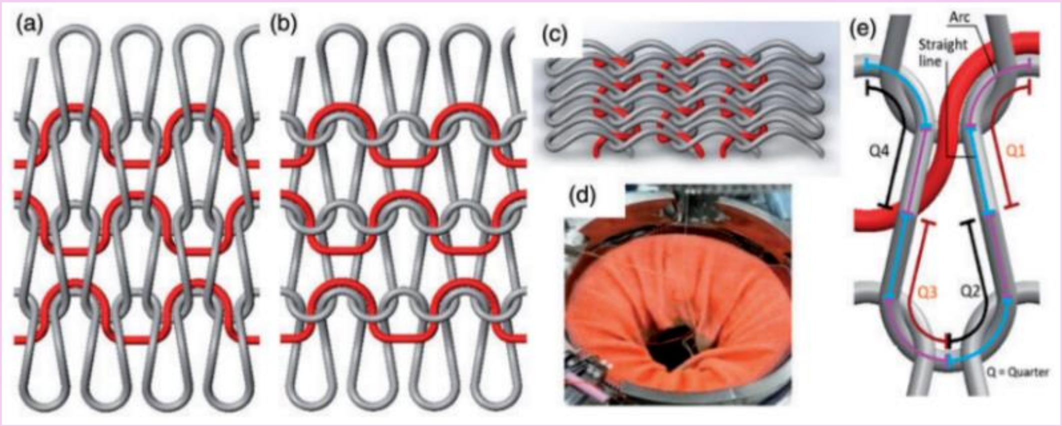

Figure 2.12 Loop pattern and geometric loop model for 1×1 laid-in structure [142].

Simultaneously, numerous researchers utilized the previously established geometric knitted loops to construct corresponding FE mechanical models for mesoscopic analysis and material simulation. For instance, Liu [141] and Wu et al. [140] presented the single jersey loop model for the geometry-dominated 3D states of deformation and stress-strain distributions in FE analysis (Fig. 2.13 (a)). Abghary [143] and Ghorbani et al. [126, 144] created a 1×1 rib loop model in an FE software environment to numerically simulate the tensile stress-strain curves. Moreover, Hessami et al. [144, 145] selected the loop density and constitutive equation with corresponding stiffness matrix as the input variables, respectively, to predict the tensile behaviors of biaxial weft knitted composites with different geometries and multiple stretching directions (course, wale, and 45°) (Fig. 2.13 (b)). Further, FE investigations in mesoscale [139, 146, 147] also demonstrated the experiment and simulation results could well predict and facilitate the weft-knitted performance, even the errors of prediction performance were between 10–16% and 7–11% for longitudinal and circumferential stretching directions, respectively [148]. However, according to the literature, limited attempts have been made on the knitted structural FE laid-in loop model for CTs as fundamental studies to lead the scientific foundation for the visualization of geometric loop deformation and stress distribution during practical stretching and wearing process.

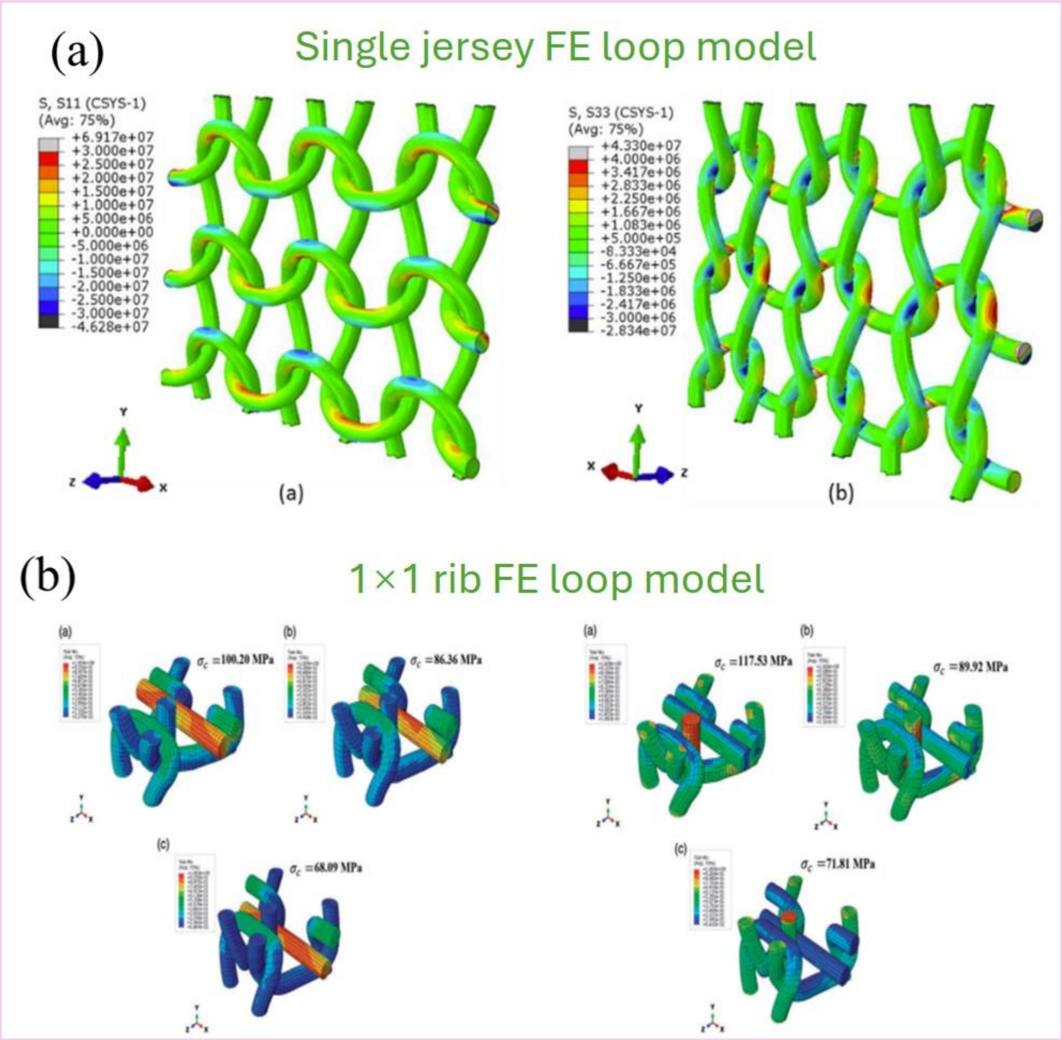

Figure 2.13 Constructed FE mechanical loop models for (a) single jersey [140], and (b) 1×1 rib structures [144].

Through the reviews related to FE macro- and meso-modeling, the numerical simulation could be utilized for the material design, property optimization, and performance evaluation of CTs. By varying the biomaterial properties of lower extremities, Chapter 5 proposed the 3D FE CT-leg systems to investigate the influences of leg ST stiffness on the pressure behaviors of CTs. In Chapter 8, by constructing various geometric leg models for needed users, FE models visually provided the pressure distributions and profiles along lower limbs. Moreover, Chapter 6 constructed the new 3D laid-in loop model to simulate the mechanical tensile behaviors of the technical knitted fabrics and visually provided the stress distributions of each loop component. Sequentially, through the proposed mesoscale loop modelling, Chapter 7 optimized and determined the yarn materials for custom CT design.

2.6 Parametric Optimization of CTs

2.6.1 Parametric Variables

3D seamless CTs formed by cylinder knitting machine, have been accepted as common compression intervention materials due to the lighter hand feelings and lower costs [89, 90]. By varying yarn-machinery parameters and knitted loop patterns, CTs with different physical dimensions and elastic tensile properties are produced for meeting the practical pressure needs through circular-knit technology.

Commonly, the knitting settings included yarn combinations, loop sizes, yarn input tensions, and knitted structures, especially for the linear and insertion densities, feeding the pre-tension of inlay yarns [92, 149]. Nevertheless, although the quantitative relationships between the knitting parameters among fabric geometric characteristics as well as pressure behaviors could be established [150], several groups of calculated numerical variables would be obtained simultaneously for the design process. For instance, in compression studies, by adjusting yarn combinations or fabric stretch ratios [80, 151], identical interfacial pressure dosages of CTs with various material properties can be achieved for compression requirements along the applied biological body. Consequently, the specific realizable knitting settings need to be optimized and confirmed for the user-oriented digitalized design prescription.

2.6.2 Optimization Methods

For multivariate parameter optimization, according to the categories and studied factors and levels, researchers employed various experimental design methodologies, such as the Taguchi design, Box-Behnken design, Central composite design, Factorial design, and Doehlert matrix design, etc. [152-154]. Additionally, grey relation analysis, response surface analysis, and neural networks are commonly applied for parametric analysis [155-158].

For example, Hafsa et al. [159] used the integration of grey relational analysis and Taguchi design to optimize the durability of sheeting fabrics, by investigating the yarn parameters, fabric tensile strength, tear strength, and abrasion resistance of developed samples were improved significantly. To provide consistent quality control, Wu et al. [160] presented the response surface analysis for parameter optimization of seamless bra cup molding. However, through the aforementioned approaches, to facilitate-further statistical parametric analysis, extensive experimental tests were required in the preparation process.

Therefore, researchers have adopted the FE parametric systems to simplify the optimization study by accurate virtual assessment. For instance, to promote the functional pressure performances of compression sportswear, Lin et al. [161] optimized the nonlinear elastic material properties and shape dimensions (thickness and tensile strain) of tubular fabrics by using the response surface method and FE model. To obtain the appropriate geometric features for manufacturing continuous fibre reinforced components, Clemens et al. [162] proposed machine-learning techniques to evaluate approximations through FE-forming results. Further, based on the experimental validation study, researchers [163, 164] also directly applied the inherent optimization module in the FE system to achieve the design and determination of production parameters. Nevertheless, fewer studies have utilized the FE optimization module to optimize the process parameters for 3D seamless CTs, and to determine the appropriate knitting materials and settings for achieving the required fabric physical morphologies and functional pressure performances.

Thus, through the quantitative equations among the knitting settings, fabric dimensions, and the generated pressure of CTs, several groups of yarn-machinery parameters would be obtained for the design process. The specific available settings need to be optimized for the user-specific requirements. FE modelling could be used for the parametric optimization to determine the appropriate design variables. Thus, through the parameterization of knitting settings and quantification of material properties, the design variables were further determined and optimized in Chapter 7, to scientifically promote the digital development of CTs with controllable performances.

2.7 Summary of Literature Review

2.7.1 Systematic Review

Through previous studies, customized CTs with fabric morphological and pressure fits could improve the medical clinic efficacy and user compliance for daily prophylaxis and CVD treatment. The double-covered yarn materials and laid-in knitted structural characteristics provided the basic elasticity and elongation requirements for CT application. Based on the Laplace's Law model, the interfacial pressure magnitudes could be predicted by the material property and body radius. Moreover, the FE simulation systems in meso- and macro-scales could be utilized for fabric tensile behavior visualization and functional performance evaluation by simulating yarn stress mappings and pressure profiles, respectively. The FE parametric systems could efficiently be used for optimizing design variables for user-oriented CT development. The subjective EWC assessments could estimate the moveable abilities and wearing comfort through practical in vivo trials.

2.7.2 Problem Statement

However, there are still some limitations and research gaps existed in the relevant study filed, as follows: (i) a complete bio-digital design, development, and biomechanical visualization system for personalized CTs with custom fit and EWC has not been established. (ii) The precise fabric morphology and pressure management of CTs need to be achieved through the efficient knitting design. (iii) The insufficient pressure supply caused by morphological profile diversities between circular leg mannequins and irregular bio-bodies limits the clinical effectiveness of CTs. (iv) The biomechanical influences of physiological tissue material characteristics of lower extremities on compression generations of CTs need to be explored systematically to improve pressure management efficacy. (v) Few studies numerically simulated laid-in loop structures in mesoscale to reveal the mechanical working mechanisms of compression fabrics for yarn material determination. (vi) The parametric optimizations of design variables are highly needed for user-oriented prescription of CT fabrication.

Consequently, the present study proposed a bio-digital design, development, and biomechanical visualization system to achieve the precise pressure management and custom fitness of CTs for individual users. Chapter 3 explored the influencing mechanisms of multiple knitting parameters on fabric properties, and then established the quantitative relationships among the parametrized knitting settings, fabric dimensions, and pressure behaviors of CTs. The corresponding equations were based on the leg mannequin measurements with circular cross sections and rigid material properties, and several groups of settings still need to be selected to obtain the specific user-oriented fabrication prescription. Thus, Chapter 4 and Chapter 5 investigated the morphological characteristics and tissue stiffness diversities on the pressure performances of CTs, respectively. Chapter 6 established the new geometric and FE mechanical laid-in loop models for the selection and optimization of yarn materials for further study. Chapter 7 optimized the design variables for the determination of user-oriented production parameters. Chapter 8 finally introduced the bio-digital design, development, and biomechanical visualization system for the custom fit CTs with EWC.

CHAPTER 3 MATERIAL PROPERTY ANALYSIS FOR SIZE AND PRESSURE CONTROL OF CTS

3.1 Introduction

For existing ready-made CTs, the selections of fabric morphological and pressure profile remain controversial. The improper morphologies of CTs led to the increasing risks of threading difficulty, wrinkle, slippage, and inadequate or excessive pressure delivery along lower limbs [37-39]. Furthermore, the ill-fitting pressure profiles of commercial CTs caused by the individual morphological diversities of lower extremities [40, 41] may not only prevent the basic treatment, but also exacerbate the unexpected tourniquet effect (such as skin break, ulcers, and blister), and limit the compromised movement and mobility during daily life [32, 43-47]. Thus, the development of CTs with user-specific suitable circumferential shape and pressure fits could improve the therapeutic efficacy and user compliance.

To achieve controllable fabric morphology and pressure performance, studies have investigated the influences of various knitting settings (e.g., knitting materials, loop patterns, and machinery parameters) on fabric properties and pressure behaviors of CTs. However, the pressure prediction could only be achieved after the fabric tests with multiple knitting attempts in the identification procedure through different yarn-machinery settings. The digital design approach to determine knitting settings needs to be proposed to efficiently develop CTs with user-required morphologies and pressure levels.

Therefore, this chapter proposed a novel design approach to achieve the digital development of CTs with precise fabric morphological and pressure management. The influencing mechanisms of each knitting setting on fabric physical-mechanical properties and pressure values were investigated fundamentally by experimental survey and correlation analysis. Based on the multiple regression model and sensitive analysis, the quantitative relationships between knitting settings with fabric morphologies and pressure performances of CTs were proposed for the yarn-machinery parameters' determination. The results provided a reference for the efficient knitting design of CT materials with controllable performances for medical treatment and human health. Additionally, combing with the influences of biological morphological characteristics (Chapter 4) and tissue stiffnesses (Chapter 5) on pressure performances, as well as the optimization of design variables by multiscale FE parametric systems (Chapter 6 and Chapter 7), the primary equations in this chapter would be further utilized in Chapter 8 for the digital design and development of custom fit CTs.

3.2 Materials and Methods

3.2.1 Preparation of CT Samples

CT samples were prepared based on various knitting settings of yarn properties and machinery parameters.

(i) *Yarn properties:* linear density (Denier) is a measure of the mass per unit length of yarn (1 Denier = the mass in grams per 9000m of yarn) and reflects a yarn's thickness or fineness [165]. The higher the Denier value, the thicker the yarn material diameter. To study the effects of the linear density of inlay yarn on the physical-mechanical and pressure properties of the fabric, three different yarn combinations with identical ground yarn and various elastic inlay yarn materials were employed to produce CT samples. Table 3.1 and Fig. 3.1 (a) illustrate the detailed characteristics of the adopted yarn materials, including nylon (polyamide) double-covered spandex (polyurethane) yarns with a linear density of 40D/40D/40D—which were used as the ground yarns (GY)—and nylon double-covered Lycra yarns with linear densities of 210D/40D/40D (YA), 280D/40D/40D (YB), and 420D/40D/40D (YC) —which were used as the inlay yarns. These double-covered yarns consisted of an elastic spandex yarn core that was surrounded by two covered yarns. The elastic core component provided high-quality tensile and recovery properties during repeated stretching, and the double-covered components improved durability, abrasion resistance, and tactile surface. The ground yarns and inlay yarns were interlaced to form CT fabrics with three types of yarn combination (GY-YA, GY-YB, and GY-YC) but the same 1×1 laid-in structural pattern (Fig. 3.1 (b)).

Table 3.1 Characteristics of the applied yarn materials

Yarn type	Yarn code	Linear density of elastic core (Denier)	Linear density of double-covered yarns (Denier)	Covering properties (circles/cm)	Yarn diameter (mm)	Young's Modulus (MPa)
Ground yarn	GY	40	40/40	30.30±0.33	0.27±0.02	0.90±0.04
Inlay yarn	YA	210	40/40	26.67±1.18	0.41±0.02	1.12±0.04
	YB	280	40/40	19.61±0.44	0.42±0.03	1.15±0.01
	YC	420	40/40	15.69±0.22	0.47±0.02	1.40±0.05

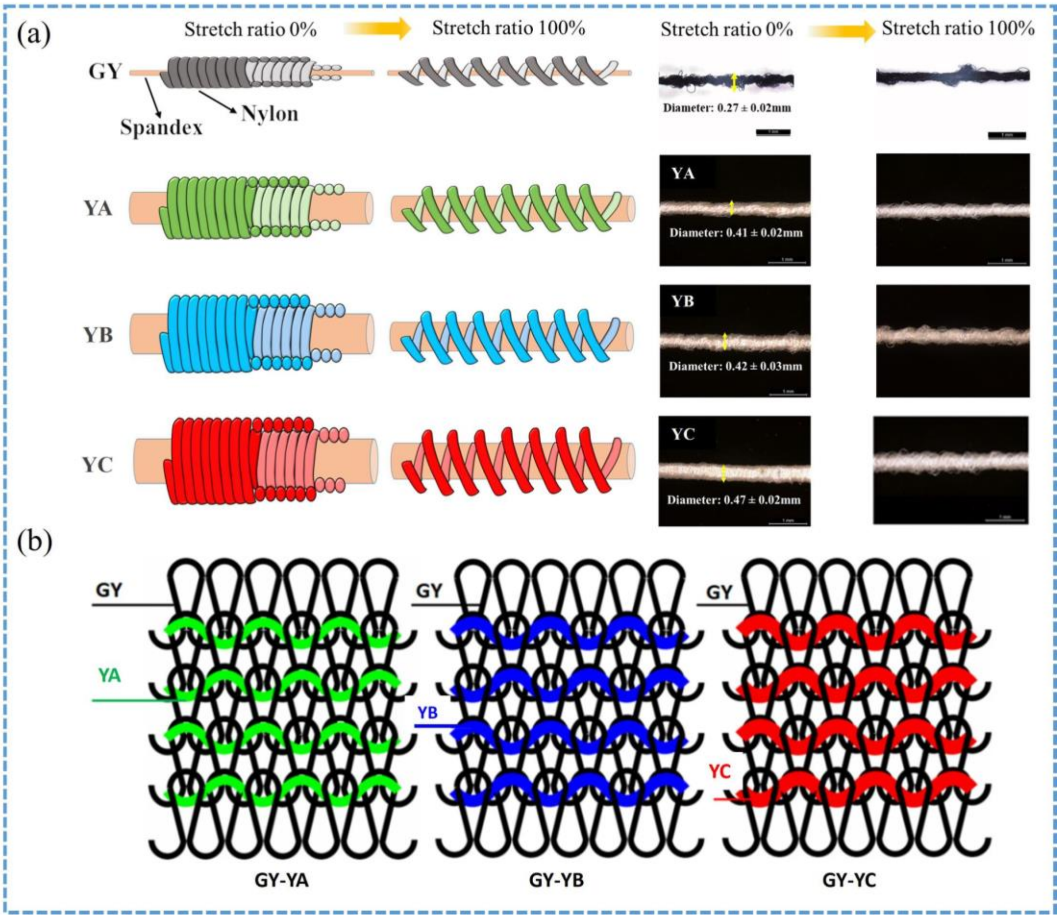

Figure 3.1 (a) Mesoscopic structures of the ground yarn and inlay yarns, (b) 1×1 laid-in knitted structure of CT fabrics with different yarn combinations.

(ii) *Machinery settings:* the CT samples were fabricated using a 3D seamless medical hosiery knitting unit (LONATI LA-45 ME, Francesco Lonati, Brescia, Italy) with a set of 4.5-inch-diameter circular needle cylinder and 400 latch needles. Four yarn feeders were used for feeding the ground yarns and inlay yarns to the core knitting zones to form CT fabrics. The first and third feeders were used for inlay yarn feeding, whereas the second and fourth feeders were employed for ground yarn feeding (Fig. 3.2 (a)). The feeding controller (PYF) and sizing motor (SMT) machine components were used to regulate the amounts of inlay yarns fed into the fabric and the sizes of the knitted loops, respectively, which influenced the physical-mechanical properties of the produced CT fabrics. Specifically, the amount of inlay yarn fed to the fabric was regulated by varying the feeding speed of PYF, and the knitting loop size was regulated by adjusting the heights of the needle beds through SMT control. Stitch cams, which are used to regulate the needle clearing level for controlling the location of loop formation, were fixed at a height of 21.5 mm in the first and third yarn feeders and at a height of 20.5 mm in the second and fourth yarn feeders during the knitting process (Fig. 3.2 (b)-(c)). These aforementioned knitting parameters were used to analyse the effects of critical machinery settings on the prepared CT fabric properties.

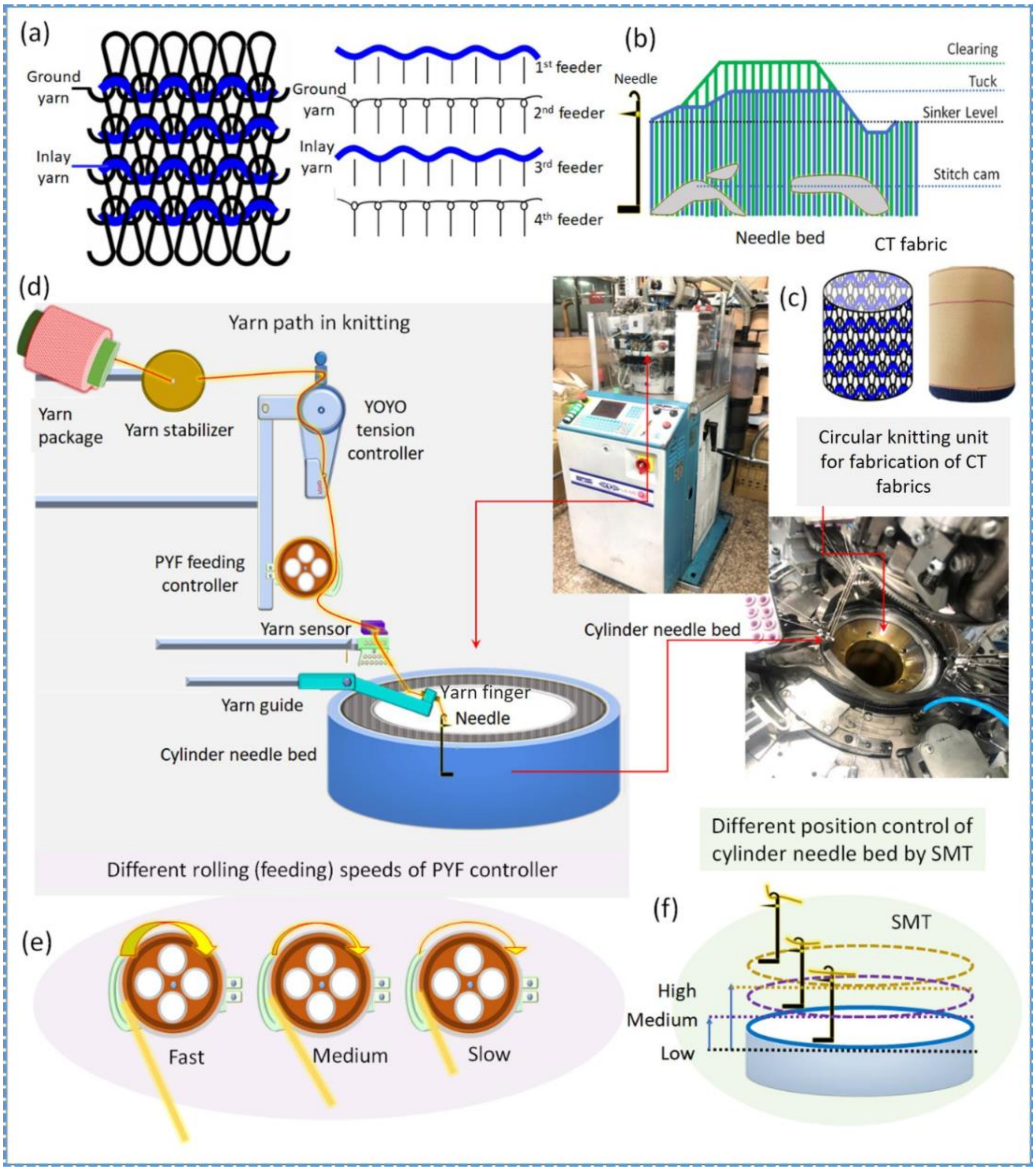

Figure 3.2 (a) 1×1 laid-in structure and four feeder settings, (b) stitch cam set at the needle bed,

(c) 3D seamless knitting unit and produced CT fabric, (d) yarn path along one of the yarn feeders, (e) different feeding speeds of PYF feeding controller, and (f) different height levels of SMT settings for the needle bed positions.

Fig. 3.2 (d)-(f) illustrates the path of the inlay yarn through one of the feeders of the knitting unit during CT fabric production. In detail, knitting yarn from a yarn cone was guided by a yarn stabiliser to enter a YOYO tension controller with a tension force of 4 cN. The feeding (rolling) speed of PYF (550 to 1300 m/min) was adjusted to control the amount of inlay yarn fed into the knitted tubular fabric. The higher the feeding speed of PYF, the more the amount of inlay yarn was fed into the knitted fabric (Fig. 3.2 (e)). The yarn then pathed the electronic sensors to the yarn finger and finally to the needle cylinder for loop knitting. The SMT regulated the knitted loop sizes by varying the heights of the needle bed (500-850 mm; Fig. 3.2 (f)). The greater the SMT value, the higher the needle bed position and the looser the knitted loops produced. The produced CT samples were ironed at a temperature of 100 °C for 10s to eliminate internal loop stresses and improve the fabrics' dimensional stability.

Tables 3.2 and 3.3 detail the CT samples (216 pieces) prepared using yarn combinations (GY−YA, GY−YB, and GY−YC) and designed machinery settings. The CT samples listed in Table 3.2 were produced by varying the feeding speed of PYF (i.e., from 550 to 1300 m/min) when the height of the needle bed (i.e., SMT setting) was fixed at 700 mm. Moreover, the CT samples listed in Table 3.3 were produced by varying the height of the needle bed via SMT (i.e., from 500 to 850 mm) when the feeding speed of PYF was fixed at 1150 m/min. These settings ensured that the influences of each knitting setting on the physical-mechanical and pressure properties of CT fabrics were examined.

Table 3.2 CT fabric samples made by different yarn combinations and PYF settings

Yarn combination I GY-YA			Yarn combination II GY-YB			Yarn combination III GY-YC		
Fabric code	PYF (m/min)	Pieces	Fabric code	PYF (m/min)	Pieces	Fabric code	PYF (m/min)	Pieces
FA1	550	3	FB1	550	3	FC1	550	3
FA2	600	3	FB2	600	3	FC2	600	3
FA3	650	3	FB3	650	3	FC3	650	3
FA4	700	3	FB4	700	3	FC4	700	3
FA5	750	3	FB5	750	3	FC5	750	3
FA6	800	3	FB6	800	3	FC6	800	3
FA7	850	3	FB7	850	3	FC7	850	3
FA8	900	3	FB8	900	3	FC8	900	3
FA9	950	3	FB9	950	3	FC9	950	3
FA10	1000	3	FB10	1000	3	FC10	1000	3
FA11	1050	3	FB11	1050	3	FC11	1050	3
FA12	1100	3	FB12	1100	3	FC12	1100	3
FA13	1150	3	FB13	1150	3	FC13	1150	3
FA14	1200	3	FB14	1200	3	FC14	1200	3
FA15	1250	3	FB15	1250	3	FC15	1250	3
FA16	1300	3	FB16	1300	3	FC16	1300	3

* GY-YA: CT fabrics (FA1-16) formed by interlooping ground yarn GY (40D/40D/40D) and inlay yarn YA (210D/40D/40D);
GY-YB: CT fabrics (FB1-16) formed by interlooping ground yarn GY (40D/40D/40D) and inlay yarn YB (280D/40D/40D);
GY-YC: CT fabrics (FC1-16) formed by interlooping ground yarn GY (40D/40D/40D) and inlay yarn YC (420D/40D/40D).

Table 3.3 CT fabrics made by different yarn combinations and SMT settings

Yarn combination I GY-YA			Yarn combination II GY-YB			Yarn combination III GY-YC		
Fabric code	SMT (mm)	Pieces	Fabric code	SMT (mm)	Pieces	Fabric code	SMT (mm)	Pieces
FM1	500	3	FN1	500	3	FO1	500	3
FM2	550	3	FN2	550	3	FO2	550	3
FM3	600	3	FN3	600	3	FO3	600	3
FM4	650	3	FN4	650	3	FO4	650	3
FM5	700	3	FN5	700	3	FO5	700	3
FM6	750	3	FN6	750	3	FO6	750	3
FM7	800	3	FN7	800	3	FO7	800	3
FM8	850	3	FN8	850	3	FO8	850	3

*GY-YA: CT fabrics (FM 1-8) formed by interlooping ground yarn GY (40D/40D/40D) and inlay yarn YA (210D/40D/40D);
GY-YB: CT fabrics (FN 1-8) formed by interlooping ground yarn GY (40D/40D/40D) and inlay yarn YB (280D/40D/40D);
GY-YC: CT fabrics (FO 1-8) formed by interlooping ground yarn GY (40D/40D/40D) and inlay yarn YC (420D/40D/40D).

3.2.2 Physical-Mechanical Measurements of CT Fabric Properties

Experiments were conducted to investigate the effects of the linear densities of inlay yarns and machinery parameters (PYF and SMT settings) on the physical-mechanical properties of the prepared CT fabrics. Mesoscopic images of the knitted fabric structural characteristics were obtained by using a Leica M165C electronic device (Wetzlar, Germany) for analysing stitch (loop) densities in an unloaded state (ASTM D1577-79). The overall stitch density D_{stitch} (stitches/cm^2) of the CT fabric was calculated as follows:

$$D_{stitch} = D_{course} \times D_{wale} \tag{3.1}$$

where D_{course} and D_{wale} are the numbers of loop stitches per centimetre of the knitted fabric along the course and wale directions, respectively. The fabric thickness (h, mm) was tested using Vernier caliper in accordance with the ASTM D1777 standard. The morphological circumference (Cir, cm) of CTs was determined from the circumference values measured at three locations, namely the middle of the sample, 1cm from the upper welt, and 1cm from the lower welts of the sample, in accordance with the ASTM D3774 standard.

The tensile behaviour of the prepared CT fabrics was investigated using the Instron 4411 uniaxial tension tester (CRE type) following the ASTM D4964 standard. Sample fabric strips with a width of 50 mm and a length of 75 mm were prepared. The two ends of these strips were fixed by using two clamps, and stretching-recovery cycles were conducted to a maximum stretch of 100% at a constant extension velocity of 300 mm/min under a standard condition (temperature: 20 ± 2 °C and relative humidity: 65% ± 2%; ISO 139:2002; Fig. 3.3 (a)-(b)). The Young's modulus (E, MPa) and elastic recovery ratio (*ER*, %) were calculated using Eqs. 3.2 and 3.3, respectively.

$$E_{course(wale)} = \frac{F}{bh\varepsilon} \tag{3.2}$$

$$ER = \frac{l_1 - l_2}{l_1} \times 100\% \tag{3.3}$$

where $E_{course(wale)}$ is the Young's modulus along the fabric course or wale directions; F is the tension force; b is the fabric's initial length; ε is the fabric's tensile ratio under a specific tension force; l_1 is the strip length under the maximum tensile ratio; and l_2 is the length once the tension force is released.

3.2.3 Pressure Measurements of CT Fabrics

The pressure (*P*, mmHg) generated at the interface between the CT fabric and the applied body directly influences the skin surface and underlying tissues in practical use, thereby affecting venous hemodynamics and the efficiency of compression therapy. Elastic CT fabrics are commonly stretched by 15%−120% [128] in their course direction to achieve the expected pressure magnitudes. To determine the *P* value for the investigated fabrics, a circular air-filled sensing probe of the Picopress$^{@}$ pressure testing system (Microlab Elettronica, Villatora, Veneto, Italy) was placed below a CT fabric on a standard leg model with an identical girth of 32.2 cm (Fig. 3.3 (c)). The course tensile ratio (ε) of each CT sample was calculated based on the leg model shape as follows:

$$\varepsilon = \frac{Cir_{Leg} - Cir}{Cir} \times 100\% \tag{3.4}$$

where Cir_{Leg} is the circumference of the leg model.

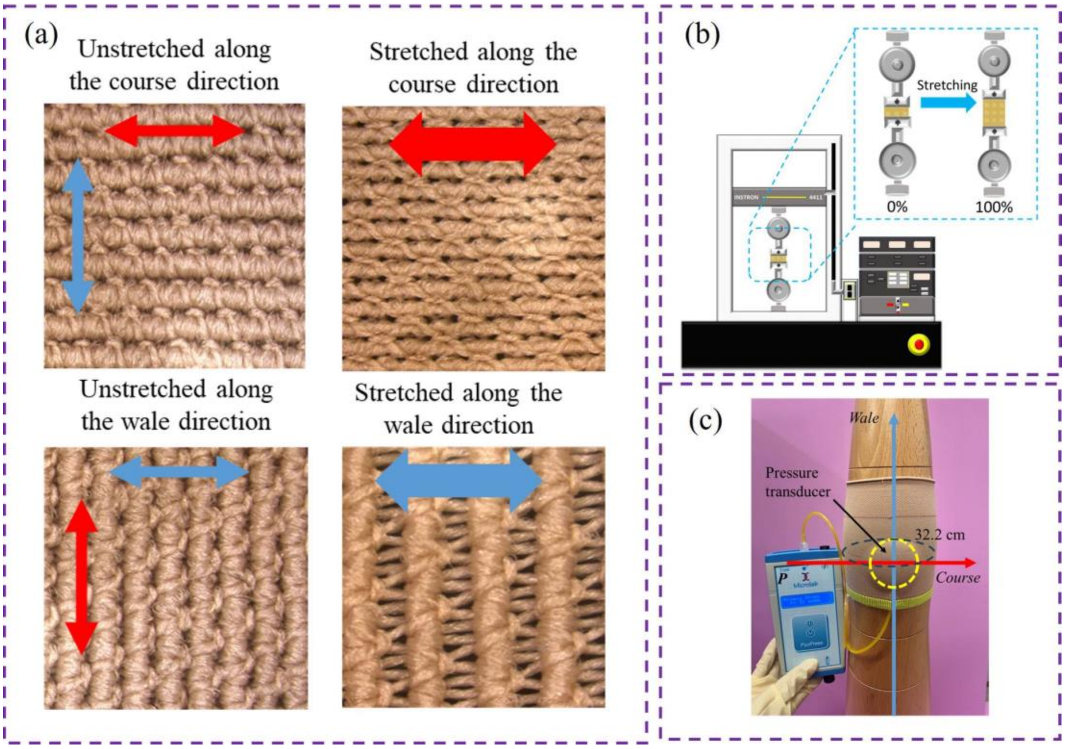

Figure 3.3 Mechanical investigations of the (a) CT fabrics under stretching along course and wale directions by (b) the uniaxial tension testing, and (c) interface pressure test using pressure transducer.

3.2.4. Parametric Analysis of Knitting Settings

- *Pearson's correlation analysis*

To investigate the influencing mechanisms of each knitting setting on physical-mechanical properties and pressure performances of the fabrics, Pearson's correlation analysis was conducted. The Pearson correlation coefficient ρ ranges from −1 to 1, with the sign and value indicating the direction and degree of correlation between the studied variables, respectively. The calculation of ρ is expressed in Eq. 3.5. The higher the absolute value of ρ, the stronger the correlation between the examined variables [166, 167].

$$\rho(\mathrm{X},\mathrm{Y})=\frac{\mathrm{cov}(\mathrm{X},\mathrm{Y})}{\sigma_X\sigma_Y}=\frac{E(XY)-E(X)E(Y)}{\sigma_X\sigma_Y} \tag{3.5}$$

where X represents the yarn (linear densities or diameters) or machinery (feeding speed or loop size setting) knitting settings, Y represents the corresponding physical-mechanical properties of (stitch density, thickness, circumferences, Young's modulus, or elastic recovery ratio) or pressure values produced by the CT sample, $cov(X,Y)$ is the covariance between X and Y, σ_X is the standard deviation of X, σ_Y is the standard deviation of Y, and $E(X)$ is the expected value of X.

- *Multiple regression modelling*

To digitalize the knitting settings, the multiple regression models, and analysis of variance (ANOVA) tests were conducted using SPSS software (version 23.0, IBM Corporation, USA) for fabric morphology and pressure control. Yarn diameter was used instead of the linear density of the yarn in the calculations (Eqs. 3.6 and 3.7), because yarn diameter directly represented the thickness or fineness of the used yarns. The fitted regression model and coefficient (R^2) were determined as follows:

$$Y = a_0 + a_1x_1 + a_2x_2 + \ldots + a_nx_n + c \tag{3.6}$$

$$R^2 = 1 - \frac{SSE}{SST} = 1 - \frac{\sum_{i=1}^{n}(y_i - \overline{y_i})^2}{\sum_{i=1}^{n}(y_i - \overline{y})^2} \tag{3.7}$$

where Y is the predicted dependent variable (P or Cir), x_n is an independent knitting setting (yarn diameter, feeding speed, or loop size setting); a_n is the coefficient value corresponding to x_n, c is the error value, SSE is the residual sum of squares (i.e., the average of the squares of the residuals of the predicted and actual P or Cir values), SST is the average of the squares of the total sum; y_i represents the data obtained before fitting, and $\overline{y_i}$ represents the data obtained after fitting.

- *Sensitivity analysis*

Sensitivity analysis was performed to identify the designed knitting settings that most strongly influenced the morphology and pressure performances of the prepared CT fabrics. The standard beta value (*β*) indicates the regression coefficient obtained after eliminating the influence of the unit of each variable. The absolute *β* value directly reflects the degree of influence of an independent knitting setting on the dependent variable (*Cir* or *P*). This value was calculated using Eq. 3.8, which is based on the proposed multiple regression models (Eq. 3.6).

$$\beta_n = \frac{a_n \times S_{x_n}}{S_Y} \tag{3.8}$$

where a_n is the nonstandardised regression coefficient. Moreover, S_{xn} and S_Y are the standard deviations of the independent setting variable and dependent setting variable, respectively.

3.2.5 Evaluation of the Quantified Digital Models

To estimate the applicability of the proposed quantified digital models for the morphological and pressure control of CTs, a series of new CT samples was fabricated for three lower limbs (code: L1, L2, and L3) with various circumferential girths and pressure degressive distributions and magnitude requirements (Table 3.4). Through the specific Cir_{Leg} and needed pressure magnitudes of each leg, the knitting settings were obtained through the quantified digital models. As shown in Fig. 3.5, the new CTs were fabricated based on the designed knitting settings through individual leg requirements. After fabrication, the circumferential dimensions and pressure performances of designed CT samples were measured. Then, deviation ratios (DROs) were calculated to compare the designed and tested fabric *Cir* and *P* values, respectively.

Table 3.4 The designed knitting settings for new CT samples

Leg code	Leg position	Cir_{Leg} (cm)	Course tensile ratio ε (%)	Designed *Cir* (cm)	Designed *P* (mmHg)	Designed sample code	Yarn combination		PYF setting (m/min)	SMT setting (mm)
L1	B	18.7	27.7	14.6	37	S1	GY	YA	750	600
	B1	20.1	35.4	14.8	33	S2	GY	YA	750	700
	C	31.8	55.6	20.4	30	S3	GY	YA	1100	700
	D	30.2	45.6	20.7	19	S4	GY	YA	1100	850
L2	B	19.5	16.2	16.8	20	S5	GY	YB	800	850
	B1	22.5	17.3	19.2	18	S6	GY	YB	950	850
	C	29.0	25.6	23.1	17	S7	GY	YB	1200	800
	D	30.5	31.5	23.2	16	S8	GY	YB	1200	850
L3	B	22.4	15.4	19.4	32	S9	GY	YC	700	850
	B1	25.1	15.0	21.8	30	S10	GY	YC	850	850
	C	30.8	27.2	24.2	29	S11	GY	YC	1300	800
	D	34.9	20.3	29.0	22	S12	GY	YC	1300	850

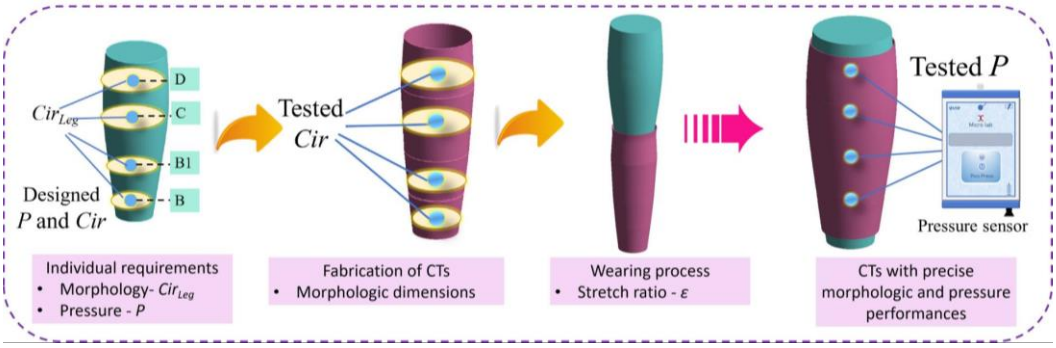

Figure 3.4 Evaluation of the proposed digital development approach.

Fig. 3.5 displays the framework of this chapter. First, the critical knitting settings and their effects on the physical-mechanical and pressure performances of the CTs were investigated experimentally. Second, the quantitative relationships between the knitting settings, morphological circumferences, and pressure values were determined through digitalized models. Third, new fabrics were developed and assessed to evaluate the applicability of the proposed approach for the digital development of CTs. The outcomes of the present study can be used to create tubular compression materials with required performances for fitting body areas.

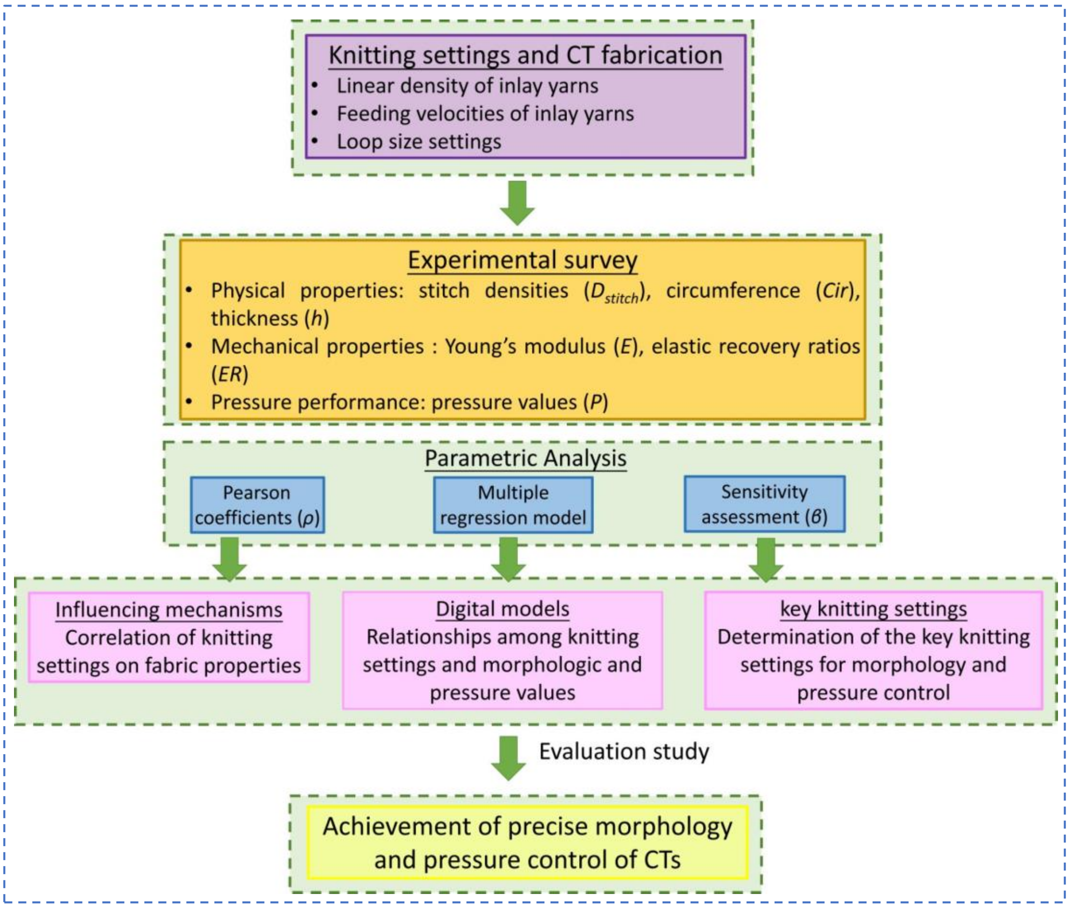

Figure 3.5 Study framework of the present chapter.

3.3 Results and Discussion

3.3.1 Effects of Knitting Settings on Fabric Properties and Pressure Values

- *Linear density of inlay yarns*

Table 3.5 indicates that the linear densities of the inlay yarns were significantly positively correlated with the circumferential dimensions [p (*Sig.*) < 0.005, $\rho(Cir)$=

0.33)] and Young's modulus of the prepared CT fabrics (Table 1, 144 pieces) along the course [p (*Sig.*) < 0.005, $\rho(E_{course}) = 0.97$)] and wale directions [p (*Sig.*) < 0.005, $\rho(E_{wale}) = 0.72$] but were significantly negatively correlated with the fabric stitch densities [p (*Sig.*) < 0.005, $\rho(D_{stitch}) = -0.58$]. Thus, through the modified Laplace's Law (Eq. 3.9) [25], the linear densities of the inlay yarns exhibited a weak correlation with the produced pressure values [p (*Sig.*) > 0.05, $\rho(P) = 0.23$] due to the simultaneous increase in the fabric circumference.

$$P = \frac{2\pi\varepsilon E_{course}}{Cir_{\mathrm{Leg}}} = \frac{2\pi E_{course}}{Cir_{Leg}} \times \left(\frac{Cir_{Leg} - Cir}{Cir} \times 100\% \right) \tag{3.9}$$

Detailly, Fig. 3.6 (a) shows the mesoscopic loop structural and macroscopic fabric morphological characteristics of the examined CTs (FA1, FB1, and FC1), which were made of three groups of yarn combinations. Under identical machinery parameters, the thicker inlay yarns laid into the CTs significantly expanded the interlaced knitted loop gaps generated by the ground yarns in the course (from 0.63 to 0.76 mm) and wale (from 0.77 to 0.94 mm) directions. Thus, diverse fabric densities and mesoscale loop characteristics led to the increasing fabric circumferential dimensions in macroscale.

Fig. 3.6 (b) and 3.6 (c) specifically illustrate the tension force-strain curves of the examined fabrics (FA1, FB1, and FC1) along their course and wale directions. The elastic core components of double-covered inlay yarn have significant influences on fabric tensile properties especially under the low fabric extension (stretch ratio of 10%) [68, 91, 92]. Thus, under the same tensile strain, the fabric FC1 made of inlay yarns (YC) with relatively high linear density of elastic spandex core produced markedly higher tension forces than did that fabric FA1 made of inlay yarns (YA) with relatively low linear density especially along the course direction, thus inducing greater tensile Young's modulus. Thus, for each knitting cycle, the fabric mechanical properties were mainly affected by the varying material compositions due to the yarn thickness. In the practical design process, even though the fabric elastic tensile properties (along the course stretching direction) of CTs could be affected by the yarn materials with different linear densities, the induced morphological circumferential diversities also need to be considered simultaneously for the achievement of expected pressure performances.

Table 3.5 Correlation among the linear density of the inlay yarns and fabric properties and pressure values

Knitting parameter	Fabric properties		Unit	Mean	SD	p (*Sig.*)	ρ
Linear densities of the inlay yarns	Physical	D_{course}	courses/cm	17.31	3.01	*	−0.36
		D_{wale}	wales/cm	24.38	1.20	***	−0.78
		D_{stitch}	stitches/cm^2	422.40	74.18	***	−0.58
		Cir	cm	20.26	3.39	***	0.33
		h	mm	0.64	0.02	--	0.16
	Mechanical	E_{course}	MPa	0.63	0.15	***	0.97
		E_{wale}	MPa	0.34	0.09	***	0.72
		ER_{course}	%	89.10	4.59	**	0.48
		ER_{wale}	%	86.94	3.55	--	0.30
	Pressure	P	mmHg	42.20	10.34	--	0.23

*: $p < 0.05$ (slight correlation); **: $p < 0.01$ (correlation); ***: $p < 0.005$ (significant correlation); --: $p > 0.05$ (no correlation)

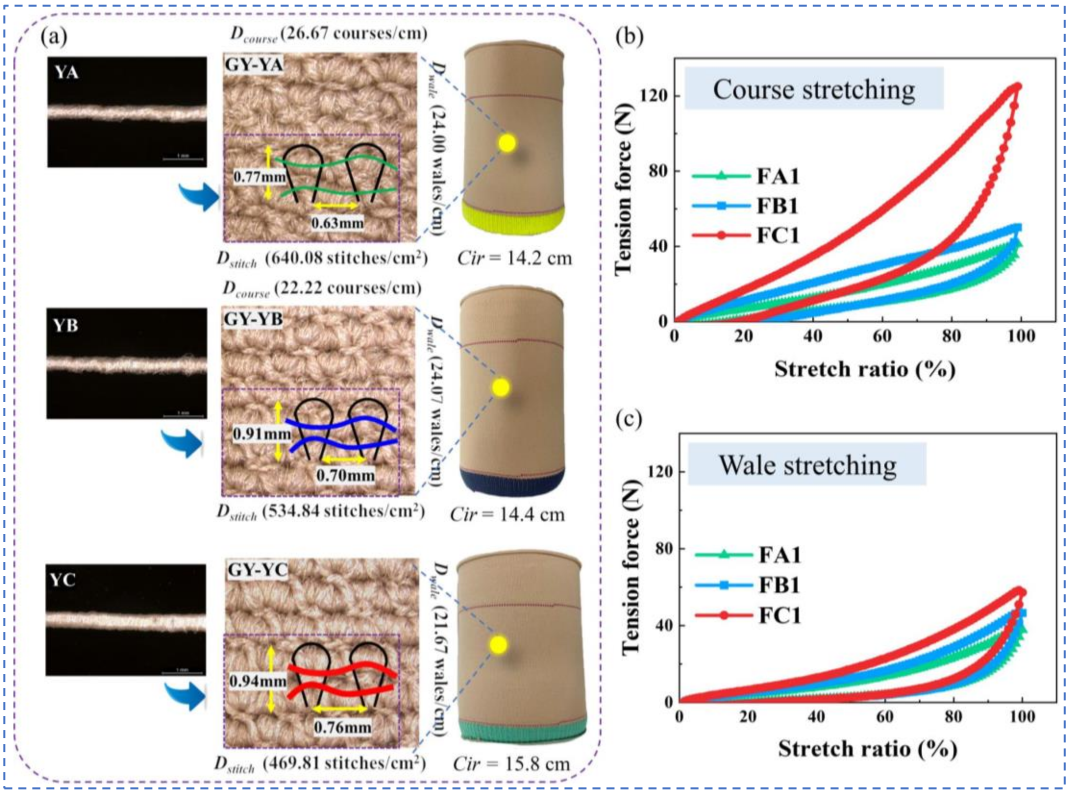

Figure 3.6 Effects of linear density of the inlay yarns on (a) mesoscopic loop structural and morphological dimensional characteristics and the tension force-strain curves of the examined CT fabrics (FA1, FB1, and FC1) along the (b) course and (c) wale directions.

- *Feeding speeds of inlay yarns*

Table 3.6 shows the effects of feeding speeds of inlay yarns on the fabric physical-mechanical and pressure properties of the prepared CT samples (Table 1, 144 pieces). The results indicate that an increase in the feeding speed of the inlay yarns by PYF (i.e., an increase in the amount of inlay yarn material fed into the knitting zone along the fabric circumferential direction) significantly increased the transverse circumferential dimensions of the CTs [p ($Sig.$) < 0.005, $\rho(Cir)$ = 0.99] but reduced the fabric stitch densities [p ($Sig.$) < 0.005, $\rho(D_{stitch})$ = −0.93] and corresponding interface pressure [p ($Sig.$) < 0.005, $\rho(P)$ = −0.99] when the CT fabric was applied to the specific object.

Fig. 3.7 specifically illustrates the effects of the feeding speeds of inlay yarns on multiple physical-mechanical properties and pressure values produced by the prepared CT fabrics as the aforementioned. During the knitting process, as shown in Fig. 3.7 (a)-(c), by increasing the PYF roller speed and yarn feeding amounts, the inlay yarn length in each loop unit was increased from 0.38 to 0.82 mm. Therefore, this also expanded the fabric's internal contacted knitted loop gaps and transverse circumferential dimensions.

Previous studies found that the pressure performances of CTs varied with fabric ε and *Cir* during the wearing process, and they also demonstrated that the feeding amounts of inlay yarns showed no significant (Fig. 3.7 (d)) with fabric tensile properties along the course stretched direction [80, 85, 93]. Further, the increased inlay yarn amounts influenced the pressure values negatively (Fig. 3.7 (e)) relating to the fabric morphological variations through the physical delivery principle of CTs (Eq. 3.9). Thus, in compression fabric development, the pressure delivery could directly be controlled by the fabric circumferential dimensions through the feeding amounts of inlay yarn.

Table 3.6 Correlation between feeding speeds of inlay yarns and fabric properties and pressure values

Knitting parameter	Fabric properties		*Unit*	Mean	SD	p (*Sig.*)	ρ
Feeding speeds of the inlay yarns	Physical	D_{course}	courses/cm	18.68	2.72	***	−0.94
		D_{wale}	wales/cm	25.85	0.64	***	0.85
		D_{stitch}	stitches/cm^2	481.40	59.27	***	−0.93
		Cir	cm	18.91	2.40	***	0.99
		h	mm	0.64	0.02	--	−0.13
	Mechanical	E_{course}	MPa	0.50	0.02	--	−0.41
		E_{wale}	MPa	0.30	0.03	***	−0.87
		ER_{course}	%	91.11	1.63	***	−0.83
		ER_{wale}	%	87.13	3.26	--	−0.21
	Pressure	*P*	mmHg	36.08	6.28	***	−0.99

*: $p < 0.05$ (slight correlation); **: $p < 0.01$ (correlation); ***: $p < 0.005$ (significant correlation); --: $p > 0.05$ (no correlation)

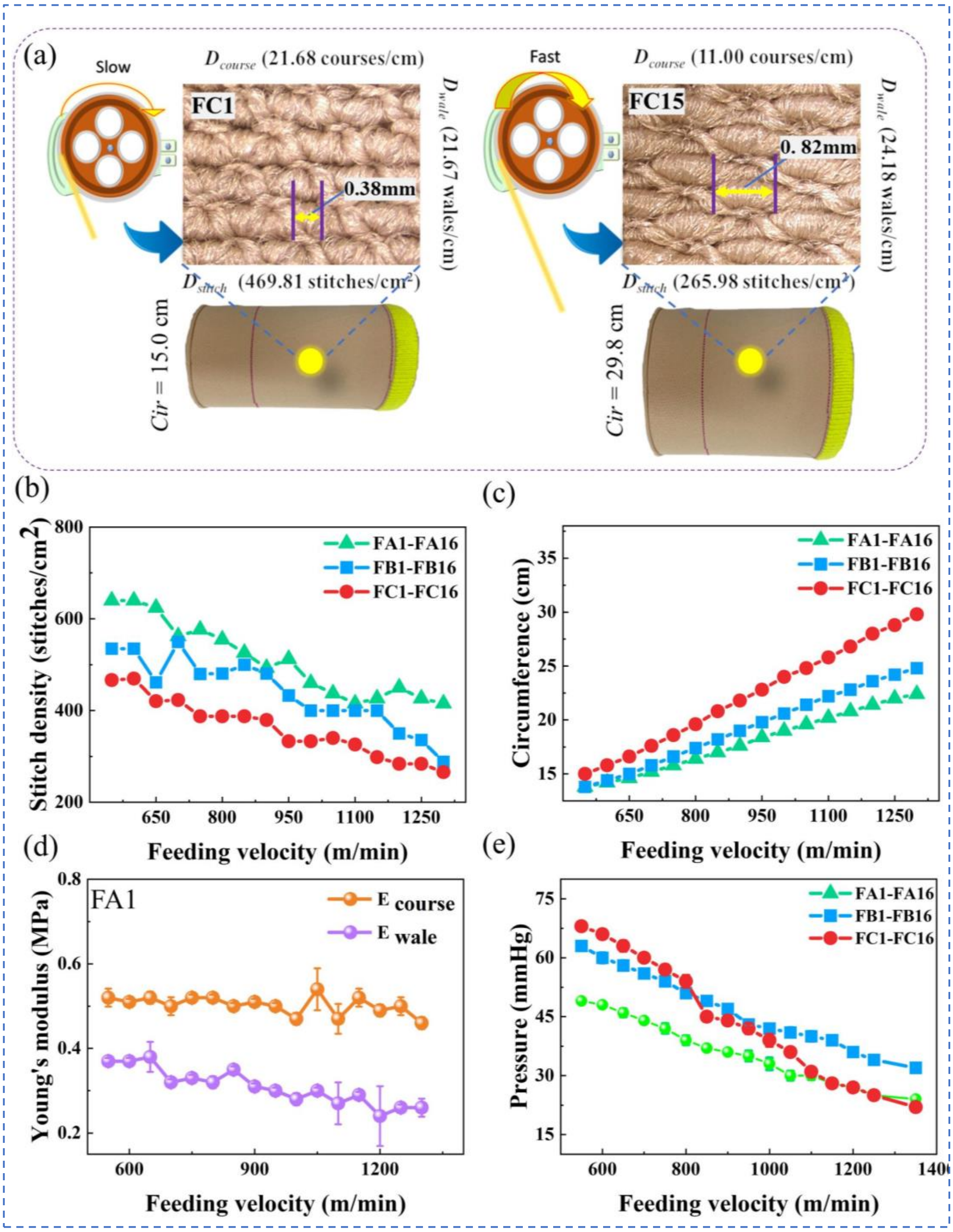

Figure 3.7 Effects of feeding speeds of the inlay yarns on (a) mesoscopic loop structural and morphological dimensional characteristics (FC1 and FC15), (b) fabric stitch densities, (c) transverse dimensions (circumference), (d) Young's moduli (FA1), and (e) produced pressure values.

- *Loop size settings*

The statistical results presented in Table 3.7 and Fig. 3.8 indicate that the loop size, which was regulated by the SMT setting, had significantly negative correlations with the fabric stitch density (p (*Sig.*) < 0.01, $\rho(D_{stitch}) = -0.85$), Young's modulus along the course (p (*Sig.*) < 0.01, $\rho(E_{course}) = -0.89$) and wale (p (*Sig.*) < 0.005, $\rho(E_{wale}) = -0.95$) directions, and pressure (p (*Sig.*) < 0.005, $\rho(P) = -0.95$) exerted by the CT samples (Table 2, 72 pieces).

The SMT settings regulated the knitted loop lengths formed by the ground yarns. An increase in the SMT setting caused an increase in the height of the cylinder needle bed (i.e., the loop formation area), which resulted in the production of a larger loop (Fig. 3.8 (a)) and smaller fabric densities (Fig. 3.8 (b)). Moreover, Fig. 3.8 (c) shows that, due to the varied loop size settings, the circumferential dimensional diversities maintained from 0.6 to 1 cm. According to the tensile tests, fabric E_{course} was influenced by the varied loop lengths of CTs (Fig. 3.8 (d)). Through the introduced working mechanisms of compression generations (Eq. 3.9), the interfacial pressure values between the CT fabric and the applied body decreased (Fig. 3.8 (e)). It indicates that the SMT settings were mainly utilized for the pressure control by the material tensile properties for CTs with determined morphology.

Table 3.7 Correlation between knitting loop sizes and fabric properties and pressure values

Knitting parameter	Fabric properties		Unit	*Mean*	SD	p (*Sig.*)	ρ
Loop size settings	Physical	D_{course}	courses/cm	15.89	0.26	***	0.97
		D_{wale}	wales/cm	26.95	1.13	**	−0.94
		D_{stitch}	stitches/cm^2	428.02	11.71	**	−0.85
		Cir	cm	20.70	0.24	*	0.93
		h	mm	0.65	0.02	--	0.79
	Mechanical	E_{course}	MPa	0.54	0.12	**	−0.89
		E_{wale}	MPa	0.32	0.13	***	−0.95
		ER_{course}	%	89.66	2.80	--	0.36
		ER_{wale}	%	87.12	3.78	--	0.50
	Pressure	P	mmHg	31.75	4.95	***	−0.95

*: $p < 0.05$ (slight correlation); **: $p < 0.01$ (correlation); ***: $p < 0.005$ (significant correlation); --: $p > 0.05$ (no correlation)

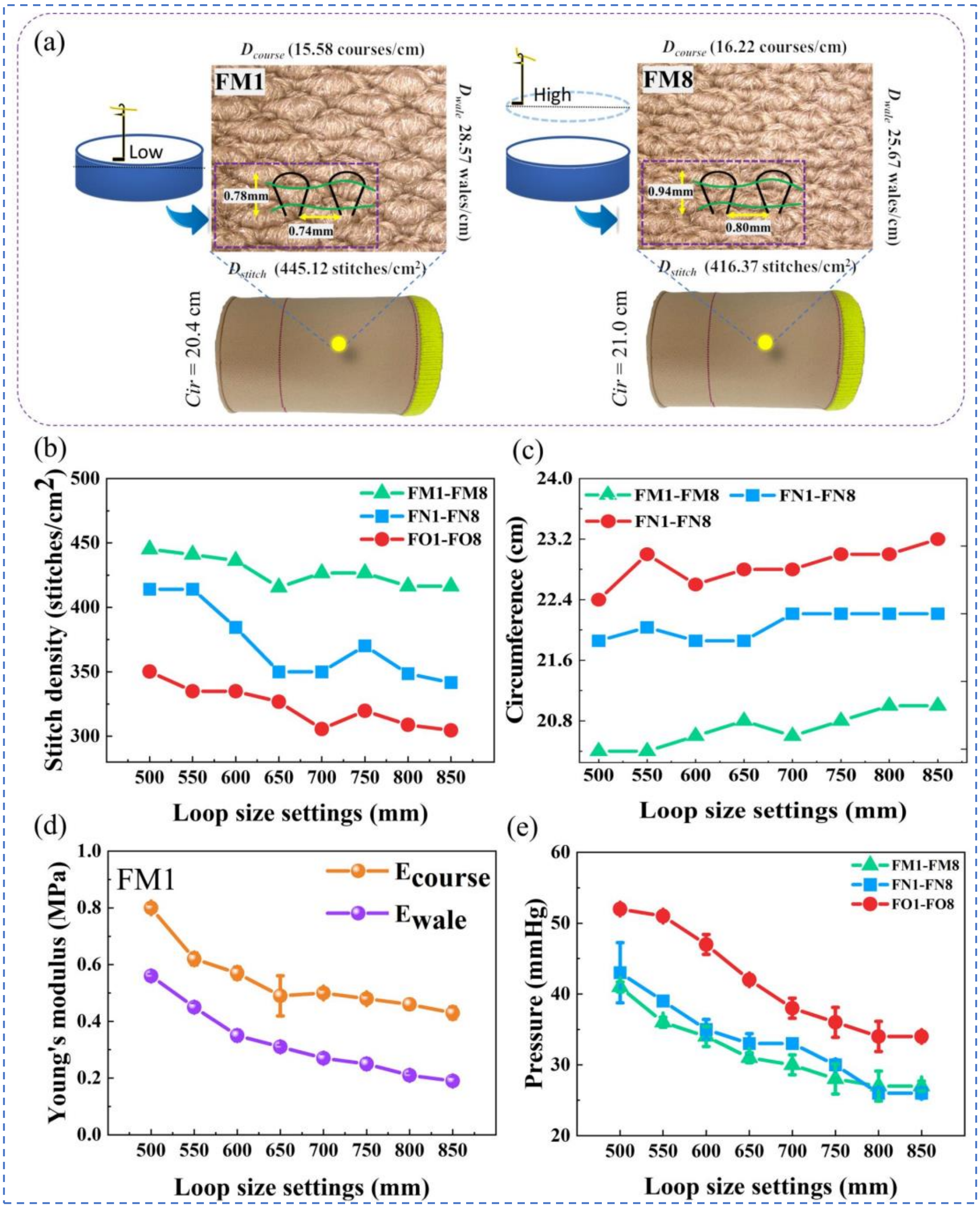

Figure 3.8 Effects of knitting loop sizes regulated by SMT settings on (a) mesoscopic loop structural and morphological dimensional characteristics (FM1 and FM8), (b) stitch densities, (c) transverse circumferences, (d) Young's moduli (FM1), and (e) pressure magnitudes of CT fabrics.

3.3.2 Digital Morphology and Pressure Models from Quantified Knitting Settings

Controlling the morphology of CTs is crucial for controlling their material tension and pressure values to achieve user compliance in compression treatment. A multiple regression model was developed based on the findings obtained from section *3.3.1* to characterise the quantitative relationships between the design knitting settings and the circumferential dimensions and pressure performances of the prepared CT fabrics (Tables 3.1 and 3.2; 216 pieces). The results of ANOVA (Table 3.8) and regression analysis indicated that the developed regression equations (Eqs. 3.10 and 3.11) had good fits [84] with the predicted circumference (R^2 = 0.96) and pressure (R^2= 0.85), respectively, indicating that the developed regression models can be used to guide the setting of multiple knitting parameters to achieve morphology and pressure control for CT fabrics in practice.

$$Cir = 0.016 \times x_1 + 0.002 \times x_2 + 84.493 \times x_3 - 33.201 \tag{3.10}$$

where *Cir* is the designed circumference of the CT fabric (cm), x_1 is the feeding speed of the inlay yarn (m/min), x_2 is the SMT setting for loop size control (mm), and x_3 is the diameter of the inlay yarn (mm).

$$P = -3.903 - 0.02 \times x_1 - 0.062 \times x_2 + 0.217 \times x_3 + 213.072 \times x_4 \tag{3.11}$$

where *P* is the designed pressure for the CT fabric (mmHg), x_1 is the feeding speed of the inlay yarn (m/min), x_2 is the SMT setting for loop size control (mm), x_3 is the tensile ratio (%) in the course direction when the fabric is worn on a body with a specific size, and x_4 is the diameter of the inlay yarn (mm).

Table 3.8-1 ANOVA and regression analysis for CT morphology control

		Sum of squares	Mean square	*F*	*Sig.*
ANOVA	Regression	990.715	330.24	485.02	***
	Residual	44.257	0.68		
	Total	1034.972			
		Coefficient	t values	*Sig.*	R^2
Regression analysis	Constant	-33.201	-15.57	***	**0.96**
	Feeding speed	0.016	31.91	***	
	Loop size settings	0.002	1.08	-	

	Inlay yarn diameter	84.493	20.84	***	

Table 3.8-2 ANOVA and regression analysis for CT pressure value control

		Sum of squares	Mean square	*F*	*Sig.*
ANOVA	Regression	4766.788	1191.70	111.37	**
	Residual	866.701	10.70		
	Total	5633.488			
		Coefficient	t values	*Sig.*	R^2
Regression analysis	Constant	-3.903	-0.56	0.58	**0.85**
	Feeding speed	-0.020	-11.03	***	
	Loop size settings	-0.062	-9.40	***	
	Tensile ratio	0.217	6.72	***	
	Inlay yarn diameter	213.07	15.00	***	

*: $p < 0.05$ (slight correlation); **: $p < 0.01$ (correlation); ***: $p < 0.005$ (significant correlation); --: $p > 0.05$ (no correlation)

3.3.3 Sensitivity Analysis for Determination of the Key Knitting Settings

According to the β values obtained in the sensitivity analysis (Fig. 3.9 (a) and (b)), the most important parameter that affected the morphological circumferences of the prepared CTs was the feeding speed of the inlay yarns ($\beta = 0.82$), followed by the yarn diameter and knitting loop size setting. Thus, by regulating the settings of PYF to control the feeding speed of the inlay yarns, one can vary the circumference of CTs to fit them to different lower bodies. Moreover, by regulating the SMT settings to adjust the knitting loop size ($\beta = -0.93$), one can control the pressure produced by CT fabrics. Consequently, by varying the settings of PYF for adjusting the fabric circumferential dimensions to ensure that the fabric fits the relevant body. And by fine-tuning the SMT settings to realise appropriate loop sizes for achieving suitable pressure levels. The aforementioned strategies enable the morphology and pressure performances of knitted compression materials to be easily controlled.

3.3.4 Evaluation of the Precision of Morphological and Pressure Models

Through the designed and measured values of the newly developed CT samples (S1-S12), the precisions for fabric morphological and pressure quantified models were within ± 0.3 cm and ± 5 mmHg, respectively. The DROs for *Cir* and *P* were approximately 1.1% and 10.8%, respectively. In contrast to previous studies [110, 168], the average pressure error ratio predicted by the fabric properties was at least 15.37%. Simultaneously, the standardized degressive pressure gradients were generated along each lower extremity. Thus, the designed morphological circumferences and pressure values agreed favourably with the measured ones, which indicated that quantitative relationships established between the knitting design settings, fabric circumferential dimensions, and pressure can guide knitting parameter design for achieving precise morphology and pressure management of CT fabrics.

This approach allowed the design and development processes of CTs to be more efficient for fitting the performance requirements of the end uses in the practice of compression therapy. Moreover, due to the material characteristics and anatomic structural differences [169], the pressure performance diversities between the leg models and biological limbs were investigated in further chapters, to facilitate the medical effectiveness of CTs in compression therapy.

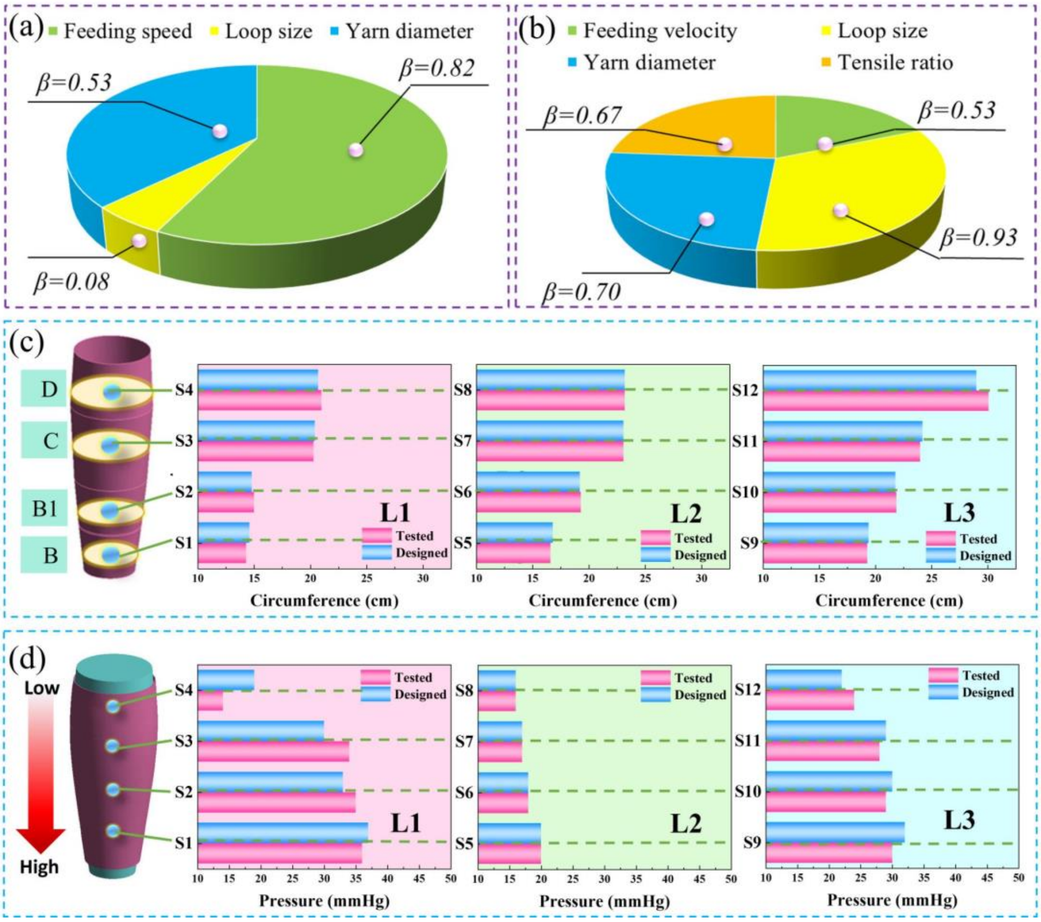

Figure 3.9 Sensitivity analysis of the key knitting parameters to control fabric (a) circumferential morphology and (b) pressure magnitudes of CT samples. Comparisons between the designed and measured (c) *Cir* and (d) *P* values of the new CT samples (S1-S12).

3.4 Summary

This chapter developed a digital approach to realise the precise morphology and pressure management for knitted CTs. This approach involves 3D seamless fabrication, experimental survey, parameter analysis, and performance evaluation. By investigating the knitting settings and their influencing mechanisms on the physical-mechanical and pressure properties of CTs, this chapter determined that the inlay yarn thickness significantly affects the stitch densities and tensile properties of CT fabrics. The feeding speed of PYF can be adjusted to control the fabric circumferential dimensions.

Additionally, the knitting loop size can then be regulated by fine-tuning the SMT settings to achieve an appropriate fabric pressure.

The quantified digital models established among multiple critical yarn-machinery settings, morphological circumferences, and pressure performances of CT fabrics reveal the complex interactive mechanisms between knitting settings and material properties. The evaluated morphological (DRO: 1.1%) and pressure (DRO: 10.8%) results showed the high acceptability of the proposed digitalized development strategy for user-oriented CTs. The outcomes of this chapter provided the primary digital equations for the efficient design and control of knitted CTs, the influences of leg irregular curvature characteristics and ST stiffness on pressure behaviors were further studied in the next two chapters, to improve functional effectiveness for these tubular CT materials in compression therapy.

CHAPTER 4 EFFECTS OF BODY MORPHOLOGICAL CHARACTERISTICS ON PRESSURE PERFORMANCES OF CTS

4.1 Introduction

Chapter 3 primarily achieved the precise fabric dimensional and pressure management of CTs through the leg mannequin measurements. In the actual wearing process, the generated insufficient pressure supply limited the efficiency of CTs due to the morphological irregularities and heterogeneous tissue properties of the biological body [170]. The inappropriate and inadequate pressure distributions may not only prevent the required treatment, but also lead to varying degrees of ischemia, necrosis, and ulcerations [43-46]. Therefore, the insufficient pressure performances of CTs need to be improved and reshaped through the optimization of pressure value gaps between the productive and bio-wearing scenario states.

3D-BS as advanced technology has been adopted extensively for the anthropometric measurements of body dimension and shape profile [171]. Particularly, in CT studies, researchers [169, 172-176] determined individual dimensional and curvature characteristics by using 2D image simulation and 3D-BS digital anthropometry, to predict the pressure performance for achieving the user-oriented size-fit of CTs. However, previous studies mainly obtained dimensional values of leg circumferences, heights, and curvature radius through the 3D scanned data, the relationship of individual curvature characteristic and irregularity of the lower limb with practical pressure generation need to be explored quantitatively, to provide a new and effective strategy for CTs with enhanced pressure performances.

Therefore, to reshape and enhance the pressure generation supplied by insufficient compression performance of CTs, this chapter adopted 3D-BS and reverse engineering technologies to quantify and classify the curvature characteristics of cross sections for biological lower extremities. Sequentially, based on the individual geometric dimensional and irregular morphological variations, the modified pressure prediction model with acceptable agreements was constructed and validated through actual wearing trials. Then, the recommended compression gaps between the cylinder wooden legs and user limbs were obtained through the proposed irregularity levels and predicted pressure values by the proposed optimized prediction model. Thus, the created novel classification strategy and quantitative prediction model could lead to a theoretical and practical reference for the scientific optimization of pressure performance for the bio-design and development of CTs. This chapter also promotes pressure fitting and enhances the medical treatment precision for textile-based compression products.

4.2 Materials and Methods

4.2.1 Acquisition of Anthropometric Data

To classify the lower limb shapes, healthy subjects with various genders and ages were recruited for establishing the database of morphological variations. To obtain the anthropometric data, a total of 22 subjects aged 28-60 years (13 females and 9 males, weight: 61.52 ± 7.18 kg, height: 1.65 ± 0.10 m, body mass index (BMI):

22.63 ± 2.54 kg/m^2) were voluntarily recruited in the Hong Kong Polytechnic University via random sampling method for data acquisition with equal probability of being selected for participation [177]. Then, to efficiently and automatically capture and extract the anthropometric characteristics of each subject, this chapter applied the contactless Anthroscan 3D Body Scanner, which conforms to DIN EN ISO20685 standard (3D scanning methods for internationally compatible anthropometric databases) [178]. Based on laser triangulation technology and a non-radiation safety light source, eight omni-directional camera sensors worked simultaneously to produce 360° body image models within 6-8 seconds. The high accuracy of applied scanner system (mean error of body circumference was less than 0.1 cm and scanning point density was 200 p/cm^2) avoided the measurement interference and invalid data caused by slight body displacement during the scanning process. Moreover, prior to data collection and lower body segmentation, participants were requested to stand steadily at the scanning platform and adopt the special posture of arm and torso separation as well as maintain a stable breathing state (Fig. 4.1 (a)).

After physical scanning operation, the scan derived cloud point data in Stereolithography (STL) format was preliminarily processed by the Geomagic Studio 2014 (64 bit) software (Raindrop Geomagic, Research Triangle Park, NC, USA). The scanned surface models were established without irrelevant noise by automatic mesh analysis, polygon optimization, and surface fitting, respectively. To digitalize the scanned images for further numerical analysis, reverse engineering was applied to reconstruct geometry solid leg models [179]. Thus, to generate accurate original contour boundary coordinate data, the extracted surface models were further imported into 3D SpaceClaim Direct Modeler (SCDM) software (ANSYS, Pennsylvania, Pittsburgh, USA) via the skin surface function for 3D entity model reconstructions and lower body required sectional extractions (Fig. 4.1 (b)). According to clinical trials and comparing investigations, researchers have commonly demonstrated the therapeutic efficacy and patient comfort of knee-length CSs [180-182]. Therefore, through the measurement guidance of clinical practice and the Germany standard of RAL-GZ 387/1, four anatomic sites (B-ankle, B1-brachial, C-calf, and D-knee) along all subject left lower limbs were determined as major studied leg sectional slices (Fig. 2.1 (a)). Thus, the 2D coordinate data (*x*, *y*) of a total of 88 slices (coded as ID 1-1-1 to ID 5-3-4) were obtained digitally by CAD (computer-aided design) system. Additionally, the number of splattering points (*n*) for each leg slice was at least 22 for further geometric calculations.

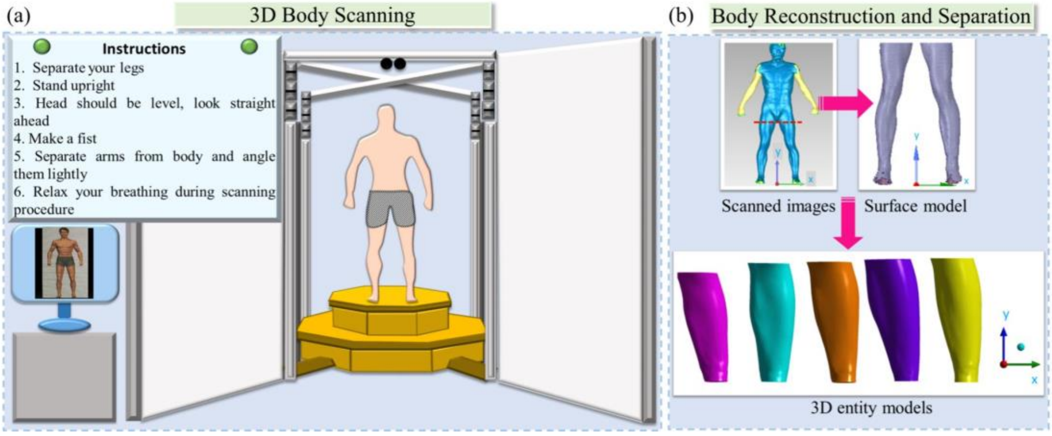

Instructions
1. Separate your legs
2. Stand upright
3. Head should be level, look straight ahead
4. Make a fist
5. Separate arms from body and angle them lightly
6. Relax your breathing during scanning procedure

Figure 4.1 (a) 3D-BS and subject's scanning posture, (b) construction and separation of 3D digitalized leg models.

4.2.2 Characterization and Classification of Lower Extremity Sectional Slices

To generate the cross-sectional leg contour curves and calculate individual geometric characteristics, the obtained point data of all slices were processed based on the curvature fitted function via MATLAB R2016a system (MathWorks. Inc., Natick, MA, USA). Firstly, as shown in Fig. 4.2 (a), according to the sequential scattering points ((x_i, y_i), i=1,2, …n), the biological irregular curve (irr-curve) centered on the centroid of O (x_0, y_0) could be plotted automatically to achieve the visualization of cross-sectional leg specific profile shape. Thus, the circumference (Cir_{Leg}) of the lower limb slice was calculated via Eq. 4.1 through 2D scattered data. Secondly, to quantify the individual characteristics of subject's leg cross sections, each irr-curve was divided into several segmented curves with different curvature radius. The curvature radius (R_1, R_2, …R_n) and curvatures ($\frac{1}{R_1},\frac{1}{R_2},...,\frac{1}{R_n}$) of irr-curve were fitted by applying the Inline function.

$$Cir_{\mathrm{Leg}}=\sqrt{\sum_{i=1}^{n}(x_{i+1}-x_i)^2+(y_{i+1}-y_i)^2} \tag{4.1}$$

Simultaneously, for comparison, based on the aforementioned curvature radius, the corresponding ideal circle curve (cir-curve) related identical slice was drawn according to the radius of R_{ideal} ($R_{ideal}=\frac{1}{n}\sum_{i=1}^{n}\sqrt{(x_i-x_0)^2+(y_i-y_0)^2}$) determined by the average distance from irr-curve to the centroid (O).

Thirdly, to characterize the irregularity of leg cross sections, the SDC of each irr-curve was estimated through Eq. 4.2. Additionally, the SDC values could reflect the discrete fluctuation degree of varying curvatures, the larger the SDC, the more obvious variation of curvature radius, the larger difference from the cir-curve, thus the greater irregularity of the subject's leg cross sections.

$$SDC=\sqrt{\frac{1}{n}\sum_{i=1}^{n}(\frac{1}{R_i}-\frac{1}{R_{ideal}})^2} \tag{4.2}$$

where R_i is the *n*th of the curvature radius.

Then, based on the afore-introduced SDC values, the IR levels were classified by using the *k*-means clustering algorithm. Through the Euclidean Distance [183, 184], related specific SDC variables of each leg slice were clustered for further exploration. Additionally, the calculation algorithms for the Cir_{Leg} and SDC value are present by Fig. 4.2 (d).

4.2.3 Construction of Pressure Prediction Model

Based on the obtained leg sectional geometric data and curvature characteristics (through section *4.2.2*), a novel pressure prediction model (PM) derived from Laplace's Law was established through the accuracy calculations of leg curvature radius, fabric strain, and fabric thickness. Firstly, for the investigation of circumferential pressure generated on leg cross sections, the PM was constructed based on a 2D polar coordinate system (ρ, θ) as shown in Fig. 4.2 (b) and Fig. 4.2 (c). The stress-strain curve of elastic fabric conforms to Hooke's Law [48], thus fabric stress can be calculated according to Eq. 4.3. Notably, the interfacial pressure is vertical to the contact body plane, thus, Young's modulus (E_{course}) represents the fabric transverse (course) mechanical properties.

$$\sigma_\rho = E_{course}\varepsilon_\rho \tag{4.3}$$

where σ_ρ and ε_ρ are the fabric stress (Pa) and fabric strain (%) along the fabric course direction. Secondly, as illustrated in Fig. 4.2 (b), the varying curvature radius of leg section (R_L) were defined as a function variable related θ, therefore, fabric displacement (u_ρ) was determined by $R_L(\theta)$-R_F (where, R_F is the radius of tubular compression fabric), thus fabric strain can be expressed as Eq. 4.4.

$$\varepsilon_\rho = \frac{\partial u_\rho}{\partial \rho} \tag{4.4}$$

where u_ρ is fabric displacement (m).

Thirdly, the compression elastic fabric with a certain thickness was assumed to consist of multiple material layers. For instance, the fabric part in contact with the body was defined as the innermost layer, conversely, the part without contact skin was the outermost layer. Therefore, as Eq. 4.5 and Fig. 4.2 (c), the cross-sectional fabric area was obtained accurately through the measured Cir_{Leg} and fabric thickness.

$$A = \oint_h 2\pi R_L dh = \oint_h Cir_{Leg} dh \tag{4.5}$$

where A is fabric cross-sectional area (m^2), and h is fabric thickness (m).

Then, the external force of the fabric can be obtained by integrating the above formula (Eq. 4.6). Consequently, the PM for the biological body with irregular morphological characteristics can be expressed as P_{PM} through Eq. 4.7.

$$F = TCir_{Leg} = A\sigma_\rho = E_{course}\frac{\partial u_\rho}{\partial \rho}\oint_h Cir_{Leg} dh \tag{4.6}$$

where F is internal force (N) and T is fabric tension (N/m).

$$P_{PM} = \frac{E_{course}\frac{\partial u_\rho}{\partial \rho}\oint_h Cir_{Leg} dh}{Cir_{Leg} R_L(\theta)}$$

(4.7)

where P_{PM} is the interfacial pressure value (Pa) along the applied irregular body.

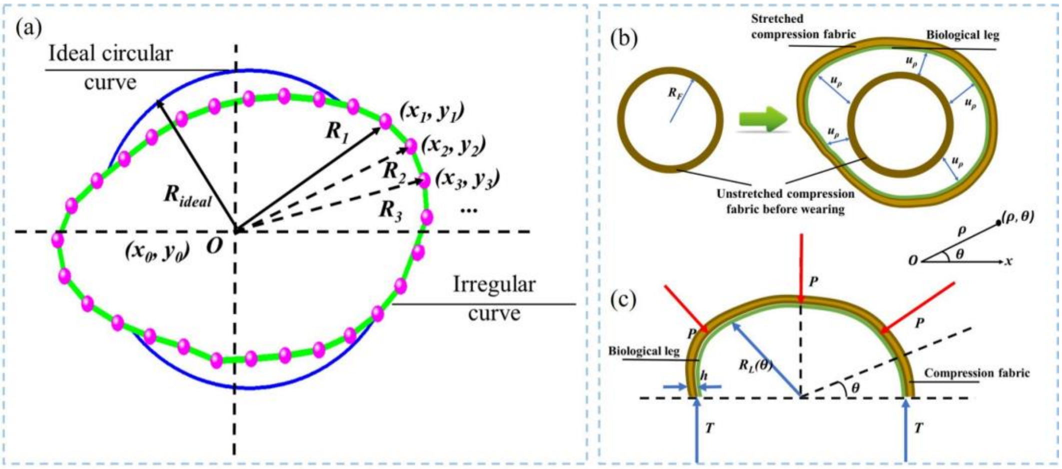

Figure 4.2 (a) Determination of geometric characteristics for defined irr-curve and ideal cir-curve, and (b), (c) mechanisms of pressure prediction model (PM).

4.2.4 Fabrication and Physical-Mechanical Properties of 3D Tubular Knitted Samples

To validate the accuracy of the proposed PM and investigate the pressure gaps between circular and irregular legs, tubular fabric samples were designed according to the 1×1 laid-in knitted loop pattern (Fig. 3.1 (b)). By adopting identical ground yarns (GY) and different linear densities of inlay yarns (YA, YB, and YC), the required knitted tubes with varying circumferential dimensions, fabric thickness, and mechanical tensile properties were fabricated by LONATI LA-45 ME 3D seamless knitting circular machine (Francesco Lonati, Brescia, Italy) (Fig. 3.2 (d)). Additionally, to facilitate further experimental investigations, the length of each tubular sample was at least 7 cm. For the instrumental tests, the fabric *Cir*, R_F, h, and E_{course} were tested through the presented methods in section *3.2.2*. Moreover, the specific tubular sample codes and physical-mechanical properties are listed in Table 4.1.

Table 4.1 Knitting yarn materials and fabric properties of tubular knitted samples

Sample	Yarn combinations	Physical-mechanical properties

code	Ground yarn	Inlay yarn	Cir / R_F (cm)	h (mm)	E_{course} (MPa)
SC1	GY	YA	14.19 / 2.26	0.67	0.38
SC2			15.39 / 2.45	0.64	0.46
SC3			16.01 / 2.55		0.44
SC4			16.83 / 2.68	0.63	0.41
SC5			17.78 / 2.83	0.66	0.35
SC6				0.68	0.33
SC7			20.60 / 3.28	0.66	0.35
SC8			20.98 / 3.34	0.65	0.33
SC9			21.98 / 3.50		0.38
SC10			29.60 / 4.71		0.61
SC11		YB	17.78 / 2.83	0.62	0.46
SC12			15.20 / 2.42		0.42
SC13			17.58 / 2.80		0.57
SC14				0.64	0.41
SC15			19.97 / 3.18	0.62	0.42
SC16		YC	18.02 / 2.87	0.69	0.94
SC17					1.27
SC18					0.65
SC19			20.80 / 3.31	0.68	0.94
SC20					0.70
SC21				0.65	0.61
SC22			24.00 / 3.82	0.68	0.70
SC23				0.65	0.61
SC24			29.60 / 4.71	0.68	0.70

4.2.5 Validation of Pressure Prediction Model

For the PM validation study, the PicoPress$^{@}$ (Microlab Elettronica, Italy) pressure tester with circular air-filled disposable transducer (sensor diameter: 5cm, sensor precision: ± 3mmHg) was utilized to obtain the interfacial pressure values along biological legs (P_B) in vivo experimental trials. As listed in Table 4.2, various bio-legs through recruited subjects with diverse circumferential dimensions were applied to facilitate the estimation of PM accuracy. Based on the appropriate fabric circumferential average tensile ratios (15%-120%) from the German standard, knitted samples with different circumferential dimensions were selected for subject pressure testing.

Table 4.2 Bio-leg circumferences and applied knitted samples for the PM validation study

Validated test code	Cir_{Leg} (cm)	Mean tensile ratio (%)	Applied fabric sample code
T1	18.72	21.64	SC2
T2	20.09	19.37	SC4
T3	21.22	37.88	SC2
T4	22.50	24.86	SC16
T5	24.26	44.15	SC4
T6	30.23	44.09	SC8
T7	31.81	44.72	SC9
T8	32.88	56.72	SC8
T9	33.13	59.28	SC20
T10	33.31	51.55	SC9
T11	35.38	47.42	SC22
T12	37.34	26.15	SC24

According to the reference [185], the mean pressure magnitude can be used as an efficient indicator of each body part. Thus, the average pressure values along each leg sectional position were determined as the compared initial data. Then, the P_{PM} can be validated through the calculated mean differences (MD, mmHg) and mean error ratios (MER, %) as defined by the following equations, respectively.

$$MD = \frac{1}{n}\sum_{n}^{i=1}\overline{(P_B - P_{PM})} \tag{4.8}$$

$$MER = \frac{1}{n}\sum_{n}^{i=1}\left(\frac{\left|P_B - P_{PM}\right|}{P_B}\times 100\%\right) \tag{4.9}$$

4.2.6 Determination of Pressure Reshape Ranges for Optimization Bio-Design

To obtain recommended reshaped pressure ranges, the interfacial P_B along various bio-bodies can be calculated through P_{PM} according to subject's Cir_{Leg} and applied fabric physical-mechanical properties. Thus, the pressure gaps (ΔP, $\Delta P = P_W - P_{PM}$) between the circular leg models (P_W) and P_{PM} can be obtained along legs with the same circumferences for the practical bio-design database. Thus, based on the calculated SDC values, recommended reshaped pressure values of CTs summarized for each clustered IR level group.

4.2.7 Data Statistical Study

Data analysis studies were performed by using the Statistical Package for the Social Science (SPSS) software (Version 23.0, IBM Corporation, USA). Based on the total slice sample size (=88 > 50), the data normality of the biological Cir_{Leg} and SDC values was objectively conducted by the Kolmogorov-Smirnov statistic [186]. The relationships of each variable were investigated by adopting the Spearman correlation test, to measure the individual correlation between two compared values [187]. The level of significance was set at $\alpha = 0.05$ in this study. For the analysis of the PM validation study, the confidence interval (CI) of MD and MER through validation data were calculated by using Eq. 4.10 [188].

$$CI = mean \pm SD \times \frac{1.96}{\sqrt{n}} \tag{4.10}$$

where n is the quantity of validated tests, and $mean$ and SD are the average value and standard deviation of MD or MER, respectively.

4.3 Results and Discussion

4.3.1 Geometric Variations of Lower Limb Sectional Slices

The data distribution and Spearman correlation result of Cir_{Leg} and SDC values are shown in Fig. 4.3. The Cir_{Leg} range for measured cross-sectional slices of the subject's lower limbs was from 17.90 cm to 44.58 cm at various determined leg positions. The SDC values of leg sectional slices varied from 1.09 to 2.55. And the Cir_{Leg} data show the non-normal distribution (*p* (*Sig.*) =0.00 <0.05), conversely, the SDC values conform to the normal distribution (*p* (*Sig.*) =0.20 >0.05). Based on the preliminary normal tested result and correlation test, the biological circumferences have no correlation with the calculated SDC values (*p* (*Sig.*) =0.40 >0.05). It indicates that the curvature characteristics are independent of leg positions with different dimensions.

Moreover, based on the correlation results, the calculated SDC values varied among not only subject lower limbs but also each leg position. In the practical application of CSs, individual physiological and anatomic differences occur frequently along the identical bio-leg, which frequently lead to the diversities of circumferential dimensions and curvature characteristics [39]. Thus, to improve the medical effectiveness and user-specific pressure fitness, individual characteristics at various positions (i.e., B, B1, C, and D) along each lower extremity need to be considered comprehensively. Consequently, this study characterized the leg slices through the curvature characteristics without consideration of the description of specific sectional leg positions for further explorations.

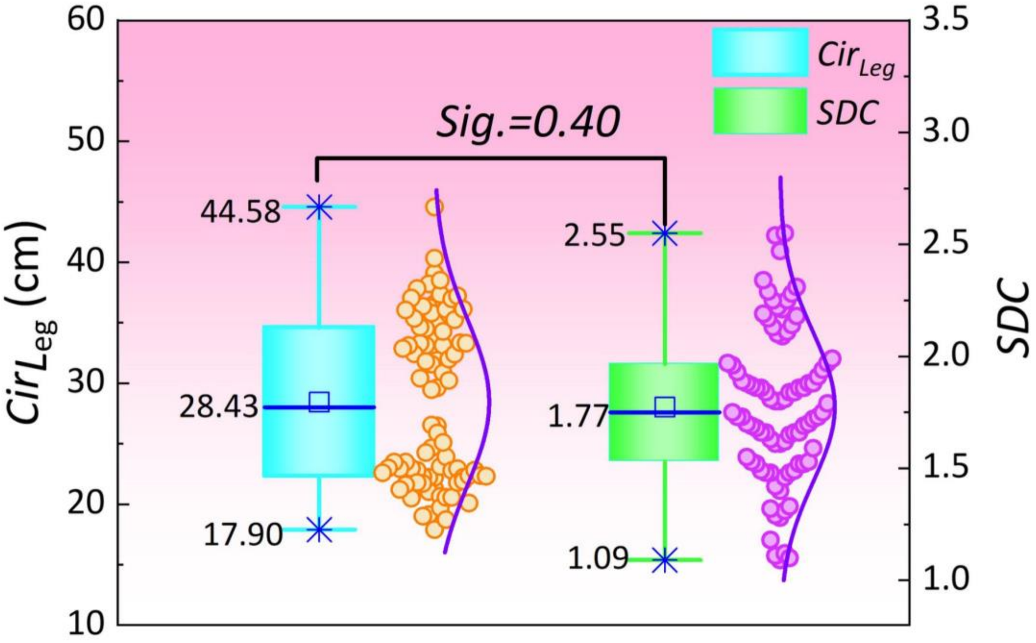

Figure 4.3 Normal data distribution and correlation result of leg Cir_{Leg} and SDC values.

4.3.2 Morphological Classification of Lower Limb Sectional Slices

As illustrated in Fig. 4.4, the sectional irr-curves and corresponding ideal cir-curves of each slice were plotted and visualized simultaneously for qualitative comparisons of morphological profile and irregular characteristics of human lower limbs. Then, the irregularities of leg slices were classified into four IR levels by the *k*-means clustering algorithm based on various quantitative estimated SDC ranges. Through the clustered ANOVA (Analysis of Variance) result, the obtained IR levels show a significant correlation (p (*Sig.*) =0.00 <0.05) with SDC values of leg slices.

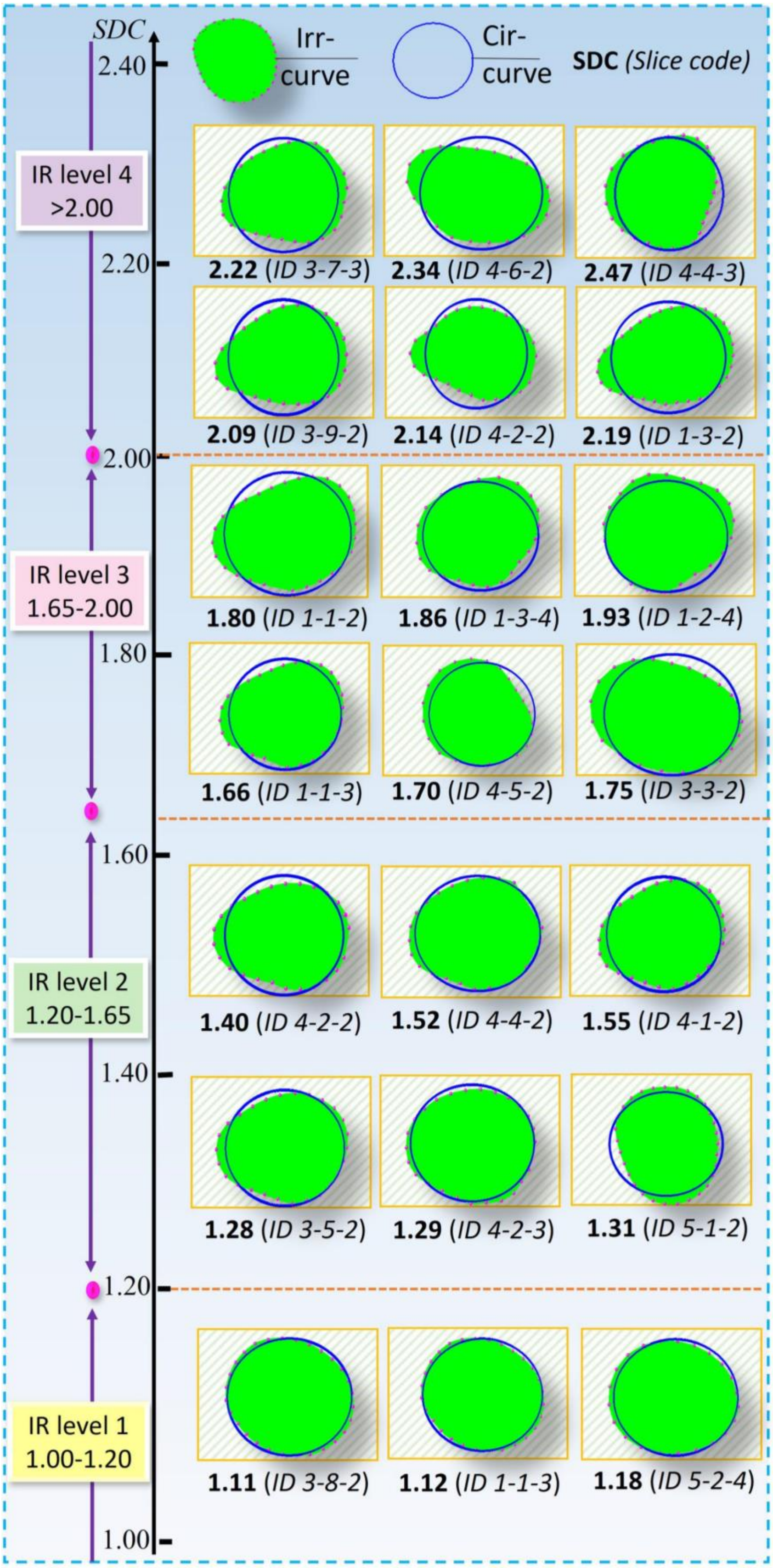

Figure 4.4 Examples of morphological visualization and morphological classification for leg slices.

Detailly, the general variation trends of the curvature radius with different irregularities are shown in Fig. 4.5 (a). It can be observed that the greater the IR level, the larger the differences of curvature radius of scattered curve points, thus the more irregular the irr-curve was. Furthermore, according to the specific limb slice quantities and proportion of each IR level in Fig. 4.5 (b), the number of leg sections with IR-3 level was approximately 45.45%, followed by the IR-2 (27.27%) and IR-4 (21.59%) levels, respectively. Additionally, 5.69% of leg slices with IR-1 level also indicate that fewer studied leg sections have the more regular curve shape. Thus, the majority of the actual morphology of biological bodies shows various curvature characteristics and irregularities.

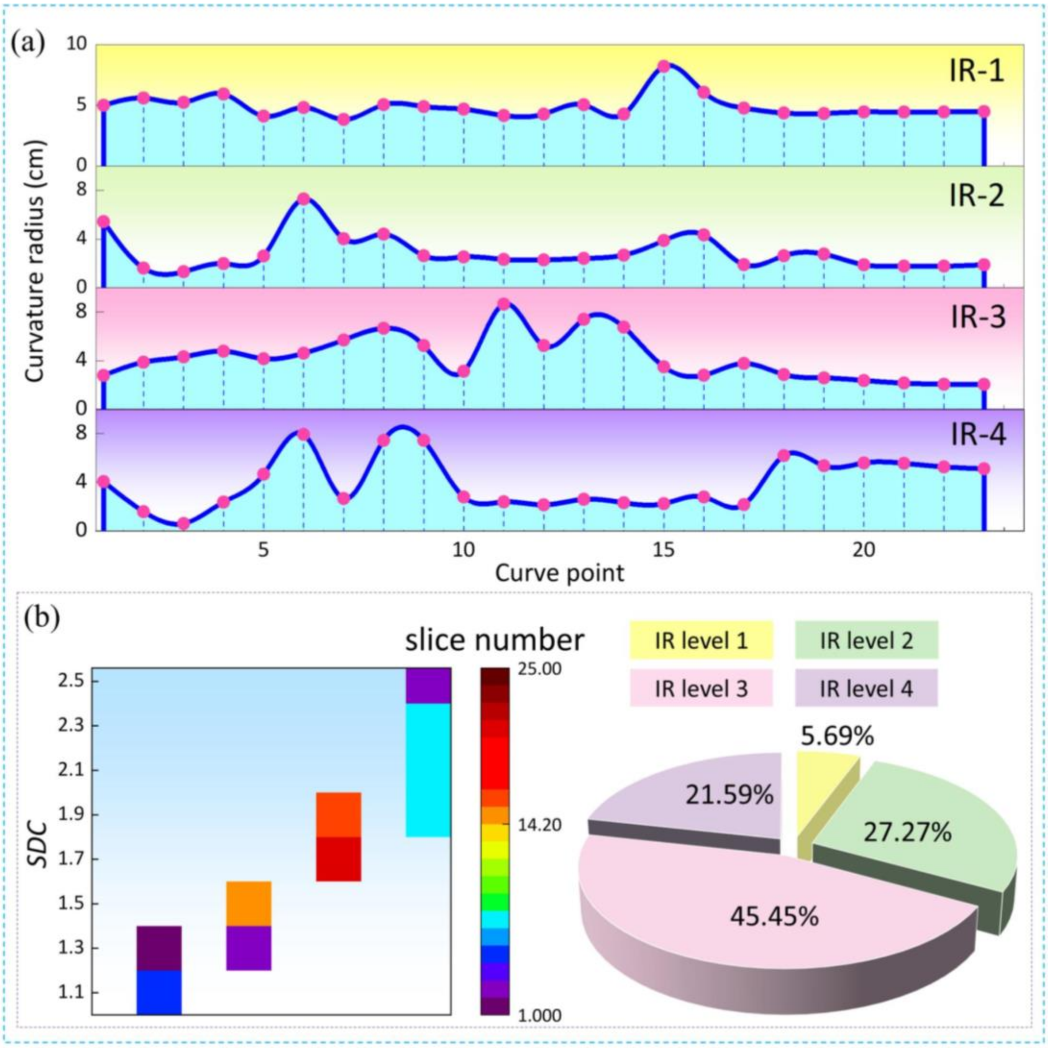

Figure 4.5 (a) Examples of curvature radius for each clustered IR level, (b) quantity distribution and percentage of leg slices with various classified IR levels.

Further, numerous studies have explored the morphological lower extremity profiles via multiple protocols [189-191] based on the image-based shape analysis, especially distinguishing the profile types as the genu val gum (X-shape) and genu varum (O-shape), or neither. Additionally, the body shape automatic recognition and clustering analysis [182, 192] are extensively applied to investigate the bio-body features for functional textile development. However, for compression therapy, based on the working mechanisms of compression generation, elastic fabrics produce the normally stretched deformation and generate interfacial pressure on the contact body surface vertically, regardless of the malalignment of the lower limb along its longitudinal length direction. Conversely, the leg sectional shape and circumferential dimensions are crucial for the pressure generations of CTs. Therefore, the investigated classification system for cross-sectional individual curvature characteristics was employed for further compression prediction study.

4.3.3 Acceptability of Pressure Prediction Model

The predicted P_{PM} and tested P_B values generated by different tubular samples and applied leg variations are compared in Fig. 4.6 (a). Through the Spearman correlation statistical analysis results, the predicted magnitudes of P_{PM} have a significant correlation (p (*Sig.*) =0.00 <0.05, ρ= 0.80) with measured values of P_B. Based on the comparison between the PM prediction and instrumental pressure measurement, the calculated *MD* and *MER* were approximately 2.53±0.52 mmHg and 13.71±2.62%, respectively (Fig. 4.6 (b)). Additionally, the *MD* and *MER* had a 95% probability of maintaining between 1.38-3.69 mmHg and 7.93-19.48% based on the calculated *CI* values.

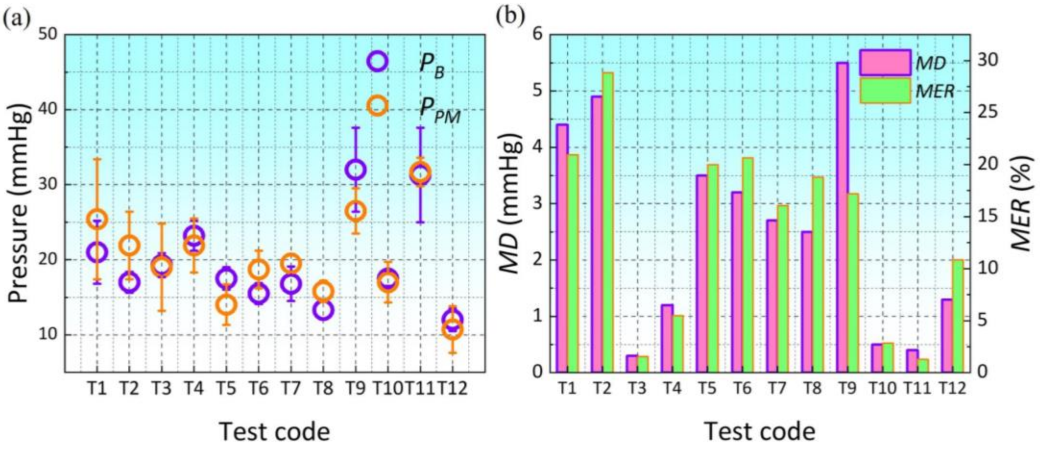

Figure 4.6 Validated results of the PM compared with wear trials.

As shown in Fig. 4.7, the fabric strain and pressure value generated by the applied irr-curve and cir-curve with identical circumferences were obtained through PM predicted and circular leg tested results. Due to the incompatible fabric stretched stress and heterogeneous deformation, the pressure values generated by compression fabrics along the irregular irr-curve show obvious differences with the cir-curve, especially for the applied body with IR-4 level of irregularity. Therefore, the individual leg profiles and irregularity contribute to uneven and insufficient pressure supply for compression therapy during the actual wearing process.

Commonly, the previous pressure prediction models were constructed based on the regular cylinder with a certain radius, which led to consistent fabric deformation and material strain along the identical body part. Simultaneously, the adopted ideal shape and unique body radius also influenced the calculation accuracy of inputting fabric area. The validated data for their models was compared through the cylinder leg measurements without the practical application of biological bodies with various individual diversities. Through literature [110, 193], the average pressure differences and error percentages of pressure models compared with leg mannequins were at least 2.10 mmHg and 15.37%, respectively. Consequently, it can be concluded that the proposed PM has good agreements with the experimental biological tested results. Thus, the calculated P_{PM} can be applied as the P_B along each irr-curve for bio-based pressure prediction.

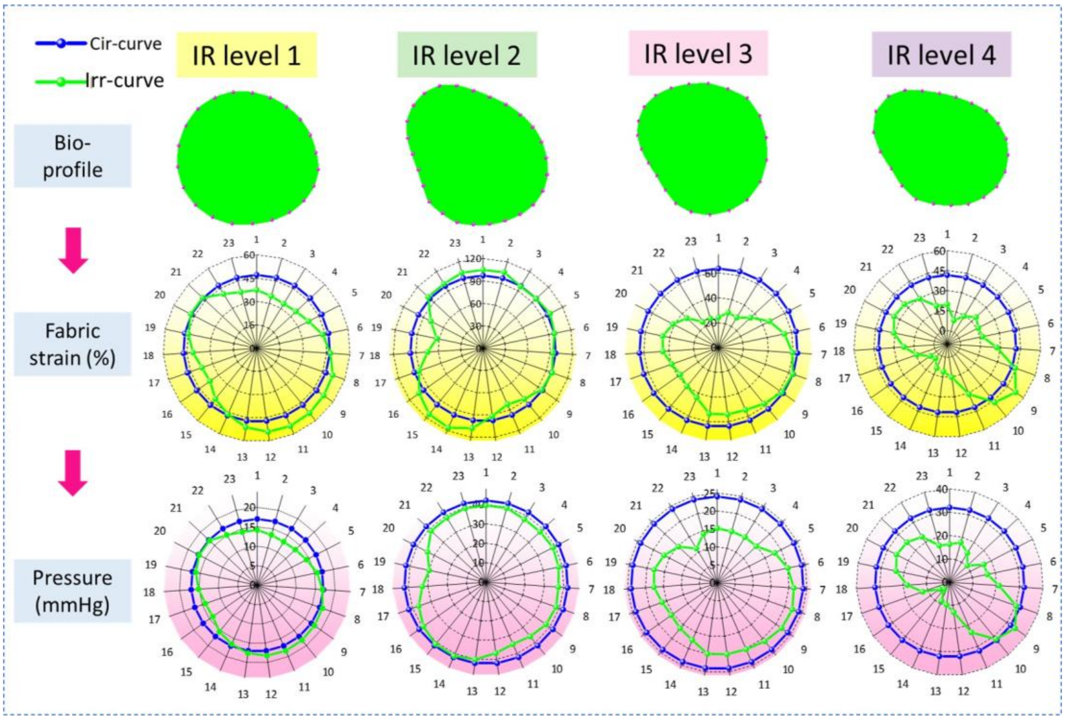

Figure 4.7 Comparisons of the fabric strain and pressure profile along the irr- and cir- curves.

4.3.4 Redistribution of Pressure Supply through Classified Irregular Levels and Constructed Pressure Prediction Model

Based on the investigated acceptability of the proposed PM, the interfacial P_B was predicted through the P_{PM}. According to the C_L, SDC values, IR levels of subjects, and corresponding applied fabric sample properties (Table 4.3), the ΔP values were obtained as shown in Fig. 4.8 (a). Moreover, according to the Spearman coefficient results, the IR levels have a strong positive correlation (p (*Sig.*) <0.05, $\rho = 0.95$) with the ΔP. It means that the insufficient compression distributions of CSs were easier generated along the more irregular bodies.

Further, extensive existing researchers have investigated pressure profile maps of CSs along compressed leg morphologies through establishing numerical mechanical simulation or experimental tests [118, 185, 194]. Nevertheless, limited studies have presented specific operable strategies for the insufficient pressure supply of CTs through quantitative magnitude guidance for practical fabrication. Therefore, through the obtained irregularities (Table 4.3) and specific pressure gap values (Fig. 4.8 (a)), the recommended reshaped pressure ranges for various individual leg irregularities were concluded as shown in Fig. 4.8 (b). For example, along the lower extremities with IR level of 4, the pressure gaps with ideal cir- legs ranged from 13.1 to 18.7 mmHg, thus its corresponding recommended reshaped pressure supply was rounded from 13 to 19 mmHg.

Table 4.3 Applied leg slices and knitted samples for prediction of pressure gaps

Compared code	Cir_{Leg} (cm)	SDC value	IR level	Applied sample
P1	21.78	1.11	IR-1	SC6
P2	35.80	1.13		SC12
P3	32.54	1.13		SC22
P4	42.82	1.15		SC11
P5	30.23	1.18		SC8
P6	28.29	1.46	IR-2	SC24
P7	34.69	1.49		SC1
P8	20.88	1.48		SC20
P9	20.86	1.51		SC3
P10	39.50	1.53		SC13
P11	35.80	1.66	IR-3	SC6
P12	22.20	1.67		SC3
P13	25.43	1.75		SC10
P14	36.57	1.86		SC5
P15	25.74	1.88		SC14
P16	20.77	2.10	IR-4	SC19
P17	22.22	2.19		SC10
P18	22.52	2.22		SC19
P19	23.09	2.48		SC7
P20	20.33	2.55		SC20

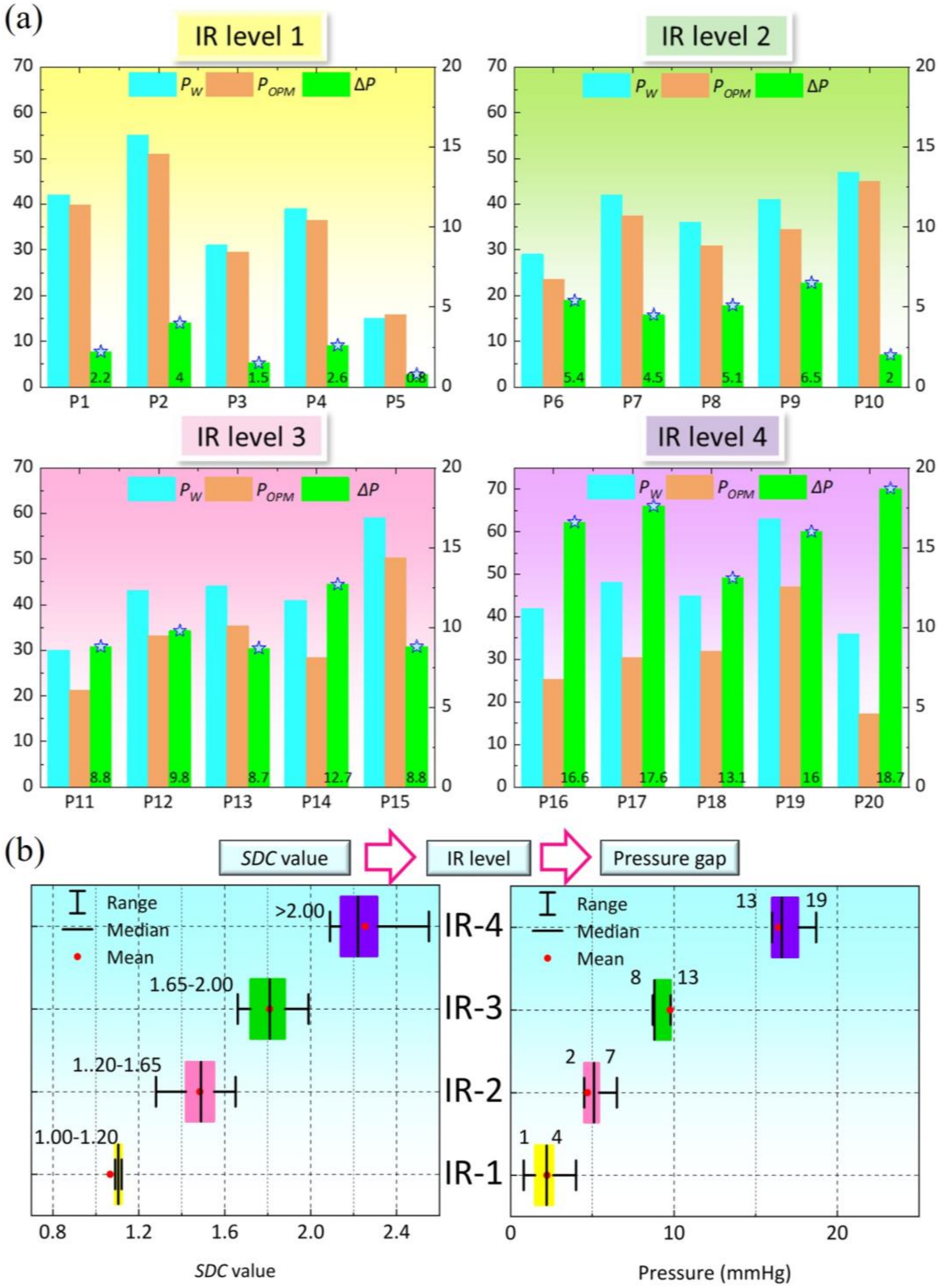

Figure 4.8 (a) Pressure values and calculated gaps (mmHg) between circular and irregular legs, (b) recommended reshaped pressure supply for various leg IR levels.

4.3.5 Application of Optimized Bio-design Approach

As illustrated in Fig. 4.9, this chapter constructed the novel irregular classification and PM systems for the lower bodies. Firstly, the original anthropometric data was obtained by the 3D-BS captured from each subject, and then based on the reverse engineering technology and digitalized 3D entity leg model, the irr-curve and cir-curve can be plotted by the scattered point data for the qualitative comparison and geometric measurement. Especially, the morphological SDC values of each leg slice were imported into the clustering algorithm and classified as four levels for cross-sectional morphological classification. Simultaneously, the new prediction approach related to characterized geometric variations was proposed with good agreements according to the practical wearing validated results. Then, the pressure gap ranges between the irr- and cir- legs were recommended for the practical CSs design and production, to reshape the pressure supply generated at various irregular user's lower limbs.

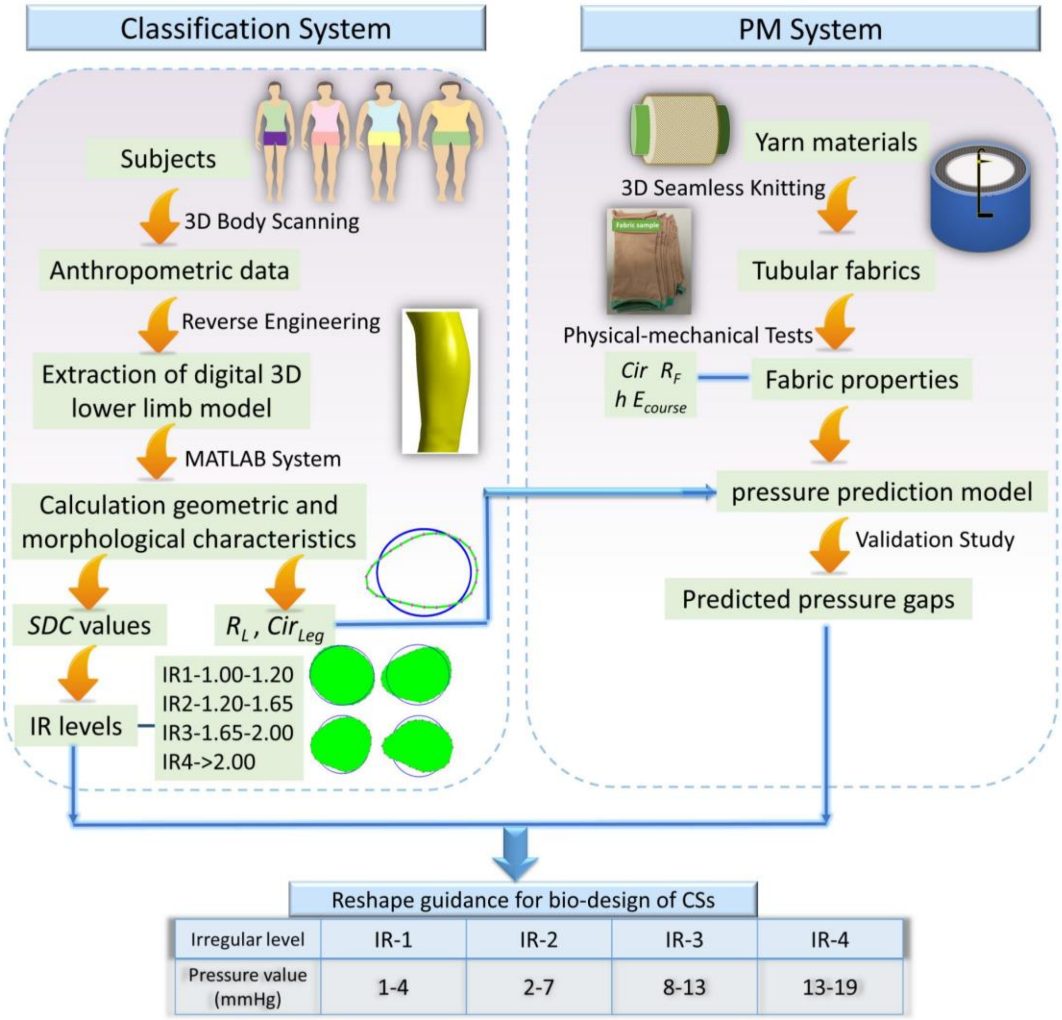

Irregular level	IR-1	IR-2	IR-3	IR-4
Pressure value (mmHg)	1-4	2-7	8-13	13-19

Figure 4.9 Framework of the classification and PM systems for redistribution of pressure generation of CSs.

Therefore, the proposed reshaped pressure supply can be applied for the digital development and fabrication of CSs (Fig. 4.10). The user-oriented body geometric and morphologic characteristics can be obtained individually, and the specific improved pressure distribution could be guided through the recommended reshaped values, to achieve the pressure-fit of CSs for targeted required users. For instance, to facilitate the pressure fitness of CSs for target users with IR-4 level and expected pressure value of 18 mmHg at the ankle (B) position, the producers could approximately provide the reshaped pressure magnitudes of 16.0 mmHg (the average value of 13-19 mmHg), thus the required design pressure is 34 mmHg for the fabrication process.

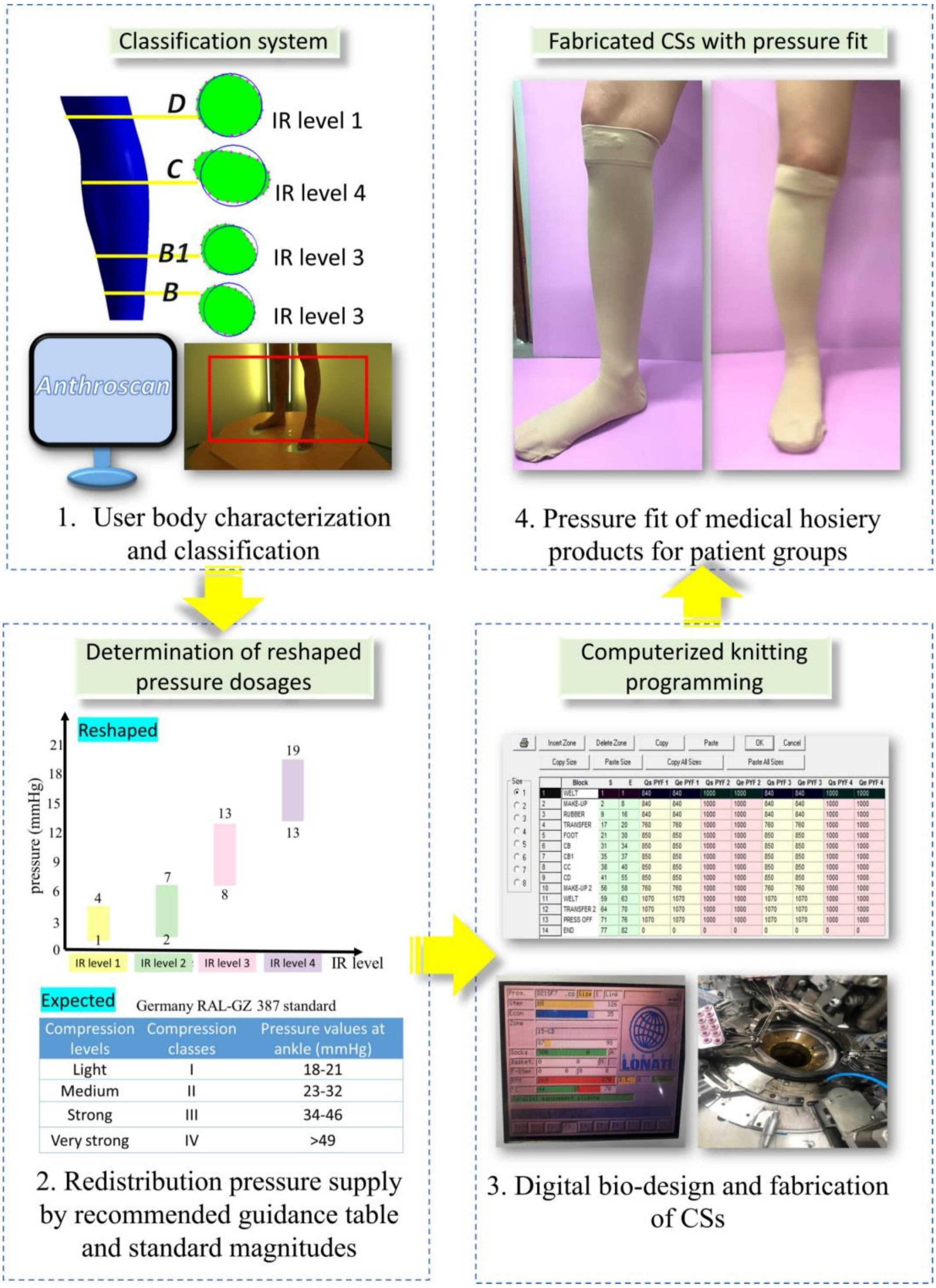

Compression levels	Compression classes	Pressure values at ankle (mmHg)
Light	I	18-21
Medium	II	23-32
Strong	III	34-46
Very strong	IV	>49

	Block	S	E	Qs PYF 1	Qe PYF 1	Qs PYF 2	Qe PYF 2	Qs PYF 3	Qe PYF 3	Qs PYF 4	Qe PYF 4
1	WELT	1	1	840	840	1000	1000	840	840	1000	1000
2	MAKE-UP	2	8	840	840	1000	1000	840	840	1000	1000
3	RUBBER	9	16	840	840	1000	1000	840	840	1000	1000
4	TRANSFER	17	20	760	760	1000	1000	760	760	1000	1000
5	FOOT	21	30	850	850	1000	1000	850	850	1000	1000
6	CB	31	34	850	850	1000	1000	850	850	1000	1000
7	CB1	35	37	850	850	1000	1000	850	850	1000	1000
8	CC	38	40	850	850	1000	1000	850	850	1000	1000
9	CD	41	55	850	850	1000	1000	850	850	1000	1000
10	MAKE-UP 2	56	58	760	760	1000	1000	760	760	1000	1000
11	WELT	59	63	1070	1070	1000	1000	1070	1070	1000	1000
12	TRANSFER 2	64	70	1070	1070	1000	1000	1070	1070	1000	1000
13	PRESS OFF	71	76	1070	1070	1000	1000	1070	1070	1000	1000
14	END	77	82	0	0	0	0	0	0	0	0

Figure 4.10 Practical application for optimization bio-design approach of CSs with pressure fit for end users.

4.4 Summary

In this chapter, to facilitate the bio-design of CTs with pressure fit for precise therapeutic management, a novel strategy was proposed for the pressure redistribution development guidance of CSs. By 3D-BS and reverse engineering technologies, the irregular curvature characteristics of cross-sectional slices were classified as four levels through the 3D entity leg model and body characterization. Simultaneously, to predict the pressure gaps between irregular and circular legs for each clustered IR level, a new pressure prediction model was established with high accuracy (mean pressure error was 2.53±0.52 mmHg) for the calculation of compression generation applied along the irregular biological bodies with individual morphological characteristics.

Through the clustered IR levels and pressure prediction results, the pressure gap ranges between the circular leg model and irregular bodies were obtained as the design guidance of CSs to enhance the functional pressure performances for medical hosiery production. This chapter facilitates the understanding of influencing mechanisms of insufficient pressure distribution and provides a reference for the bio-design and fabrication of compression materials, thus promoting the user compliance and clinical treatment efficiency of CTs in compression therapy.

Furthermore, in Chapter 3, the pressure magnitude requirements could be achieved directly through the digitalized pressure models relating to the yarn and machinery knitting setting values for precise pressure achievement along leg models with circular sectional profiles and rigid material properties. The body morphological characteristics of compression generations were explored in this chapter, therefore, in the next chapter, the biomechanical influences of lower limb ST stiffness were further investigated for the improvement of users' pressure fitness of CTs.

CHAPTER 5 EFFECTS OF BIOLOGICAL TISSUE STIFFNESS ON PRESSURE PERFORMANCES OF CTS

5.1 Introduction

For the morphological variations of the lower extremity, Chapter 4 explored the impacting mechanisms of body cross-sectional irregularities on functional compression performances of CTs. The irregular leg patterns led to uneven pressure magnitudes caused by the non-constant fabric stretching strains. For lower limb tissues, based on the leg's physiological structure and sectional segmentation, three components with varying composition have been identified, including the superficial (i.e., adipose tissues, skin, and veins), deep (i.e., muscles, tendons, and veins) STs and hard tissues (i.e., tibia and fibula bones), respectively [195]. Therefore, except for the rigid support (i.e., bones), to replace traditional rigid mannequin materials and improve the accuracy of experimental pressure estimation, in previous studies, researchers selected alternative ST materials, such as silicone and flexible polyurethane foam [196-198]. Using these, researchers have developed substitutable leg models for the design and interfacial pressure testing of CTs. Nevertheless, to date, there is a lack of research that fundamentally explores the effects of bio-material mechanical stiffness of lower limbs on pressure distributions of CTs. The design guidance and leg mannequin selection criteria need to be established for the development and pressure assessment of compression functional fabrics.

Moreover, the previously proposed FE models were established for user-specific mechanical analysis with their biomaterial tissue characteristics. Limited studies have investigated the pressure performance diversities caused by lower limb stiffness variations through parametric comparisons. Based on characterization studies, ST stiffness values possibly vary due to not only the studied anatomical locations and muscle-measured states, but also the individual characteristics, such as gender [199], aging [200], disease progression, occupation [201], and rehabilitation status [202]. The garment-based pressure diversities caused by the mechanical ST properties of bio-legs remain controversial. Thus, the influencing mechanisms, and quantitative relationships of various ST biomaterial parameters relating to pressure generation diversities of compression fabrics need to be explored systematically, to facilitate the material design, pressure dosage selection, and compression prediction of CTs.

To improve the pressure fits for end users, this chapter explored the biomechanical interactions between CTs and lower extremities with various tissue material characteristics. The independent leg ST stiffness influences on pressure behaviors of CTs were systematically investigated through FE CT-leg simulation modelling, theoretical analysis, and experimental validation studies. The compared results facilitate the scientific development of pressure dosages for CTs and promote model material selection for pressure evaluations. The constructed 3D homogenous FE CT-leg systems also achieve effective assessment and pressure performance prediction for user-oriented applications.

5.2 Materials and Methods

To investigate the biomechanical influences of lower limb ST stiffness on the pressure performance of CTs, this chapter adopted FE modelling, theoretical analysis, and experimental validation, respectively. As illustrated in Fig. 5.1, the 3D FE homogenous modelling system was constructed through the reconstructed entity legs established by 3D-BS and reverse engineering technologies. The acceptability of proposed FE models was examined by 3D printing legs with controlled lower limb morphological shapes and identical material characteristics. Then, the pressure performance diversities between legs with varied ST stiffness were qualitatively compared through the FE CT-leg systems by inputting varying biomaterial parameters. Simultaneously, the theoretical contact analysis model was constructed to quantitatively explore the impacting mechanisms of tissue stiffness on pressure behaviors of CTs by inputting leg circumferential deformation data. Finally, the applicability of the findings was validated by experiments in this chapter.

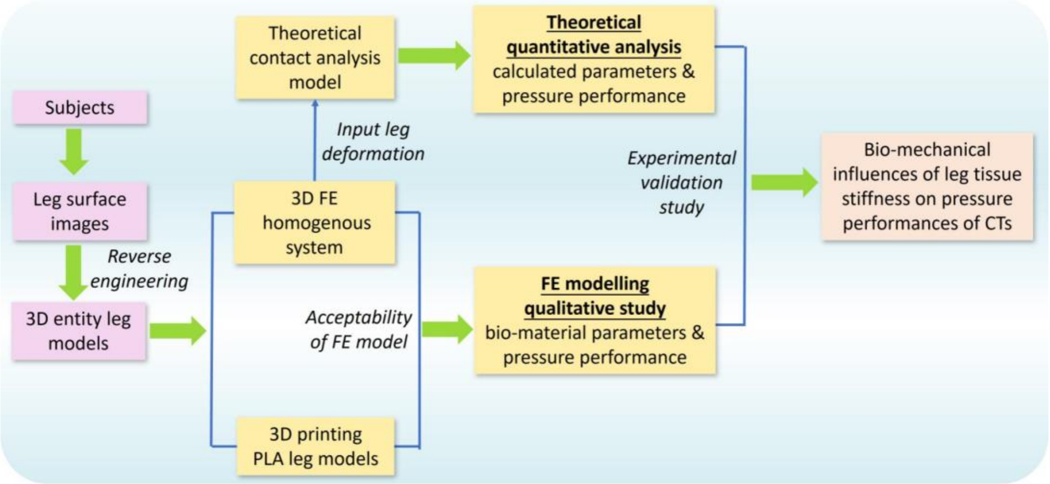

Figure 5.1 Framework of this chapter.

5.2.1 Subject Information

To provide the geometric leg models for data comparison by varying the ST stiffnesses, three healthy subjects (code: SU1, SU2, and SU3) with various genders, ages, and leg shape profiles participated voluntarily for FE modelling constructions and experimental investigations. The basic individual information and BMI of each subject are as follows, i) S1: male, age: 32 years old, height: 1.80 m, BMI: 17.7 kg/m^2, ii) S2: female, age: 50 years old, height: 1.57 m, BMI: 25.6 kg/m^2, and iii) S3: male, age: 61 years old, height: 1.60 m, BMI: 22.2 kg/m^2.

5.2.2 Preparation and Physical-Mechanical Properties of CTs

In practical clinical treatments, pressure magnitudes exerted by CTs are classified as different compression levels through the standard of Germany RAL-GZ 387/1 by varying textile material stiffness. Thus, according to the measurement guidance (Fig. 2.1 (a)) and determined subject body dimensions (Fig. 5.2), different compression knitted fabrics were designed to achieve the standardized pressure magnitudes for the light (Class: I) and strong (Class: III) levels of compression generation. Lycra-based elastic yarn materials with various linear densities were adopted as the ground and inlay yarn components according to the designed 1 × 1 laid-in knitted loop pattern. By adjusting the knitting yarn combinations and machinery parameters, tubular CTs with diverse physical and mechanical properties were prepared using the LONATI LA-45 ME 3D seamless knitting machine (Francesco Lonati, Brescia, Italy).

For experimental physical tests, the fabric circumferential radius (R_F) and longitudinal lengths (L_F), fabric thickness (h), and mass densities of CTs were obtained according to the standards of ASTM D3774, ASTM D1777 and ASTM D 3776/D 3776M-09a, respectively. For mechanical tensile behaviors, the elastic Young's modulus along the course (E_{course}) and wale (E_{wale}) stretching directions and Poisson's ratio (v_F) were tested by utilizing the Instron 4411 universal tension tester (Norwood, MA, USA) referred to the ASTM D2256 standard. Fabric shear modulus (G_F) was obtained by the Kawabata (KES-FB3) pure shear testing assessment system. The applied CTs and corresponding measured fabric properties are listed in Table 5.1.

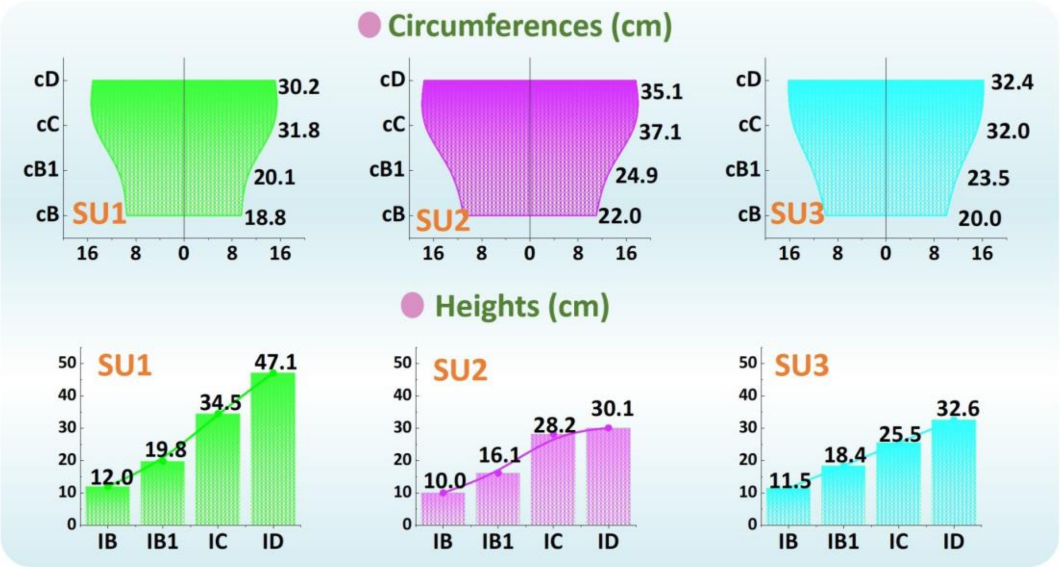

Figure 5.2 The circumferences and heights of each recruited subject leg.

Table 5.1 Measured fabric properties of CT knitted materials

			Physical property				Mechanical property			
Subject	Class	Leg part	R_F (cm)	L_F (cm)	h (mm)	Mass density (kg/m^3)	E_{course} (MPa)	E_{wale} (MPa)	v_F	G_F (MPa)
SU1	I	B	2.52	6.0	0.66	479.3	0.35	0.16	0.21	0.14
		B1	2.79	6.5	0.67	468.2	0.33	0.15	0.21	0.14
		C	3.57	7.5	0.68	481.3	0.37	0.21	0.20	0.17
		D	3.50	7.0	0.67	480.6	0.38	0.20	0.20	0.16
	III	B	2.42	6.0	0.62	503.6	0.42	0.14	0.22	0.17
		B1	2.79	6.5	0.64	481.5	0.41	0.17	0.23	0.17
		C	3.25	7.5	0.66	479.3	0.35	0.16	0.21	0.14
		D	3.22	7.0	0.68	468.2	0.33	0.15	0.21	0.14

SU2	I	B	2.84	5.5	0.69	484.7	0.38	0.21	0.21	0.14
		B1	3.22	6.0	0.67	468.2	0.37	0.15	0.21	0.15
		C	3.57	6.5	0.67	486.0	0.38	0.21	0.20	0.15
		D	3.50	6.0	0.66	485.4	0.37	0.20	0.19	0.14
	III	B	2.83	5.5	0.62	503.7	0.45	0.19	0.23	0.18
		B1	2.87	6.0	0.67	484.9	0.38	0.22	0.20	0.15
		C	3.22	6.5	0.68	468.2	0.34	0.15	0.20	0.14
		D	3.25	6.0	0.66	480.1	0.33	0.16	0.20	0.14
SU3	I	B	2.79	5.5	0.68	468.2	0.33	0.15	0.21	0.14
		B1	3.22	6.0	0.68	484.4	0.38	0.21	0.21	0.15
		C	3.50	7.0	0.67	487.3	0.38	0.21	0.20	0.16
		D	3.57	6.5	0.67	486.3	0.38	0.21	0.21	0.15
	III	B	2.80	5.5	0.64	532.7	0.76	0.27	0.25	0.30
		B1	2.83	6.0	0.62	503.6	0.42	0.18	0.22	0.17
		C	3.25	7.0	0.66	479.3	0.35	0.16	0.21	0.14
		D	3.22	6.5	0.68	468.2	0.33	0.15	0.21	0.14

5.2.3 Development of 3D Printing Rigid Leg Models

To obtain the lower body surface images for further model reconstruction and 3D printing manufacturing, the handheld professional EinScan-Pro 2X PLUS 3D Scanner (Shining 3D Tech. Co., Ltd. Hangzhou, China) and Solid Edge Shining 3D Edition software were applied with high scan accuracy (scan precision was 0.04 mm) and efficiency (scan speed was 1,500,000 dots/s) [203]. Based on the LED light source, participants were requested to stand steadily with torso separation at the instructed boundary pattern markers (Fig. 5.3 (a)). Then, by stably moving and operating the scanner 360° around each subject, the entire lower body surface was produced in cloud points for data acquisition. After body capturing, the 3D entity models were obtained by the presented methods in section *4.2.1*.

After entity model reconstruction, as shown in Fig. 5.3 (b), rigid leg models were fabricated by the advanced large-scale FDM (fused deposition modelling) Creatbot

D600 Pro 3D printer (build volume: 600 mm^3, precision: 0.05 mm). The sustainable filament materials of Poly Lactic Acid (PLA) are commonly utilized as raw materials in bioprinting, biomedical, tissue engineering, and smart textile industries, etc. [204, 205]. Thus, PLA filaments were applied as the printing materials for replacing the rigid wood lower limb mannequins' in vitro compression measurements due to PLA's excellent mechanical properties (tensile strength: 46.8 MPa, compressive strength: 17.9 MPa, Young's modulus: 3.0 GPa) [206]. By 3D printing manufacturing, three PLA-based rigid leg models for each subject with various morphological and geometric characteristics were developed for further pressure estimations.

5.2.4 Determination of Soft Tissue Stiffness Properties

To independently investigate the impact mechanisms of various ST stiffnesses on pressure performances of CTs, the ST mechanical properties of human lower extremities (below the knee) were referred from relevant previous literature measured by various protocols and subject groups [122, 185, 207, 208]. The muscle compositions were determined as the major studied components accounting for its proportion ranging from approximately 85% to 94% (Fig. 5.3 (c)) [209]. Thus, in this chapter, the digitalized Young's modulus (E_s) range of leg ST (muscle) stiffness was 0.0014-0.0030 MPa and divided into three levels (LS-1: 0.0014 MPa, LS-2: 0.0022 MPa and LS-3: 0.0030 MPa) for further comparisons in the FE modelling system.

Moreover, to obtain the exact ST stiffness values of studied subjects, the real-time SWE was performed by using Aixplorer$^{@}$ MultiWave ultrasound system (Supersonic Imagine, Aix-en-Provence, France), to provide the quantitative color-coded map (rectangular box: 1 cm × 1.5 cm) of lower limb tissue elasticity on an anatomic standard B-Mode image (Fig. 5.3 (d)). To ensure elasticity mapping with the SWE sequence, the parameters were set as the musculoskeletal preset, and tissue tuner at 1540 m/s, resolution mode enabled, respectively. For each subject, the depth setting was fixed at 2 cm to display the entire muscle during examination [210]. For physical testing, two leg regions (the ankle and calf) with four directions (anterior, posterior, medial, and lateral) were measured using a SuperLinear™ SL10-2 transducer array (element number:192, bandwich:2-10 MHz). Then, the E_s for each subject was determined by the calculated average values (listed in Table 5.2) through Eq. 5.1.

$$E_S = 3\rho_m {v_{swe}}^2 \tag{5.1}$$

where ρ_m is the muscle density (1000 kg/m^3), and v_{swe} is the shear wave velocity range of 0-7.7 m/s [211].

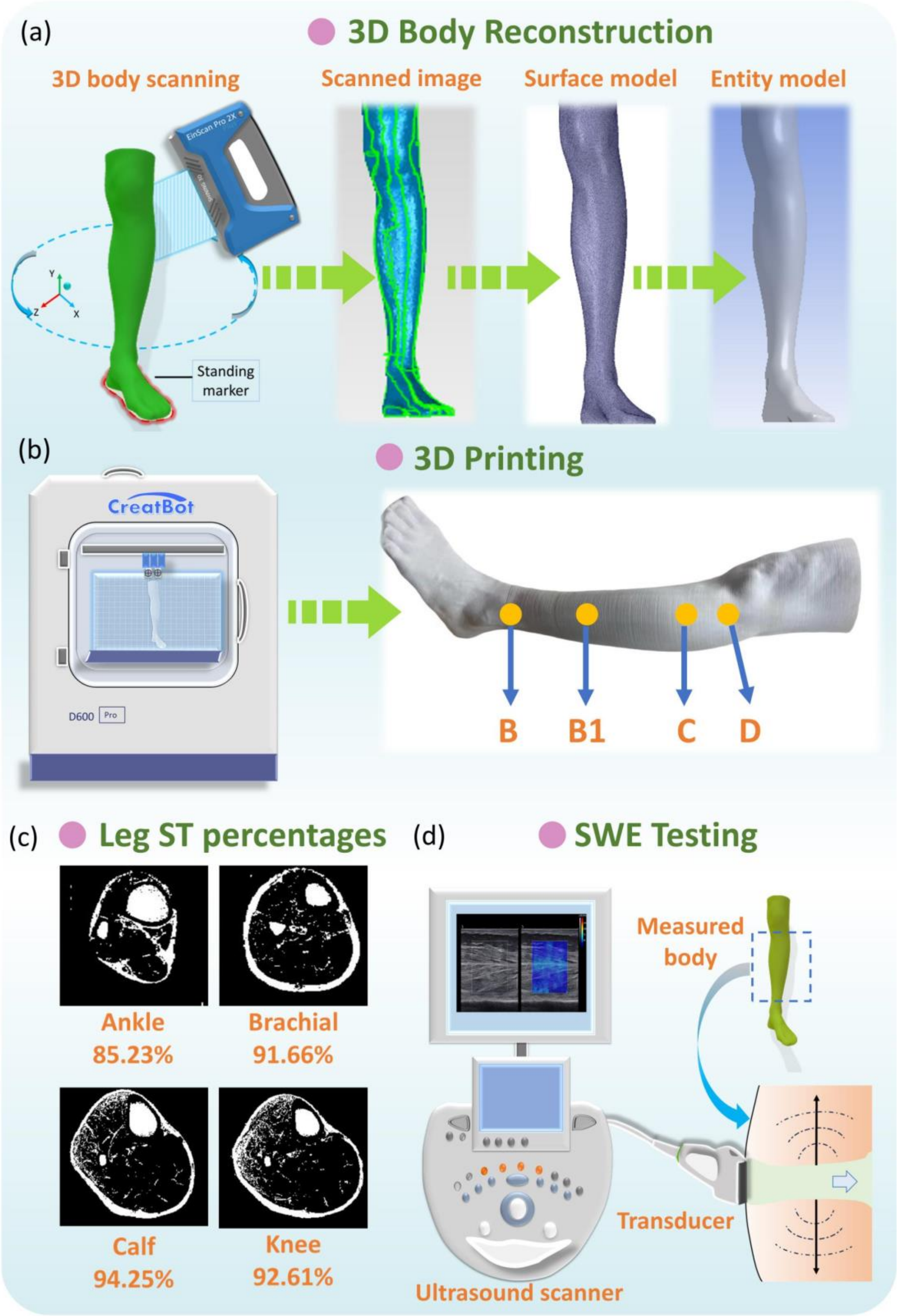

Figure 5.3 (a) Anthropometric data acquisition and reconstruction of lower limbs, (b) 3D printing of rigid PLA-based leg models, (c) ST percentages of each leg position, and (d) SWE testing for the lower extremity.

Table 5.2 Measured E_S through the SWE testing

Subject code	Leg position	E_S (MPa)	Mean E_S (MPa)

SU1	B	0.001975	0.002040
	C	0.002145	
SU2	B	0.002678	0.002976
	C	0.003273	
SU3	B	0.003700	0.002750
	C	0.001800	

5.2.5 Construction of 3D FE Homogenous CT-Leg Systems

Firstly, the geometric models of FE-based CTs were constructed according to the specific physical dimensions (R_F and L_F, Table 5.1) of actual fabrics by adopting the ANSYS Workbench Design Modeler software (v19.2, ANSYS, Pennsylvania, Pittsburgh, USA). The knitted CTs were commonly assumed as the orthotropic elastic materials [117], and the inputting fabric property parameters of mass densities, E_{course}, E_{wale}, v_F, and G_F were based on the experimental material data (Table 5.1). In the compression analysis, the Neo-Hookean model was typically used for mechanical analysis and pressure prediction, and the STs were modeled as hyperelastic, incompressible, homogeneous, and isotropic materials. Additionally, the constitutive equation is as follows [212]:

$$A = C_{10}\left(\overline{I}_1 - 3\right) + D_1\left(J - 1\right)^2 \tag{5.2}$$

where A denotes the strain energy density, $\overline{I}_1$ is the first deviatoric strain variant, and J is the Jacobian determinant of the deformation gradient. C_{10} and D_1 can be expressed below under a linear elastic condition, as follows,

$$C_{10} = \frac{S}{2}, D_1 = \frac{B}{2} \tag{5.3}$$

where S and B are the shear and bulk modulus (for the incompressible materials, the J

value is 1) [213], respectively.

Thus, for the lower limbs, the mechanical properties of 3D rigid and bio-soft legs were obtained through the Young's modulus of PLA printing material (3GPa) and biological ST stiffness (S1-0.0034 MPa, S2-0.0050 MPa, S3-0.0046 MPa), respectively. Then, as shown in Fig. 5.4 (a), to simulate the practical wearing process and analyze the interfacial pressure behaviors of CTs, the constructed leg models (obtained by section *4.2.2*) and applied CTs of each subject were imported into the Ansys LS-DYNA explicit dynamic solver, to solve the nonlinear dynamic equilibrium equation based on the center difference method [214, 215].

Secondly, as shown in Fig. 5.4 (b), according to the geometric characteristics of simulated components, CT (shell element) and leg model (solid entity element) were meshed by linear Quadrilateral Dominant and Tetrahedrons elements, respectively. The mesh sensitivity study was performed with various mesh size combinations to examine the mesh independence of proposed FE systems. Through the compared results, 8 mm and 7 mm per element were meshed for CT and leg models, respectively. Thus, the element/node numbers in biomechanical systems for the S1, S2, and S3 subjects were approximately 38500/12300, 60000/14300, and 32000/8000, respectively. The frictional nonlinear contact with a coefficient of 0.2 [216] was applied to simulate the interfacial contact conditions.

Thirdly, to promote dynamic wearing and the sliding process, the upper and bottom external surfaces of each leg model were fixed to facilitate tubular CTs longitudinal sliding freely from the distal to the proximal lower limb (Fig. 5.4 (c)). To ensure the exact deformation and stretching evenly by the leg model along the transverse direction, the boundary conditions were determined as the longitudinal CT sliding displacements (approximately SU1-43.9 cm, SU2-34.0 cm, and SU3-37.0 cm) for pressure behavior simulation. Additionally, the simulated pressure magnitudes along the 3D-printed rigid legs, and soft legs with three ST stiffness levels (i.e. LS-1: 0.0014 MPa, LS-2: 0.0022 MPa and LS-3: 0.0030 MPa) , were defined as P_{LM} and P_{LS}, respectively.

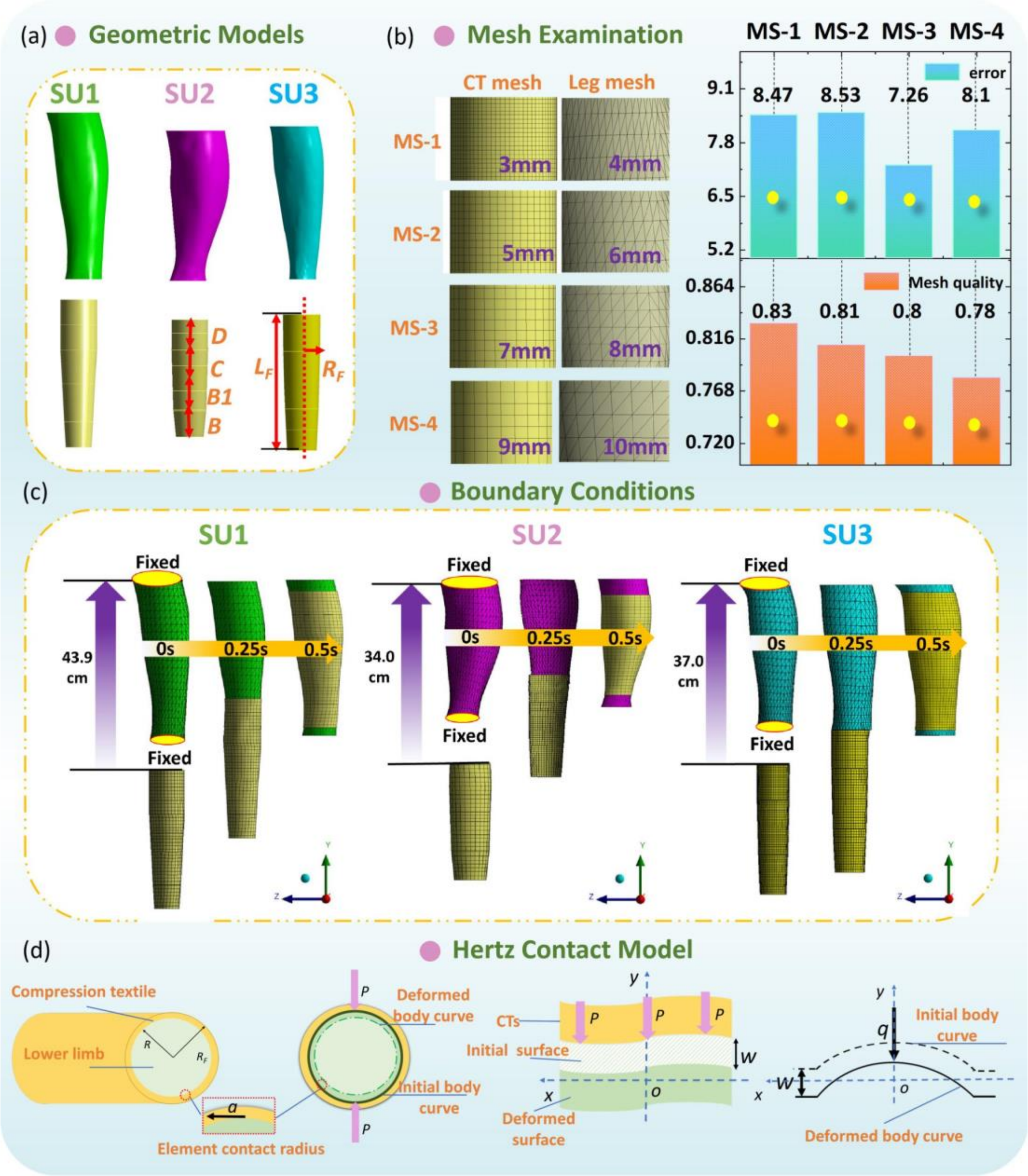

Figure 5.4 (a) Geometric models, (b) mesh sensitivities study of 3D FE homogenous modelling**.** (c) Boundary conditions and dynamic wearing process of each FE model. (d) Theoretical

contact model for CT-leg system.

5.2.6 Theoretical Contact Analysis Model

To theoretically analyze the impact mechanisms of tissue stiffness on pressure distributions of CTs, the Hertz contact theory (HzT) was used. The HzT model fundamentally leads the basic understanding of the indentation and mechanical interaction between elastic solids [217, 218], for investigating the geometrical displacement effects on local elastic deformation properties and pressure performances. For CT-leg systems (Fig. 5.4 (d)), the assumptions of HzT are as follows: i) the fabric-tissue contact area can be divided into finite element contacts. Each element contact can be analyzed as two camber concave contacts, ii) the radius of the contact circle is relatively smaller than those of the elastic fabric and deformed lower extremity, iii) no displacement changes along fabric thickness direction, and iv) during the wearing process, only the normal pressure is generated and transmitted between the frictionless full contact interface.

The initial HzT model showed the quantitative relationships among the unit pressure magnitude with the deformed body displacements, the physical dimensions and mechanical properties of applied legs and CTs as Eq. 5.4 [219].

$$\omega = (k + k_F)\frac{\pi q}{4a}(2a^2 - r^2) \tag{5.4}$$

where w is the body deformed displacement (m), k and k_F are the elastic mismatch factors (Pa^{-1}) of leg and CT fabric, respectively. q is the unit pressure value (Pa), r is the point distance from the contact circle surface to the center of the contact circle (defined as zero due to consumption of the full contact condition), and *a* is the radius of the contact circle (m).

The elastic mismatch factors are determined by the mechanical properties of CTs and lower limbs. Thus, *k* and k_F are given by Eq. 5.

$$k=\frac{1-v^2}{\pi E_s},\quad k_F=\frac{1-v_F^2}{\pi E_{course}} \tag{5.5}$$

where E_s and *v* (where *v* is 0.5 [220]) are the tensile elastic Young's modulus (Pa) and Poisson's ratios of the applied body (along the transverse direction), respectively.

After deformation, as in Eq. 5.6, Hertz also derived the *a* and *q* of the contact surface through the determined variables (such as *k*, R_F, etc.) of the two contacting materials.

$$a=[\frac{3\pi F(k+k_F)RR_F}{4(R+R_F)}]^{1/3},\quad q=\frac{3F}{2\pi}[\frac{8a^2(R+R_F)}{3F(k+k_F)RR_F}]^{2/3} \tag{5.6}$$

where *F* is the applied normal load of external force (N), and *R* is the radius (m) of the applied leg.

Additionally, through the definition function of interfacial pressure (*P*, Pa), it can be obtained through the applied normal load and contact area (Eq. 5.7).

$$P=\frac{F}{2\pi a^2} \tag{5.7}$$

Therefore, based on the aforementioned HzT model and FE simulated leg circumferential displacements of *w*, the pressure ratios (*ΔP*) between the rigid leg models and soft legs with various stiffness properties can be compared quantitively (Eq. 5.8).

$$\Delta P=\frac{P_{LM}}{P_{LS}}=\frac{w_r}{w_s}\times\frac{(k_s+k_F)}{(k_r+k_F)}=\frac{w_{ratio}}{k_{ratio}} \tag{5.8}$$

where w_r and w_s, k_r and k_s are the deformed displacements and elastic mismatch factors along the rigid and soft legs, respectively. w_{ratio} and k_{ratio} are the deformed displacement and elastic mismatch ratios compared between the rigid and soft legs.

5.2.7 Acceptability Analysis of FE Modelling and Experimental Validation

The acceptability of 3D FE homogenous leg models was validated by comparing the simulated P_{LM} and measured P_{rigid} data obtained along the constructed FE-based and printed PLA leg models with identical mechanical properties (Young's modulus: 3.0 GPa) and leg morphologies. The pressure prediction errors were compared by DRO values (Eq. 5.9).

$$DRO = \frac{\left|P_{rigid} - P_{LM}\right|}{P_{rigid}} \times 100\% \tag{5.9}$$

To validate the accuracy and applicability of the major findings in this chapter, the pressure values obtained from the user-specific FE CT-leg model, user-oriented 3D printed rigid leg model, and biological leg were compared. The interfacial pressure applied along biological bodies (P_{bio}) was experimentally measured by utilizing the Picopress$^{@}$ (Microlab Elettronica, Italy) pressure tester (measurement range: 0-189 mmHg, and precision: ±3 mmHg).

5.2.8 Data Analysis

Data analysis was performed using the Statistical Package for the Social Sciences (SPSS) software (Version 23.0, IBM Corporation, USA). Based on the processed sample size (n<50), the data normal distribution examinations were objectively conducted by applying the Shapiro-Wilk statistic software [221]. Then, the correlations and significant differences between each variable were tested by Pearson correlation analysis and paired t-test, respectively [222, 223]. The level of significance was set at $\alpha = 0.05$.

5.3 Results and Discussion

5.3.1 Acceptability of 3D FE Homogenous CT-Leg System

Fig. 5.5 (a) and Fig. 5.5 (b) show the simulated subject-specific P_{LM} and measured P_{rigid} values supplied by CTs and corresponding calculated DRO*s* of each compression level. Applying the elastic compression fabrics with various circumferential dimensions and tensile properties, the indicated light (Class I) and strong (Class III) pressure ranges and standardized degressive pressure gradients were generated along the lower extremities. Specifically, the P_{LM} generated by Class I tubular fabrics at the ankle (B) positions of subjects SU1, SU2, and SU3 were 18.02±2.36 mmHg, 21.05±3.87 mmHg, and 19.52±4.46 mmHg, respectively. For compression Class III, the P_{LM} values at the B positions of subjects SU1, SU2, and SU3 were 34.00±8.09 mmHg, 34.50±3.96 mmHg, and 37.39±4.35 mmHg, respectively. Compared to the measured P_{rigid}, the mean DRO of the constructed FE modelling was approximately 7.45%. Additionally, based on the Shapiro-Wilk statistic results and normal data distribution curves (Fig. 5.5 (c)), the simulated P_{LM} of Class I (p ($Sig.$) <0.05, $\rho = 0.73$) and Class III (p ($Sig.$) <0.05, $\rho = 0.93$) CTs were compared as the reasonable agreements with the tested P_{rigid} data, respectively [224, 225]. These results indicated that the established 3D FE homogenous CT-leg systems could be applied for our further explorations with high acceptability and simulation accuracy.

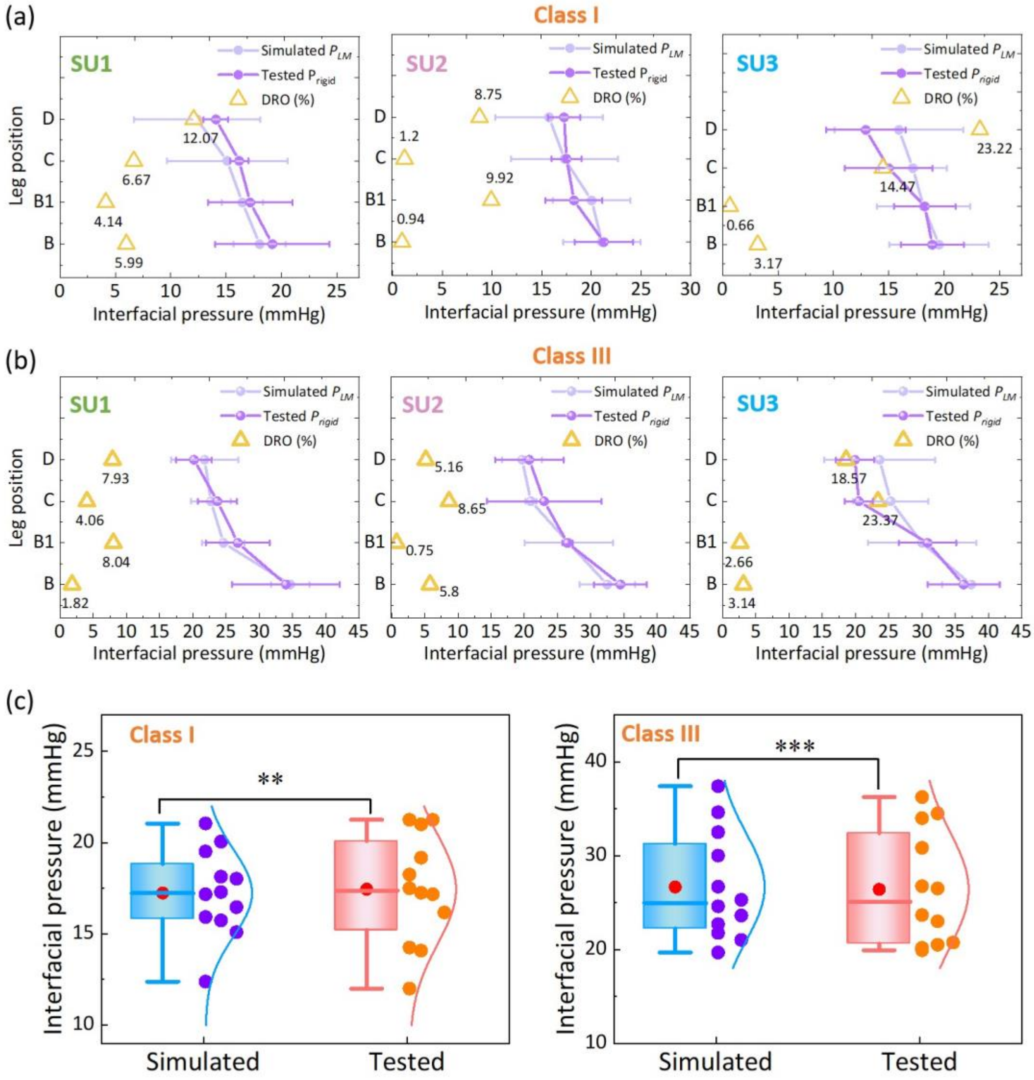

Figure 5.5 Pressure comparisons between the FE simulated and experimentally measured values for (a) Classes I and (b) III CTs. (c) Data distribution and correlation analysis of FE-based and tested pressure values.

5.3.2 FE Comparison between Various Leg Tissue Stiffnesses

To qualitatively investigate the pressure behaviors along lower bodies with various lower limb tissue characteristics, Fig. 5.6 (a) shows the average compression along the simulated rigid (P_{LM}) and soft legs (P_{LS}) with different ST stiffnesses supplied by CTs.

By varying the inputted leg mechanical properties, the exerted interfacial pressure profiles were slightly varied in the proposed 3D FE homogenous systems. Further, according to the results of paired-t tests (Fig. 5.6 (b)), pressure behaviors showed no significant differences among each compared tissue groups under the light (p ($Sig.$) >0.05) and strong (p ($Sig.$) >0.05) compression levels. It can be demonstrated that the compression performances of CTs with each pressure delivery level have no correlations with tissue characteristics of soft human bio-bodies as well as the applied rigid leg mannequins.

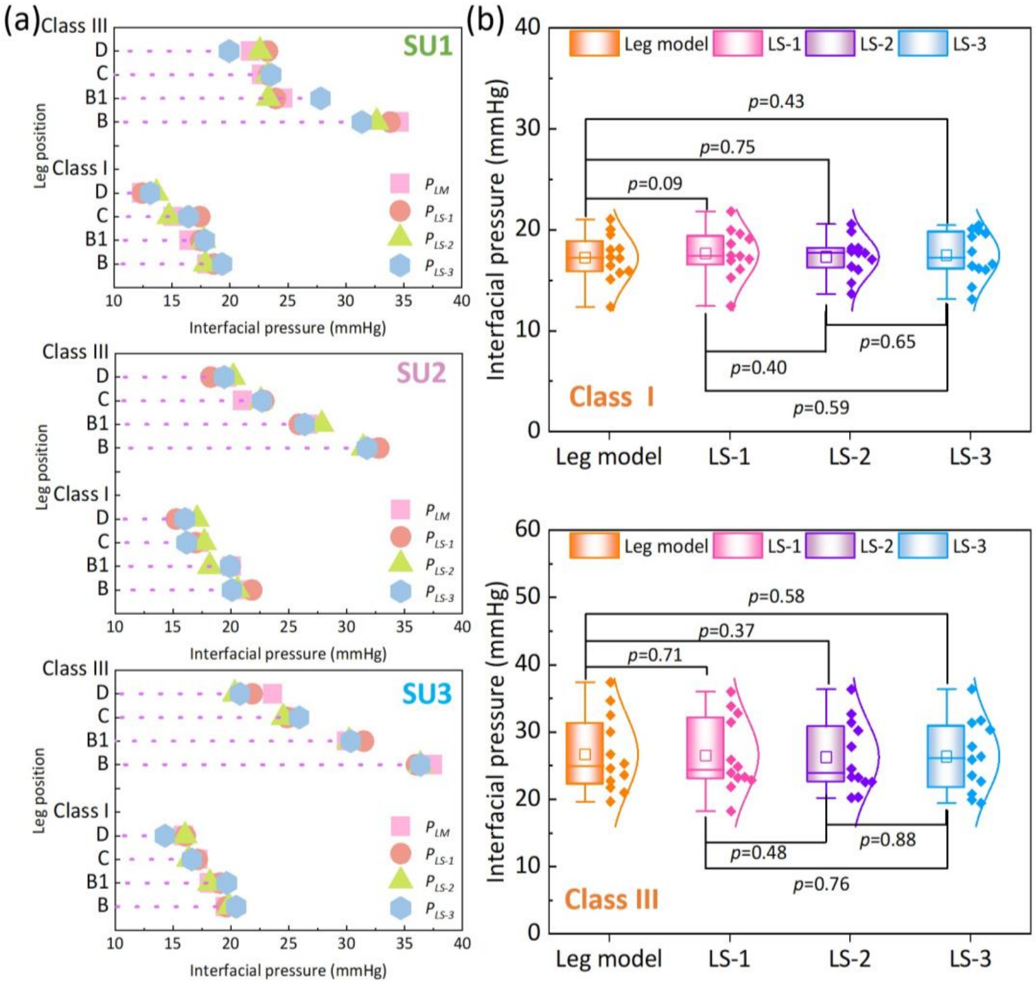

Figure 5.6 (a) Interfacial pressure values generated by different legs with various ST stiffness properties, (b) comparisons of pressure performances generated by Class I and Class III CTs between each leg stiffness group.

5.3.3 Parametric Variation Analysis through Theoretical HzT Model

Based on the HzT model, the pressure ratios (ΔP) were determined by the relationships of the leg deformed displacement (w_{ratio}) and tissue elastic factor (k_{ratio}) ratios. Through the constructed homogenous FE systems with various compression generations and ST stiffness properties, the exported leg circumferential deformed displacements and calculated parameters derived by the HzT model are shown in Fig. 5.7 (a). For the circumferential deformed variable of w, it increased with the pressure distribution levels (p ($Sig.$) <0.05, $\rho = 0.46$), and conversely, decreased with the ST stiffness characteristics (p ($Sig.$) <0.05, $\rho = -0.53$). For example, Fig. 5.7 (b) shows the compared images plotted by the original bio-body curves, and deformed body curves generated along simulated rigid and soft legs, respectively. The mean w value under the light compression level (Class I) and maximum ST tissue magnitude (LS-3) was approximately 3.61±0.26 mm. In Contrast, under the Class III and minimum ST tissue magnitude (LS-1), the w value was approximately 11.06±1.36 mm. Based on the w variations, the compressed lower limb cross-sectional circumferences varied from 2.27±0.14 cm to 6.95±0.74 cm (from the B to D positions). Thus, the leg circumferential displacements deformed by the interfacial interaction between the body surface and CTs were influenced by the external pressure levels and body ST stiffness.

Further, through the calculated parameters of w_{ratio} and k_{ratio}, the pressure diversities of ΔP between the simulated rigid (P_{LM}) and soft (P_{LS}) legs were also obtained quantitatively. ST stiffness properties showed significant positive correlations with deformed variables of w_{ratio} (p ($Sig.$) < 0.05, $\rho = 0.64$) and tissue-related defined variables of k_{ratio} (p ($Sig.$) <0.05, ρ= 0.77), but no correlation with the ΔP (p ($Sig.$) >0.05, ρ= -0.19). These results indicated that although the external tension forces generated by CTs positively affected the lower body displacements, the compressed deformed geometric variations caused by diverse tissue stiffness did not lead to proportional changes in pressure performance diversity.

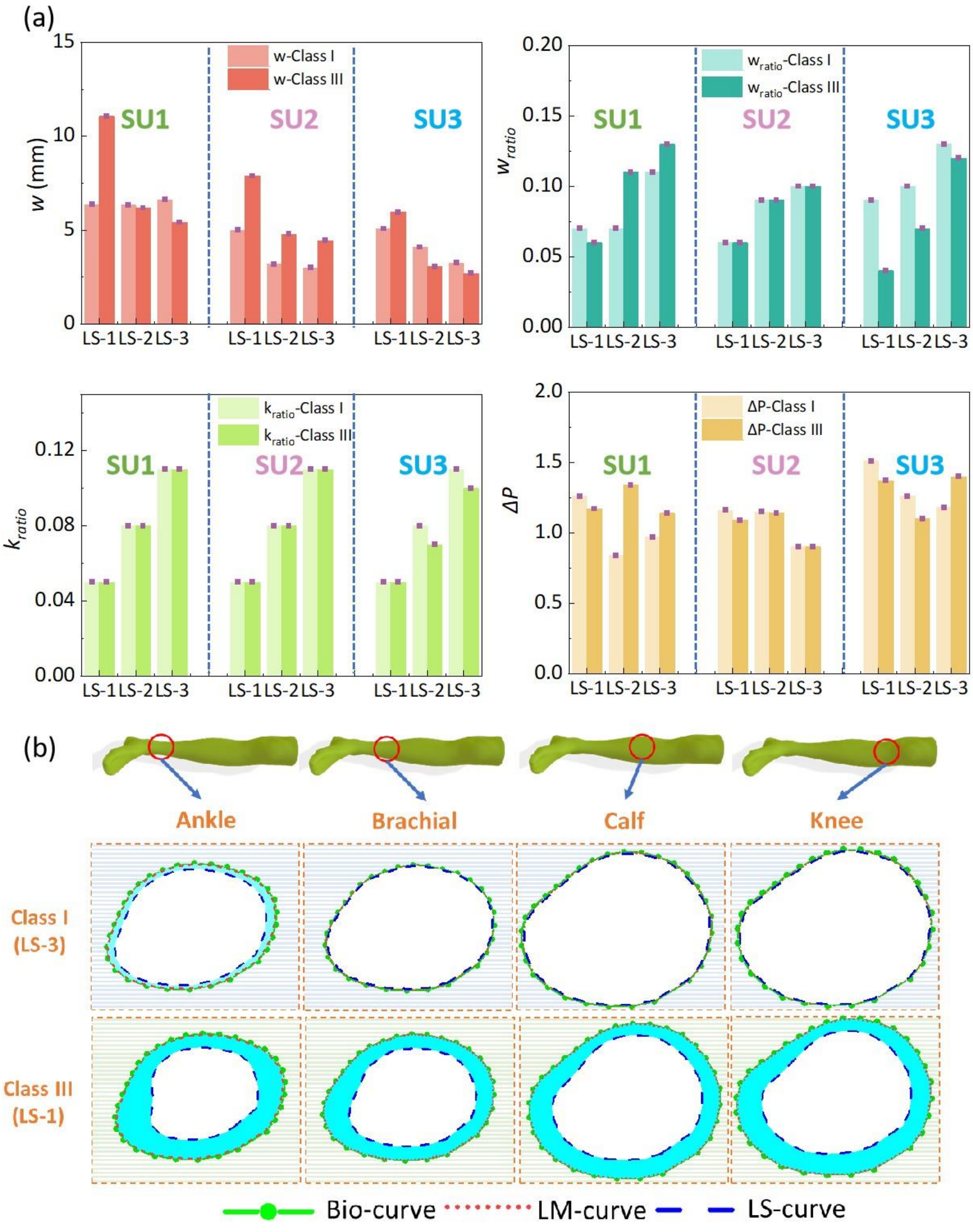

Figure 5.7 (a) Exported deformed leg circumferential displacements and calculated parameters through HzT model of Class I and Class III CTs. (b) Plotted body curves with diverse ST tissue properties and external compressions (from subject SU1).

5.3.4 Experimental Validation

Fig. 5.8-5.10 present the subject-specific pressure visualized mappings with Class I and Class III compression levels delivered by CTs. The inputting leg mechanical properties were derived from the SWE testing data of each biological body. The standardized pressure gradients and distributions were exerted along each lower extremity and showed individual profile features relating to their morphological characteristics. In addition, the pressure behaviors along the simulated FE systems (P_{LS}), biological bodies (P_{bio}), and 3D printing models (P_{rigid}) were compared by performing statistical tests. The pressure performances of CTs distributed along biological legs have significant correlations with pressure data obtained by the simulated FE systems (p (*Sig.*) <0.05, $\rho = 0.97$) and the measured pressure along the printing leg mannequins (p (*Sig.*) <0.05, $\rho = 0.96$). Therefore, the proposed 3D FE homogenous CT-leg systems could in practice replace the bio-legs for efficient pressure prediction simulations. Also, the nonsignificant correlations between the ST tissue characteristics and pressure diversities are validated by experimental tests.

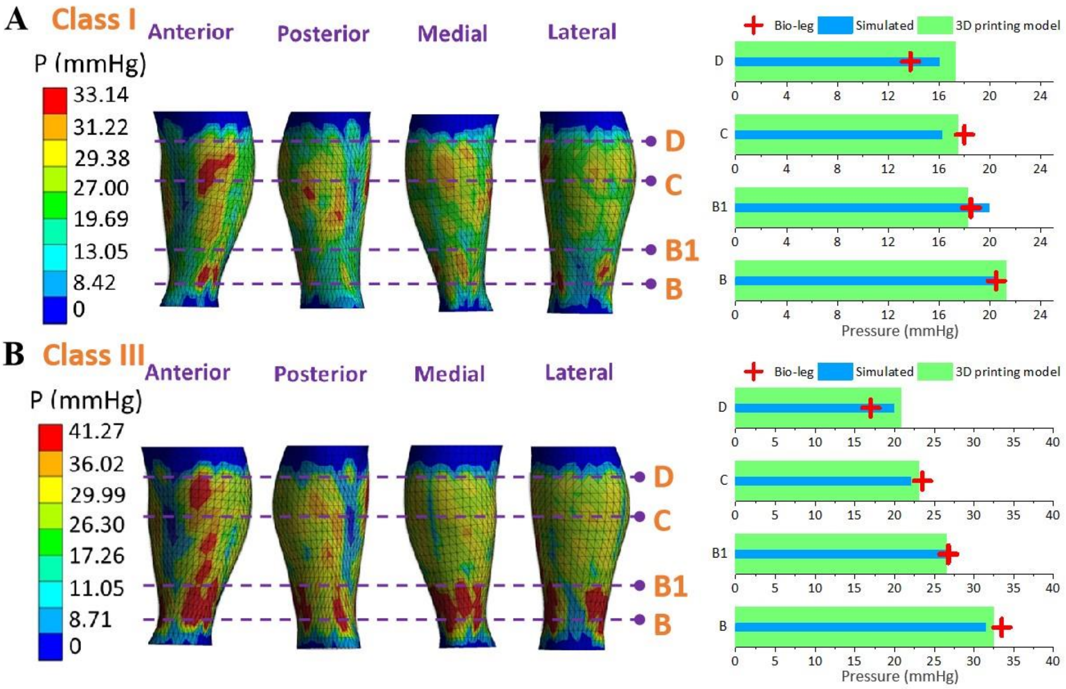

Figure 5.8 Pressure mappings and experimental validation results of compression Classes I and III for subject SU1.

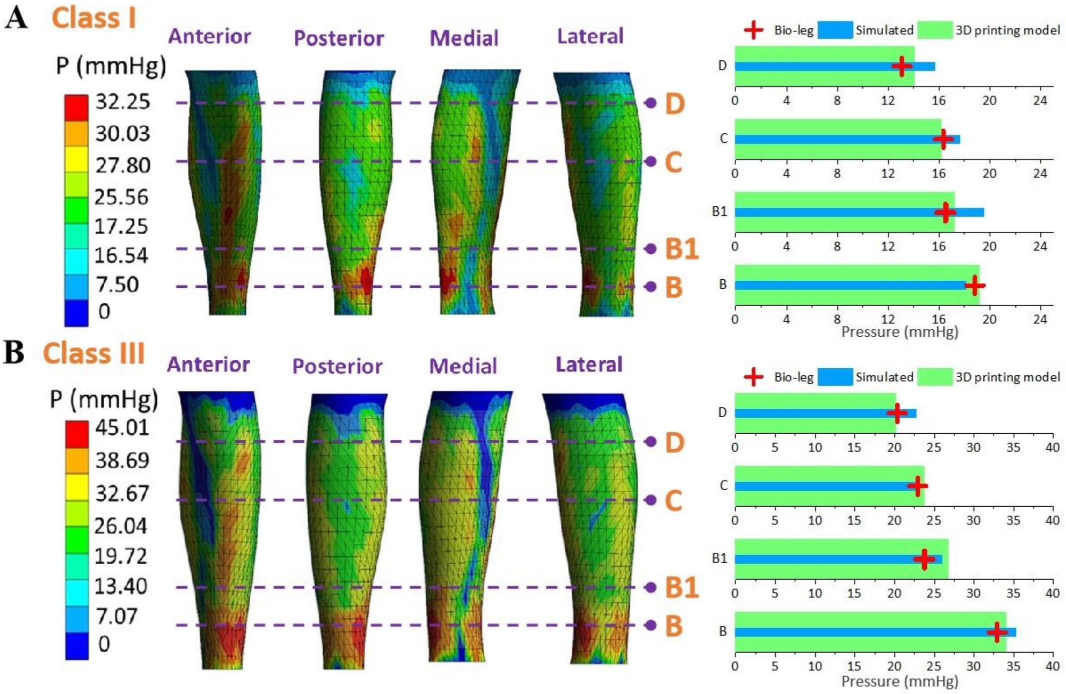

Figure 5.9 Pressure mappings and experimental validation results of compression Classes I and III for subject SU2.

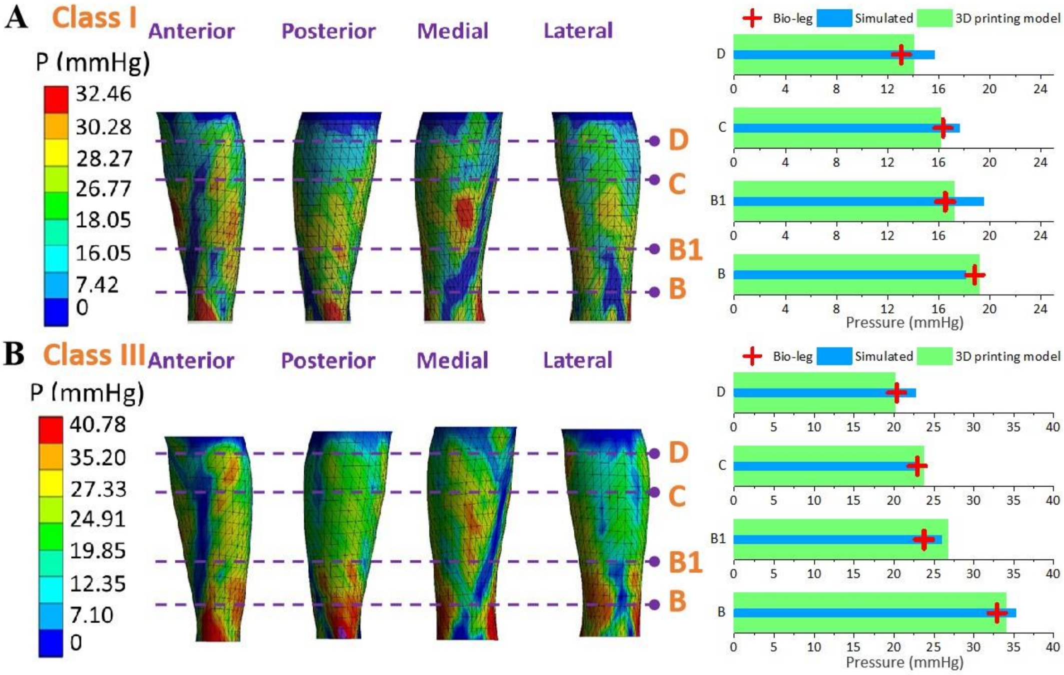

Figure 5.10 Pressure mappings and experimental validation results of compression Classes I and III for subject SU3.

In relevant existing FE CT-leg systems, the lower limbs were reconstructed through medical captured images (i.e., MRI or CT), and each leg slice was processed individually for composition segmentation and tissue characterization. The mechanical properties of each part of slice were also determined exactly through regional bio-material measurement. After physical data acquisition and mechanical FE modelling construction, their simulated pressure differences were approximately 5.9% to 21.4% [209, 226, 227]. For the proposed user-oriented FE models, the lower legs were constructed as simplified homogenous models based on 3D body scanning rather than medical operating equipment with complex physiological structural characteristics. The verification results demonstrate that the timesaving and effective CT-leg systems with exact scanned morphological profiles and geometric shapes could facilitate the basic interfacial pressure performance visualization and functional assessment for FE compression studies. Thus, the biomaterial characteristics of the studied main muscle compositions could represent leg mechanical properties in compression simulation to achieve efficient pressure prediction and parameter optimization for the development of CTs.

In previously related studies [227, 228], ST stiffness varied during the muscle activation states. For instance, muscular contraction and power production could cause around 150% greater increase in stiffness due to ankle dorsiflexion in the moving process. And for the patient groups with health conditions, ST stiffness caused by progressive muscular diseases also increased by approximately 120% compared with the control groups [229]. Based on these ST mechanical variations, the E_S of biological legs could approach maximumly 0.0045 MPa in dynamic muscle activities, which is still far smaller than the studied rigid leg model (3.0 GPa). Therefore, the main findings for CTs in this chapter can be applied not only for different bio-bodies with individual tissue diversities but also in various practical wearing and motion scenarios. Through the obtained pressure mappings of simulated results, the insufficient and peak focal pressures were distributed unevenly along each lower extremity. Thus, the biomechanical system could also provide the design strategy [230] for user-oriented therapeutic CTs with enhanced medical functions and wearing comfort.

Similarly, based on the HzT model, the pressure ratios were determined by the relationships of the leg deformed displacement and tissue elastic factor ratios. The leg-deformed displacements were varied caused by the external compression levels. In practical application, through the commercial recommended size selection tables [231], the circumferential dimension ranges between each size of CTs also commonly span around 2 cm to 7 cm for identical compression levels, which are consistent with the previously calculated variations of circumference values (2.27 cm to 6.95 cm). For elastic CTs, the pressure performances (*P*) are mechanically determined by the fabric tensions (*T*) and body girths (*C*) through the Laplace' Law (*P*=*T*/*C*) [232, 233]. Therefore, through the prescribed pressure ranges of 18-46 mmHg and required CT stretched ratios (15%-80%) [234], the garment-based transverse tensile stresses (0.05-0.80 MPa) were relatively smaller to generate the adequate deformed indentations along various biological bodies with diverse tissue properties. Therefore, for the design and development of compression textile-based therapeutic stockings, the pressure behaviors have no correlations not only with body tissue characteristics, but also with the leg mannequin material selections in compression experimental estimations.

5.4 Summary

This chapter systematically investigated the biomechanical influences of tissue properties on pressure performances of CTs through FE modelling, theoretical contact modelling, and experimental study. The proposed simplified FE 3D homogeneous CT-leg systems effectively and accurately simulated the interfacial pressure behaviors. The pressure performances of CTs showed no statistically significant differences with the applied lower limbs or leg models with various mechanical tissue properties. The leg circumferential deformations were positively increased by the external fabric tension forces. However, these displacement variations caused by varied bio-material stiffness could not lead to regular changes in pressure distributions.

Thus, the visualized FE homogenous models provide an efficient biomechanical simulation approach for user-specific pressure prediction and performance evaluation of CTs. The influencing mechanisms of leg tissue properties on pressure behaviors of textile-based materials also lead the scientific design principles for the development of CTs with pressure fitness in compression therapy. Therefore, the outcomes of this chapter provide not only the bio-design strategy for the pressure management of CTs, but also accurate analytical approaches of functional pressure assessments for tailoring rehabilitation equipment and monitoring treatment in compression therapy.

CHAPTER 6 MESOSCALE LAID-IN LOOP MODELLING FOR YARN MATERIAL DETERMINATION

6.1 Introduction

Related studies have explored the influences of the yarn counts and insertion densities of inlay materials on the physical-mechanical properties and pressure performances of compression fabrics through experimental testing and qualitative analyses [91, 93, 235]. Limited studies have used integrated geometric models and FE simulations to explore the mechanical mechanisms of laid-in weft-knitted compression (LWC) materials. The working mechanics of LWC materials need to be explored in mesoscale by analyzing structural deformation, yarn stress, and pressure performance under dynamic stretching.

Therefore, to facilitate the yarn selection and pressure performance prediction of LWC biomedical materials by simulating the geometric loop deformation and stress distribution during the practical stretching and wearing process, the present chapter constructed the novel 3D mesoscale geometric and FE models for 1×1 laid-in loop structures based on real loop characteristics in knitting; these models can be used to visually and quantitively analyze the stress-strain properties of LWC materials along the wale and course directions. The simulated data were validated against experimental measures under uniaxial stretches (tensile ratios of 0%-80%). The modelled laid-in mesoscopic loops promoted the basic understanding of the mechanical contributions of different loop components in knitted fabrics and guided the yarn material selections for improvement of required mechanical functions. This chapter also contributes to the formulation of more complex weft-knitted CT materials with laid-in loop structures under dynamic stretching and facilitates the effective prediction of pressure performance, and optimization of production parameters for cost-effective consumption.

6.2 Materials and Methods

6.2.1 Physical-Mechanical Characteristics of LWC Materials

Because of their superior elasticities and tenacities, covered synthetic yarn materials have been widely used in knitted CT textiles [236]. In the present chapter, Nylon (polyamide) double-covered Lycra (polyurethane) materials were applied as ground yarns and inlay yarns, respectively, for the fabrication of LWC fabrics by using a computerized 3D seamless circular knitting unit (Lonati-LA-45ME, Francesco Lonati, Brescia, Italy). In the fabricated yarn structure, elastic Lycra yarn formed the core that provided the required fabric elongation and recovery during repeated stretching. This core was surrounded by Nylon yarns that improved the fabric abrasion resistance and durability. To study the influences of different inlay yarns on the mechanical properties of the prepared fabrics, three types of inlay materials (YA, YB, and YC) with distinct linear densities were interlooped with one type of ground yarn (GY) to form three types of LWC fabrics with 1×1 laid-in loop structures. Specifically, within one knitting cycle, the ground yarns formed knitted loops regularly in the second and the fourth courses, whereas the inlay yarns formed tuck loops and miss stitches alternatively at the first and third courses. For property investigation, the mesoscopic geometries and structures of the yarn and fabric materials were analyzed using a Leica M165C microscope (Leica Microsystems, Wetzlar, Germany) according to the ASTM D1577-79 standard. The mass densities (mass per unit volume) of the yarns and fabrics were measured using a Shimadzu AY120 electronic balance (Shimadzu Co., Kyoto, Japan) according to the ISO 2060:1996 and ASTM D 3776/D 3776M-09a standards, respectively. Moreover, the fabric thickness was determined using Vernier calipers in accordance with the ASTM D1777 standard. Tables 6.1a and 6.1b present the obtained physical properties of the adopted yarn and fabric materials. These properties were used as input parametric values for the constructed 3D mesoscale laid-in models, which are described in sections *6.2.2* and *6.2.3*.

Table 6.1a Physical properties of the used yarn materials

Yarn code	Yarn type	Yarn count (Denier)		Mass density (g/cm^3)	Yarn diameters (mm)		
		Elastic Lycra core	Double covered Nylon		Before knitting	After knitting	Variation Δ%
GY	Ground yarn	40	40/40	0.91	0.27	0.12	55.56
YA	Inlay yarn	210	40/40	0.84	0.41	0.21	48.78
YB	Inlay yarn	280	40/40	0.61	0.42	0.29	30.95
YC	Inlay yarn	420	40/40	0.70	0.47	0.32	31.91

Table 6.1b Physical properties of the produced LWC fabrics

Fabric code	Yarn combination	Course density (courses/cm)	Wale density (wales/cm)	Mass density (kg/m^3)	Thickness (mm)
FA	GY-YC	25.68	24.32	503.83	0.68
FB	GY-YB	22.22	24.07	530.61	0.69
FC	GY-YC	21.68	21.67	510.70	0.69

To analyze the tensile behaviors of the applied yarn (thread) materials, stress-relaxation tests were performed using the Instron 4411 universal tension tester (Norwood, MA, USA) in accordance with the ASTM D2256 standard. Five samples for each type of yarn material were stretched to the maximum strain of 50% under a strain speed of 300 mm/min. The Young's modulus of the elastic yarns was measured under the maximum stretching with time. The values of the mechanical tensile properties of the inlay yarns YA, YB, and YC decreased with loading time, presenting linear viscoelastic properties (Fig. 6.1). Detailly, the tensile behavior of linear viscoelastic yarn materials can be described using the Maxwell mechanical model, which comprises spring and dashpot parts [237, 238] (Fig. 6.1 (a)). This model can be used to simultaneously determine the elastic solid and viscous fluid properties of viscoelastic yarn materials through stress-relaxation tests. The time-domain constitutive equation for the studied materials is presented in Eq. 6.1 [239]. The Prony series was used to represent the time-dependent behaviors of the yarn materials and to calculate their relaxation moduli over time. The stress of the yarn materials $\sigma(t)$ can be determined by using the Prony series, as expressed in Eq. 6.2.

$$\sigma(t) = \int_{\infty}^{t} C(t-\tau)\frac{d\varepsilon}{d\tau}d\tau \tag{6.1}$$

where C is the relaxation modulus, ε is yarn strain, and t and τ are the loading and relaxation times, respectively.

$$E(t) = G_1 \times \exp(-\frac{1}{\tau} \times t) + E_{\infty} \tag{6.2}$$

where $E(t)$ is the Young's modulus of the yarn during the relaxation time, E_{∞} is the long-term Young's modulus after the yarn material is completely relaxed, G_1 is the Prony series, t is loading time, and τ is the relaxation time.

To verify the adopted Maxwell model, the experimental and simulated $E(t)$ values of the studied yarn materials were compared. The simulated and experimental $E(t)$ values were highly correlated with each other (p *(Sig.)* < 0.001) and had a reliable fit ($\rho = 0.96$) (Fig. 6.1 (b)). The yarn function coefficients of the Prony series and the relaxation time were calculated using MATLAB R2016a software (MathWorks, Inc., Natick, MA, USA) according to the results of the stress-relaxation stretching tests, which were also used as the input parameters for FE loop modelling (section *6.2.3*). Table 6.2 lists the obtained initial and residual Young's moduli, Prony series, relaxation time, and Poisson's ratios of the yarn materials [38].

Table 6.2 Determined tensile properties of the applied yarn materials

Yarn code	Poisson's ratio	E (MPa)		ΔE (%)	Prony series G_1	Relaxation time τ (s)
		Initial E (MPa)	Residual E (MPa)			
GY	0.3	0.90	0.90	/	/	/
YA	0.3	2.51	1.38	45.02	1.16	73.42
YB	0.3	2.41	1.44	40.25	1.00	72.74
YC	0.3	2.40	1.74	27.50	0.66	84.55

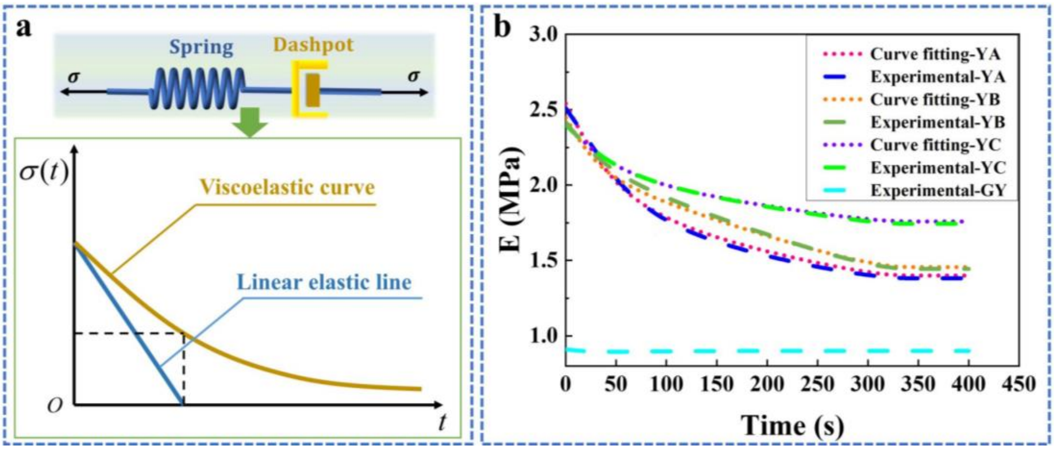

Figure 6.1 (a) Maxwell mechanical model describes the tensile behavior of linear viscoelastic yarn materials. (b) Experimental and fitted time-relaxation curves of the tested elastic ground (GY) and inlay yarn (YA, YB, and YC) materials.

6.2.2 3D Geometric Loop Modelling of LWC Materials

Geometric mesoscale loop models for 1×1 laid-in weft-knitted fabrics were constructed. In these models, inlay and ground yarns were represented as compressible, cylindrical, and homogeneous elastic rods that did not undergo plastic deformation under external tensile forces [240]. In this chapter, the technical back of the fabrics was used as the main view to construct 3D geometric loop models for numerical simulation. Fig. 6.2 illustrates a 1×1 laid-in LRU that comprised two knitted ground loops (blue) and two courses of inlay yarns (green) in the technical front and back views, which were built based on realistic knitting loop structures. A needle loop, V-shaped legs, and a sinker loop were constructed in one knitted ground loop.

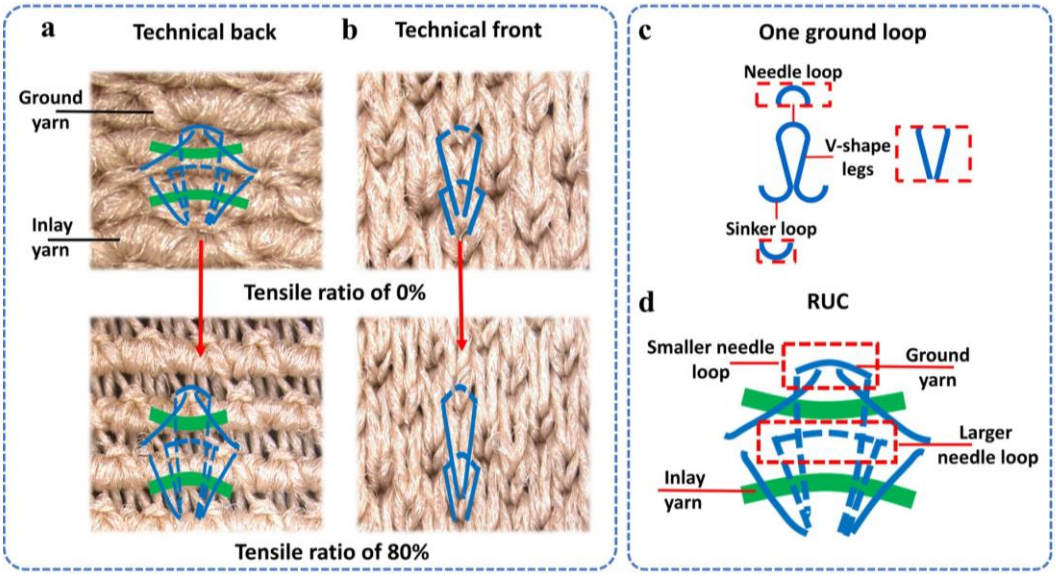

Figure 6.2 (a) Technical back and (b) front views of laid-in knitted structure under the unstretched state and tensile ratios of 80%, respectively. (c) The components of knitted ground loop included the V-shape legs, sinker loop, and needle loop. (d) 1×1 laid-in LRU was divided into the smaller and larger needle loops for geometric characteristic analysis.

A coordinate system was established for a 3D geometric loop model of LWC material fabrics. The *x*-axis, *y*-axis, and *z*-axis were set along the course, wale, and thickness directions, respectively, and their common origin was denoted *O* (Fig. 6.3 (a) and Fig. 6.3 (b)). In technical front and back views, the right and left parts of an LRU were symmetrical with respect to the *y*-axis. The main structural parameters of an LRU included the course distance (*c*), wale distance (*w*), the diameters of ground (*d*), and inlay yarns (*D*). Additionally, the defined distances (i.e. *t1*, *t2*, *t3*) between each loop component are illustrated as shown in Fig. 6.3 (a) and Fig. 6.3 (b).

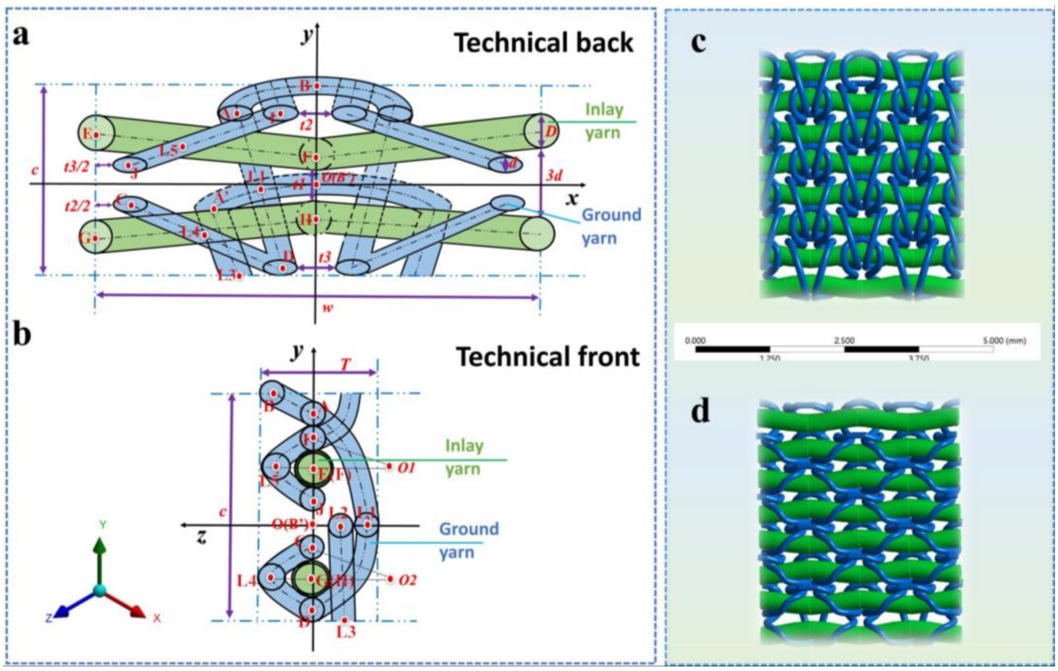

Figure 6.3 1×1 laid-in LWC structures were defined as various parts through the (a) technical back and (b) side views. The built 3D geometric model of LWC fabric with 1×1 laid-in loop structures in terms of the technical (c) front and (d) back views.

● *Ground yarn model*

To construct a 3D geometric model of the ground yarns, the 3D parts **AB** and **A'B'** of a needle loop were constructed according to the following equation:

Part **AB**

$$\left\{ x \in \left(\frac{2d-w}{4}, \frac{w-2d}{4}\right) \right\}$$

$$A\left(\frac{2d-w}{4}, \frac{3d}{2}+D\right) \quad B\left(0, \frac{c}{2}\right)$$

$$y = \frac{2(3d+2D-c)}{2d-w}x + \frac{c}{2} \tag{6.3}$$

Part **A'B'**

$$\left\{ x \in \left(\frac{-2d-w}{4}, \frac{w+2d}{4}\right) \right\}$$

$$A'\left(\frac{-2d-w}{4}, \frac{c-3d-2D}{2}\right) \; B'(0,0)$$

$$y = \frac{2(3d+2D-c)}{2d+w}x \tag{6.4}$$

Because the actual geometry of the sinker loops in a laid-in loop structure is strongly affected by inlay yarns, parts **CD** and **IJ** are defined according to Eqs. 6.5 and 6.6, respectively, on the basis of the determined t_2 and t_3 values.

Part **CD**

$$\left\{x\in\left(\frac{t_3+d-w}{2},\frac{-t_3-d}{2}\right)\cup\left(\frac{t_3+d}{2},\frac{w-t_3-d}{2}\right)\right\}$$

$$C\left(\frac{t_3+d-w}{2},-d\right)\ D\left(\frac{-t_3-d}{2},\frac{-c+d}{2}\right)$$

$$y=\frac{c-3d}{2t_3+2d-w}x-\left[\frac{cd+ct_3+dt_3-cw+dw+d^2}{2(2d+2t_3-w)}\right] \tag{6.5}$$

Part **IJ**

$$\left\{x\in\left(\frac{t_3+d-w}{2},\frac{-t_3-d}{2}\right)\cup\left(\frac{t_3+d}{2},\frac{w-t_3-d}{2}\right)\right\}$$

$$I\left(\frac{-t_2-d}{2},\frac{3d}{2}+D\right)\ J\left(\frac{t_3+d-w}{2},d\right)$$

$$y=\frac{d+2D}{w-t_2-t_3-2d}x+d-\frac{(t_3+d-w)(d+2D)}{2(w-t_2-t_3-2d)} \tag{6.6}$$

Thus, parts **AD** and **A'I** of the V-shaped legs were constructed according to Eqs. 6.7 and 6.8, respectively.

Part **AD**

$$\left\{x\in\left(\frac{2d-w}{4},\frac{-t_3-d}{2}\right)\right\}$$

$$A\left(\frac{2d-w}{4},\frac{3d}{2}+D\right)\quad D\left(\frac{-t_3-d}{2},\frac{-c+d}{2}\right)$$

$$y=\frac{2(c+2d+2D)}{2t_3-w+4d}x+\frac{(4Dd+4Dt_3-2cd+6dt_3+cw-dw+8d^2)}{2(2t_3+4d-w)} \tag{6.7}$$

Part **A'I**

$$\left\{x\in\left(\frac{-2d-w}{4},\frac{-t_2-d}{2}\right)\right\}$$

$$A'(\frac{-2d-w}{4},\frac{c-3d-2D}{2})\quad I(\frac{-t_2-d}{2},\frac{3d}{2}+D)$$

$$y=\frac{2(c-6d-4D)}{2t_2-w}x+\frac{c-3d-2D}{2}+\frac{(2d+w)(c-6d-4D)}{2(2t_2-w)} \qquad (6.8)$$

● *Inlay yarn model*

In the 3D geometric model of the inlay segment, the upper and lower inlay yarns were symmetrically distributed along a knitting course. Parts **EF** and **GH** of the upper and lower inlay yarns can be defined as follows (their distance along the y-axis is denoted as t_1):

Part **EF**:

$$\{x\in(-w,w)\}$$

$$E(-\frac{w}{2},\frac{3d+D}{2})\quad F(0,\frac{t_1+D}{2})$$

$$y=-\left(\frac{3d-t_1}{w}\right)x+\left(\frac{t_1+D}{2}\right) \qquad (6.9)$$

Part **GH**:

$$\{x\in(-w,w)\}$$

$$G(-\frac{w}{2},-\frac{3d+D}{2})\quad H(0,-\frac{t_1+D}{2})$$

$$y=\left(\frac{3d-t_1}{w}\right)x-\left(\frac{t_1+D}{2}\right) \qquad (6.10)$$

● *Fabric thickness model*

In the fabric thickness model, the plane in which parts **EF** and **GH** were located was defined as the central plane, and the thickness part near the technical back of the fabric was defined as the positive direction of the *z*-axis direction. The fabric thickness T was used to describe the geometric structure of the fabric in a side view. Parts CD and IJ of the ground yarns were assumed to intersect the inlay yarns at points *L4* and *L5*, respectively. These parts can be defined as half-circle trajectories with the center points

$$O_1(\frac{D+2.5d}{2},-\frac{9(D+2.5d)-(2T+D-3d)^2}{12(2T+D-3d)}) \text{ and } O2(\frac{-d-c}{4},-\frac{3(-d-c)^2}{16(2T+D-3d)}+\frac{2T+D-3d}{12}),$$

respectively, by using Eq. 6.11.

$$(y-a)^2+(z-b)^2=R^2 \qquad (6.11)$$

where (a,b) were the centers of the circles, and R was the diameter.

Thus, **IJ** and **CD** parts can be expressed as follows:

Part **IJ**

$$y \in (-d,\frac{-c+d}{2})$$

$$L5(\frac{-c-d}{4},\frac{2T+D-3d}{6}) \quad I(\frac{3d+2D}{2},0) \quad J(d,0)$$

$$(y-\frac{D+2.5d}{2})^2+\left[z+\frac{9(D+2.5d)^2-(2T+D-3d)^2}{12(2T+D-3d)}\right]^2=\left[\frac{(2T+D-3d)^2+9(D+2.5d)^2}{12(2T+D-3d)}\right]^2$$

(6.12)

Part **CD**

$$y \in (d,\frac{3d+2D}{2})$$

$$L4(\frac{-d-c}{4},\frac{2T+D-3d}{6}) \quad C(-d,0) \quad D(\frac{-c+d}{2},0)$$

$$(y-\frac{-c-d}{4})^2+\left[z+\frac{3(-c-d)^2}{16(2T+D-3d)}-\frac{2T+D-3d}{12}\right]^2=\left[\frac{(2T+D-3d)}{12}+\frac{3(-d-c)^2}{16(2T+D-3d)}\right]^2$$

(6.13)

Similarly, a quarter circle of part **L3I** with a diameter of $\frac{2T+D-3d}{6}$ can be presented below:

Part **L3I**:

$$y \in (\frac{c}{2},\frac{3d+2D}{2}) \cup (\frac{3d+2D}{2}+\frac{2T+D-3d}{6}-c,-\frac{c}{2})$$

$$L3(\frac{3d+2D}{2}+\frac{2T+D-3d}{6}-c,-\frac{2T+D-3d}{6})$$

$$\left[y-(\frac{3d+2D}{2}+\frac{2T+D-3d}{6}-c)\right]^2+z^2=(\frac{2T+D-3d}{6})^2 \tag{6.14}$$

Points *B* and *L2* are the vertices of needle loops **AB** and **A'B'**; thus, the definitions of parts **AB** and **L2L3** in the side view can be simplified by Eqs. 6.15 and 6.16, respectively.

Part **AB**:

$$y\in(\frac{3d+2D}{2},\frac{c}{2})$$

$$A(\frac{3d+2D}{2},0) \quad B(\frac{c}{2},\frac{2T+D-3d}{6})$$

$$z=\frac{2T+D-3d}{3(c-3d-2D)}(y-\frac{3d+2D}{2}) \tag{6.15}$$

Part **L2L3**:

$$y\in(0,\frac{3d+2D}{2}+\frac{2T+D-3d}{6}-c)$$

$$L2(0,-\frac{2T-3d+D}{6})$$

$$z=-\frac{2T-3d+D}{6} \tag{6.16}$$

Part **AD** for the larger knitted sinker loop was defined as the parabolic trajectory along the negative *z*-axis direction. This part can be expressed using Eq. 6.17.

Part **AD**:

$$y\in(-c,c)$$

$$A(\frac{3d+2D}{2},0) \quad D(\frac{-c+d}{2},0) \quad L1(\frac{4d+2D-c}{4},-\frac{4T-3d-D}{6})$$

$$z=\frac{(D-4T+3d)}{3\left[(2D+c)^2+4(2Dd+cd+d^2)\right]}\left[-8y^2+4y(2D-c+4d)+2(c-d)(2D+3d)\right] \tag{6.17}$$

The constructed 3D geometric model of laid-in weft-knitted loop fabric is shown in Fig. 6.3 (c) and Fig. 6.3 (d).

6.2.3 FE Mechanical Modelling for LWC Materials

The mechanical properties of LWC materials are influenced by the adopted yarns and loop structures. To analyze the tensile behaviors of the examined LWC fabrics, FE mesoscale models were constructed using ANSYS Workbench Design Modeler v19.2 (ANSYS, Pittsburgh, PA, USA) according to the developed 3D geometric laid-in loop models described in section *6.2.2*. The central difference method (CDM) was adopted to simulate the dynamic process of loop stretching and the linear viscoelastic properties of the inlay yarn materials. This method was implemented using the explicit dynamic solver in LS-DYNA software according to the conservation relationship between momentum and energy in the Lagrangian system. Eqs. 6.18-6.20 present the integration rules used in the CDM for discretizing the nonlinear algebraic equation for the calculation to be more accurate and more efficient [241].

$$M\ddot{x}^n = P^n - F^n + H^n \tag{6.18}$$

$$\dot{x}_i^{\frac{n+1}{2}} = \dot{x}_i^{\frac{n-1}{2}} + \ddot{x}_i^n \Delta u^n \tag{6.19}$$

$$\dot{x}_i^{n+1} = \dot{x}_i^n + \dot{x}_i^{\frac{n+1}{2}} \Delta u^{\frac{n+1}{2}} \tag{6.20}$$

where *M* is the diagonal mass matrix, $\dot{x}_i$ is the velocity, $\ddot{x}^n$ is the node acceleration component, *P* is the load, *F* is the stress component, and *H* is a damping hourglass. The superscripts *i* and *u* refer to the increment number and time, respectively.

Because of the similarities in the discretization along the orthogonal direction of the ground and inlay yarn elements, the FE yarn model was meshed using tetrahedral solid elements. Mesh sensitivity analysis was performed using mesh sizes of 0.06, 0.08, and 0.10 mm per element to examine the mesh independence of the constructed FE loop models (Fig. 6.4 (a)), respectively. The FE yarn model exhibited similar Young's modulus values under these mesh sizes, with the highest mesh quality (0.82) being achieved under a mesh size of 0.08mm (Fig. 6.4 (b)). Therefore, this mesh size was applied in the FE laid-in loop model for numerically analyzing the tensile behaviors of the yarns and LWC fabrics. A nonlinear frictional contact condition with a frictional coefficient of 0.30 was applied in the ground and inlay yarn models according to the augmented Lagrange equation and the physical properties of the yarns [242]. To achieve realistic simulations of the uniaxial stretching of the knitted laid-in fabrics, this study fixed the first knitting course and the rightmost part of each course in the loop model at locations where the displacements of all nodes were 0 along the *x*-, *y*-, and *z*-directions. The tensile behaviors of the laid-in loops under 0%-80% stretching were simulated, which fall in the elongation range of Germany RAL-GZ 387/1 quality standard for medical compression hosiery [243]. Thus, the loop displacements near the externally loaded end were relatively close to the maximum loop displacement values in the course and wale directions (approximately 2.70 mm and 3.31 mm), respectively. For instance, Fig. 6.5 (a) and Fig. 6.5 (b) display the structural deformation of the LWC fabric (FC) comprising ground loops (GY) and inlay yarns (YC) under strains of 0%-80%. As the strain increased, the displacements of the laid-in loops also increased, especially along the wale direction. Through the actual electronic scanned images, the simulated morphologies of the stretched loops were consistent with the practical deformations caused by the uniaxial tensile forces in practical stretching tests. Additionally, the determined physical-mechanical properties of the yarn materials (yarn densities, Young's moduli, shear moduli, bulk moduli, and Prony coefficients) were used as the input parameters in the constructed 3D FE laid-in loop models.

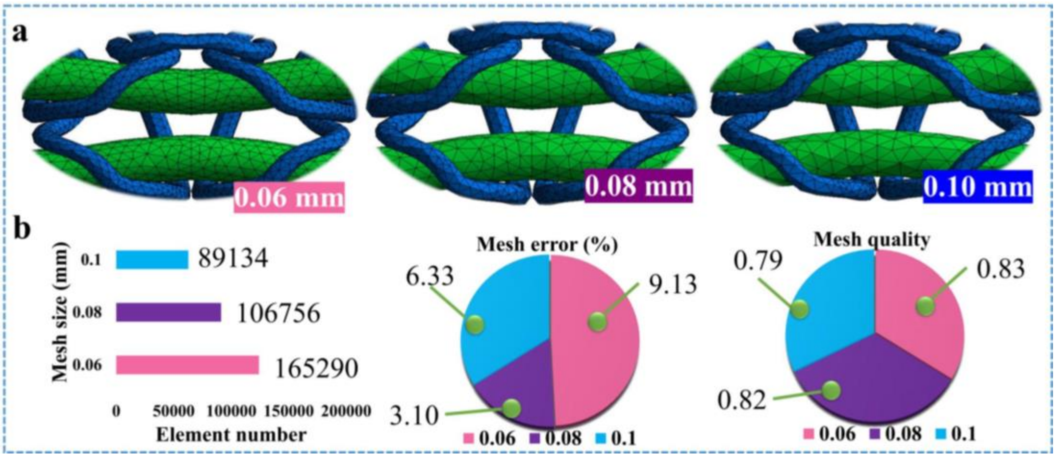

Figure 6.4 (a) This study adopted mesh sizes of 0.06mm, 0.08mm and 0.10mm for comparison. (b) The independence examination (mesh element, mesh error and mech quality) of mechanical laid-in loop models performed by applied mesh sizes.

6.2.4 Tensile Behavior Validation for LWC Materials

To verify the constructed 3D FE laid-in loop models, experimental tests were conducted. The stress-strain curves of the studied sample fabrics (FA, FB, and FC) were obtained by conducting uniaxial stretching tests on them by using an Instron 4411 tension tester (Norwood, MA, USA). Two clamps with a width of 75 mm were used to stretch the sample fabrics (75 mm×75 mm) by 80% at a speed of 300 mm/min (ASTM D4964) along the course and wale directions (Fig. 6.5 (c)). The elastic moduli (E_{fabric}) of the fabric samples were determined using Eq. 6.21. The simulated elastic moduli were calculated according to the loop stresses determined along the course and wale directions under different stretching ratios. The DROs between the simulated (E_{simul}) and measured Young's moduli (E_{exp}) were determined using Eq. 6.22.

$$E_{fabric} = \frac{F_{fabric}}{bT\varepsilon_F} \tag{6.21}$$

where F_{fabric} was the tension force, b and T were the fabric length and thickness, respectively, and ε_F was the fabric extension stretched by the specific tension force.

$$DROs = \frac{\left|E_{simul} - E_{exp}\right|}{E_{exp}} \times 100\% \tag{6.22}$$

In general, the constructed 3D mesoscale geometric models and FE simulations were used to investigate the structural deformation and stress variations of the laid-in weft-knitted fabrics prepared using different combinations of yarn materials with different properties under controlled strains. Through modelling and simulation, the validated 3D geometric models and FE models provide a visual tool for intuitively understanding the mechanical functions of the ground and inlay yarns of LWC fabrics along the course and wale directions. Moreover, these results aid in the selection of yarn materials for knitted compression textiles with suitable mechanical properties and pressure performances.

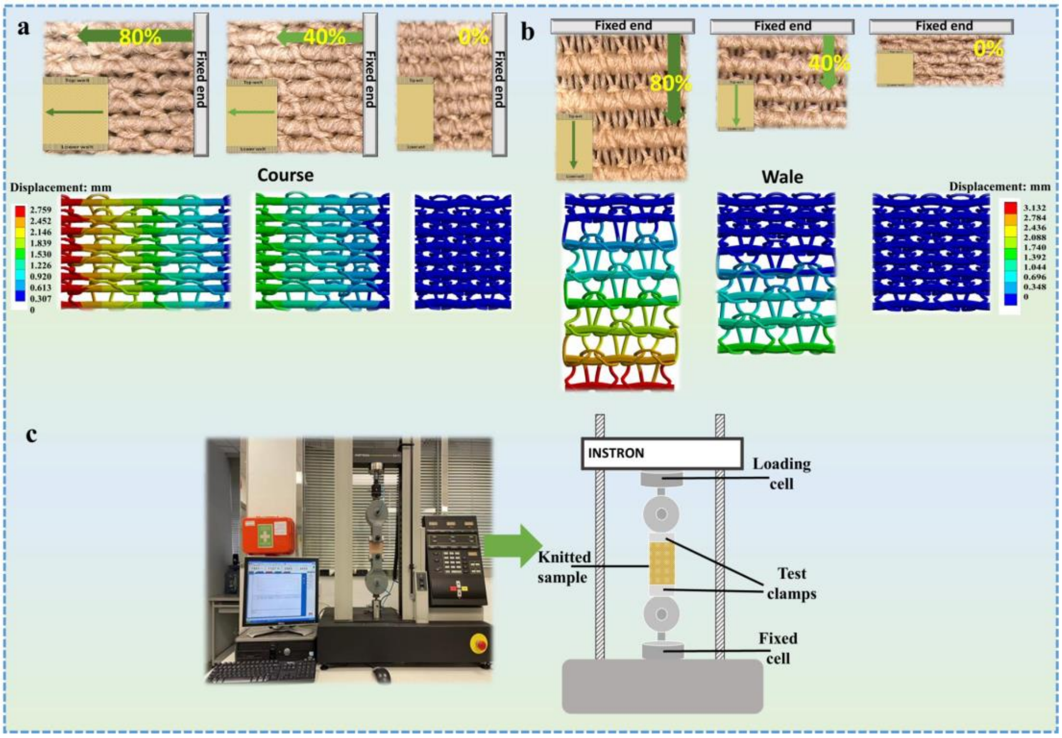

Figure 6.5 The structural deformation of 1×1 laid-in studied CT samples along (a) the course

and (b) the wale directions under different strains (from 0% to 80%). (c) Tensile validation tests of the LWC fabric samples under the course and wale stretching loading.

6.3 Results and Discussion

6.3.1 Simulated Tensile Properties

The simplified LRU quantities were extracted and applied to efficiently describe the simulated mechanical mappings by our proposed FE systems. Fig. 6.6 (a) and Fig. 6.6 (b) show the simulated tensile stresses of the laid-in knitted loop models constructed using the studied ground yarn (GY) and different inlay yarns (YA, YB, and YC) under uniaxial stretching along the course and wale directions, respectively. As the stretching increased from 0%-80%, the tensile stresses of the elastic yarns increased, especially for the fabrics (FC) made of inlay yarns (YC) with high linear densities. Moreover, Fig. 6.7 (a) and Fig. 6.7 (b) depict the details of the simulated stress distribution profiles of the FC fabric along the elastic loops by the constructed mesoscale FE laid-in loop model. For fabric stretching in course direction (Fig. 6.7 (a)), the inlay yarns, which had higher linear densities and were floated and tucked with the ground loops, produced considerably higher stresses than did the ground yarns, especially at the interlooped regions with the knitted ground yarns. By contrast, for fabric stretching in the wale direction (Fig. 6.7 (b)), the stresses produced by the ground yarns were remarkably higher than those produced by the inlay yarns, especially in the needle loops, sinker loops, and V-shaped legs of the knitted ground loops.

For the quantitative investigations, Fig. 6.7 (c) and Fig. 6.7 (d) further compare the stress variations of the FA fabric made of the ground yarn (GY) and inlay yarn (YA).

With the increasing of tensile strains, the ground and inlay yarns produced the maximum stresses of approximately 0.01 MPa and 0.76 MPa, respectively, along the course direction (Fig. 6.7 (c)); conversely, along the wale direction (Fig. 6.7 (d)), ground and inlay yarns produced the maximum stresses of approximate 0.36 MPa and 0.56 Pa, respectively. The tensile properties of inlay yarns would dominate the cross-sectional stretching ability and pressure exertion of LWC fabrics in use, while the tensile properties of ground yarns would dominate the longitudinal stretching ability relating to pull-on performances in dynamic wearing. In previous studies [241], the developed LWC fabrics were empirically prepared by the thicker inlay yarn materials to generate relatively larger fabric tensions and pressure distributions along corresponding targeted user bodies. The results provide evidence-based guidance that can be used in the appropriate selection of yarn materials for LWC fabrics to ensure that the desired mechanical properties along the course and wale directions can be achieved for these fabrics.

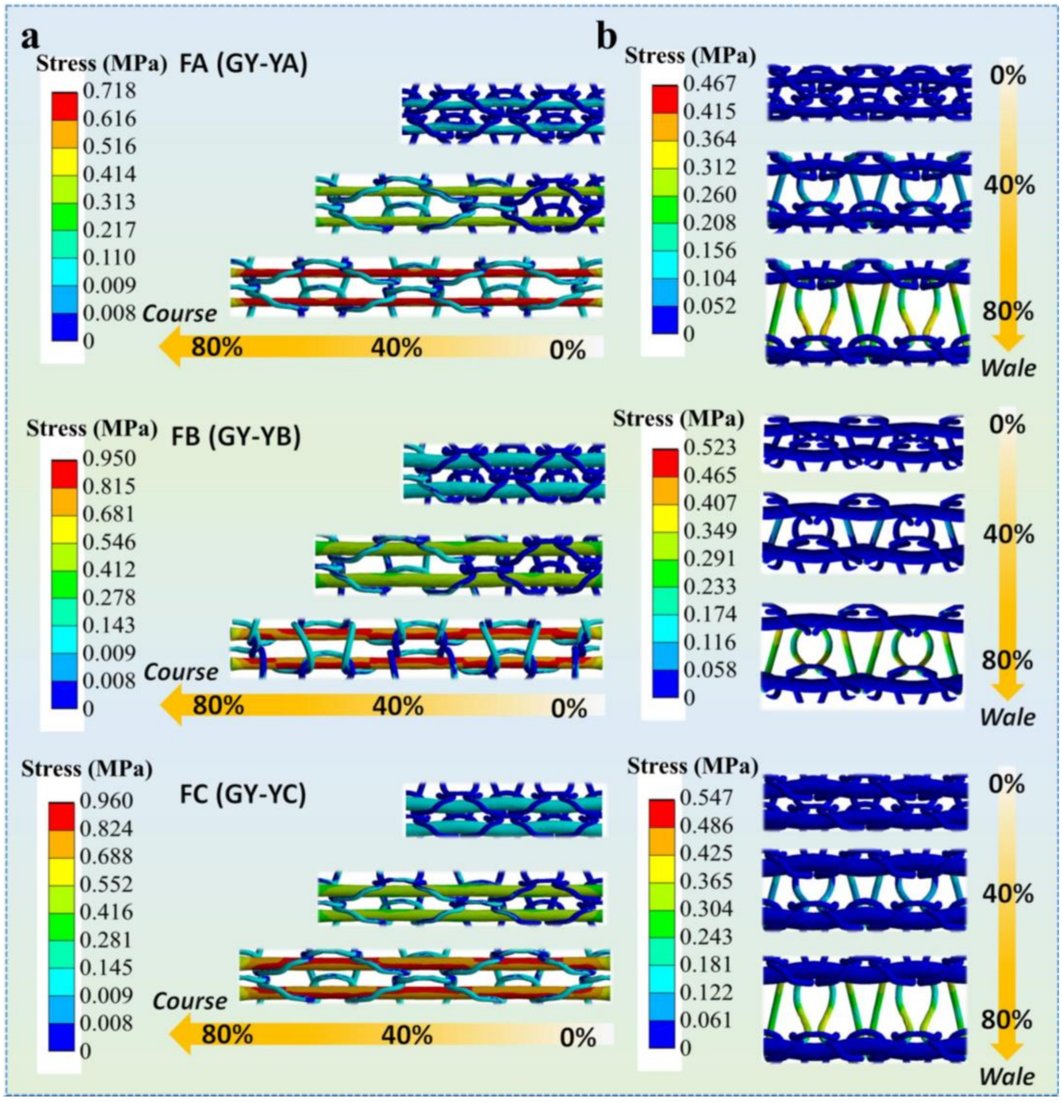

Figure 6.6 The simulated tensile stress mappings of the studied LWC samples (FA, FB, and FC) along (a) the course and (b) the wale directions under different strains (from 0% to 80%).

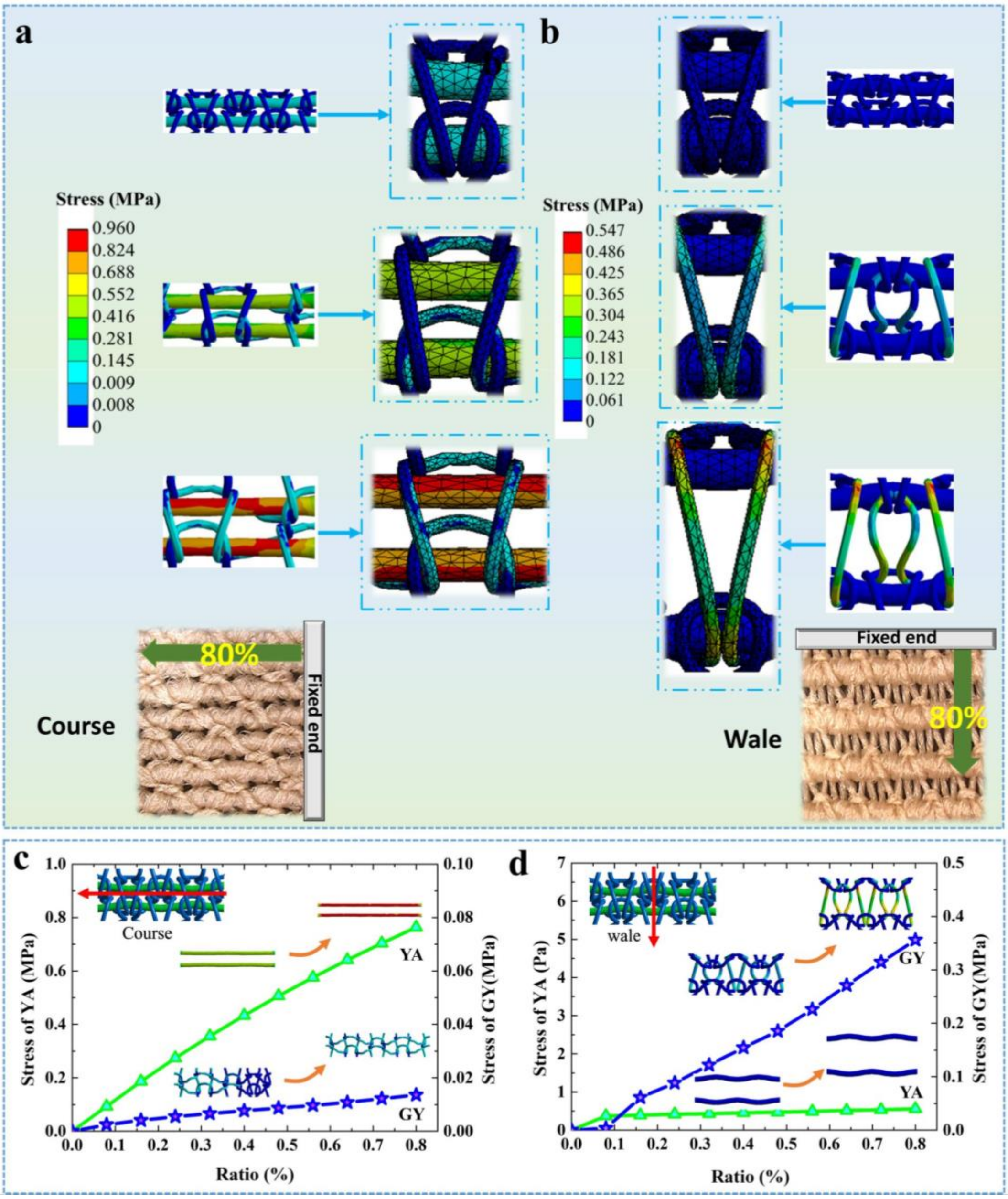

Figure 6.7 Comparisons of the stress variations of the ground (GY) and inlay (YC) yarns along (a) the course and (b) wale directions under different strains. Quantitative investigations of the sample fabric FA along (c) the course and (d) wale directions under stretches.

6.3.2 Validation of Proposed FE Mesoscale Models

Fig. 6.8 displays the simulated and experimental stress-strain curves of the studied LWC fabrics. The goodness of fit (R^2) of all the stress-strain curves exceeded 0.96 [128], which confirmed the linear elastic properties of the studied LWC fabrics under controlled strains. Moreover, through the Pearson correlation statistical analysis, the simulated and experimental stress-strain curves exhibited a good agreement with each other (p $(Sig.) < 0.001$, $\rho = 0.97$) [244, 245] along the course and wale directions. Fig. 6.9 (a) and Fig. Fig. 6.9 (b) indicate that the E_{simul} values along the course direction were generally greater than those along the wale direction, which indicates that the studied LWC fabrics had anisotropic properties. Commonly, the thicker inlay materials were laid into the fabric as long floating threads along the course direction, therefore inlay threads deformed and then produced stress as the principal strain plane during the course stretches. Conversely, the basic plain ground structure, especially the V-shape leg part was mainly loaded under the wale stretching. After the knitted process, due to the loop intervals and interaction forces between each yarn component, thus, the generated fabric Young's modulus was smaller than Young's modulus of applied inlay yarns.

The average DRO between the E_{simul} and E_{exp} was approximately 10.22%, and the DRO in the course and wale directions ranged from 6.33% to 14.71% and from 5.41% to 13.04%, respectively. Thus, the constructed FE laid-in weft-knitted loop model had higher simulation accuracy than the relevant models proposed in previous studies (e.g., the reported average DRO values ranged from 15% to 35% [145, 243-245]. Consequently, this model can be effectively applied for simulating the mechanical properties (e.g., Young's moduli and tensile stresses) of LWC fabrics at a 3D mesoscale. Furthermore, the reduced DRO of this model could relate to this newly proposed simulation approach. Because the attenuation of the internal stress of synthetic polymer yarns can influence the mechanical properties of knitted elastic fabrics over time [246, 247], prior to the simulation, this chapter investigated the viscoelastic properties of the studied yarn materials. The Prony series equations and coefficients used in this study not only reflected the essential tensile properties of the examined yarn materials under constant stretching loading but also enabled the parameterization of the time-dependent tensile features of these materials. This parametrization enabled more detailed simulation and allowed the constructed 3D geometric and mechanical loop models to represent the tensile behaviors of the examined LWC fabrics effectively under varying strain conditions. The deviations between the simulated and measured Young's moduli may be due to the following reasons caused by the study hypothesis and assumptions. First, the simulated curve morphologies of the 3D geometric models possibly deviated marginally from the optically surveyed loop structures, especially for the part hidden behind the observed loop structures. Second, the used structural parameter values (c, w, and T) in the geometric models could exist deviations from the values of the fabric samples made of yarn materials with different linear densities. Third, the yarn diameters and cross-sectional profiles before and after the knitting process might have varied because of the yarn tension caused by fabric processing, resulting in a certain deviation in the simulated values.

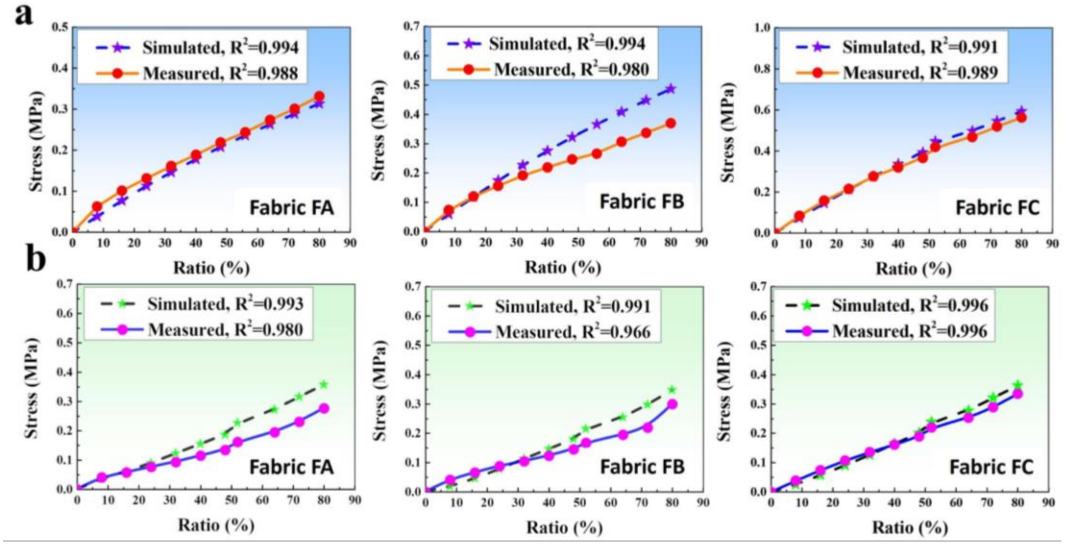

Figure 6.8 Tensile stress-strain curves of the studied LWC fabrics of FA, FB and FC along the (a) course and (b) wale directional stretches.

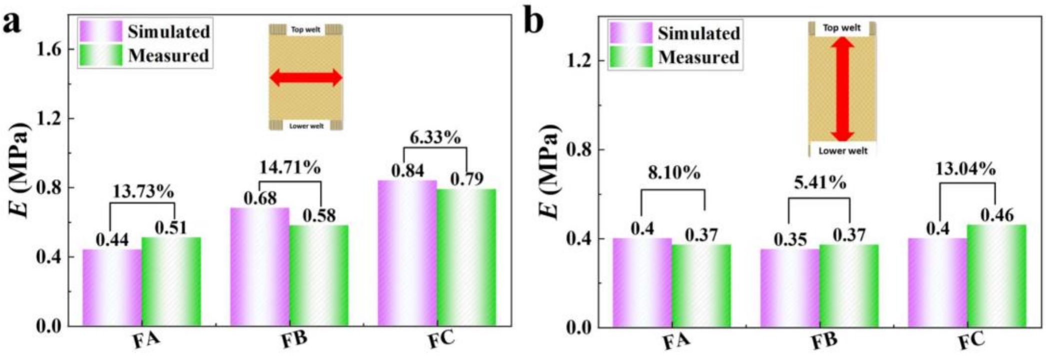

Figure 6.9 The simulated and measured Young's moduli *E* and calculated DRO values of the studied LWC samples (FA, FB, and FC) under the (a) course and (b) wale stretches, respectively.

6.4 Summary

This chapter developed a novel 3D mesoscale geometric model for LWC materials and conducted FE simulation on the structural deformation and tensile behaviors of these biomedical materials. The morphologic displacements, tensile stresses, and Young's moduli of the studied LWC fabrics, which were made of distinct inlay yarns, were numerically analyzed. The proposed 3D FE loop models effectively represented the tensile properties of the investigated fabrics in simulations. These simulations not only quantified the dynamic stress variations of the laid-in knitted loops under different tensile strains but also revealed that the ground yarns and inlay yarns played different roles in stress loading under strains along the course and wale directions. The results of this chapter provide evidence-based guidance that can be used in the appropriate selection of yarn materials for LWC fabrics to ensure that the desired mechanical properties can be achieved for these fabrics. Through the validation results (mean *DRO*: 10.22%). This chapter facilitates the design and optimization of knitted compression biomedical textiles for achieving specific pressure functions in various applications. Additionally, the proposed 3D mesoscale models would be used for the optimization of yarn materials in Chapter 7.

CHAPTER 7 PARAMETRIC OPTIMIZATION OF DESIGN VARIABLES FOR USER-ORIENTED CTS

7.1 Introduction

The quantitative relationships among the knitting settings (yarn-machinery parameters), fabric morphological characteristics, and pressure behaviors were fundamentally established by Chapter 3. However, several groups of calculated numerical yarn-machinery settings were obtained simultaneously by existing digitalized equations (Eqs. 3.10 and 3.11). Consequently, the specific available and realizable knitting settings, and corresponding applied yarn materials as well as fabric stretch ratios still need to be optimized for fabrication operation.

Further, the inherent optimization module in FE software system [163, 164] could be efficiently applied to achieve the design and determination of production parameters. Fewer studies have utilized the FE optimization module to develop and optimize the process parameters for determining the appropriate knitting materials and setting variables of 3D seamless CTs.

Therefore, to scientifically design the knitting yarn-machinery settings for development of CTs with controllable morphological profiles and pressure performances, based on Chapter 6, this chapter employed the theoretical analysis, FE parametric macro-, and meso-models to optimize the designed variables. Through the theoretical analysis models, the optimized variations (i.e. yarn combinations, fabric stretch ratios, applied body dimensions, and fabric mechanical properties) were determined for the constructions of parametric multiscale FE models (i.e. mesoscale of loop models and macroscale of leg-CT model). Then, the yarn combinations and stretch ratios were optimized for the specific knitting setting determinations of user-oriented CTs. Consequently, this chapter provides an operable approach for the optimization design variables (i.e. yarn combinations and fabric stretch ratios) of CTs and facilitates the medical effectiveness of personalized compression knits for clinic therapy.

7.2 Materials and Methods

7.2.1 Determination of Optimized Variations

- *Modified Laplace's Law model in the macroscale*

The fabric reduction factor (*FRF*) of compression materials defined as fabric stretch ratios is generated by the dimensional diversities between the fabrics and the applied bodies. According to the modified Laplace's Law (Eqs. 2.1 and 3.9) and the definition of *FRF*, the pressure values could be obtained by Eq. 7.1. In Chapter 3, the yarn-machinery settings showed no correlations with fabric thickness (*h*). The interfacial pressure (*P*) of CTs have correlations with the applied leg circumferences (Cir_{Leg}), *FRF*, and Young's moduli along the fabric course direction (E_{course}).

$$P = \frac{2\pi \times FRF \times E_{course} \times h}{Cir_{\mathrm{Leg}}} \tag{7.1}$$

- *Laid-in ROM model in mesoscale*

Elastic knitted fabrics as composite textile materials contain various yarns blended by diverse physical specifications or hybrid fiber contents for functional requirements [248-250]. Basically, the existing literature [251, 252] explored the mechanisms of knitted composites consisting of the matrix and reinforcement materials using meso-mechanical models. Especially, the rule of mixture (ROM) derived by the volume fraction of the composite constituents was adopted for the material property investigations of polymer composites [253, 254]. Thus, through the ROM, Young's modulus and Poisson's ratio of knitted composites can be determined by the combination of mechanical characteristics of each material composition through Eq. 7.2.

$$E_1 = E_g V_g + E_i V_i ; v_{12} = v_g V_g + v_i V_i \tag{7.2}$$

where the notations of *1* and *2* correspond to the 1st and 2nd principal stress directions, thus notation of *12* represents the planar defined by the 1st and 2nd principal directions. The *g* and *i* are the material compositions of matrix and reinforcement, respectively.

As shown in Fig. 7.1, the laid-in CTs are fabricated by different yarn counts (or raw material) of ground and inlay yarns. Based on the afore-introduced ROM, the whole laid-in fabric can be divided into composition cycles. For each composition cycle in laid-in knitted composites, the thicker inlay yarns are assumed as the reinforcement materials along the 1st principal stress direction. Conversely, the ground yarns are considered as the matrix materials along the 2nd principal stress direction. Therefore, the fabric mechanical properties can be obtained by laid-in ROM through the quantitative combinations of material characteristics in each composition cycle. The specific angles of θ_l are defined by the fabric course and the 1st principal stress direction based on varying machinery settings relating to the loop geometric morphology. Thus, the laid-in ROM can be expressed as Eq. 7.3.

$$\begin{aligned}
E_{course} &= [\frac{1}{E_1}\cos^4\theta_l + (\frac{1}{G_{12}} - \frac{2v_1}{E_1})\cos^2\theta_l\sin^2\theta_l + \frac{1}{E_2}\sin^4\theta_l]^{-1} \\
E_{wale} &= [\frac{1}{E_1}\sin^4\theta_l + (\frac{1}{G_{12}} - \frac{2v_1}{E_1})\cos^2\theta_l\sin^2\theta_l + \frac{1}{E_2}\cos^4\theta_l]^{-1} \\
G_{course-wale} &= [2(\frac{2}{E_1} + \frac{2}{E_2} + \frac{4v_1}{E_1} - \frac{1}{G_{12}})\cos^2\theta_l\sin^2\theta_l + \frac{1}{G_{12}}(\cos^4\theta_l + \sin^4\theta_l)]^{-1}
\end{aligned} \tag{7.3}$$

where the $G_{course\text{-}wale}$ presents the shear modulus along the fabric course and wale direction. θ_l is the angle contained by the 1st principal direction and *x-axis* (fabric course direction).

Thus, through Eqs. 7.2 and 7.3, the mechanical characteristics of ground and inlay yarns, as well as the loop geometric morphology, have influences on the tensile properties of laid-in knitted CT fabrics.

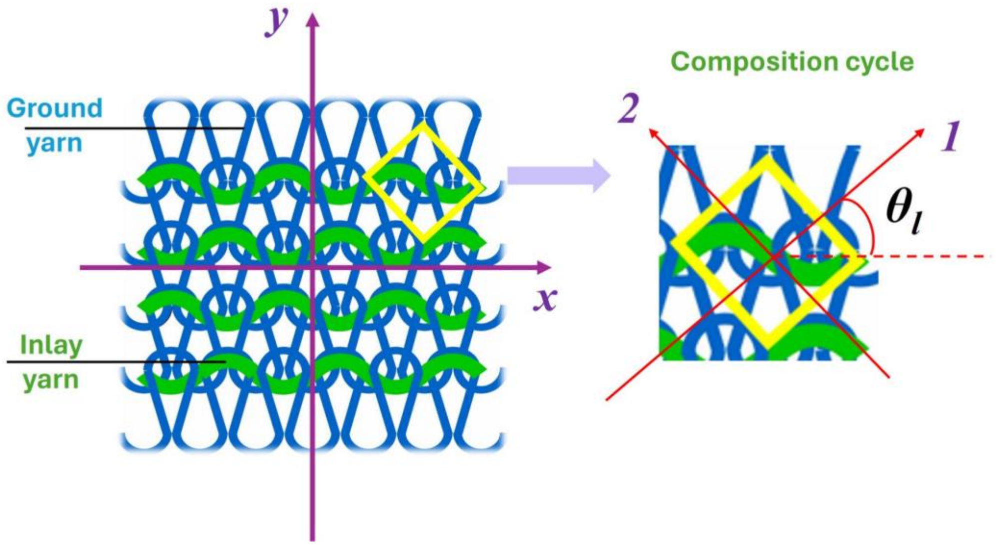

Figure 7.1 Theoretical analysis models of the laid-in ROM for CTs.

7.2.2 Design Principle of Knitting Settings

Through the macroscale modified Laplace's Law and mesoscale laid-in ROM model, the circumferences of applied bodies, fabric Young's modulus, *FRF*, mechanical properties of elastic yarns, as well as loop geometric characteristics were determined for the optimization of CTs. According to Chapter 6, for laid-in CTs, inlay yarns with different material mechanical properties caused by various physical specifications showed significant influences on fabric course tensile elastic modulus (E_{course}) by acting as the main stressed yarn materials during stretching states. Therefore, identical ground yarn (GY) with various linear densities of inlay yarns (YA, YB, and YC) were used as three types of yarn combinations for CT fabrication. In this chapter, tubular fabrics with diverse physical dimensions and mechanical tensile properties were prepared by the professional 3D seamless cylinder knitting machine (LONATI LA-45 ME, Francesco Lonati, Brescia, Italy) through adjustments of machinery settings. Detailly, as presented in Chapter 2, loop size settings (SMT; range: 500-850 mm) correlated with fabric E_{course} and pressure magnitudes caused by different mesoscopic loop geometric characteristics. In addition, the feeding velocities (PYF; range: 550-1300 m/min) of inlay yarn determine the fabric circumferences and thus control the pressure values by varying FRF relating the dimensional differences between the fabric circumferences (Cir) with applied body girths (Cir_{Leg}).

Therefore, four knitted tubular samples were prepared for the investigation of fabric properties as the optimization of initial input knitting parameters. Knitted samples F1 and F2 were generated by applying different loop size settings. Knitted samples F1, F3, and F4 were fabricated using various inlay yarns with the same mesoscopic loop geometric parameters. The applied yarns and corresponding characteristics are listed in Table 3.1. The designed knitting parameters and tested material physical-mechanical characteristics are shown in Table 7.1.

Table 7.1 Sample codes and measured properties of tubular fabrics

Fabric code	Yarn combination		Loop size settings (mm)	Stitch density (stitches/cm^2)	Mass density (Kg/m^3)	E_{course} (MPa)
	Ground yarn	Inlay yarn				
F1	GY	YA	500	416.17	524.78	0.61
F2			850	364.20	468.19	0.22
F3		YB	500	415.03	528.02	0.76
F4		YC		414.99	524.29	1.17

** Feeding velocities of inlay yarns for all knitted samples were 1250 m/min.*

7.2.3 Optimization of Design Variables by FE Parametric Models

The knitting parameters for the mechanical properties of elastic yarns and fabrics, knitted loop characteristics, and *FRF* for different leg circumferences were the designed variables, to achieve the optimizations of CT properties with various morphological profiles and pressure performances. The geometric mesoscale and macroscale models were established by applying the ANSYS Workbench Design Modeler software (v19.2, ANSYS, Pennsylvania, Pittsburgh, USA). The compression levels, measurement guidance, and circumference ranges of lower extremity, as well as fabric tensile ratios (15%-120%), were standardized based on the Germany RAL-GZ 387/1. Thus, due to the dynamic simulation and deformation requirements in actual application scenario (15%-80%), the established geometric models were imported into the LS-DYNA explicit dynamic solver for the construction of mechanical models. The design optimization module of the ANSYS inherent code was conducted for the FE parametric investigations.

- *FE macroscale parametric model*

For the macroscale model, the designed variables included applied body dimensions (Cir_{Leg}), *FRF,* and fabric mechanical properties (E_{course}) for the optimizations of CT pressure values. Through the standardized compression levels and residual pressure ratios at the ankle position (as shown in Fig. 7.2 (a) and (b)), the calculated pressure magnitude ranges of each leg point are listed in Table 7.2. The quantitative equations were established by leg mannequins in Chapter 3, thus, for a quick calculation, the heights of the wooden regional leg model with circular sectional profile and the applied tubular CTs for targeted body parts were simplified and constructed with 30 cm and 10 cm, respectively (Fig. 7.2 (c)). To promote the optimization of CT stretched states, the dimensional diversities between the fabric and each leg part were applied for the achievements of different *FRF* settings. Based on the referred circumferential dimensional ranges and corresponding tensile ratio requirements (from the stretched ratio of 15%), the initial fabric *Cir* for the lower limb B and C parts were 15.7 cm and 24.0 cm, respectively (calculated by Eq. 3.4). For the mechanical system, the wooden leg models were assumed as the isotropic elastic materials with Young's modulus of 1000 Pa, and Poisson's ratio of 0.4 [255]. Through the explorations of section *7.2.2*, E_{course} of fabric samples generated by various yarn-machinery knitting settings for macroscale optimization ranged from 0.22 MPa to 1.17 MPa (Table 7.1). Further, the employed mesh types, mesh sizes (Fig. 7.2 (d)), and contact properties were performed as presented in Chapter 5. To ensure the exact deformation and stretch evenly by the wooden leg model along the transverse direction, the boundary condition was determined as the longitudinal sliding displacement (approximately 60.2 cm) of CT for pressure behavior simulation. Moreover, to simplify the optimization process, B and C parts were determined as the studied positions, and then according to the circumferential ranges and stocking profile requirements (Fig. 7.2 (b)), the *FRF* values of B1 and D parts could be obtained.

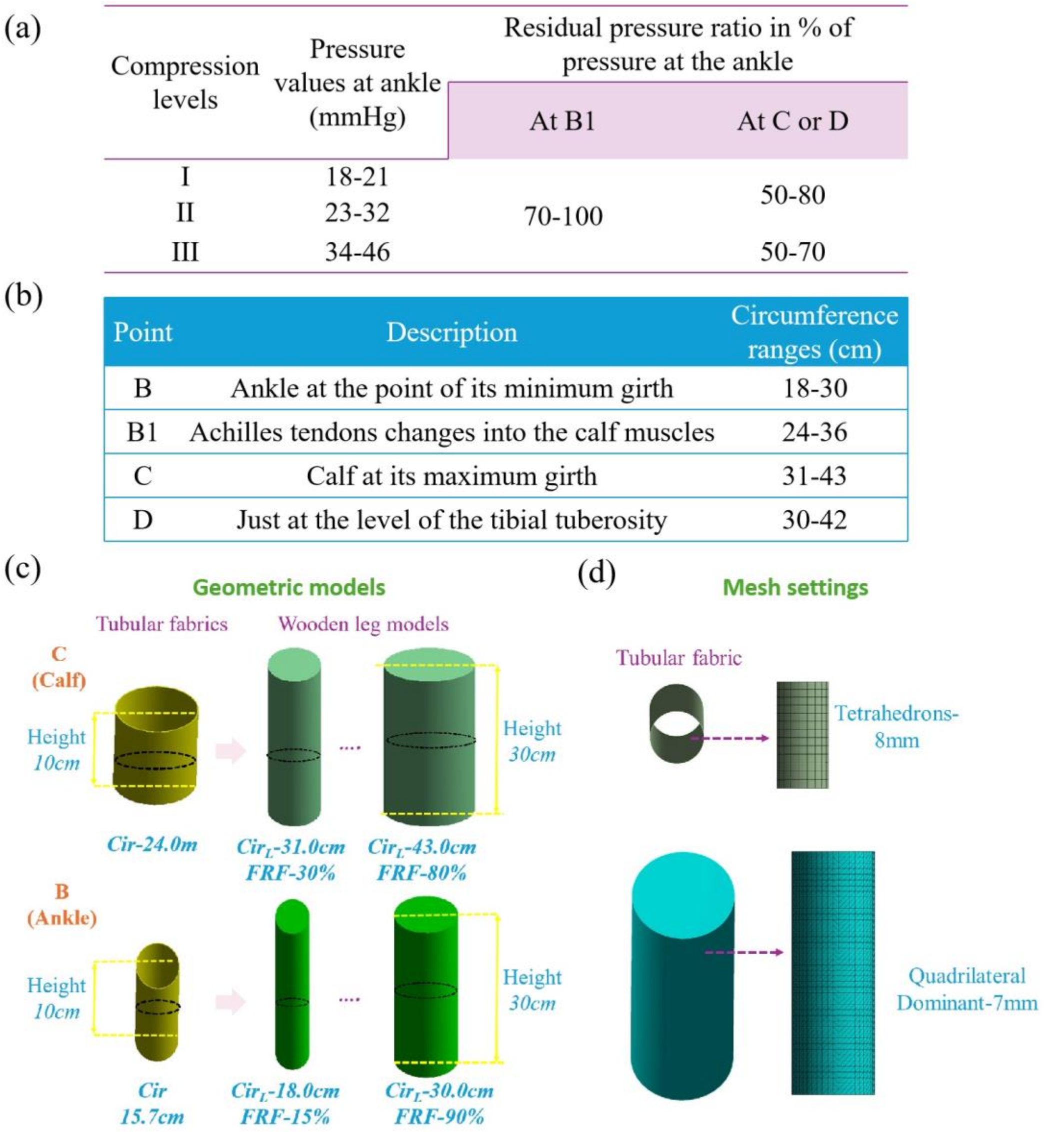

(a)

Compression levels	Pressure values at ankle (mmHg)	Residual pressure ratio in % of pressure at the ankle	
		At B1	At C or D
I	18-21	70-100	50-80
II	23-32		
III	34-46		50-70

(b)

Point	Description	Circumference ranges (cm)
B	Ankle at the point of its minimum girth	18-30
B1	Achilles tendons changes into the calf muscles	24-36
C	Calf at its maximum girth	31-43
D	Just at the level of the tibial tuberosity	30-42

Figure 7.2 (a) Compression residual ratios at the ankle position and (b) leg circumferences from the German standard of RAL-GZ 387/1. (c) Constructed geometric models for different *FRF* settings. (d) Mesh settings for FE macroscale parametric models.

Table 7.2 Pressure values calculated through the standardized residual pressure ratios

Compression level	Pressure magnitude ranges at each leg position (mmHg)			
	B	B1	C	D

I	18-21	16.2-18.9	11.7-13.7	10.8-12.6
II	23-32	20.7-28.8	15.0-20.8	13.8-19.2
III	34-46	30.6-41.4	22.1-29.9	20.4-27.6

Note: the applied residual pressure ratios of B, B1, C, and D were 100%, 90%, 65%, and 50%, respectively.

- *FE mesoscale parametric model*

For mesoscale model, to facilitate the material selections for CTs through the optimization of fabric mechanical properties (E_{course}), the designed variables were yarn combinations with different Young's moduli of inlay yarns and laid-in geometric characteristics through various parametric machinery loop size settings. Firstly, 3D laid-in geometric and FE mechanical loop models were constructed as referred to Chapter 6 through the investigations of knitted structural characteristics and loop realistic morphologies (Fig. 7.3). The defined geometric parameters were obtained by the mesoscopic observed values of samples F1 and F2 from Table 7.1. Thus, based on the practical stretched ratios of CTs, the loop displacements were 2.50 mm and 3.78 mm as the boundary conditions for SMT settings of 500 mm and 850 mm, respectively.

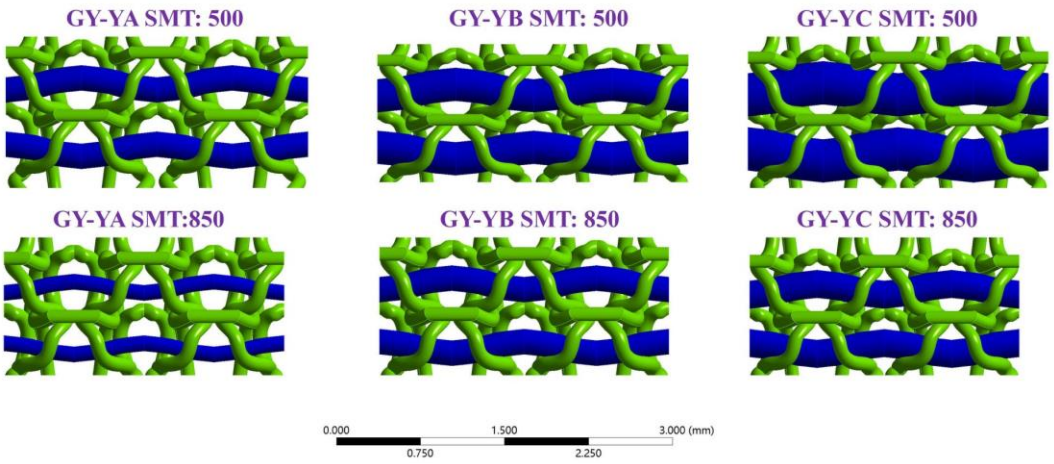

Figure 7.3 Established laid-in geometric loop models with different yarn combinations and loop size settings (SMT; unit: mm)

7.3 Results and Discussion

7.3.1 Optimized Variations of Fabric Properties for CTs

According to the modified Laplace's Law and FE parametric macroscale models, the optimized *FRF* and material Young's modulus for leg positions (B and C) with various circumferential dimensions were obtained as listed in Table 7.3. According to the optimized data, the *FRF* values were only determined by corresponding Cir_{Leg} ranges. For instance, the *FRF* of the calf position was less than that of the ankle due to the anatomic morphological characteristics of the average circumference values. Thus, the sizes of commercial compression products even for different pressure generations also depend on the user's body dimensions to facilitate the wearing process based on the biological leg profile. Moreover, compression levels were determined by varying fabric elastic modulus with identical circumference of applied body and fabric stretched deformation. Due to the required degressive compression gradient, the pressure magnitudes and fabric E_{course} were reduced from the B to the C parts generally. Therefore, the optimized results of different lower limb parts were decided by their specific dimensions and pressure needs for practical development.

Table 7.3 Optimized design variables for each pressure level at different leg positions

Leg position	Cir_{Leg} (cm)	E_{course} (MPa)	*FRF* (%)	Compression levels
B (ankle)	18-30	0.35-0.38	20-35	I
		0.47-0.61		II
		0.66-1.17		III
C (Calf)	31-43	0.22-0.38	35-80	I
		0.33-0.47		II
		0.38-0.89		III

Through the laid-in ROM and FE parametric mesoscale models, Fig. 7.4 and Table 7.4

show the stress-strain curves and fabric Young' modulus values obtained based on the different loop morphologies of each yarn combination, respectively. The linear density of inlay yarns have positive correlations with fabric E_{course}. Young's modulus of tubular fabrics made by yarn combination of GY-YC could range from 0.61MPa to 1.17MPa with various loop size settings. Nevertheless, the compression knits generated by GY-YA could only achieve E_{course} of 0.22MPa to 0.61MPa. Therefore, for the development of CTs, the applications of yarn materials were determined by fabric mechanical tensile properties to achieve the compression requirements of CT.

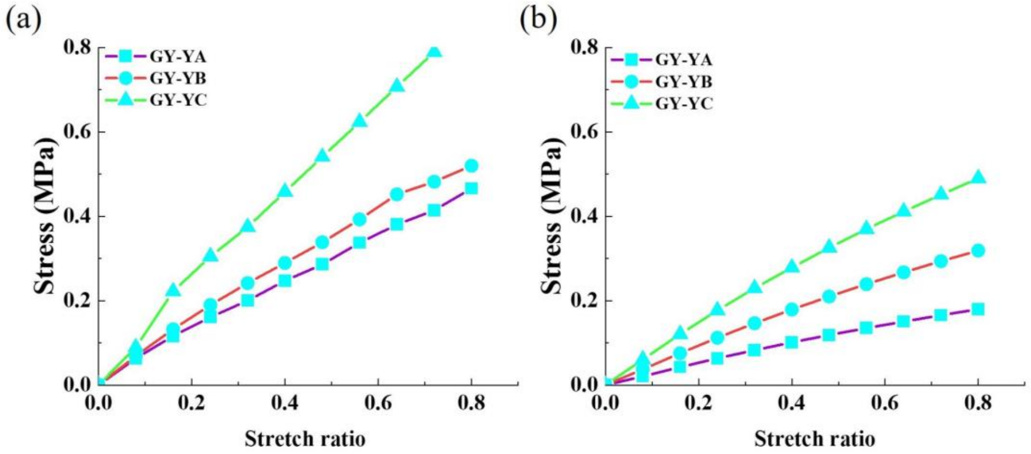

Figure 7.4 Stress-strain curves of CTs with loop size settings (SMT) of (a) 500 mm and (b) 850 mm.

Table 7.4 Optimized design variables for fabric tensile properties

Yarn material combination	Loop size setting ranges (mm)	E_{course} (MPa)
GY-YA	500-850	0.61-0.22
GY-YB	500-850	0.76-0.41
GY-YC	500-850	1.17-0.61

7.3.2 Designed Knitting Variables of CTs

Based on the efficiency fabrication principle, the applied yarn combinations were identical for each knitted part of CTs. To facilitate the development of CT products, based on Fig. 7.2 (b) and Table 7.2, through the optimized results of ankle and calf parts, the *FRF* values and yarn combinations of brachial (B1) and knee (D) positions were obtained for each pressure level (as listed in Table 7.5). Thus, through the practical user leg circumferences and needed pressure levels, the optimized *FRF* and applied yarn combinations could be guided for CT design. Then the machinery settings, such as the feeding velocities of inlay yarn and loop size settings, could be calculated by the digitalized equations as presented in Chapter 3 for the fabrication of user-oriented CTs.

Table 7.5 Optimized yarn combinations and *FRF* at each studied leg position

Leg position	Cir_{Leg} (cm)	Compression levels	*FRF*	Yarn combinations
B (Ankle)	18-30	I	20%-35%	GY-YA
		II		GY-YB
		III		GY-YC
B1 (Brachial)	24-36	I	25%-45%	GY-YA
		II		GY-YB
		III		GY-YC
C (Calf)	31-43	I	55%-80%	GY-YA
		II		GY-YB
		III		GY-YC
D (Knee)	30-42	I	50%-75%	GY-YA
		II		GY-YB
		III		GY-YC

7.4 Summary

This chapter optimized the design variables for development of user oriented CTs through the theoretical analysis and FE multiscale parametric models. Based on the modified Laplace's Law and laid-in ROM models, the *FRF*, E_{course}, and mechanical properties of inlay yarns were determined as optimized variations. The design variables were optimized by the FE macro- and meso- parametric models. The applied yarn combinations and fabric stretch ratios were recommended according to the compression levels and leg circumferences. Thus, based on the proposed digitalized equations in Chapter 3, the specific knitting settings could be calculated for the user-oriented CT development.

CHAPTER 8 DEVELOPMENT OF CUSTOMIZED CTS WITH ERGONOMIC WEARING COMFORT

8.1 Introduction

Chapter 3 proposed the digitalized fabric morphological and pressure equations through the leg mannequin measurements with circular sectional profiles and rigid material properties. Simultaneously, the obtained several groups of calculated numerical settings need to be optimized for CT fabrication. Thus, Chapter 4 and Chapter 5 quantified the influences of body morphological characteristics and tissue stiffness on pressure performances of CTs, and Chapter 6 and Chapter 7 optimized the design variables by theoretical analysis and multiscale parametric models. Therefore, the pressure fitness and precise management of CTs could be achieved through individual biological characterization, redistribution of pressure values, and digitalization of knitting settings. Consequently, in this chapter, to improve the custom fit and EWC for physical compression therapeutic modalities, personalized CTs were developed with individual functional requirements and subjective comfortable perceptions. Through 3D reconstruction and body characterization, the geometric and morphological variations of lower limbs were obtained as the bio-design strategies for the determination of digitalized knitting settings. After 3D advanced seamless fabrication, the pressure performances and EWC of CTs were evaluated by the proposed biomechanical FE CT-leg systems and VAS assessments, respectively. The present chapter provides operable guidance for the bio-design and manufacturing of biomedical therapeutic materials with precise pressure management and enhanced wearing comfort.

8.2 Materials and Methods

8.2.1 Subject Recruitment

To verify the acceptable and availability of proposed comprehensive framework for customized CTs, three healthy subjects (code: SS1, SS2, and SS3) were voluntarily recruited at The Hong Kong Polytechnic University campus with various ages, genders, weights, leg shapes, and personal occupations. Through the CEAP criteria and clinical presentation [256], their prescribed pressure levels (SS1-Class I; SS2-Class II; SS3-Class III) for physical-based compression therapy were referred to the Germany RAL-GZ 387/1 standard (Fig. 2.1 (c)). The individual information and BMI of each subject were as follows: 1) SS1: female, age: 51 years old, height: 1.57 m, BMI: 25.6 kg/m^2; 2) SS2: male, age: 33 years old, height: 1.80 m, BMI: 17.7 kg/m^2; 3) SS3: female, age: 28 years old, height: 1.68 m, BMI: 20.6 kg/m^2.

8.2.2 Anthropometric Characterization and Optimization of Pressure Distribution

Based on the section of *4.2.1*, 3D entity lower limb models (left) of recruited subjects were reconstructed for body morphological characterization and biomechanical performance evaluation. And then, the splattering points were obtained for the further body characterization and data calculation. Through the reconstructed lower extremity models, the digitalized 2D coordinate data was processed by using the MATLAB R2016a system (MathWorks. Inc., Natick, MA, USA). Based on the randomized clinic experiments [257, 258], the below-knee length of CTs with improved wearing comfort could efficiently prevent vein thrombosis and thrombotic syndrome. Thus, four (B, B1, C and D) anatomic sites were determined as the major studied leg positions for the bio-fabrication of CTs. As shown in Fig. 8.1 (a)-(c), the leg cross-sectional biological curves were plotted by the sequential scattering points ((x_i, y_i), $i = 1,2, \ldots, n$) for geometric calculation and shape recognition. Further, the curvature radii (R_1, R_2, ..., R_n) and curvatures ($\frac{1}{R_1}, \frac{1}{R_2}, \ldots, \frac{1}{R_n}$) of each slice were obtained by applying the Inline function, and dimensional circumferences (Cir_{Leg}) of the subject's lower limbs were calculated through $Cir_{Leg} = \sqrt{\sum_{i=1}^{n} (x_{i+1} - x_i)^2 + (y_{i+1} - y_i)^2}$ (Fig. 8.2 (a)). In Chapter 4, the insufficient pressure supply caused by biological irregular shape diversities was optimized by the redistribution development guidance. Detailly, based on the characterized SDC values of each slice, the profile irregularities of leg cross sections could be classified by our clustered IR levels. Then, referring to the recommended optimization strategies, the reshaped pressure values (P_{RS}) of each leg position for all subjects were obtained to scientifically enhance the delivered dosages of CTs. Through the standardized compression levels and gradient residual pressure ratios (Fig. 7.2 (a)), the specific expected pressure magnitudes (P_{EX}; averaged by the corresponding pressure level ranges) were designed as illustrated by Fig. 8.2 (b). Therefore, the required pressure values (P_{RQ}; $P_{RQ}=P_{EX}+P_{RS}$) were obtained as the functional individual requirements for the further knitting variable design of CTs and achievements of precise compression management. For instance, for the B position of subject SS1, the calculated

SDC value and corresponding IR level were 1.25 and 2, respectively. Thus, through the reshaped P_{RS} of 5mmHg and expected P_{EX} of 20mmHg, the practical P_{RQ} dosage was optimized as 25mmHg for CT manufacturing.

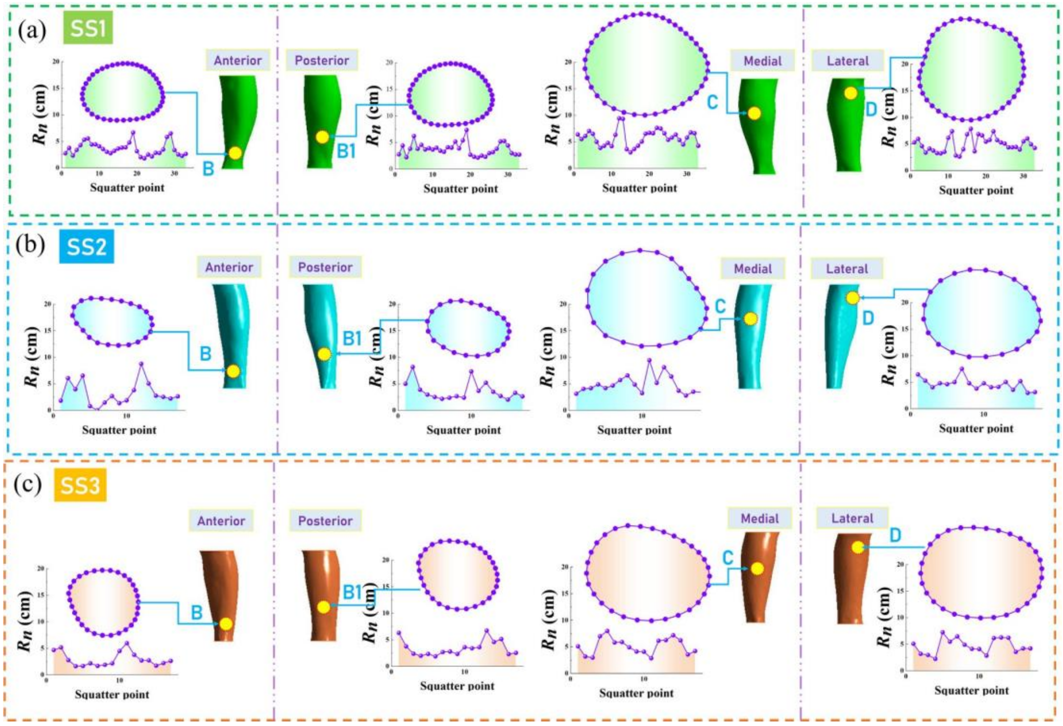

Figure 8.1 The reconstructed lower extremity models and plotted biological curves as well as the corresponding curvature radii of studied cross-sectional slices for subjects (a) SS1, (b) SS2, and (c) SS3, respectively.

8.2.3 Bio-Digital Design and Fabrication of Customized CTs

In this chapter, three yarn combinations of GY−YA, GY−YB and GY−YC were applied for the fabrication of personalized CTs with various material mechanical property requirements (Fig. 8.2 (c)). The circular seamless CTs were developed by the 1×1 laid-in weft-knitted structure through 3D LONATI LA-45 ME advanced medical knitting machine (Francesco Lonati, Brescia, Italy). To effectively design the yarn and machinery variables, the quantitative relationships between the fabric circumferences (*Cir*; cm) and pressure values (P_{RQ}; mmHg) were fitted by our previous explorations through Eqs. 3.10 and 3.11, respectively. Thus, the specific applied yarn material combinations and machinery parameters for each customized CT were digitally determined. Moreover, the practical fabric course stretch ratios were referred to as the optimized *FRF* values through Table 7.6, and inlay yarn diameters were used to replace the yarn linear density to simplify the parametric calculations. Through the quantitative equations, the yarn-machinery knitting settings for each CT were obtained as listed in Table 8.1.

Table 8.1 Designed knitting settings of personalized CTs for recruited subjects

Applied user	Pressure level	Part	Yarn combinations	Inlay yarn diameter (mm)	*Cir* (cm)	PYF values (m/min)	SMT values (mm)	*FRF* (%)
SS1	I	B	GY−YA	0.41	17.60	1010	700	25
		B1			19.92	1150		
		C			22.22	1300	850	67
		D			21.94	1280	750	60
SS2	II	B	GY−YB	0.42	15.67	840	550	20
		B1			16.48	890	700	22
		C			20.38	1130	750	56
		D			20.13	1120	850	50
SS3	III	B	GY−YC	0.47	16.37	620	700	24
		B1			18.41	740		26
		C			20.68	890	850	61
		D			21.16	920		55

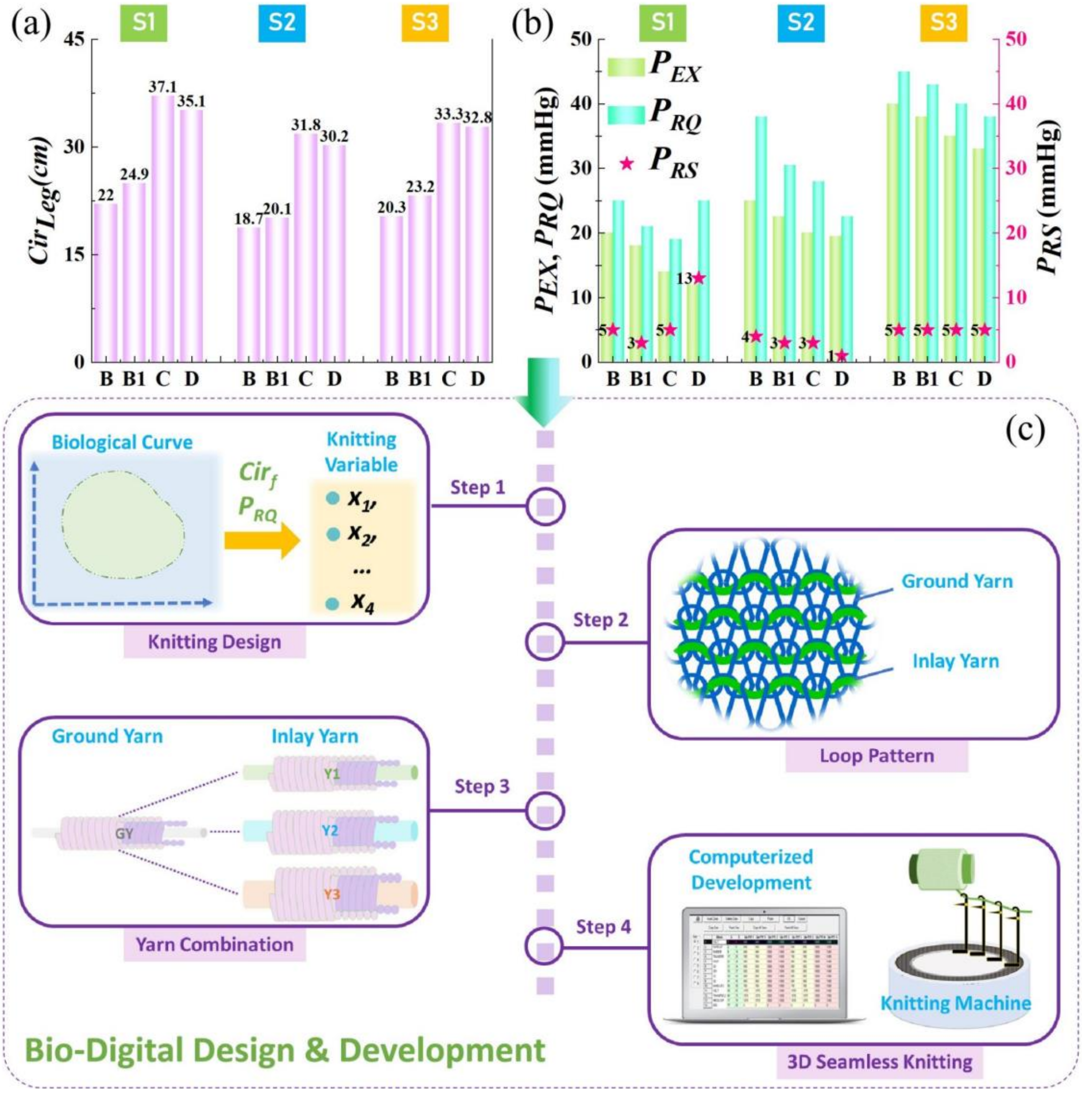

Figure 8.2 (a) The leg dimensional circumferences were characterized as the basic size design strategy for development of personalized CTs. (b) The practical pressure magnitudes of each leg position for each subject were determined by their expected and reshaped pressure dosages. (c) The bio-digital design and development of personalized CTs.

8.2.4 Construction of User-Specific Biomechanical Modelling

The 3D FE CT-leg biomechanical modelling was established to visually evaluate the pressure performances of personalized CTs, as illustrated by Fig. 8.3 (a). Based on the experimental investigations (sections of *3.2.3* and *6.2.1*), the corresponding values of fabric mass density, E_{course}, E_{wale}, v, G, were imported into the CT-leg system as the inputting material characteristics. Moreover, through Chapter 5, the biomaterial ST stiffness showed no correlations with pressure performances of CTs, thus, the determined tissue properties (C_{10}) were 0.003 MPa for each FE system. The longitudinal displacements (SS1: 34cm; SS2: 44cm; SS3: 36cm) of CTs were determined as the boundary conditions of biomechanical system for pressure behavior visualization. Moreover, to estimate the acceptability of proposed FE models, the validation study was conducted to compare the simulated and tested *P* values by in vivo measurements by the Picopress$^{@}$ pressure tester.

8.2.5 Experimental Protocol and Data Analysis for EWC Evaluation

To evaluate the subjective EWC of designed customized CTs, the VAS assessments were applied to estimate the movement ability and comfortable sensation by wearing trials. Participants were instructed to wear the personalized CTs in a controlled standard environment (temperature of 25±1 °C and relative humidity of 70±5%; ASTM D1776-04) for 24 hours to achieve the equilibrium status prior to use. Detailly, three phases were included to simulate the practical application scenarios [259] (Fig. 8.3 (b)): i) phase I: 10-min test in a sitting position for the stabilization of CTs and acclimatization; ii) phase II: 10-min static standing for active recovery; iii) phase III: 10-min walk at a speed of 5 km/h as normal activity in daily life. Then, the critical VAS scoring forms with ratings of 1 to 5 for the studied four leg positions were required to be filled by participants during each phase interval (5 min for each survey fulfillment) (Fig. 8.3 (c)). Moreover, the Pearson correlation tests were conducted to further investigate the relationship between the compression levels with the EWC of CTs [260]. The collected ranking scores for EWC evaluation were analyzed by the Statistical Package for the Social Sciences (SPSS) software (Version 23.0, IBM Corporation, USA). Additionally, the level of significance was set at α = 0.05 [261].

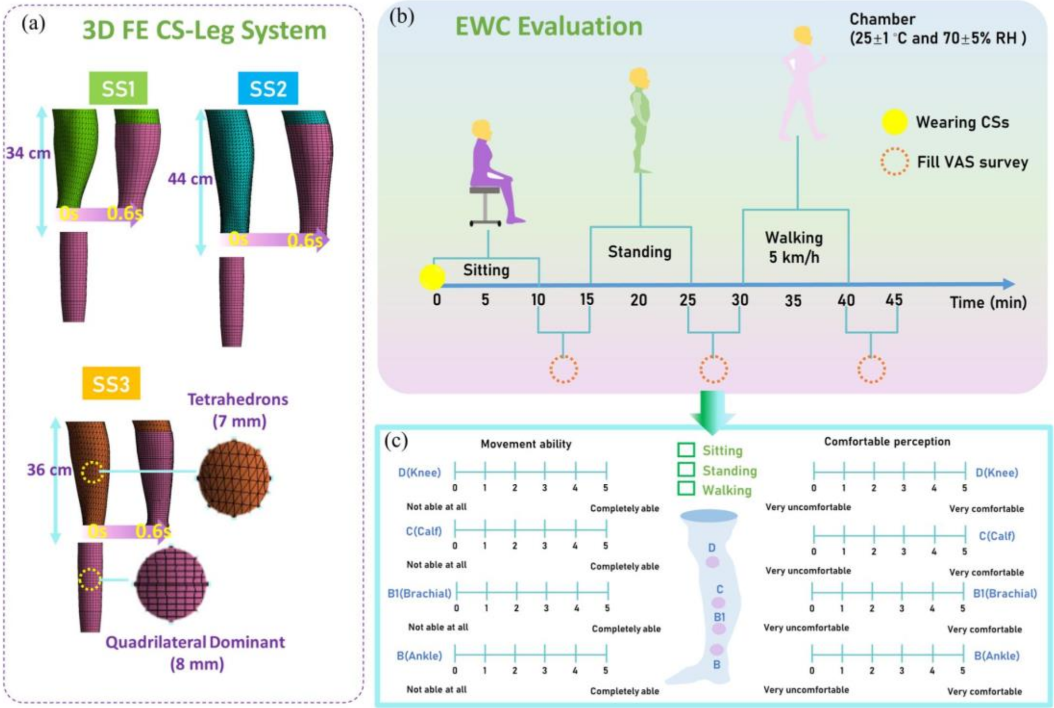

Figure 8.3 (a) The established 3D FE CT-leg systems for pressure performance visualization of recruited subjects of SS1, SS2, and SS3. (b) For estimations of the movement ability and wearing comfort, the wearing trial experimental protocol was designed, and (c) the VAS scoring was utilized for EWC evaluation of developed user-oriented CTs.

8.3 Results and Discussion

8.3.1 Physical-Mechanical Properties and Morphological Fit of Developed Customized CTs

Through the experimental sample testing, the physical-mechanical properties of each studied stocking part of developed personalized CTs were listed in Table 8.2. Firstly, as reported findings in Chapter 3, accepted for fabric *h*, the *LD* and mass density of knitted CTs varied related to the applied yarn combinations and machinery parameters [81].

Generally, fabric *LD* was decreased from the B to D stocking parts varied by the formed loop sizes through the adjustment of loop length settings (Fig. 8.4). Moreover, for different compression levels of CT shells, the increased inlay yarn diameters positively influenced the fabric mass densities. Secondly, as shown in Fig. 8.5 (a), the mean error ratio of fabric *Cir* between the designed and fabricated CTs was approximately 3.87±3.70%. Thus, the stocking dimensions could achieve the basic size fitness for each subject [150]. Thirdly, for the mechanical tensile behaviors, through the physical mechanisms of the Laplace's Law, the generated compression magnitudes were fundamentally determined by the textile tensions and Young's moduli along the fabric circumferential stretched directions [262]. Therefore, the measured E_{course} values varied for material mechanical requirements caused by the designed loop length settings and applied yarn combinations. Detailly, as illustrated in Fig. 8.5 (b), the knitted samples (yarn combination: GY−YC) for compression of Class III could generate higher material tensions under the identical uniaxial stretched ratios. Thus, the applied inlay yarn thickness could positively impact the material mechanical stiffness for required pressure generations.

During wearing process, the stretched CTs were provided sustainable tensions for interfacial pressure generations [263]. The corresponding fabric tensile ratios were determined by the dimensional diversities between CTs and applied biological bodies. For readymade commercial CTs, the fabric *Cir* of each part was designed by various manufacturers for extensive user groups. Nevertheless, the provided size tables and recommended selections could not simultaneously conform to the leg morphological variables. The oversized CTs could not generate required pressure dosages along lower extremities, conversely, the undersized CTs may lead to excessive compressions, unexpected tourniquet effect, and wearing discomfort [94]. Thus, based on the 3D body scanning and reverse engineering technologies, biological geometric circumferences and morphologic profiles of each subject were characterized by the obtained anthropometric data. Through the calculated Cir_{Leg} values and standardized stretch ratios (15%−120%) [262], the *Cir* of each part for user oriented CTs were achieved through the designed yarn-machinery knitting settings. Therefore, the customized CTs based on individual leg geometric parameters could facilitate the achievements of pressure precision and user adherence [264].

Table 8.2 Measured fabric physical-mechanical properties of fabricated CTs

Applied user	Part	Physical properties			Mechanical properties			
		h (mm)	LD (stitches/cm^2)	mass density (g/m^2)	E_{course} (MPa)	E_{wale} (MPa)	v	G (MPa)
SS1	B	0.63	426.72	481.27	0.38	0.21	0.20	0.16
	B1	0.63	426.72	481.13	0.37	0.21	0.20	0.16
	C	0.65	416.37	468.19	0.33	0.15	0.21	0.14
	D	0.63	406.33	481.27	0.37	0.19	0.20	0.15
SS2	B	0.62	414.03	510.20	0.57	0.34	0.20	0.24
	B1	0.62	349.98	529.95	0.43	0.23	0.22	0.18
	C	0.62	345.16	503.62	0.42	0.18	0.22	0.17
	D	0.64	341.64	481.51	0.41	0.17	0.23	0.17
SS3	B	0.64	305.74	532.74	0.76	0.27	0.25	0.30
	B1	0.64	302.58	532.55	0.75	0.27	0.25	0.30
	C	0.65	302.10	521.61	0.61	0.19	0.27	0.24
	D	0.65	300.48	521.51	0.60	0.19	0.27	0.26

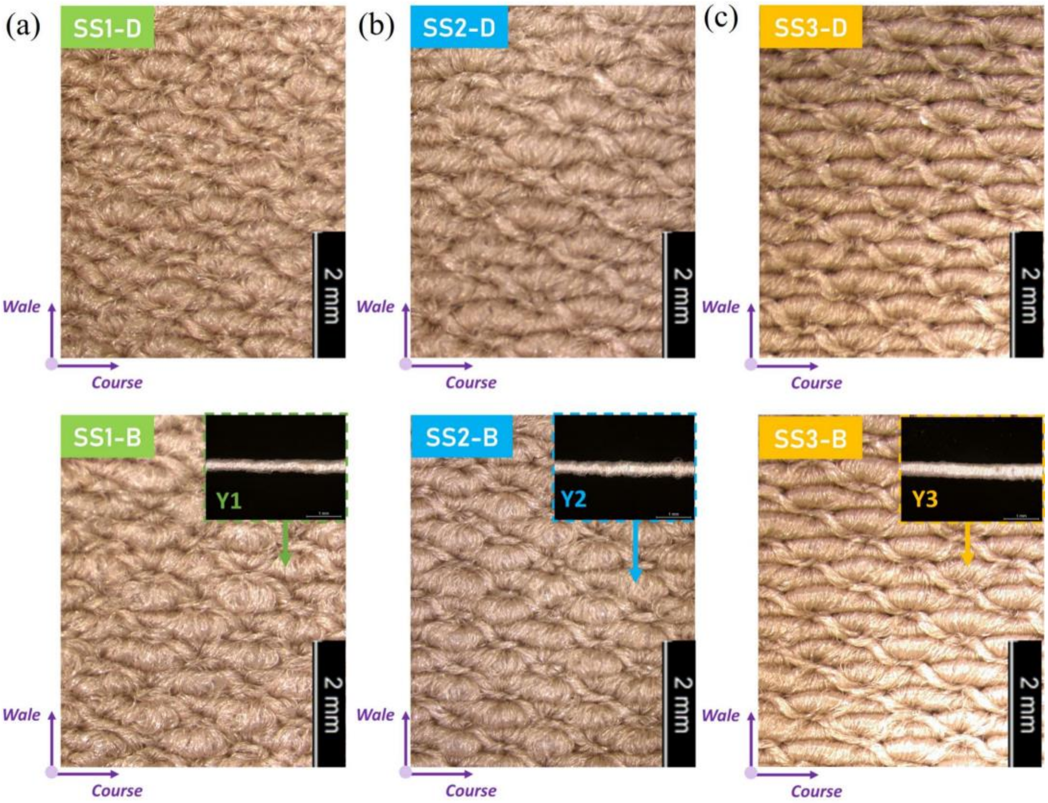

Figure 8.4 The microscopic images of developed knitted CT samples (B-ankle, D-knee) for subjects (a) SS1, (b) SS2, and (c) SS3, respectively.

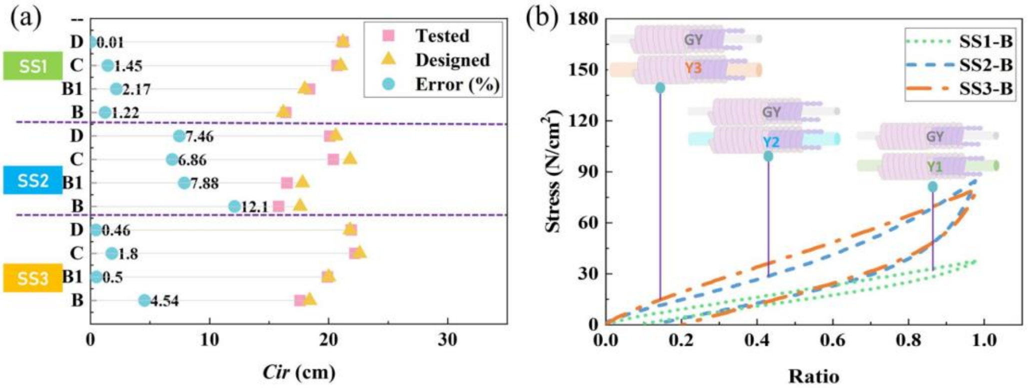

Figure 8.5 (a) Fabric morphological comparisons between the designed and fabricated personalized CTs. (b) Mechanical tensile behaviors of knitted CT samples (stocking part of B) with various yarn combinations along the fabric course (circumferential) stretching direction.

8.3.2 Validation of Proposed User-Specific FE CT-Leg System

To validate the prediction precision and acceptability of proposed user-specific FE modelling, the measured and simulated pressure values of each CT were compared as shown in Fig. 8.6. For example, the tested pressure magnitudes at the leg positions of B, B1, C and D for subject SS1 were approximately 19.49±3.27 mmHg, 18.75±2.18 mmHg, 19.91±2.85 mmHg and 14.42±3.59 mmHg, respectively (Fig. 8.6 (a)). Similarly, the simulated pressures were about 22.84±5.41 mmHg, 23.67±6.42 mmHg, 16.55±7.71 mmHg and 12.41±4.48 mmHg, respectively. For the customized CTs prepared for subject SS3, the prediction error ratios for studied lower limb positions of B, B1, C and D were 8.43%, 4.73%, 1.42% and 1.68% (Fig. 8.6 (c)), respectively. Through calculations, the averaged error ratio of established FE CT-leg modelling was approximately 11.00±7.78%. Furthermore, the Pearson test results showed that the measured results had significant correlations (p (*Sig.*) <0.01, ρ= 0.96) with the simulated data (Fig. 8.6 (d)). Thus, the constructed FE mechanical modelling with user morphologic characteristics and biomechanical properties could be accurately utilized for the pressure prediction and mapping visualization of CTs.

Previously, the pressure evaluations were commonly performed by the instrumental sensor devices in vivo testing. However, for biological bodies, due to the individual anatomic structural characteristics, the irregular interfacial body surfaces and sectional curvatures could lead to uneven and insufficient pressure generations. Thus, the obtained regional magnitudes could not reflect the practical pressure profiles distributed by the applied CTs. Moreover, in relevant compression simulation models, the pressure performances, biomechanical transmission behaviors of internal tissue stress, and venous hemodynamics could be simulated by constructed 3D modelling. Nevertheless, their geometric body models were established by extensively scanned slices through the

MRI or CT. For our proposed FE system, through the 3D body scanning and reconstructed lower extremity models, the visualization of pressure performances could be efficiently achieved. Additionally, the predicted errors of existed models were ranged from 6.0% to 21% [126, 194]. Therefore, the constructed FE CT-leg system could be applied for the pressure performance evaluation and material property optimization with acceptable accuracy and simulation efficiency.

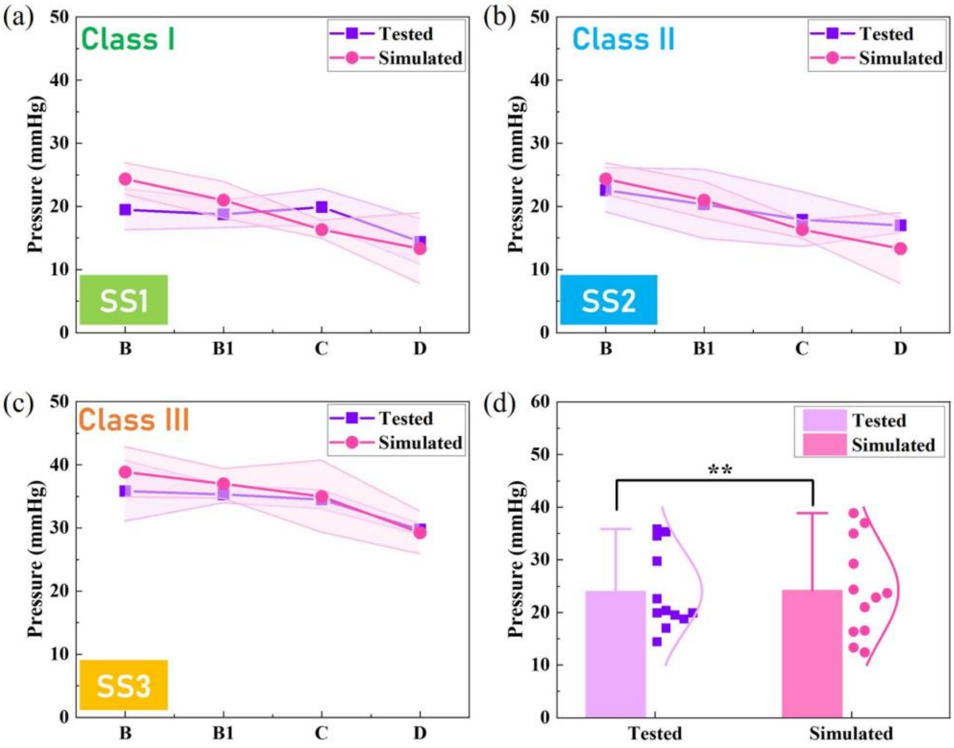

Figure 8.6 Experimental measurement results and simulated data by FE CT-leg systems for subjects (a) SS1, (b) SS2, and (c) SS3, respectively. (d) Pressure comparisons and data correlation between the tested and simulated values of prepared customized CTs. (**: $p < 0.01$: significant correlation).

8.3.4 Pressure Performance Evaluation of Developed Customized CTs

Through the proposed 3D FE modelling, the pressure mappings exerted by developed CTs along the lower extremities of each subject were visualized as shown in Fig. 8.7.

Generally, the gradient pressure distributions were degressively from the distal to the proximal regions generated by customized CTs through the development processes. Further, to evaluate the pressure fitness of CTs, the expected compression exertions (P_{EX}) and practical pressure values (P) were compared as shown in Fig. 8.8. Detailly, referred to the Germany standard, subject SS1 expected compressions (Class I) were ranged from 18 mmHg to 21 mmHg, the tested pressure dosage at the leg B position was 19.49±3.27 mmHg (Fig. 8.8 (a)). For subjects SS2 (Fig. 8.8 (b)) and SS3 (Fig. 8.8 (c)), the delivered interfacial pressures were 23.59±3.51 mmHg and 35.84±4.80 mmHg, respectively. Moreover, through the correlation analysis, the tested P data had good agreements (p (*Sig.*) <0.01, $\rho = 0.97$) with the designed P_{EX} values (Fig. 8.8 (d)), and the mean pressure error ratio was 10.08±7.75%. Therefore, the developed personalized CTs could achieve pressure fitness and medical therapeutic functions for applied users with various requirements.

Moreover, in previous studies [174], customized CTs were developed according to the measured *Cir* values and expected pressure levels. The pressure error ratios between the designed and practical tested values were approximately 5%−52% [265]. However, in the development process, their referred quantitative relationships between the yarn-machinery variable with pressure values were fitted through the leg mannequin measurement with ideal circular cross-sectional profiles. Thus, in the present chapter, to promote pressure fitness, the insufficient compression exertions caused by individual irregular leg shapes were improved scientifically based on the reshaped bio-design guidance. Through the performance evaluated results, the compression levels and gradient distributions of each developed CT conform to the Germany standard (SS1-Class I; SS2-Class II; SS3-Class III; Fig. 2.1 (c)) and specific pressure prescription. Thus, the proposed bio-design and development strategies could be utilized for the manufacturing of CTs with extensive personal requirements in healthcare, medical, and rehabilitation domains [266].

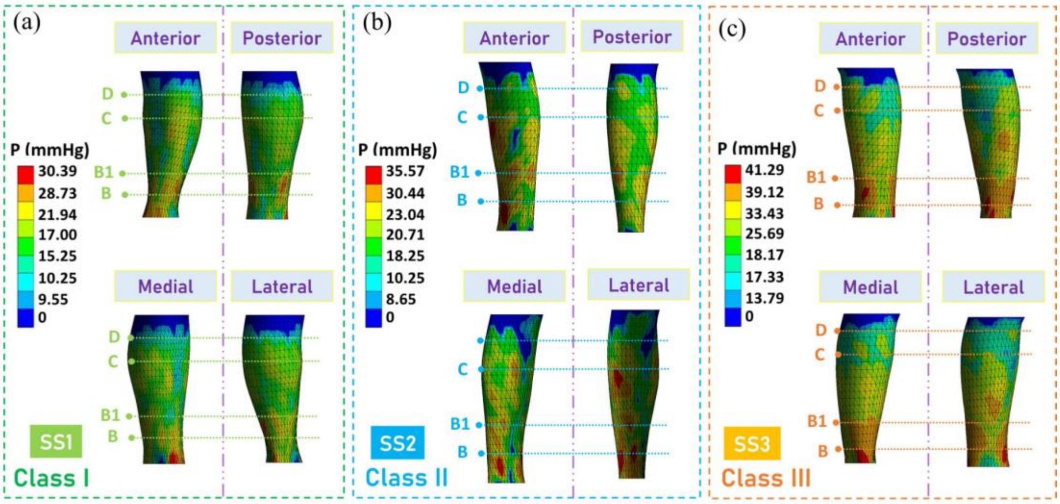

Figure 8.7 Pressure profile mappings of FE CT-leg modelling systems for subjects (a) SS1, (b) SS2, and (c) SS3, respectively.

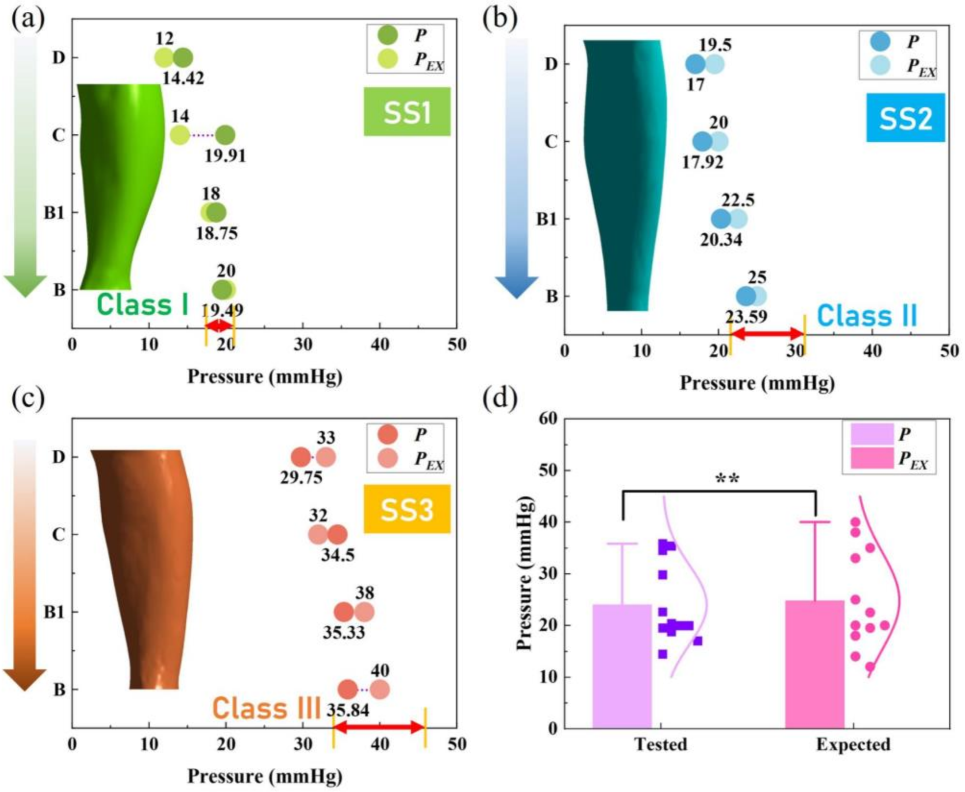

Figure 8.8 Pressure distribution evaluations of the developed customized CTs for subjects (a) SS1, (b) SS2, and (3) SS3, respectively. (d) Data comparison between the user-expected and actual tested interfacial pressure dosages of CTs (**: $p < 0.01$: significant correlation).

8.3.5 EWC Evaluation of Developed Customized CTs

The subjective VAS scoring results through the subject wearing trials for the EWC assessment of fabricated CTs were as shown in Fig. 8.9. Generally, the developed customized CTs for each subject had acceptable movement abilities and wearing comfort in practical application [87]. The elastic knitted CTs for subject SS1 had flexible mobility and comfortable perception during the sitting, standing, and walking states due to the relatively lower stocking compression of Class I (Fig. 8.9 (a) and Fig. 8.9 (c)). Thus, the fabric-stretched tensions for lower levels of pressure generation positively enhanced the EWC of therapeutic compression biomaterials. Through the correlation analysis, the generated increasing compression classes significantly decreased (*p* (*Sig.*) <0.01, ρ= -0.92) the EWC of CTs. Further, through the applied scenario comparisons, during the dynamic processes of muscular activity, fabric mechanical tensile stresses varied by leg morphological variations led to uncomfortable feeling and moveable limitations. Therefore, compared with the active walking states, the sitting and standing postures could subjectively benefit the movement ability and wearing comfort, respectively (Fig. 8.9 (b) and Fig. 8.9 (d)).

Commonly, the material design, structural development, and fabrication technique crucially contributed to the EWC for CTs. In the present study, the selection of double-covered yarn materials improved the fabric flexibility based on its excellent mechanical elastic recovery properties. Moreover, for the designed 1×1 laid-in loop pattern, the combinations of the ground and inlay yarn components could provide the basic fabric dimensional stabilities during the wearing stretching process. For the machinery parameter design, the stocking dimensional profiles and gradient mechanical material stiffness were achieved by varying the inlay yarn feeding speeds and loop length settings. Therefore, the proper material morphology, functional pressure distribution requirements, and freedom of body movement simultaneously promoted the EWC in practical application.

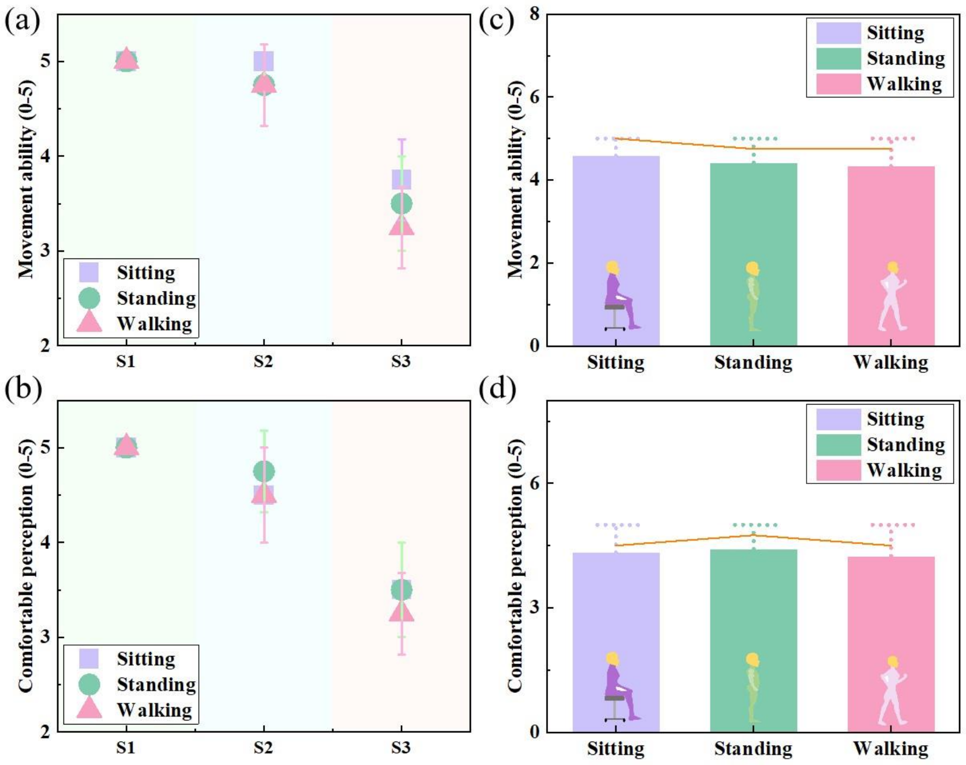

Figure 8.9 (a) Movement ability and (b) comfortable perception assessments of the developed customized CTs through various subject EWC evaluations. (c) Movement ability and (d) comfortable perception comparisons during various applied body postures.

8.4 Summary

The present chapter fabricated the personalized therapeutic CTs for needed users with individual morphological and compression requirements. Through reverse engineering technology and body anthropometric characterization, the anatomic biological profiles and geometric variables were obtained as the basic design strategies of material morphology and pressure optimization. The applied knitting yarn combinations and machinery parameters were digitally obtained for the 3D seamless fabrication. Then, through the reconstructed geometric lower extremity models and determined tissue stiffness, the user-specific 3D FE CT-leg modellings with high prediction accuracy (error ratio: 11.00±7.78%) were established for the biomechanical evaluation of pressure performances. Based on the practical wearing trials, the interfacial compressions of developed customized CTs had good agreements with the expected data (pressure error ratio: 10.08±7.75%). Moreover, through the subjective VAS assessments, the EWC of CTs had significant (p (*Sig.*) <0.01, $\rho = -0.92$) correlations with the exerted pressure levels. Thus, through the proposed bio-digital design, development, and biomechanical visualization systems, this chapter provided a comprehensive manufacturing approach for biomedical materials and promoted precise pressure management for textile-based compression therapy.

CHAPTER 9 CONCLUSIONS AND FUTURE WORK

9.1 Conclusions

In this study, the bio-digital design, development, and biomechanical visualization systems were proposed for the custom fit CTs with controllable pressure performances and comfortable perceptions for required users. The results revealed that the digitalized quantitative equations and optimized design variables could be used for the efficient functional design and performance control of user-oriented CTs. The clustered biological morphological characteristics and novel pressure model facilitated the optimization of the bio-design of CTs. The body tissue stiffness showed no correlation with the pressure performances of CTs. The established 3D FE CT-leg systems could be effectively utilized for the visualization of pressure mappings. Moreover, the subjective EWC evaluation results indicated the CTs had good moveability and comfortable perception.

To achieve the proposed six research objectives, the following studies were performed:

(i) For objective 1 (to study the effects of multiple knitting settings on fabric physical-mechanical properties and pressure performances of CTs), Chapter 3 investigated the influencing mechanisms of digitalized knitting settings on the physical-mechanical and pressure properties of CTs. This chapter determined that the feeding speed of inlay yarns and loop settings can be adjusted to control the fabric circumferential dimensions and knitting loop sizes. The inlay yarn thickness significantly affects the stitch densities and tensile properties of CT fabrics. The quantified digital models established between multiple yarn-machinery settings showed the high acceptability of the proposed digitalized development strategy for fabric morphological (DRO: 1.1%) and pressure (DRO: 10.8%) control.

(ii) For objective 2 (to investigate the body morphological variations of lower extremities on compression generations of CTs), Chapter 4 adopted 3D-BS and reverse engineering technologies to quantify and classify the curvature characteristics of cross sections for biological lower extremities. The irregular curvature variations of cross-sectional slices were classified into four levels. Simultaneously, a new pressure prediction model was established with high accuracy (mean pressure errors was 2.53±0.52 mmHg) to predict the pressure values of CTs generated along various legs. Through the clustered IR levels and pressure prediction results, the pressure gap ranges between the circular leg model and irregular bodies were obtained as the design guidance to enhance the functional pressure performances of CTs. Moreover, this chapter also indicated that the incompatible fabric stretched stress and heterogeneous deformation frequently caused the pressure value differences between applied bodies.

(iii) For objective 3 (to explore the effects of physiological tissue characteristics of lower extremities on compression generations of CTs), Chapter 5 explored the biomechanical interactions between CTs and lower extremities with various tissue material characteristics. The independent leg stiffness influences on pressure behaviors of CTs was systematically investigated through FE CT-leg simulation modelling, theoretical analysis, and experimental validation. The pressure performances of CTs showed no statistically significant differences with the applied lower limbs or leg models with various mechanical tissue properties. The leg circumferential deformations were positively increased by the external fabric tension forces. However, these displacement variations caused by varied biomaterial stiffness could not lead to regular changes in pressure distributions.

(iv) For objective 4 (to construct the mesoscale modelling for loop component simulation and yarn material determination of CTs), Chapter 6 established the novel 3D mesoscale geometric and FE models for 1×1 laid-in loop structures based on real loop characteristics to visually and quantitatively analyze the stress-strain properties of LWC materials. The results revealed that the ground yarns and inlay yarns played different roles in stress loading under strains along the course and wale directions. Through the validation results (mean error ratio: 10.22%), the proposed 3D mesoscale models could be used for the optimization of yarn materials.

(v) For objective 5 (to optimize the design variables through multiscale theoretical analysis and parametric models for CTs, Chapter 7 employed the theoretical analysis, FE parametric macro- and meso-models to optimize the designed variables. Based on the modified Laplace's Law and laid-in ROM models, the *FRF*, E_{course}, and mechanical properties of inlay yarns were determined as optimized variations. The design variables were optimized by the FE macro- and meso- parametric models. The applied yarn combinations and fabric stretch ratios were recommended according to the required compression levels and leg circumferences.

(vi) For objective 6 (to build a realization system for a digitalized design-development-evaluation framework of functional CTs with custom fit and EWC), Chapter 8 fabricated the personalized therapeutic CTs for needed users with individual fabric morphological and compression requirements. The anatomic biological profiles and geometric variables of leg cross sections were obtained as the basic design strategies of material morphology and pressure optimization. The applied knitting yarn combinations and machinery parameters were digitally obtained for the 3D seamless fabrication. Then, through the reconstructed geometric lower extremity models and determined tissue stiffness, the user-specific 3D FE CT-leg modellings were established for the biomechanical evaluation of pressure performances. Based on the practical wearing trials, the interfacial compressions of developed customized CTs had good agreements with the expected data. Moreover, through the subjective VAS assessments, the EWC of CTs had significant correlations with the exerted pressure levels.

9.2 Research Contributions

Based on the proposed bio-digital design, development, and biomechanical visualization systems, the major findings were listed as follows:

(i) The established digitalized equations can be used for precise fabric morphological and pressure control of CTs.

(ii) The clustered irregular levels and pressure prediction models provided a novel strategy as the pressure redistribution development guidance of CTs.

(iii) The proposed FE 3D homogeneous CT-leg systems effectively and accurately simulated the interfacial pressure behaviors.

(vi) The laid-in mesoscale models provided evidence-based guidance for the appropriate selection of yarn materials and fabric mechanical behavior visualization.

(v) The design variables of yarn combinations and fabric stretch ratios were optimized for the specific knitting setting determinations for the development of user-oriented CTs.

(vi) The comprehensive system provided an operable strategy for the bio-design and manufacturing of CTs.

Therefore, this study provided new systems for the bio-digital design, development, and biomechanical visualization of biomedical therapeutic materials with precise pressure management and enhanced wearing comfort, thereby improving the effectiveness and practical user compliance of CT products.

9.3 Limitations and Future Work

For the proposed comprehensive manufacturing and evaluation systems, several research limitations exist in the present study, as follows:

(i) for achievements of controllable fabric morphology and pressure behavior of CTs, our proposed equations were established based on the digitalization of the applied yarn-machinery knitting settings and laid-in knitted structures. Thus, these quantitative relationships could be only utilized for the adopted yarn combinations and knitting machine.

(ii) the pressure performances of CTs were estimated according to the values averaged by the four directions of each studied leg position. Thus, the pressure distributions showed uneven profiles along each leg height level and may result in discomfort wearing perceptions during practical applications.

(iii) in our proposed 3D FE CT-leg systems, the CTs were simplified as the linear elastic materials. Thus, the influences caused by the time-dependent behaviors on functional pressure performances of CTs during the long-term wearing process especially during dynamic physical activities need to be investigated.

(iv) the interfacial pressures of CTs were visualized for functional performance evaluation, thus, the influences of external compression on internal muscular stress and venous hemodynamics are not included.

(v) this study was performed to theoretically explore the influencing mechanisms of biological variations on pressure behaviors, and to build the primarily comprehensive framework to develop the customized CTs. Thus, several healthy subjects were recruited for feasibility evaluation of proposed design strategy.

Therefore, through the introduced limitations, the following research objectives will be explored in future work.

(i) To improve the user-compliance of CTs, more yarn materials, especially natural and biodegradable fibers will be utilized as the yarn compositions to enhance the comfortable perceptions and moisture management for the improvement of wearing comfort.

(ii) To facilitate the development of CTs with individual mechanical requirements, more knitted patterns with various structural characteristics will be designed and applied to reshape the uneven pressure profiles by varying fabric tensions.

(iii) To accurately simulate the pressure generation of CTs in long-term applications, the viscoelastic behaviors of CTs and body physical dynamic states will be considered in the 3D FE modelling. The mechanical variations caused by the time-dependent properties would be quantified for effective performance prediction.

(iv) To evaluate the external pressure behaviors on the internal tissue stress and venous hemodynamics, the 3D entity tissue-vein models will be established for the construction of multiple physics FE modelling.

(v) To improve the applicability of proposed design approach, more subjects with various healthy conditions and leg disease symptoms would be recruited to facilitate practical clinic effectiveness of user-specific CTs.

REFERENCES

1. Raju, S., P.J. Neglén, *Chronic venous insufficiency and varicose veins.* New England Journal of Medicine, 2009. **360**(22): p. 2319-2327.
2. Cires-Drouet, R.S., L. Fangyang, S. Rosenberger, M. Startzel, M. Kidwell, J. Yokemick, T. McDonald, M. Carlin, J. Sharma, J.D. Sorkin, *High prevalence of chronic venous disease among health care workers in the United States.* Journal of Vascular Surgery: Venous and Lymphatic Disorders, 2020. **8**(2): p. 224-230.
3. Ordi, J., L. Salmerón, F. Acosta, I. Camacho, N.J. Marín, *Study of prognostic factors and prevalence of post-thrombotic syndrome in patients with deep vein thrombosis in Spain.* Medicina Clínica (English Edition), 2016. **146**(2): p. 49-54.
4. Al Shammeri, O., N. AlHamdan, B. Al-Hothaly, F. Midhet, M. Hussain, A.J. Mohaimeed, *Chronic venous insufficiency: prevalence and effect of compression stockings.* International Journal of Health Sciences, 2014. **8**(3): p. 231.
5. Agale, S.V. *Chronic leg ulcers: epidemiology, aetiopathogenesis, and management*. Ulcers, 2013. (1): p. 413604.
6. Diken, A., A. Yalçınkaya, E. Aksoy, S. Yılmaz, K. Özşen, T. Sarak, K.J.P. Çağlı, *Prevalence, presentation and occupational risk factors of chronic venous disease in nurses.* Phlebology, 2016. **31**(2): p. 111-117.
7. Liu, R., X. Guo, T.T. Lao, T.J. Little, *A critical review on compression textiles for compression therapy: Textile-based compression interventions for chronic venous insufficiency.* Textile Research Journal, 2017. **87**(9): p. 1121-1141.
8. Gupta, D., *Functional clothing—definition and classification.* Indian Journal of Fibre & Textile Research, 2011. p. 321-326.
9. Berszakiewicz, A., A. Sieroń, Z. Krasiński, A. Cholewka, A.J. Stanek, A.P. Alergologii, *Compression therapy in venous diseases: current forms of compression materials and techniques.* Advances in Dermatology and Allergology/Postępy Dermatologii i Alergologii, 2020. **37**(6): p. 836.
10. Ramelet, A.A., *Compression therapy.* Dermatologic Surgery, 2002. **28**(1): p. 6-10.
11. Nair, B., *Compression therapy for venous leg ulcers.* Indian Dermatology, 2014. **5**(3): p. 378.
12. Guo, X., H. Cui, X.J. Wen, *Treatment of varicose veins of lower extremity: A literature review.* International Journal of Clinical and Experimental Medicine, 2019. **12**(3): p. 2142-2150.
13. Liu, R., *Comfort and mechanical function of compression stockings.* The Hong Kong Polytechnic University, 2006.
14. Espeit, L. T.J.P. Lapole, *Effects of graduated compression stockings, local vibration and their combination on popliteal venous blood velocity.* Phlebology, 2020. **35**(7): p. 505-512.
15. Atkins, R., W. K. Lam, A.T. Scanlan, C.M. Beaven, M.J. Driller, *Lower-body compression garments worn following exercise improves perceived recovery but not subsequent performance in basketball athletes.* Journal of Sports Sciences, 2020. **38**(9): p. 961-969.
16. Chiang, N., O. Rodda, S. Oldham, J. Sleigh, T.J.P. Vasudevan, *Effects of compression therapy and venous surgery on tissue oxygenation in chronic venous disease.* Phlebology, 2019. **34**(7): p. 474-480.
17. Lee, D.C., H.K.W. Law, A. Ali, S.E. Sheridan, S.H. Wong, S.W. Lee, *Compression garment-*

induced leg changes increase hemodynamic responses in healthy individuals. International Journal of Sports Medicine, 2020. **41**(01): p. 3-11.

18. Broatch, J.R., N. Brophy-Williams, E.J. Phillips, S.L. Halson, S. Barnes, D.J. Bishop, *Compression garments reduce muscle movement and activation during submaximal running.* Medicine and Science in Sports and Exercise, 2020. **52**(3): p. 685.
19. Mota, G.R., M.A. Simim, I.A. Dos-Santos, J.E. Sasaki, M.J. Marocolo, *Effects of wearing compression stockings on exercise performance and associated indicators: a systematic review.* Journal of Sports Medicine, 2020. **11**: p. 29.
20. Moñux, G., M. Serna-Soto, F. Plá-Sanchez, J.J. Zamorano-León, A. Segura, R. Rial, G. Freixer, K. Zekri-Nechar, C. Hugo-Martínez, J. Serrano, *Compression stockings attenuate the expression of proteins associated with vascular damage in human varicose veins.* Journal of Vascular Surgery: Venous and Lymphatic Disorders, 2021. **9**(2): p. 428-434.
21. Naci, B., S. Ozyilmaz, N. Aygutalp, R. Demir, G. Baltaci, Z.J. Yigit, *Effects of Kinesio Taping and compression stockings on pain, edema, functional capacity and quality of life in patients with chronic venous disease: a randomized controlled trial.* Clinical Rehabilitation, 2020. **34**(6): p. 783-793.
22. Djalalov, S., S. Sehatzadeh, D.H. Keast, W. Wong, *Economic evaluation of compression stockings for the prevention of venous leg ulcer recurrence in ontario.* Journal of Wound Care, 2020. **29**(3): p. 141-151.
23. Dissemond, J., K. Kroeger, M.J. Stuecker, V. Z. Dermatologie, *Evidence of compression therapy with special consideration of medical adaptive compression systems.* Der Hautarzt, 2020. **71**(4): p. 301-308.
24. Ontario. H., *Compression stockings for the prevention of venous leg ulcer recurrence: a health technology assessment.* Health Technology Assessment Series, 2019. **19**(2): p. 1.
25. Ayala-García, M.A., J.S. Reyes, N. Muñoz Montes, E.J.P. Guaní-Guerra, *Frequency of use of elastic compression stockings in patients with chronic venous disease of the lower extremities.* Phlebology, 2019. **34**(7): p. 481-485.
26. Ayala, A., J.D. Guerra, J.H. Ulloa, L.J.P. Kabnick, *Compliance with compression therapy in primary chronic venous disease: results from a tropical country.* Phlebology, 2019. **34**(4): p. 272-277.
27. Kankam, H.K., C.S. Lim, F. Fiorentino, A.H. Davies, M.S. Gohel, *A summation analysis of compliance and complications of compression hosiery for patients with chronic venous disease or post-thrombotic syndrome.* European Journal of Vascular and Endovascular Surgery, 2018. **55**(3): p. 406-416.
28. Chitambira, F., *Patient perspectives: explaining low rates of compliance to compression therapy.* Journal of the Australian Wound Management Association, 2019. **27**(4): p. 168-174.
29. Gong, J.M., J.S. Du, D.M. Han, X.Y. Wang, S. Qi, *Reasons for patient non-compliance with compression stockings as a treatment for varicose veins in the lower limbs: a qualitative study.* Plos One, 2020. **15**(4): p. e0231218.
30. Coghlan, N., J. Copley, T. Aplin, J. Strong, *How to improve compression garment wear after burns: Patient and therapist perspectives.* Burns, 2019. **45**(6): p. 1447-1455.
31. Tandler, S.F., *Challenges faced by healthcare professionals in the provision of compression hosiery to enhance compliance in the prevention of venous leg ulceration.* EWMA Journal, 2016. **16**(1).

32. Liu, R., T.T. Lao, T.J. Little, X. Wu, X. Ke, *Can heterogeneous compression textile design reshape skin pressures? a fundamental study.* Textile Research Journal, 2018. **88**(17): p. 1915-1930.

33. Liu, R., T.T. Lao, S. Wang, *Technical knitting and ergonomical design of 3D seamless compression hosiery and pressure performances in vivo and in vitro.* Polymers, 2013. **14**(8): p. 1391-1399.

34. Cheng, Z., V. Kuzmichev, D. Adolphe, *A digital replica of male compression underwear.* Textile Research Journal, 2020. **90**(7-8): p. 877-895.

35. Kim, H., M. Damhorst, *The relationship of body-related self-discrepancy to body dissatisfaction, apparel involvement, concerns with fit and size of garments, and purchase intentions in online apparel shopping.* Textile Research Journal, 2010. **28**(4): p. 239-254.

36. Laxa, M., S. John, J. Mathew, C. Kopecky, A. Campbell, D. Gumban, K. Kitchen, E. Sandle, C. Kachamkodom, B.J. Thomas, *One size does not fit all: nurse education for properly fitted anti-embolism compression stockings.* Journal of PeriAnesthesia Nursing, 2016. **31**(4): p. e39.

37. Jindal, R., J.F. Uhl, J.P. Benigni, *Sizing of medical below-knee compression stockings in an Indian population: a major risk factor for non-compliance.* Phlebology, 2020. **35**(2): p. 110-114.

38. Wade, R., F. Paton, N.J. Woolacott, *Systematic review of patient preference and adherence to the correct use of graduated compression stockings to prevent deep vein thrombosis in surgical patients.* Journal of Advanced Nursing, 2017. **73**(2): p. 336-348.

39. Nørregaard, S., S. Bermark, F.J. Gottrup, *Do ready-made compression stockings fit the anatomy of the venous leg ulcer patient?* Journal of Wound Care, 2014. **23**(3): p. 128-135.

40. Lurie, F., M. Passman, M. Meisner, M. Dalsing, E. Masuda, H. Welch, R.L. Bush, J. Blebea, P.H. Carpentier, M.J. De-Maeseneer, *The 2020 update of the CEAP classification system and reporting standards.* Journal of Vascular Surgery: Venous and Lymphatic Disorders, 2020. **8**(3): p. 342-352.

41. Carman, T.L., A. Al-Omari, *Evaluation and management of chronic venous disease using the foundation of CEAP.* Current Cardiology Reports, 2019. **21**(10): p. 1-8.

42. Partsch, H., *Compression therapy: clinical and experimental evidence.* Annals of Vascular Diseases, 2012. p. 68.

43. Winslow, E.H., D.L. Brosz, *Graduated compression stockings in hospitalized postoperative patients: correctness of usage and size.* AJN The American Journal of Nursing, 2008. **108**(9): p. 40-50.

44. Buset, C.S., J. Fleischer, R. Kluge, N.T. Graf, G. Mosti, H. Partsch, C. Seeli, F. Anzengruber, M. Kockaert, M.J. Hübner, *Compression stocking with 100% donning and doffing success: an open label randomised controlled trial.* European Journal of Vascular and Endovascular Surgery, 2021. **61**(1): p. 137-144.

45. Reich-Schupke, S., F. Feldhaus, P. Altmeyer, A. Mumme, M.J.P. Stücker, *Efficacy and comfort of medical compression stockings with low and moderate pressure six weeks after vein surgery.* Phlebology, 2014. **29**(6): p. 358-366.

46. Nelson, E.A., S. Bell-Syer, *Compression for preventing recurrence of venous ulcers.* Cochrane Database of Systematic Reviews, 2014(9).

47. Bjork, R., S.J. Ehmann, *STRIDE professional guide to compression garment selection for the lower extremity.* Journal of Wound Care, 2019. **28**(Sup6a): p. 1-44.

48. Liu, Y., H. Hu, L. Zhao, H. Long, *Compression behavior of warp-knitted spacer fabrics for*

cushioning applications. Textile Research Journal, 2012. **82**(1): p. 11-20.

49. Konarska, M., K. Soltynski, I. Sudol-Szopinska, A.J.F. Chojnacka, *Comparative evaluation of clothing thermal insulation measured on a thermal manikin and on volunteers.* Fibres and Textiles in Eastern Europe, 2007. **15**(2): p. 73.
50. Jin, Z., D. Chen, Y. Yang. *Research of effect of ergonomics on athletic shoes and costume design project*. International Conference on Education Technology, Management and Humanities Science (ETMHS 2015), 2015. Atlantis Press.
51. Jayasinghe, K., N. Seram, *The ergonomic factors: A study on active wear.* University of Moratuwa, Sri Lanka, 2017.
52. Teyeme, Y., B. Malengier, T. Tesfaye, I. Ciesielska-Wrobel, A.B.H. Musa, L.J. Langenhove, *A review of contemporary techniques for measuring ergonomic wear comfort of protective and sport clothing.* Autex Research Journal, 2021. **21**(1): p. 32-44.
53. Liu, R., B. Xu, C.Y. Ye. *Biodigital design and functional visualization of multi-class personalized compression textiles for ergonomic fit*. International Conference on Applied Human Factors and Ergonomics, 2019.
54. Dan, R., X. Fan, Z. Shi, M. Zhang, *Finite element simulation of pressure, displacement, and area shrinkage mass of lower leg with time for the top part of men's socks.* The Journal of The Textile Institute, 2016. **107**(1): p. 72-80.
55. Son, S., *Effect of different types of firefighter station uniforms on wearer mobility using range of motion and electromyography evidence.* Textile Research Journal, 2019. **21**(2): p. 209-219.
56. Teyeme, Y., B. Malengier, T. Tesfaye, I. Ciesielska-Wrobel, A.B. Musa, L. Langenhove, *A review of contemporary techniques for measuring ergonomic wear comfort of protective and sport clothing.* Autex Research Journal, 2021. **21**(1): p. 32-44.
57. Baek, H.J., H.S. Kim, M. Ahn, H. Cho, S.J. Ahn, *Ergonomic issues in brain-computer interface technologies: current Status, challenges, and future direction.* Computational Intelligence and Neuroscience: CIN, 2020. p. 4876397:1-4876397:2.
58. Cheng, Z., X. Wu, V. Kuzmichev, D.J.S. Adolphe, *The influence of major ergonomic factors on the demand for underwear in the highly educated male group.* Sustainability, 2022. **14**(19): p. 12464.
59. Ke, Y., Q.Zheng, *Development of mining workwear with high ergonomic performance fabrics based on the modular design concept.* Ergonomics, 2023. **29**(2): p. 547-554.
60. Barhoumi, H., S. Marzougui, S.B. Abdessalem, *A novel design approach and ergonomic evaluation of Class I compression legging.* International Journal of Clothing Science and Technology, 2022. **34**(2): p. 273-284.
61. Jung, W. K., S.M. Lee, S.H. Ahn, J. Park, *Development and assessment of a knitted shape memory alloy-based multifunctional elbow brace.* Journal of Industrial Textiles, 2022: p. 13.
62. Barhoumi, H., S. Marzougui, S.B. Abdessalem, *A novel design approach and ergonomic evaluation of Class I compression legging.* International Journal of Clothing Science and Technology, 2022. **34**(2): p. 273-284.
63. Partsch, H., M. Clark, S. Bassez, J.P. Benigni, *Measurement of lower leg compression in vivo: recommendations for the performance of measurements of interface pressure and stiffness.* Dermatologic Surgery, 2006.
64. Encan, B.C., A. Marmaralı, *Effect of yarn type on performance of diabetic socks.* Indian Journal of Fibre & Textile Research (IJFTR), 2022.

65. Hu, J., J.J. Lu, *Recent developments in elastic fibers and yarns for sportswear.* Textiles for Sportswear, 2015: p. 53-76.

66. Hu, J., J. Lu, Y. Zhu, *New developments in elastic fibers.* Polymer Reviews, 2008. **48**(2): p. 275-301.

67. Liu, R., X. Guo, T.T. Lao, T. Little, *A critical review on compression textiles for compression therapy: Textile-based compression interventions for chronic venous insufficiency.* Textile Research Journal, 2017. **87**(9): p. 1121-1141.

68. Bera, M., R. Chattopadhyay, D. Gupta, *Influence of linear density of elastic inlay yarn on pressure generation on human body.* Journal of Industrial Textiles, 2016. **46**(4): p. 1053-1066.

69. Wang, Y., Y. Cui, P. Zhang, X. Feng, J. Shen, Q. Xiong, *A smart mannequin system for the pressure performance evaluation of compression garments.* Textile Research Journal, 2011. **81**(11): p. 1113-1123.

70. Alisauskiene, D., D. Mikucioniene, L. Milasiute, *Influence of inlay-yarn properties and insertion density on the compression properties of knitted orthopaedic supports.* Fibres & Textiles in Eastern Europe, 2013. **21**(6): p. 74-78.

71. Gohar, E., A.J. Mazari, *Effect of multiple use on the durability of compression socks.* Fibres Textile, 2020. **3**: p. 64-69.

72. Özbayrak, N., Y. Kavuşturan, *The effects of inlay yarn amount and yarn count on extensibility and bursting strength of compression stockings.* Textile and Apparel, 2009. **19**(2): p. 102-107.

73. Xiong, Y. and X.M. Tao, *Compression garments for medical therapy and sports.* Polymers, 2018. **10**(6): p. 663.

74. Sang, J.S., M.S. Lee, M.J. Park, *Structural effect of polyester SCY knitted fabric on fabric size, stretch properties, and clothing pressure.* Fashion and Textiles, 2015. **2**(1): p. 1-9.

75. Soltanzadeh, Z., N. Shaikhzadeh, M. Haghpanahi, M.J.F. Mohajeri-Tehrani, *Prediction of compression properties of single jersey weft-knitted fabric by finite element analysis based on the hyperfoam material model.* Fibres & Textiles in Eastern Europe, 2016. **2**(116): p. 82-88.

76. Barhoumi, H., S. Marzougui, S.B. Abdessalem, *Influence of manufacturing parameters of knitted compression fabric on interface pressure.* Indian Journal of Fibre & Textile Research (IJFTR), 2018. **43**(4): p. 426-433.

77. Yuan, Y., J. Zhong, X. Ru, B. Liu, *Correlation of yarn feeding to the dimensional and elastic parameters of tubular knitted fabric.* Textile Research Journal, 2022. **92**(3-4): p. 446-455.

78. Gaied, I., S. Drapier, B. Lun, *Experimental assessment and analytical 2D predictions of the stocking pressures induced on a model leg by medical compressive stockings.* Journal of Biomechanics, 2006. **39**(16): p. 3017-3025.

79. Bruniaux, P., D. Crepin, B. Lun, *Modeling the mechanics of a medical compression stocking through its components behavior: part 1–modeling at the yarn scale.* Textile Research Journal, 2012. **82**(18): p. 1833-1845.

80. Chattopadhyay, R., D. Gupta, M. Bera, *Effect of input tension of inlay yarn on the characteristics of knitted circular stretch fabrics and pressure generation.* Journal of the Textile Institute, 2012. **103**(6): p. 636-642.

81. Liu, R., T.T. Lao, S. Wang, *Impact of weft laid-in structural knitting design on fabric tension behavior and interfacial pressure performance of circular knits.* Journal of Engineered Fibers and Fabrics, 2013. **8**(4): p. 154.

82. Laplanche, M.A., E. Drean, R. Convert, L. Schacher, *New method to measure compression*

stockings transparency. Journal of Industrial Textiles, 2014. **43**(4): p. 577-592.

83. Ke, W., G.M. Rotaru, J. Hu, R. Rossi, X. Ding, and S. Derler, *In vivo measurement of the friction between human skin and different medical compression stockings.* Tribology Letters, 2015. **60**(1): p. 1-9.

84. Sarı, B., N.J. Oğlakcıoğlu, *Analysis of the parameters affecting pressure characteristics of medical stockings.* Journal of Industrial Textiles, 2018. **47**(6): p. 1083-1096.

85. Narayana, H., J. Hu, B. Kumar, S. Shang, M. Ying, R.J. Young, *Designing of advanced smart medical stocking using stress-memory polymeric filaments for pressure control and massaging.* Materials Science and Engineering: C, 2018. **91**: p. 263-273.

86. Zhang, L., G. Sun, J. Li, Y. Chen, X. Chen, W. Gao, W. Hu, *The structure and pressure characteristics of graduated compression stockings: experimental and numerical study.* Textile Research Journal, 2019. **89**(23-24): p. 5218-5225.

87. Kırcı, F., E. Karamanlargil, S.C. Duru, B. Nergis, C.J.F. Candan, *Comfort properties of medical compression stockings from biodesigned and cotton fibers.* Polymers, 2021. **22**(10): p. 2929-2936.

88. Maity, S., K. Singha, P. Pandit, *Production of seamless knitted apparels*. Advanced Knitting Technology, 2022. p. 203-218.

89. Saini, N., S. Yadav, *Applications of compression garments.* Textile and Apparel Designing, 2022.

90. Reich-Schupke, S., M. Stücker, *Round-knit or flat-knit compression garments for maintenance therapy of lymphedema of the leg?–review of the literature and technical data.* Journal der Deutschen Dermatologischen Gesellschaft, 2019. **17**(8): p. 775-784.

91. Ališauskienė, D., D. Mikučioniene, L.J.F. Milašiute, *Influence of inlay-yarn properties and insertion density on the compression properties of knitted orthopaedic supports.* Fibres and textiles in Eastern Europe, 2013. **6**(102): p. 74-78.

92. Ališauskienė, D., D. Mikučionienė, *Prediction of compression of knitted orthopaedic supports by inlay-yarn properties.* Materials Science, 2014. **20**(3): p. 311-314.

93. Mikučionienė, D., L. Milašiūtė, *Influence of knitted orthopaedic support construction on compression generated by the support.* Journal of Industrial Textiles, 2017. **47**(4): p. 551-566.

94. Lozo, M., I. Lovričević, Ž. Pavlović, Z.J. Vrljičak, *Designing compression of preventive compression stockings.* Journal of Engineered Fibers and Fabrics, 2021. **16**: p. 15-16.

95. Chen, Q., P. Ma, H. Mao, X. Miao, G.J. Jiang, *The effect of knitting parameter and finishing on elastic property of PET/PBT warp knitted fabric.* Autex Research Journal, 2017. **17**(4): p. 350-360.

96. Siddiqui, M.O.R., A. Muhammad, M. Zubair, S.J.T. Danmei, *Prediction of air permeability of knitted fabric by using computational method.* Textile and Apparel, 2018. **28**(4): p. 273-279.

97. Unal, P.G., M.E. Üreyen, D.J.F. Mecit, *Predicting properties of single jersey fabrics using regression and artificial neural network models.* Polymers, 2012. **13**(1): p. 87-95.

98. Carpus, E., A. Dorogan, C. Mihai, I.J. Birliba, *Correlation study of multifunctional knitted textile structures characteristics.* De Redactie, 2017. p. 130.

99. Caggiati, A., *Fascial relationships of the short saphenous vein.* Journal of Vascular Surgery, 2001. **34**(2): p. 241-246.

100. Caggiati, A., *Fascial relationships of the long saphenous vein.* Circulation, 1999. **100**(25): p. 2547-2549.

101. Youn, Y.J., J. Lee, *Chronic venous insufficiency and varicose veins of the lower extremities.* The

Korean Journal of Internal Medicine, 2019. **34**(2): p. 269.

102. Lee, C.W.D., *The efficacy of sports compression garment on recovery hemodynamic responses and subsequent exercise performance after fatigue exercise*. The Chinese University of Hong Kong. 2019.

103. Mestre, S., J. Triboulet, C. Demattei, F. Veye, M. Nou, A. Pérez-Martin, M. Dauzat, I. Quéré, *Acute effects of graduated and progressive compression stockings on leg vein cross-sectional area and viscoelasticity in patients with chronic venous disease.* Journal of Vascular Surgery: Venous and Lymphatic Disorders, 2022. **10**(1): p. 186-195.

104. Zhuang, Z., D. Ai, Y. Yao, L. Zheng, J. Qin, D. Chen, S. Chai, J. Lu, Q. Jiang, X.J. Li, *The changes of the calf-vein deformation and femoral vein peak velocity during ankle pump exercise with or without graduated compression stockings.* BMC Musculoskeletal Disorders, 2022. **23**(1): p. 1-10.

105. Lim, C.S., A.H. Davies, *Graduated compression stockings.* Canadian Medical Association Journal, 2014. **186**(10): p. E391-E398.

106. Partsch, H., *Physics of Compression.* Published by Guset User, 2015.

107. Spiridon, M., D.J.M. Corduneanu, *Chronic venous insufficiency: a frequently underdiagnosed and undertreated pathology.* Mædica, 2017. **12**(1): p. 59.

108. Barhoumi, H., S. Marzougui, S.B.J. Abdessalem, *Clothing pressure modeling using the modified Laplace's law.* Clothing and Textiles Research Journal, 2020. **38**(2): p. 134-147.

109. Hui, C.L., S.F. Ng, *Model to predict interfacial pressures in multilayer elastic fabric tubes.* Textile Research Journal, 2001. **71**(8): p. 683-687.

110. Leung, W., D. Yuen, S.P. Ng, S.Q. Shi, *Pressure prediction model for compression garment design.* Journal of Burn Care & Research, 2010. **31**(5): p. 716-727.

111. Siddique, H.F., A.A. Mazari, A. Havelka, Z.J.F. Kus, *Performance characterization and pressure prediction of compression socks.* Polymers, 2020. **21**(3): p. 657-670.

112. Teyeme, Y., B. Malengier, T. Tesfaye, S. Vasile, W. Endalew, L. Langenhove, *Predicting compression pressure of knitted fabric using a modified laplace's law.* Materials, 2021. **14**(16): p. 4461.

113. Li, Q., G. Sun, Y. Chen, X. Chen, Y. Shen, H. Xie, Y. Li, *Fabricated leg mannequin for the pressure measurement of compression stockings.* Textile Research Journal, 2022: p. 16.

114. Lurie, F., R.J.P. Kistner, *Variability of interface pressure produced by ready-to-wear compression stockings.* Phlebology, 2014. **29**(2): p. 105-108.

115. Ghosh, S., A. Mukhopadhyay, M. Sikka, K.J. Nagla, *Pressure mapping and performance of the compression bandage/garment for venous leg ulcer treatment.* Journal of Tissue Viability, 2008. **17**(3): p. 82-94.

116. Hsu, T.R., *The finite element method in thermomechanics*. Springer Science & Business Media, 2012.

117. Ye, C., R. Liu, *Biomechanical prediction of veins and soft tissues beneath compression stockings using fluid-solid interaction model.* International Journal of Biomedical and Biological Engineering, 2020. **14**(10): p. 285-290.

118. Lu, Y., D. Zhang, L. Cheng, Z. Yang, J. Li, *Evaluating the biomechanical interaction between the medical compression stocking and human calf using a highly anatomical fidelity three-dimensional finite element model.* Textile Research Journal, 2021. **91**(11-12): p. 1326-1340.

119. Avril, S., P. Badel, L. Dubuis, P.Y. Rohan, J. Debayle, S. Couzan, J.F. Pouget, *Patient-specific*

modeling of leg compression in the treatment of venous deficiency, Patient-Specific Modeling in Tomorrow's Medicine, 2011, Springer. p. 217-238.

120. Dubuis, L., P.Y. Rohan, S. Avril, P. Badel, J. Debayle. *Patient-specific FE model of the leg under elastic compression*. 10th International Symposium on Computer Methods in Biomechanics and Biomedical Engineering, 2012.

121. Nemati, S., S. Shojaei, *Investigating effect of compression stocks on tissues of legs.* Materials, 2019. **2**(2): p. 14-20.

122. Han, Y., J. He, Y.J. Lu, *Sensitivity of the properties of the graduated compression stocking and soft tissues on the lower limb-stocking interfacial pressure using the orthogonal simulation test.* Medical Engineering & Physics, 2021. **95**: p. 84-89.

123. Zhang, M., H. Dong, X. Fan, R.J. Dan, *Finite element simulation on clothing pressure and body deformation of the top part of men's socks using curve fitting equations.* International Journal of Clothing Science and Technology, 2015. **27**(2) p. 207-220.

124. Yu, A., K.L. Yick, S.P. Ng, J. Yip, Y. Chan, *Numerical simulation of pressure therapy glove by using finite element method.* Burns, 2016. **42**(1): p. 141-151.

125. Cagle, J.C., P.G. Reinhall, K.J. Allyn, J. McLean, P. Hinrichs, B.J. Hafner, J.E. Sanders, *A finite element model to assess transtibial prosthetic sockets with elastomeric liners.* Medical & Biological Engineering & Computing, 2018. **56**(7): p. 1227-1240.

126. Ghorbani, E., H. Hasani, R.J. Nedoushan, *Finite element modelling the mechanical performance of pressure garments produced from elastic weft knitted fabrics.* The Journal of The Textile Institute, 2019. **110**(5): p. 724-731.

127. Ghorbani, E., H. Hasani, R.J. Nedoushan, N.J.F. Jamshidi, *Finite element modeling of the compression garments structural effect on the pressure applied to leg.* Polymers, 2020. **21**(3): p. 636-645.

128. Ye, C.Y., R. Liu, X.B. Wu, F.Y. Liang, M.T. Ying, J.Y. Lv, *New analytical model and 3D finite element simulation for improved pressure prediction of elastic compression stockings.* Materials & Design, 2022. **217**: p. 110634.

129. Heydon, R., *Finite element analysis of knee articular cartilage*. Ryerson University, 2011.

130. Parker, M., *Identification of the mechanical properties of living skin: an instrumentation and modelling study*. ResearchSpace@ Auckland, 2016.

131. Ranger, B.J., K.M. Moerman, B.W. Anthony, H. Herr, *Constitutive parameter identification of transtibial residual limb soft tissue using ultrasound indentation and shear wave elastography.* Journal of the Mechanical Behavior of Biomedical Materials, 2023. **137**: p. 105541.

132. Frauziols, F., P.Y. Rohan, P. Badel, S. Avril, J. Molimard, L.J Navarro, *Patient-specific modelling of the calf muscle under elastic compression using magnetic resonance imaging and ultrasound elastography.* Computer Methods in Biomechanics and Biomedical Engineering, 2013. **16**(Suppl 1): p. 332-3.

133. Mo, F., Y. Li, J. Li, S. Zhou, Z.J. Yang, *A three-dimensional finite element foot-ankle model and its personalisation methods analysis.* International Journal of Mechanical Sciences, 2022. **219**: p. 107108.

134. Hessami, R., A.A. Yazdi, A.J. Mazidi, *Investigation of tensile and flexural behavior of biaxial and rib 1× 1 weft-knitted composite using experimental tests and multi-scale finite element modeling.* Journal of Composite Materials, 2019. **53**(23): p. 3201-3215.

135. Wu, J., Z. Jin, J. Jin, Y. Yan, J.J. Tao, *Study on the tensile modulus of seamless fabric and tight*

compression finite element modeling. Textile Research Journal, 2020. **90**(1): p. 110-122.

136. Sha, S., A. Geng, Y. Gao, B. Li, X. Jiang, H. Tao, L. Luo, X. Yuan, H. Ke, X. Hu, *Review on the 3-D simulation for weft knitted fabric.* Journal of Engineered Fibers and Fabrics, 2021. **16**: p. 15589250211012527.

137. Li, Y., L. Yang, S. Chen, L.J.M. Xu, *Three dimensional simulation of weft knitted fabric based on surface model.* Mathematical and Computer Modelling, 2014. **18**: p. 52-57.

138. Wadekar, P., V. Perumal, G. Dion, A. Kontsos, D. Breen, *An optimized yarn-level geometric model for finite element analysis of weft-knitted fabrics.* Computer Aided Geometric Design, 2020. **80**: p. 101883.

139. Ghatrenabi, M.H., H. Dabiryan, H.J.F. Nosraty, *Modeling the geometry of weft-knitted integrated preforms as reinforcement of composite joints.* Polymers, 2021. **22**(9): p. 2572-2580.

140. Wu, L., F. Zhao, J. Xie, X. Wu, Q. Jiang, J. Lin, *The deformation behaviors and mechanism of weft knitted fabric based on micro-scale virtual fiber model.* International Journal of Mechanical Sciences, 2020. **187**: p. 105929.

141. Liu, D., D. Christe, B. Shakibajahromi, C. Knittel, N. Castaneda, D. Breen, G. Dion, A.J. Kontsos, *On the role of material architecture in the mechanical behavior of knitted textiles.* International Journal of Solids and Structures, 2017. **109**: p. 101-111.

142. Fong, K.W., S.Q. Li, R. Liu, *A new geometric model of laid-in weft-knitted fabrics.* Textile Research Journal, 2021. **91**(17-18): p. 2087-2105.

143. Abghary, M.J., H. Hasani, R.J.F. Nedoushan, *Numerical simulating the tensile behavior of 1× 1 rib knitted fabrics using a novel geometrical model.* Polymers, 2016. **17**(5): p. 795-800.

144. Hessami, R., A. Alamdar Yazdi, A.J. Mazidi, *The effect of loop density on the tensile behavior of biaxial weft knitted composites using both experimental tests and numerical method.* Journal of Industrial Textiles, 2021. **51**(1): p. 48-67.

145. Abghary, M.J., R.J. Nedoushan, H.J. Hasani, *Multi-scale modeling the mechanical properties of biaxial weft knitted fabrics for composite applications.* Applied Composite Materials, 2017. **24**(4): p. 863-878.

146. Karimian, M., H. Hasani, S. Ajeli, *Numerical modeling of bagging behavior of plain weft knitted fabric using finite element method.* Indian Journal of Fibre & Textile Research, 2014.

147. Abghary, M.J., R.J. Nedoushan, H.J.F. Hasani, *Simulation of the spherical deformation of biaxial weft-knitted fabrics using meso and macro models.* Polymers, 2016. **17**(10): p. 1702-1708.

148. Yekrang, J., D. Semnani, A.Z. Seyghlani, *Simulation and characterization of the mechanical properties of knitted esophageal stents using finite element and mathematical models.* Journal of Industrial Textiles, 2022. **51**(5): p. 7835S-7859S.

149. 	Ališauskienė, D., D. Mikučioniene, L. Milašiute, *Influence of inlay-yarn properties and insertion density on the compression properties of knitted orthopaedic supports.* Fibres and Textiles in Eastern Europe, 2013. **6**(102): p. 74-78.

150. Wang, Y.R., L.L. Gu, *Predictability of pressure characterization of medical compression stockings (MCSs) directly based on knitting parameters.* Polymers, 2022. **23**(2): p. 527-536.

151. Bandari, S.S., A. Asayesh, M.J.F. Latifi, *The effect of fabric structure and strain percentage on the tensile stress relaxation of rib weft knitted fabrics.* Polymers, 2020. **21**: p. 921-929.

152. Gautam, G.D., D.R. Mishra, *Dimensional accuracy improvement by parametric optimization in pulsed Nd: YAG laser cutting of kevlar-29/basalt fiber-reinforced hybrid composites.* Journal of

the Brazilian Society of Mechanical Sciences and Engineering, 2019. **41**: p. 1-22.

153. Shafiq, F., M.N. Pervez, M.M. Jilani, Z. Sarwar, H. Hasani, Y.J. Cai, *Structural relationships and optimization of resin-finishing parameters using the taguchi approach.* Cellulose, 2018. **25**: p. 6175-6190.

154. Sridharan, V., N.J. Muthukrishnan, *Optimization of machinability of polyester/modified jute fabric composite using grey relational analysis (GRA).* Procedia Engineering, 2013. **64**: p. 1003-1012.

155. Lusi, N., D.R. Pamuji, A. Fiveriati, A. Afandi, G.S. Prayogo. *Application of taguchi and grey relational analysis for parametric optimization of end milling process of ASSAB-XW 42*. International Seminar of Science and Applied Technology (ISSAT 2020), 2020. Atlantis Press.

156. Li, T. T., X. Zhang, L. Wu, H. Peng, B.C. Shiu, C.W. Lou, J.H. Lin, *Polyethylene terephthalate/basalt stab-resistant sandwich composites based on the box–behnken design: parameter optimization and empirical regression model.* Materials, 2020. **22**(7): p. 2391-2407.

157. Jansson, N., W. Wakeman, J.S. Månson, *Optimization of hybrid thermoplastic composite structures using surrogate models and genetic algorithms.* Composite Structures, 2007. **80**(1): p. 21-31.

158. Zimmerling, C., C. Poppe, O. Stein, L.J.M. Kärger, *Optimisation of manufacturing process parameters for variable component geometries using reinforcement learning.* Materials & Design, 2022. **214**: p. 110423.

159. Jamshaid, H., N. Ahmad, U. Hussain, R.J. Mishra, *Parametric optimization of durable sheeting fabric using taguchi grey relational analysis.* Journal of King Saud University-Science, 2022. **34**(4): p. 102004.

160. Wu, L., K. Yick, S. Ng, J. Yip, K.W. Kong, *Parametric design and process parameter optimization for bra cup molding via response surface methodology.* Expert Systems with Applications, 2012. **39**(1): p. 162-171.

161. Lin, Y., K.F Choi, M. Zhang, Y. Li, A. Luximon, L. Yao, J.Y. Hu, *An optimized design of compression sportswear fabric using numerical simulation and the response surface method.* Textile Research Journal, 2012. **82**(2): p. 108-116.

162. Zimmerling, C., D. Dörr, F. Henning, L. Kärger, *A machine learning assisted approach for textile formability assessment and design improvement of composite components.* Composites Part A: Applied Science and Manufacturing, 2019. **124**: p. 105459.

163. Tserpes, K., A.S. Koumpias, *A numerical methodology for optimizing the geometry of composite structural parts with regard to strength.* Composites Part B: Engineering, 2015. **68**: p. 176-184.

164. Ha, G.X., D. Marinkovic, M.W. Zehn, *Parametric investigations of mechanical properties of nap-core sandwich composites.* Composites Part B: Engineering, 2019. **161**: p. 427-438.

165. Venable, C.S, *Plasticity as applied to viscose and artificial silk.* The Journal of Physical Chemistry, 2002. **29**(10): p. 1239-1243.

166. Cohen, I., Y. Huang, J. Chen, J. Benesty, *Pearson correlation coefficient.* Noise Reduction in Speech Processing, 2009. p. 1-4.

167. Thakkar, A., D. Patel, P. Shah, *Pearson correlation coefficient-based performance enhancement of vanilla neural network for stock trend prediction.* Neural Computing and Applications, 2021. **3**(2): p. 1-16.

168. Siddique, H. F., A. A. Mazari, A. Havelka, Z. J. Kus, *Performance characterization and pressure prediction of compression socks.* Fibers and Polymers, 2020. (21) p. 657-670.

169. Siddique, H.F., A.A. Mazari, A. Havelka, Z. Kus, *Performance characterization and pressure prediction of compression socks.* Fibers and Polymers, 2020. **21**(3): p. 657-670.

170. Liu, R., J. Liu, T.T. Lao, M. Ying, X.B. Wu, *Determination of leg cross-sectional curvatures and application in pressure prediction for lower body compression garments.* Textile Research Journal, 2019. **89**(10): p. 1835-1852.

171. Maqsood, M., Y. Nawab, J. Umar, M. Umair, K. Shaker, *Comparison of compression properties of stretchable knitted fabrics and bi-stretch woven fabrics for compression garments.* The Journal of The Textile Institute, 2017. **108**(4): p. 522-527.

172. Bartol, K., D. Bojanić, T. Petković, T. Pribanić, *A review of body measurement using 3D scanning.* IEEE Access, 2021. **9**: p. 67281-67301.

173. Dan, R., X.R. Fan, L.B. Xu, M. Zhang, *Numerical simulation of the relationship between pressure and material properties of the top part of socks.* The Journal of The Textile Institute, 2013. **104**(8): p. 844-851.

174. Wang, Y.R., L.L. Gu, *Patient-specific medical compression stockings (MCSs) development based on mathematic model and non-contact 3D body scanning.* The Journal of The Textile Institute, 2022. p. 1-10.

175. Gao, Z., T. Liu, C. Shi. *The research of medical compression stockings equipment based on 3D scanner*. International conference on Applied Science and Engineering Innovation, 2015. Atlantis Press.

176. Lindell, E., H. Tingsvik, L. Guo, J. Peterson, *3D body scan as anthropometric tool for individualized prosthetic socks.* Autex Research Journal, 2021. **22**(3): p. 350-357.

177. Liu, R., B. Xu. *3D digital modeling and design of custom-fit functional compression garment*. International Conference on Artificial Intelligence on Textile and Apparel, 2018. Springer.

178. Panacek, E.A., C.B. Thompson, *Sampling methods: selecting your subjects.* Air Medical Journal, 2007. **26**(2): p. 75-78.

179. Bonin, D., S. Wischniewski, M. Peters, D. Radke, *Anthropometric measure extraction and offset calculation for 3D body scan data, obtained from an epidemiological health study*. DHM2020, IOS Press. 2020. p. 11-17.

180. Shuxian, Z., W.H. Zhao, B.H. Lu, *3D reconstruction of the structure of a residual limb for customising the design of a prosthetic socket.* Medical Engineering & Physics, 2005. **27**(1): p. 67-74.

181. Sajid, M., N. Tai, G. Goli, R. Morris, D. Baker, G. Hamilton, *Knee versus thigh length graduated compression stockings for prevention of deep venous thrombosis: a systematic review.* European Journal of Vascular and Endovascular Surgery, 2006. **32**(6): p. 730-736.

182. Ayhan, H., E. Iyigun, S. Ince, M.F. Can, S. Hatipoglu, M. Saglam, *A randomised clinical trial comparing the patient comfort and efficacy of three different graduated compression stockings in the prevention of postoperative deep vein thrombosis.* Journal of Clinical Nursing, 2015. **24**(15-16): p. 2247-2257.

183. Lee, Y., K. Kim, S. Kang, J.y. Kim, S. Kim, T. Kim, J. Jung. *Compression stocking length effects on oedema, pain, and satisfaction in nursing students: A pilot randomized trial*. Healthcare. 2012. **8**(2): p. 149.

184. Fabbri, R., L.D.F. Costa, J.C. Torelli, O.M. Bruno, *2D Euclidean distance transform algorithms: a comparative survey.* ACM Computing Surveys, 2008. **40**(1): p. 1-44.

185. Na, S., L. Xumin, G. Yong. *Research on k-means clustering algorithm: An improved k-means*

clustering algorithm. Third International Symposium on Intelligent Information Technology and Security Informatics, 2010.

186. Dubuis, L., S. Avril, J. Debayle, P. Badel, *Identification of the material parameters of soft tissues in the compressed leg.* Computer Methods in Biomechanics and Biomedical Engineering, 2012. **15**(1): p. 3-11.

187. Mishra, P., C.M. Pandey, U. Singh, A. Gupta, C. Sahu, A. Keshri, *Descriptive statistics and normality tests for statistical data.* Annals of Cardiac Anaesthesia, 2019. **22**(1): p. 67.

188. Meng, C., X.S. Jiang, J. Wang, X.M. Wei. *The complex network model for industrial data based on Spearman correlation coefficient*. International Conference on Internet of Things (iThings) and IEEE Green Computing and Communications (GreenCom) and IEEE Cyber, Physical and Social Computing (CPSCom) and IEEE Smart Data (SmartData). 2019.

189. Hazra, A., *Using the confidence interval confidently.* Journal of Thoracic Disease, 2017. **9**(10): p. 4125.

190. Tanaka, M., A. Sogabe. *A measuring system of the legs shape by using the kinect sensor*. Annual Conference of the Society of Instrument and Control Engineers of Japan (SICE), 2017.

191. Kulesh, P., L. Solomin, *Relationships between reference lines altered during leg shape correction as requested by the patient.* Genij Ortopedii, 2021.

192. Sjöstrand, Y., *Straight or bent legs?: On variation among the elks of the Naemforen rock carvings.* Fornvännen, 2010. **105**(1): p. 9-19.

193. Berszakiewicz, A., A. Sieroń, Z. Krasiński, A. Cholewka, A. Stanek, *Compression therapy in venous diseases: physical assumptions and clinical effects.* Advances in Dermatology and Allergology, 2020. **37**(6): p. 842.

194. Macintyre, L., M. Baird, P. Weedall, *The study of pressure delivery for hypertrophic scar treatment.* International Journal of Clothing Science and Technology, 2004. **16**(1/2): p. 173-183.

195. Ghorbani, E., H. Hasani, R.J. Nedoushan, N.J.F. Jamshidi, *Finite element modeling of the compression garments structural effect on the pressure applied to leg.* Fibers and Polymers, 2020. **21**: p. 636-645.

196. Cieślak, M., A. Karaszewska, E. Gromadzińska, K. Śledzińska, *I-SCAN method for the assessment of pressure exerted by textile products.* Fibres and Textiles in Eastern Europe, 2016. **6**(120): p. 121-127.

197. Li, Q., G. Sun, Y. Chen, X. Chen, Y. Shen, H. Xie, Y. Li, *Fabricated leg mannequin for the pressure measurement of compression stockings.* Textile Research Journal, 2022. **92**(19-20): p. 3500-3510.

198. Yu, W., J.T. Fan, and X.M. Qian, X.M. Tao, *A soft mannequin for the evaluation of pressure garments on human body.* Sen'i Gakkaishi, 2004. **60**(2): p. 57-64.

199. Frauziols, F., P. Badel, L. Navarro, J. Molimard, N. Curt, S. Avril, *Subject-specific computational prediction of the effects of elastic compression in the calf*, Biomechanics of Living Organs, 2017: p. 523-544.

200. Morse, C.I., *Gender differences in the passive stiffness of the human gastrocnemius muscle during stretch.* European Journal of Applied Physiology, 2011. **111**(9): p. 2149-2154.

201. Ochi, M., K. Kohara, Y. Tabara, T. Kido, E. Uetani, N. Ochi, M. Igase, T. Miki, *Arterial stiffness is associated with low thigh muscle mass in middle-aged to elderly men.* Atherosclerosis, 2010. **212**(1): p. 327-332.

202. Hobara, H., K. Kimura, K. Omuro, K. Gomi, T. Muraoka, M. Sakamoto, K. Kanosue,

Differences in lower extremity stiffness between endurance-trained athletes and untrained subjects. Journal of Science and Medicine in Sport, 2010. **13**(1): p. 106-111.

203. Le Sant, G., A. Nordez, R. Andrade, F. Hug, S. Freitas, R. Gross, *Stiffness mapping of lower leg muscles during passive dorsiflexion.* Journal of Anatomy, 2017. **230**(5): p. 639-650.
204. Amornvit, P., S Sanohkan, *The accuracy of digital face scans obtained from 3D scanners: an in vitro study.* International Journal of Environmental Research and Public Health, 2019. **16**(24): p. 5061.
205. Tümer, E.H., H. Erbil, *Extrusion-based 3D printing applications of PLA composites: a review.* Coatings, 2021. **11**(4): p. 390.
206. Plesec, V., J. Humar, P. Dobnik-Dubrovski, G. Harih, *Numerical analysis of a transtibial prosthesis socket using 3D-printed bio-based PLA.* Materials, 2023. **16**(5): p. 1985.
207. Gregor, A., E. Filová, M. Novák, J. Kronek, H. Chlup, M. Buzgo, V. Blahnová, V. Lukášová, M. Bartoš, A. Nečas, *Designing of PLA scaffolds for bone tissue replacement fabricated by ordinary commercial 3D printer.* Journal of Biological Engineering, 2017. **11**: p. 1-21.
208. Frauziols, F., P.Y. Rohan, P. Badel, S. Avril, J. Molimard, L. Navarro, *Patient-specific modelling of the calf muscle under elastic compression using magnetic resonance imaging and ultrasound elastography.* Computer Methods in Biomechanics and Biomedical Engineering, 2013. **16**(sup1): p. 332-333.
209. Dubuis, L., C.Y. Rohan, S. Avril, P. Badel, J. Debayle, *Patient-specific computational models: tools for improving the efficiency of medical compression stockings*, Computational Biomechanics for Medicine: Models, Algorithms and Implementation, 2013. Springer. p. 25-37.
210. Ye, C.Y., R. Liu, M.T. Ying, F.Y. Liang, Y. Shi, *Characterizing the biomechanical transmission effects of elastic compression stockings on lower limb tissues by using 3D finite element modelling.* Materials & Design, 2023. **232**: p. 112182.
211. Ternifi, R., M. Kammoun, P. Pouletaut, M. Subramaniam, J.R. Hawse, S.F. Bensamoun, *Ultrasound image processing to estimate the structural and functional properties of mouse skeletal muscle.* Biomedical Signal Processing and Control, 2020. **56**: p. 101735.
212. Dubois, G.J., D. Bachasson, L. Lacourpaille, O. Benveniste, J.Y. Hogrel, *Local texture anisotropy as an estimate of muscle quality in ultrasound imaging.* Ultrasound in Medicine & Biology, 2018. **44**(5): p. 1133-1140.
213. Rackauskaite, E., P. Kotsovinos, G. Rein, *Model parameter sensitivity and benchmarking of the explicit dynamic solver of LS-DYNA for structural analysis in case of fire.* Fire Safety Journal, 2017. **90**: p. 123-138.
214. Liu, Y., *ANSYS and LS-DYNA used for structural analysis.* International Journal of Computer Aided Engineering and Technology, 2008. **1**(1): p. 31-44.
215. Arnold, N., J. Scott, T. Bush, *A review of the characterizations of soft tissues used in human body modeling: Scope, limitations, and the path forward.* Journal of Tissue Viability, 2023. **32**(2): p. 286-304.
216. Affagard, J.-S., S.F. Bensamoun, P. Feissel, *Development of an inverse approach for the characterization of in vivo mechanical properties of the lower limb muscles.* Journal of Biomechanical Engineering, 2014. **136**(11): p. 111012.
217. Huzni, S., F. Oktianda, S. Fonna, F. Rahiem, L. Angriani, *The use of frictional and bonded contact models in finite element analysis for internal fixation of tibia fracture.* Frattura ed Integrità Strutturale, 2022. **16**(61): p. 130-139.

218. Chen, D., Z. Ye, Z. Pan, Y. Zhou, J. Zhang, *A permeability model for the hydraulic fracture filled with proppant packs under combined effect of compaction and embedment.* Journal of Petroleum Science and Engineering, 2017. **149**: p. 428-435.

219. Zhang, Z., D. Yangyang, H. Yanwei, *Analytical nonlinear response for a rotor with the Hertz contact and clearance.* Mechanics, 2019. **25**(6): p. 473-479.

220. Khot, S., U. Borah, *Finite element analysis of pin-on-disc tribology test.* International Journal of Science and Research, 2015. **4**(4): p. 1475-1480.

221. Colombo, G., C. Comotti, D.F. Redaelli, D. Regazzoni, C. Rizzi, A. Vitali. *A method to improve prosthesis leg design based on pressure analysis at the socket-residual limb interface*. International Design Engineering Technical Conferences and Computers and Information in Engineering Conference, 2016. 50077.

222. Razali, N.M., Y.B. Wah, *Power comparisons of shapiro-wilk, kolmogorov-smirnov, lilliefors and anderson-darling tests.* Journal of Statistical Modeling and Analytics, 2011. **2**(1): p. 21-33.

223. Bolboaca, S.D., L. Jäntschi, *Pearson versus Spearman, Kendall's tau correlation analysis on structure-activity relationships of biologic active compounds.* Leonardo Journal of Sciences, 2006. **5**(9): p. 179-200.

224. Tang, K., J. Fan, J. Zhang, M. Sarkar, C.W. Kan, *Effect of softeners and crosslinking conditions on the performance of easy-care cotton fabrics with different weave constructions.* Fibers and Polymers, 2013. **14**: p. 822-831.

225. Shahzad, M., A. Kamran, M.Z. Siddiqui, M. Farhan, *Mechanical characterization and FE modelling of a hyperelastic material.* Materials Research, 2015. **18**(5): p. 918-924.

226. Huang, X., J. Sun, J. Li, *Finite element simulation and experimental investigation on the residual stress-related monolithic component deformation.* The International Journal of Advanced Manufacturing Technology, 2015. **77**: p. 1035-1041.

227. Dai, X.Q., R. Liu, Y. Li, M. Zhang, Y.L. Kwok, *Numerical simulation of skin pressure distribution applied by graduated compression stockings.* Computational Textile, 2007: p. 301-309.

228. Bosnic, M., A. Rasoulian, S.C. Brandon, *Investigating the effects of activation state and location on lower limb tissue stiffness.* Journal of Biomechanics, 2022. **135**: p. 111032.

229. Korff, T., S.L. Horne, S.J. Cullen, A.J. Blazevich, *Development of lower limb stiffness and its contribution to maximum vertical jumping power during adolescence.* Journal of Experimental Biology, 2009. **212**(22): p. 3737-3742.

230. Lin, C.W., P.H. Tsui, C.H. Lu, Y.H. Hung, M.R. Tsai, J.Y. Shieh, W.C. Weng, *Quantifying lower limb muscle stiffness as ambulation function declines in duchenne muscular dystrophy with acoustic radiation force impulse shear wave elastography.* Ultrasound in Medicine & Biology, 2021. **47**(10): p. 2880-2889.

231. Fontanella, C.G., A. Arduino, I. Toniolo, C. Zampieri, L. Bortolan, E.L. Carniel, *Computational methods for the investigation of ski boots ergonomics.* Sports Engineering, 2021. **24**(1): p. 15.

232. Reich-Schupke, S., S. Surhoff, M. Stücker, *Pressure profiles of sport compression stockings.* Journal der Deutschen Dermatologischen Gesellschaft, 2016. **14**(5): p. 495-506.

233. Nørregaard, S., S. Bermark, F. Gottrup, *Do ready-made compression stockings fit the anatomy of the venous leg ulcer patient?* Journal of Wound Care, 2014. **23**(3): p. 128-135.

234. Aghajani, M., A.A. Jeddi, M.A. Tehran, *Investigating the accuracy of prediction pressure by laplace law in pressure-garment applications.* Journal of Applied Polymer Science, 2011.

121(5): p. 2699-2704.

235. Ng, S. F., C.L. Hui, *Pressure model of elastic fabric for producing pressure garments.* Textile Research Journal, 2001. **71**(3): p. 275-279.

236. Bera, M., R. Chattopadhyay, D. Gupta, *Influence of linear density of elastic inlay yarn on pressure generation on human body.* Journal of Industrial Textiles, 2016. **46**(4): p. 1053-1066.

237. Kannan, T.G., C.M. Wu, K. Cheng, *Effect of different knitted structure on the mechanical properties and damage behavior of Flax/PLA (Poly Lactic acid) double covered uncommingled yarn composites.* Composites Part B: Engineering, 2012. **43**(7): p. 2836-2842.

238. Maklewska, E., A. Nawrocki, J. Ledwoń, K. Kowalski, *Modelling and designing of knitted products used in compressive therapy.* Fibres & Textiles in Eastern Europe, 2006. **5**(59): p. 111--113.

239. Liu, X., T. Tang, W. Yu, R. Pipes, *Multiscale modeling of viscoelastic behaviors of textile composites.* International Journal of Engineering Science, 2018. **130**: p. 175-186.

240. Mirakhorli, S., A. Asayesh, *Evaluating the tensile stress relaxation of rib weft-knitted fabrics using viscoelastic models.* Mechanics of Time-Dependent Materials, 2022: **27**(4): p. 1-17.

241. Akhundov, V., *Axisymmetric deformation of cylinders made of homogeneous and fiber-reinforced elastic materials in butt-end torsion.* Mechanics of Composite Materials, 2010. **46**(2): p. 183-200.

242. Nasiri, E.,Y. Liu, *Development of a detailed 3D FE model for analysis of the in-plane behaviour of masonry infilled concrete frames.* Engineering Structures, 2017. **143**: p. 603-616.

243. Datta, M.K., B. Behera, A. Goyal, *Prediction and analysis of compression behaviour of warp-knitted spacer fabric with cylindrical surface.* Journal of Industrial Textiles, 2019. **48**(9): p. 1489-1504.

244. Liu, R., Y. Kwok, Y. Li, T. Lao, X. Zhang, *Quantitative assessment of relationship between pressure performances and material mechanical properties of medical graduated compression stockings.* Journal of Applied Polymer Science, 2007. **104**(1): p. 601-610.

245. Cherradi, Y., H. Kebir, A. Boukhriss, H. Ennamiri, M. Benyoucef, *Mechanical behaviour of 3D monofilament knitted fabrics: modeling, simulation and validation.* Journal of Industrial Textiles, 2022. **51**(4_suppl): p. 5774S-5793S.

246. Xu, W., Z. Dong, P. Ma, *Finite element analyses of auxetic warp-knitted fabric deformation behaviors under low-velocity impact loading.* The Journal of The Textile Institute, 2020. **111**(11): p. 1578-1586.

247. Liu, H., X. Tao, K. Choi, B. Xu, *Analysis of the relaxation modulus of spun yarns.* Textile Research Journal, 2010. **80**(5): p. 403-410.

248. Makarov, A., N. Pereborova, A. Litvinov, I. Volkova, *Modeling of deformation and relaxation processes of polymer yarn products.* Fibre Chemistry, 2021. **53**(4): p. 229-231.

249. Hasan, K.F., P.G. Horváth, T. Alpár, *Potential fabric-reinforced composites: a comprehensive review.* Journal of Materials Science, 2021. **56**(26): p. 14381-14415.

250. Shekarchizadeh, N., R. Jafari Nedoushan, T. Dastan, H. Hasani, *Experimental and numerical study on stiffness and damage of glass/epoxy biaxial weft-knitted reinforced composites.* Journal of Reinforced Plastics and Composites, 2021. **40**(1-2): p. 70-83.

251. Yan, R., Q. Zhang, B. Shi, S. Liu, Z. Qin, L. Jia, *Investigation on low-velocity impact and interfacial bonding properties of weft-knitted UHMWPE reinforced composites.* Journal of Industrial Textiles, 2022. **51**(3): p. 5370S-5388S.

252. Vignoli, L.L., M.A. Savi, P.M. Pacheco, A. Kalamkarov, *Comparative analysis of micromechanical models for the elastic composite laminae.* Composites Part B: Engineering, 2019. **174**: p. 106961.
253. Madenci, E., Y.O. Özkılıç, L. Gemi, *Experimental and theoretical investigation on flexure performance of pultruded GFRP composite beams with damage analyses.* Composite Structures, 2020. **242**: p. 112162.
254. Mansor, M., S. Sapuan, E. Zainudin, A. Nuraini, A. Hambali, *Stiffness prediction of hybrid kenaf/glass fiber reinforced polypropylene composites using rule of mixtures (ROM) and rule of hybrid mixtures (RoHM).* Journal of Polymer Materials, 2013. **30**(3): p. 321-334.
255. Malviya, R.K., R.K. Singh, R. Purohit, R. Sinha, *Natural fibre reinforced composite materials: Environmentally better life cycle assessment–A case study.* Materials Today Proceedings, 2020. **26**: p. 3157-3160.
256. Lurie, F., M. De Maeseneer, *The 2020 update of the CEAP classification: what is new?* European Journal of Vascular and Endovascular Surgery, 2020. **59**(6): p. 859-860.
257. Byrne, B., *Deep vein thrombosis prophylaxis: the effectiveness and implications of using below-knee or thigh-length graduated compression stockings.* Heart & Lung, 2001. **30**(4): p. 277-284.
258. Prandoni, P., A.W. Lensing, M.H. Prins, M. Frulla, A. Marchiori, E. Bernardi, D. Tormene, L. Mosena, A. Girolami, *Below-knee elastic compression stockings to prevent the post-thrombotic syndrome: a randomized, controlled trial.* Annals of Internal Medicine, 2004. **141**(4): p. 249-256.
259. Leung, K., K. Shin, F. Han, J. Jiao, *Ergonomic mastectomy bra design: Effect on core body temperature and thermal comfort performance.* Applied Ergonomics, 2021. **90**: p. 103249.
260. Manfei, X., D. Fralick, J. Zheng, B. Wang, C. Feng, *The differences and similarities between two-sample t-test and paired t-test.* Shanghai Archives of Psychiatry, 2017. **29**(3): p. 184.
261. Amrhein, V., F. Korner-Nievergel, T. Roth, *The earth is flat (p> 0.05): significance thresholds and the crisis of unreplicable research.* PeerJ, 2017. **5**: p. e3544.
262. Nørregaard, S., S. Bermark, F. Gottrup, *Do ready-made compression stockings fit the anatomy of the venous leg ulcer patient?* Journal of Wound Care, 2014. **23**(3): p. 128-135.
263. Sau-Fun, N., H. Chi-Leung, L. Fan, *Development of medical garments and apparel for the elderly and the disabled.* Textile Progress, 2011. **43**(4): p. 235-285.
264. Yang, W., Y. Xiong, S. Wang, H. Ren, C. Gong, Z. Jin, J. Wen, W. Zhang, X. Tao, C. Li, *A randomized controlled trial of standard vs customized graduated elastic compression stockings in patients with chronic venous disease.* Journal of Vascular Surgery: Venous and Lymphatic Disorders, 2023. **12**(2): p.101678.
265. Wang, Y.R., L.L. Gu, *Patient-specific medical compression stockings (MCSs) development based on mathematic model and non-contact 3D body scanning.* The Journal of The Textile Institute, 2023. **114**(8): p. 1157-1166.
266. Aydin, A., R. Atiç, Z. Aydin, C. Alemdar, M. Karakoç, K. Nas, S. Em, *Effects of the use of conventional versus computer-aided design/computer-aided manufacturing sockets on clinical characteristics and quality of life of transfemoral amputees.* Journal of Clinical and Experimental Medicine, 2019. **10**(1): p. 67-71.